School of Chemical and Petroleum Engineering

Department of Chemical Engineering

Graphene-based nanocarbons for catalytic degradation of aqueous contaminants

Stacey Indrawirawan

This thesis is presented for the Degree of

Doctor of Philosophy

Of

Curtin University

October 2016

Declaration

To the best of my knowledge and belief this thesis contains no material previously published by any other person except where due acknowledgement has been made. This thesis contains no material which has been accepted for the award of any other degree or diploma in any university.

Signature:

Date: 17th October 2016

I dedicate this thesis to my parents,

Lindrasari Horeb and Hendra Indrawirawan,

for their support, guidance, encouragement and love.

I love you all very much.

Acknowledgement

I would like to express my gratitude towards my supervisor Professor Shaobin Wang for his guidance, patience and encouragement in conducting this project. Professor Shaobin Wang is a very inspiring role model whom encouraged me to do research project under his supervision during my bachelor and PhD. Without his guidance and encouragement, I would not be able to complete my PhD and thesis.

I would also like to express my gratitude equally towards my co-supervisor Associate Professor Hongqi Sun. He has helped me tremendously throughout my PhD years. I am very thankful of his advices and past experiences that he shared, which have been very valuable to me. I would not be able to publish any journal papers without his help, guidance and input for my manuscripts.

Thank you very much for both Professor Shaobin Wang and Associate Professor Hongqi Sun for sparing their busy time whenever I had problems regarding my results and experiments. It is a great honour to be one of their students and be part of their amazing research group.

I would also like to thank Professor Shaomin Liu as the chairman of the thesis committee for his encouragement and support during my project.

I am also thankful of all lab technicians, Karen Hayes, Jason Wright, Araya Abera, Dipok Sarker, Ann Carroll, Melina Miralles, Xiao Hua, Yu Long, Andrew Chan, and Guanliang Zhou for preparing chemicals and guiding me on how to operate the equipments in the lab. Special thanks to Roshanak Doroushi and Anja Werner. Without their constant help and understanding, my experiments would not continue smoothly and progress at all.

I am also thankful to my fellow research friends; Xiaoguang, Shizen, Zana, Jian Kang, Ping, Huayang, Wenjie, Chen, Xiaochen, Qi, Jijiang, Yilin, Min, Fenny, Eugene, Qiaoran, Li, Yazi, Heng, Fern, and Yuxian. Thank you very much for all your help during my experiments, moral supports and encouragement you all gave me. I really enjoy our time together in and outside lab.

Last but not least, I would like to thank my family, Lindra, Hendra, Jessica and Alex for their love, constant support and encouragement. I truly thank mom and dad for always listening to my complaints and worries during my PhD, also supporting me academically and financially. Without them, I would not be able to go this far in my study and complete it successfully. Not forgetting Mojo, Missy, Tilly and Luffy, thank you for being there for me and being cute and adorable. Love you all.

Abstract

In this study, advanced oxidation processes (AOPs) have been chosen to treat organic pollutants from the waste water. AOPs can completely decompose organic contaminants by generating reactive radicals, hydroxyl ($OH^{\bullet}$) and sulfate ($SO_4^{\bullet-}$) radicals. This study is focused on catalytic oxidation of organic pollutants in both binary and ternary systems. Organic pollutants that are used in this study are phenol, nitrobenzene (NB) and methylene blue (MB). Graphene, nitrogen doped graphene (N-rGO), various metal-doped N-rGO, graphene nanoplate (GNP), fullerene (C60), single-walled carbon nanotube (SWCNT), nitrogen doped SWCNT (N-SWCNT) and mesoporous carbons are used for adsorption and catalytic activation with oxidants for phenol and NB degradation. Oxidants used are mainly peroxymonosulfate (PMS), persulfate (PDS) and H_2O_2. Photodegradation behaviours of phenol and MB are observed using various metal-doped N-rGO. N-rGO was synthesized using ammonium nitrate as N precursor and thermal annealed at different temperatures, while N-SWCNT was synthesized using urea as N precursor and thermal annealed at low temperature. The carbon catalysts were also used to observe the adsorption behaviour in phenol, NB, and MB degradation. The physical properties of these carbon catalysts are studied using various characterisation techniques. Electron paramagnetic resonance (EPR) is used in order to investigate the generation of free radicals formed during the degradation process. It was observed that free radicals, $OH^{\bullet}$ and $SO_4^{\bullet-}$ radicals, are generated in catalytic activation of both PMS and PDS. $SO_4^{\bullet-}$ radicals are the dominant radicals in phenol degradation, while $OH^{\bullet}$ radicals are the dominant radicals in NB degradation. These radicals along with reaction temperature, aqueous pH and properties of catalysts play significant roles in catalytic oxidation of phenol and NB. Varying catalyst loading, oxidant loading and initial contaminant concentration will also affect the degradation performance of organic contaminants.

Publications by the Author

Published and accepted papers:

1. **S. Indrawirawan**, H.Q. Sun, X.G. Duan, S.B. Wang, Low temperature combustion synthesis of nitrogen-doped graphene for metal-free catalytic oxidation, J. Mater. Chem. A, 2015; 3: 3432-3440.
2. **S. Indrawirawan**, H.Q. Sun, X.G. Duan, S.B. Wang, Nanocarbons in different structural dimensions (0-3D) for phenol adsorption and metal-free catalytic oxidation, Appl. Catal. B-Environ., 2015; 179: 352-362.
3. Duan XG, Sun HQ, Kang J, Wang YX, **Indrawirawan S**, Wang SB. Insights into heterogeneous catalysis of persulfate activation on dimensional-structured nanocarbons. ACS Catal. 2015; 5(8): 4629-36.
4. Duan XG, Ao ZM, Sun HQ, **Indrawirawan S**, Wang YX, Kang J, et al. Nitrogen-doped graphene for generation and evolution of reactive radicals by metal-free catalysis. ACS Appl. Mater. Interterfaces. 2015; 7(7): 4169-78.
5. Duan XG, **Indrawirawan S**, Sun HQ, Wang SB. Effects of nitrogen-, boron-, and phosphorus-doping or codoping on metal-free graphene catalysis. Catal. Today. 2015; 249: 184-91.
6. Wang YX, **Indrawirawan S**, Duan XG, Sun HQ, Ang HM, Tade MO. New insights into heterogeneous generation and evolution processes of sulfate radicals for phenol degradation over one-dimensional alpha-MnO2 nanostructures. Chem. Eng. J. 2015; 266: 12-20.
7. He JJ, Sun HQ, **Indrawirawan S**, Duan XG, Tade MO, Wang SB. Novel polyoxometalate@g-C3N4 hybrid photocatalysts for degradation of dyes and phenolics. J. Colloid Interface Sci. 2015; 456: 15-21.
8. Li D, Xie L, Fu M, Zhang J, **Indrawirawan S**, Zhang Y, Yu Y, Tang S. Synergistic Effects of Lanthanum-Pentaerythritol Alkoxide with Zinc Stearates and with β-diketone on the Thermal Stability of Poly(vinyl chloride) Thermal Stability. Polym. Degrad. Stab. 2015; 114: 52-59.

Manuscript submitted or in preparation:

1. **S. Indrawirawan**, H.Q. Sun, X.G. Duan, S.B. Wang, Temperature-dependent radical generation in peroxymonosulfate activation for catalytic oxidation of nitrobenzene. (**Submitted**)
2. **S. Indrawirawan**, H.Q. Sun, X.G. Duan, S.B. Wang, Radicals generation in metal-free persulfate activation. (**To be submitted**)

Content

CHAPTER 1. INTRODUCTION

1.1 Background

Environmental issues have become a major concern throughout the world especially at present era. These issues include climate change, air pollution, water pollution, food scarcity, plastic and toxic waste generation, energy consumption, drought, and many more [1-2]. Environmental issues increase with the expansion of population. Among these issues, water has gained more attention because it is wide and crucial resource in our daily life [3-4]. Solving water pollution would be an ideal way for the growing demand to gain more freshwater resources. People use water for drinking, agriculture (food source), cleaning and washing (for health and hygienic purpose). In 2002 World Health Organization (WHO) reported that 1.7 million people die each year from the unsafe water [5]. The average water footprint for a country is 1240 m^3/person/year, while 50% of the global water footprint is only covered by Brazil, China, Indonesia, India, Nigeria, Pakistan, USA, and Russia [6]. Climates, agriculture water usage and water consumption are the main factors considered in the water footprints [6].

The number of industrial and manufacturing plants increases with the growing population, thus water pollution in ocean, lakes, and rivers are becoming worse and worse [7]. Wastes discharged by industries generally contain inorganic and organic contaminants. Inorganic contaminants are contaminants from mineral sources [8]. Some of them are biodegradable but most of them are very difficult in biodegradation. Examples of inorganic contaminants are sand, salt, non-metal compounds (nitrogen, calcium, sodium, sulphur, ammonia) and metal compounds (cadmium, mercury, magnesium, zinc, iron, cobalt, manganese) [2, 8-9]. They are very reactive, hazardous and cause deoxygenation that reduces the oxygen concentration in water [2, 8]. This will be dangerous for the aquatic lives that reside in the lakes, rivers, or oceans [10-11]. Due to the heavy metal content, many inorganic contaminants are very toxic. Organic contaminants are synthetic and biodegradable contaminants from plants or animals sources. Few examples of organic contaminants are detergent,

oil, dyes, fuels, pesticides, paper, phenol, food waste, organic acids and many more [2, 11-12]. Synthetic organic contaminants involving chemicals in the stream are highly toxic. Biodegradable contaminants reduce the oxygen concentration in water due to their decomposition into simpler and harmless substances [2].

Many technologies have been developed to solve the water-related issues. Examples of water purification technologies are adsorption, conventional oxidation, membrane separation, distillation, filtration, flocculation, advanced oxidation processes (AOPs), wet air oxidation, coagulation and stripping techniques, etc [13-14]. Among these technologies, AOPs have been an effective approach for aqueous contaminant degradation due to their ability to degrade both low and high concentrations of contaminants in the water [15]. AOPs have several advantages compared to other water purification methods, such as a faster degradation rate, minimum residues, lower energy consumption, space optimisation and in-situ treatment [7]. Water pollution issues will never end until everyone in this world involves and takes care of our environment.

1.2 Objectives

The main objectives of this research are to develop highly efficient and robust non-metal and metal doped graphene for catalytic oxidation of aqueous organic contaminants, such as phenol, nitrobenzene and methylene blue. With the addition of peroxymonosulfate (PMS), persulfate (PDS) or hydrogen peroxide (H_2O_2), the effects of the carbon catalysts on degradation of contaminants are investigated.

The specific objectives include:

a. To synthesize nitrogen and various metal doped graphene for catalytic oxidation.
b. To investigate the prepared nitrogen doped graphene for activation of PMS for oxidation of phenol solution.
c. To investigate the prepared nitrogen doped graphene for activation of PMS and PDS for oxidation of nitrobenzene solution.
d. To investigate 0D to 3D nano carbon materials in adsorption and PMS activation for phenol degradation.

e. To investigate the performances of various metal doped graphene in catalytic and photocatalytic oxidation of phenol and methylene blue dye solution.
f. To study the kinetic and activation energy.
g. To investigate the mechanism of PMS and PDS activation for generation of hydroxyl and sulfate radicals.

1.3 Thesis Organisation

Chapter 1: Introduction

This chapter outlines current waste water issues and various technologies that have been developed in order to minimise these problems. The aim and objectives of this project are also discussed in this chapter.

Chapter 2: Literature review

This chapter presents different water purification technologies such as adsorption and advanced oxidation processes (AOPs) for organic contaminant removal in waste water. Catalyst preparation, comparison of binary and ternary systems AOPs are further discussed in this chapter. Various characterization techniques are also discussed.

Chapter 3: ***Low temperature combustion synthesis of nitrogen-doped graphene for metal-free catalytic oxidation. (J. Mater. Chem. A, 2015, 3: 3432-3440)***

This chapter investigates aqueous phenol degradation behaviour with the activation of peroxymonosulfate by nitrogen doped graphene. Nitrogen doped graphene was synthesized and thermally annealed at different temperatures in the range of 300 to 400 °C.

Chapter 4: ***Nanocarbons in different structural dimensions (0–3D) for phenol adsorption and metal-free catalytic oxidation. (Appl. Catal. B, 2015, 179: 352-362)***

This chapter reports adsorption and peroxymonosulfate activation for the degradation of phenol solution using 0D to 3D carbon nano materials, such as fullerene (0D), single-walled carbon nanotube (1D), graphene nanoplate (2D), and hexagonally and cubically ordered mesoporous carbon (3D). These materials were thermally annealed

at 350 °C, where the physical properties, phenol adsorption and oxidation were further investigated.

Chapter 5: Temperature-dependent radical generation in metal-free peroxymonosulfate activation for catalytic oxidation of nitrobenzene.

This chapter investigates nitrobenzene degradation using peroxymonosulfate with and without the addition of nitrogen doped single-walled carbon nanotube at different reaction temperatures in the range of 5 to 75 °C. The mechanism and dominant radical species are also presented in this chapter.

Chapter 6: Radicals generation in metal-free persulfate activation.

This chapter investigates nitrobenzene degradation using persulfate with and without the addition of nitrogen doped single-walled carbon nanotube at different reaction temperatures in the range of 5 to 75 °C. The mechanism and dominant radical species are also presented in this chapter.

Chapter 7: Modified nitrogen doped graphene by various metals for catalytic and photocatalytic oxidation of organic contaminants

This chapter reports the synthesis of nitrogen doped graphene doped by various metals such as cobalt, iron, nickel, silver and platinum. Catalytic oxidation of phenol was observed using peroxymonosulfate, persulfate and hydrogen peroxide. Further investigation was done in photodegradation of phenol and methylene blue with the help of radiation of ultraviolet and visible light.

Chapter 8: Conclusion

This chapter summarizes the research outcomes and also provides some recommendations for future research.

References

1. Trofimenko, N., Climate Change: Current Issues. **2011**.
2. Nesaratnam, S. T., *Water Pollution Control*. Wiley: **2014**.
3. Singh, N.; Thakur, A. K.; Sharma, P. L.; Sharma, P., *Climate Change and Environmental Issues*. Energy and Resources Institute: **2016**.

4. Afroz, R.; Masud, M. M.; Akhtar, R.; Duasa, J. B., Water pollution challenges and future direction for water resource management policies in Malaysia. *Environment and Urbanization Asia* **2014,** *5* (1), 63-81.

5. Organization, W. H., *The world health report 2002: reducing risks, promoting healthy life*. World Health Organization: **2002**.

6. Hoekstra, A. Y.; Chapagain, A. K., Water footprints of nations: water use by people as a function of their consumption pattern. *Water resources management* **2007,** *21* (1), 35-48.

7. Rao, D. G.; Senthilkumar, R.; Byrne, J. A.; Feroz, S., *Wastewater Treatment: Advanced Processes and Technologies*. Taylor & Francis: **2012**.

8. Manahan, S. E., *Hazardous Waste Chemistry, Toxicology, and Treatment*. Taylor & Francis: **1990**.

9. Grushko, Y. M., *Handbook of Dangerous Properties of Inorganic And Organic Substances in Industrial Wastes*. Taylor & Francis: **1992**.

10. Kramer, D. L., Dissolved oxygen and fish behavior. *Environmental biology of fishes* **1987,** *18* (2), 81-92.

11. District, M. M. S., Organic Waste Compounds in Streams: Occurrence and Aquatic Toxicity in Different Stream Compartments, Flow Regimes, and Land Uses in Southeast Wisconsin, 2006–9.

12. Leenheer, J.; Noyes, T., Effects of organic wastes on water quality from processing of oil shale from the Green River Formation, Colorado, Utah, and Wyoming. *US Geol. Surv., Prof. Pap.;(United States)* **1986,** *75* (1338).

13. Loures, C. C.; Alcântara, M. A.; Izário Filho, H. J.; Teixeira, A.; Silva, F. T.; Paiva, T. C.; Samanamud, G. R., Advanced oxidative degradation processes: fundamentals and applications. *Int Rev Chem Eng* **2013,** *5* (2), 102-120.

14. Liang, H. W.; Ting, Y. Y.; Sun, H. Q.; Ang, H. M.; Tade, M. O.; Wang, S. B., Solution combustion synthesis of Co oxide-based catalysts for phenol degradation in aqueous solution. *Journal of Colloid and Interface Science* **2012,** *372*, 58-62.

15. Parsons, S., *Advanced Oxidation Processes for Water and Wastewater Treatment*. IWA Publishing: **2004**.

CHAPTER 2. LITERATURE REVIEW

2.1 Introduction

One of the most critical issues in today's industrialization era is environmental pollution. Lakes, rivers and oceans are being overwhelmed with the organic and inorganic pollutants from waste water. Heavy metals, organics and toxic gases are some examples that cause pollution [1]. A variety of water treatment technologies have been employed to eliminate this issues. Adsorption and advanced oxidation processes (AOPs) have attracted many attentions as the most effective techniques for the removal of aqueous contaminants.

Adsorption is an excellent water purification technique due to its ability to remove both organic and inorganic contaminants. It is a very simple process and energy efficiency. It involves a separation and transferable processes between the target contaminants from aqueous into the adsorbent phase [2]. This adsorbent waste can be hazardous due to the accumulation of the contaminants in it and causing secondary pollution. Therefore AOPs, an emerging water treatment method has gained worldwide attentions due to the complete decomposition of organic pollutants [3-4].

AOPs can generate reactive species radicals such as hydroxyl ($OH^{\bullet}$) and sulfate radicals ($SO_4^{\bullet-}$) which have higher oxidation potential (2.8 eV and 2.6 eV, respectively) compared to that of ozone and hydrogen peroxide with oxidation potential of 2.07 eV and 1.77 eV, respectively [5-8]. Strong oxidants such as peroxymonosulfate (PMS) and peroxydisulfate or persulfate (PDS) can be activated to generate $OH^{\bullet}$ and $SO_4^{\bullet-}$ radicals or both by thermal (heat), UV light, transition metals, activated carbon, nano-carbons, microwave and integrated techniques which will then decompose the organic pollutants [9-11]. The abilities of the two radicals in degradation of environmental pollutants lie in the right combination of the pollutant, oxidant, and activation by the techniques as mentioned above. The combination of pollutants and either oxidant or catalyst is assigned to the binary pollutant degradation system; whereas, the combination of pollutant and oxidant activated by thermal (heat), UV light, transition metals, activated carbon, nano-carbons

techniques is assigned to the ternary pollutant degradation system.

Many adsorbents and catalysts are metal-based materials which are expensive and toxic [12-14]. This will result in secondary contamination and therefore metal-free catalysts such as carbon nano-materials are more favourable for environmental remediation.

2.2 Adsorption

Adsorption has gained many researchers' interests during the past decades. Adsorption is one of the most effective methods for removal of organic and inorganic contaminants. It is a purification and separation process between the target contaminants and the adsorbent phase [2]. Adsorption process occurs when a substance is separated from one phase at the surface of another. Adsorption can happen in solid-liquid and solid-gas systems [15].

Figure 2.1 shows the adsorption mechanism. Adsorbent is basically the solid material acting as the surface provider for adsorption, while adsorbate is the species/target contaminants that will be adsorbed. Desorption is the reverse process where the adsorbate is released from the surface of the adsorbent phase, which can be seen in **Figure 2.1** [16].

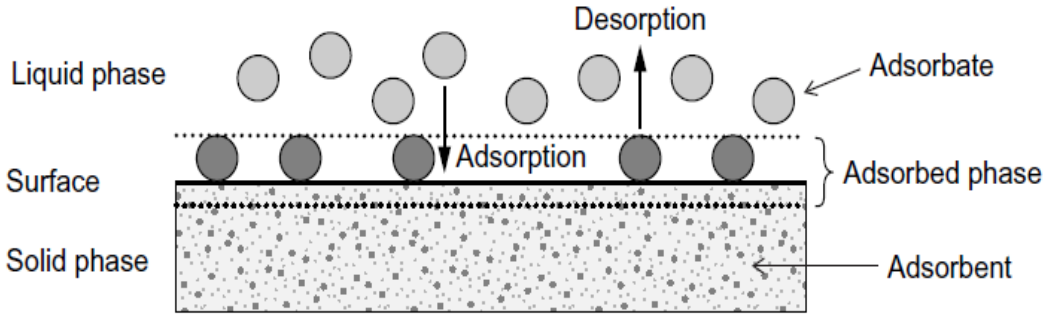

Figure 2.1. Schematic diagram of adsorption process [16]

2.2.1 Types of Adsorption

Chemical adsorption, also called chemisorption, is an adsorption process where chemical bonds are involved when the solid surface interacts with the adsorbed molecules. The attractive forces for chemisorption between the adsorbent and adsorbate are similar to the covalent bonds between atoms [17]. It occurs only as a

monolayer and due to the strong forces, the substances chemisorbed on solid surface can hardly be removed [15, 18].

On the other hand, physical adsorption called physisorption, is an adsorption process where physical forces are involved when the solid surface interacts with the adsorbed molecules. The attractive forces between the adsorbent and adsorbate come from the van der Waals forces [19]. Physisorption is reversible because the van der Waals forces are not strong enough [17].

Table 2.1. Comparison of chemisorption and physisorption

Chemisorption	Physisorption
Strong chemical bonds	Weak van der Waals forces
Monolayer adsorption	Multilayer adsorption
(Langmuir isotherm model)	(BET isotherm model)
Surface specific	No surface specific
Takes place at high temperatures	Takes place at low temperatures
Non-reversible	Reversible
Electron transfer and activated	No electron transfer and non-activated

2.2.2 Adsorption Isotherms

Adsorption isotherm describes the relationship in equilibrium condition between the amounts adsorbed by an adsorbent with the amount of adsorbate left [2, 20]. The most commonly used adsorption isotherms are BET (Brunauer, Emmet, and Teller), Langmuir, and Freundlich isotherms.

BET isotherm describes that molecules can be adsorbed in more than one layer. BET equation is expressed by the equation [20]:

$$\frac{C_e}{q_e(C_s - C_e)} = \frac{1}{q_s C_{BET}} + \frac{(C_{BET} - 1)}{q_s C_{BET}}\left(\frac{C_e}{C_s}\right) \qquad (2.1)$$

Where, C_e is the equilibrium concentration, C_s is the adsorbate concentration, C_{BET} is the BET adsorption capacity.

Langmuir isotherm applies for the adsorption of single layer. Langmuir equation is expressed by the equation [21]:

$$\frac{C_e}{q_e} = \frac{1}{bq_{max}} + \frac{C_e}{q_{max}} \qquad (2.2)$$

Where, q_e is the adsorbed concentrate, and q_{max} and b are constants for adsorption.

Freundlich isotherm applies for heterogeneous surface with different adsorption sites. The equation is expressed by the equation [21]:

$$q_e = K_f C_e^{\frac{1}{n}} \qquad (2.3)$$

Where, K_f and n are the Freundlich constants.

2.2.3 Types of adsorbents

There are many materials that can be used as an adsorbent. **Table 2.2** shows the list of basic types of industrial adsorbents. There are several factors needed to be considered in selecting the appropriate adsorbents, for example, kinetic properties, selectivity, adsorption capacity, wastewater composition, environmental impact and the cost of adsorbent [22]. Different adsorbents have different porous structures, sizes and shapes which also play an important role. The porosity is classified into three categories: micropores (smaller than 1 nm), mesopores (between 1-25 nm), and macropores (larger than 25 nm) [17].

Table 2.2. Basic types of industrial adsorbents [23]

Carbon adsorbents	Mineral adsorbents	Other adsorbents
Active carbons	Clay minerals	Synthetic polymers
Carbonaceous nanomaterials	Metal oxides	Mixed sorbents
Fullerenes	Metal hydroxides	Composite adsorbents
Activated carbon fibres	Silica gels	
Heterofullerenes	Zeolite	
Molecular carbon sieves	Pillared clays	
Mesocarbon microbeads	Activated alumina	
	Inorganic nanomaterials	
	Porous clay hetero-structures	

Even though activated carbon is expensive, it is the most commonly used adsorbent in adsorption process. It can be easily regenerated for re-use, but the adsorption efficiency decreases along with increasing number of regeneration. For the activated carbon, there are two different heterogeneous surfaces which come from two sources known as geometrical and chemical routes. The surface geometrical heterogeneity is ascribed to the differences in size and shape of pores, cracks, pits and steps. The surface chemical heterogeneity is related to the different functional groups which are mainly oxygen groups that are located most frequently at the edges along with various surface impurities [24].

2.2.4 Factors affecting adsorption

There are various factors affecting adsorption process, such as surface area, solution pH, temperature and initial concentration of the contaminant or adsorbate [15]. At pH lower than 5, the adsorption efficiency is decreased; where the rate of removal increases with a higher pH [15, 25]. At a constant pH, higher initial concentration will result in a lower rate of adsorption [26]. Adsorption is an exothermic process, therefore, efficiency of adsorption increases when the temperature is higher [27-28]. Adsorption is a surface process, hence the specific surface area (SSA) of the adsorbent will affect the adsorption and a larger porosity of adsorbate will enhance adsorption [16]. **Table 2.3** lists the advantages and disadvantages of adsorption.

Table 2.3. Advantages and disadvantages of adsorption

Advantages	Disadvantages
Simple design and operation	High cost
Able to remove both organic and inorganic contaminants	Sludge ballasting might occurred (depending on the type of adsorbents)
Able to regenerate the used adsorbent	Adsorbent waste can be hazardous due to the accumulation and transferability of the contaminant from aqueous to the adsorbent
Energy efficiency	

2.2.5 Adsorption application in phenol removal

Among many other organic contaminants, phenol has attracted to many researchers. The process of phenol removal in adsorption of activated carbon is explained further.

The process of adsorption of phenol on activated carbon is generally classified as physisorption or chemisorption [29]. Physisorption of phenol depends strictly on the porosity (surface geometrical heterogeneity) of the activated carbon, whereas chemisorption depends on the availability of the basal planes in the activated carbon (surface chemical heterogeneity) [29]. The presence of surface oxygen sites on carbon surface has been reported to have a capacity of chemisorption for binding phenol [24]. Phenols have weak acidic properties. In order to improve the adsorption of phenol, it is preferable for activated carbon to have the basic surface. Some of the oxygen groups such as carbonyl, carboxyl, phenolic hydroxyl and lactonic are acidic, whereas pyrone, chromene and quinone are basic [24, 29].

Three possible interactions between phenol and carbon surface have been proposed:
(a) A donor-acceptor complex interaction between the negatively charged aromatic ring of phenol and the positively charged basal plane of carbon containing oxygen functional groups [30]
(b) A dispersive interaction between the phenol aromatic rings and the π-electrons of the graphitic carbon basal planes [31]
(c) An electrostatic attraction and repulsion when ions are present [32]

2.3 Advanced oxidation processes

Advanced oxidation processes (AOPs) are emerging and effective water purification methods. This technique has attracted interests due to the complete decomposition, high efficiency and simplicity to remove organic contaminants in waste water [9, 33]. AOPs rely on highly reactive free radicals, mainly hydroxyl radicals, $OH^{\bullet}$, which have a higher oxidation potential (2.8 eV) compared to that of ozone and hydrogen peroxide with oxidation potential of 2.07 eV and 1.77 eV, respectively [5-6, 34]. The stronger the oxidizing agent is, the easier and faster the decomposition of the target pollutants can be. **Table 2.4** lists the common oxidizing agents and their oxidizing potentials [35].

Table 2.4. Oxidizing agents and potential

Oxidizing agents	Oxidizing potential (eV)
Fluorine	3.03
Hydroxyl radical	2.8
Atomic Oxygen	2.42
Ozone	2.07
Hydrogen peroxide	1.77
Permanganate	1.67
Chlorine	1.36
Bromine	1.09

$OH^{\bullet}$ radicals demonstrate important characteristics such as [5]:

1. highly reactive
2. powerful oxidation ability
3. being easily produced
4. electrophilic in behaviour
5. non-selective

$OH^{\bullet}$ radicals are highly reactive due to their unpaired electrons. Degradation of contaminants will occur after ozone, hydrogen peroxide, or similar oxidants are initiated to produce unpaired electrons, which then generate $OH^{\bullet}$ radicals.

The effectiveness of AOPs depends on the physical and chemical properties of pollutants, operating conditions, and the types of AOPs and its aptitude to generate $OH^{\bullet}$ radicals [36]. **Table 2.5** lists the advantages and disadvantages of AOPs

Table 2.5. Advantages and disadvantages of AOPs [9-10, 37].

Advantages	Disadvantages
Fast rate of reaction	Complete mineralization does not occur
Efficient to degrade all organic contaminants	Rely on pH control and oxidant concentration
Minimum by-product formation	High operation cost
Low energy consumption	Continuous chemicals supply
Emerging technologies	Production of more hydrophilic residuals
Low chemical usage	

In-situ treatment	

There are many types of AOPs, such as photocatalysis, Fenton reaction and ozonation processes which will be explained further in this chapter.

2.3.1 Photocatalysis

In this process, the generation of $OH^{\bullet}$ radicals occurs in the presence of ultraviolet (UV) light or visible light, oxygen or water and a catalyst. Titanium dioxide (TiO_2), a photosensitive semiconductor, is the commonly used catalyst in photocatalysis reaction because it is inexpensive, non-toxic, highly stable, biologically inert, and efficient in oxidation [38-39]. The band gap energy of TiO_2 (anatase) is 3.2 eV. **Table 2.6** shows the value of band gap energy for several commonly used semi-conductor catalysts.

Table 2.6. Band gap energy and activation wavelength for commonly used semi-conductor catalysts [40-42]

Catalyst	Band gap energy (eV)	Activation wavelength (nm)
TiO_2 (anatase)	3.2	387
GaAs	1.4	887
Fe_2O_3	2.2	565
CdS	2.4	497
ZnO	3.2	390
WO_3	2.8	443
SnO_2	3.5	318

The formation of electron-hole pairs needs photon energy to overcome the band gap energy between the valence bands (VB) and conduction bands (CB). When a semi-conductor is exposed to photon illumination, it will generate electron-hole pairs. If $hv\ (photon\ energy) > E_g$ (band gap energy) the electrons will be excited and migrate to the conduction band. Photocatalysis occurs when these electron-hole pairs diffuse out to the surface of the crystal and involves in chemical reactions with electron donors and acceptors [43-45]. The schematic diagram of the reaction can be seen in **Figure 2.2.**

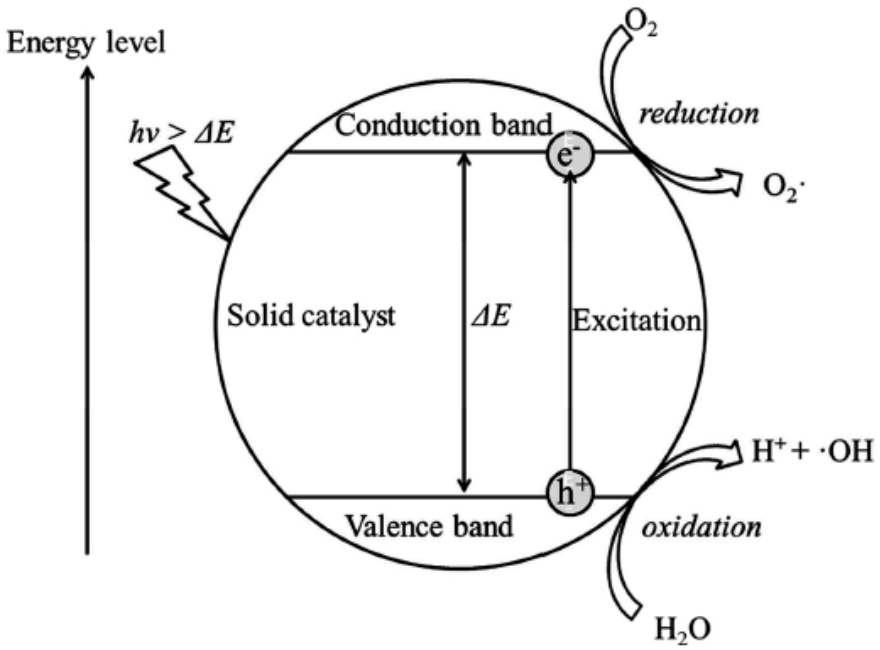

Figure 2.2. Schematic diagram of photocatalysis process [46]

The initial reaction mechanism is as follow [47-48]:

$$TiO_2 + hv \rightarrow e^- + h^+ \quad (2.4)$$

$$h^+ + OH^- \rightarrow {}^{\bullet}OH \quad (2.5)$$

$$Ti^{4+} + e^- \rightarrow Ti^{3+} \quad (2.6)$$

$$Ti^{3+} + O_{2ads} \rightarrow Ti^{4+} + O^-_{2ads} \quad (2.7)$$

$${}^{\bullet}OH + pollutant \rightarrow oxidised\ pollutant \quad (2.8)$$

$$h^+ + e \rightarrow thermal\ heat\ or\ luminescence \quad (2.9)$$

Photocatalysis can also convert target contaminants into carbon dioxide (CO_2) and water under ambient condition without the addition of heat, chemical reactants [49-51]. The advantages of this process are no waste disposal problem, low cost, complete mineralization, and mild temperature and pressure conditions required [52-53]. Several factors affecting photocatalysis play an important role in determining its effectiveness, such as initial contaminant concentration, presence of anions and cations, pH level of the aqueous contaminant, light intensity and wavelength, adsorption, and reaction temperatures [54].

2.3.2 Fenton reaction

Fenton reaction is one of AOPs involving hydrogen peroxide (H_2O_2) as an oxidizing agent and ferrous iron (Fe(II)) as a metal catalyst via electron transfers [55-56]. Fe(II) is oxidized to Fe(III) when ferrous iron reacts with H_2O_2, which also generating hydroxyl radicals and hydroxyl ions [57]. Then hydroxyl radicals oxidize the target organic contaminant.

The Fenton reactions involve the following reactions [58]:

$$Fe^{2+} + H_2O_2 \rightarrow Fe^{3+} + {}^{\bullet}OH + OH^- \quad (2.10)$$

$$OH^{\bullet} + RH \rightarrow R^{\bullet} + H_2O \quad (2.11)$$

$$R^{\bullet} + Fe^{3+} \rightarrow R^{+} + Fe^{2+} \quad (2.12)$$

$$Fe^{2+} + OH^{\bullet} \rightarrow Fe^{3+} + OH^- \quad (2.13)$$

$$Fe^{3+} + H_2O_2 \leftrightarrow Fe\cdots OOH^{2+} + H^+ \quad (2.14)$$

$$Fe\cdots OOH^{2+} \rightarrow HO_2^{\bullet} + Fe^{2+} \quad (2.15)$$

$$H_2O_2 + Fe^{2+} \rightarrow OH^{\bullet} + OH^- + Fe^{3+} \quad (2.16)$$

$$OH^{\bullet} + RH \rightarrow R^{\bullet} + H_2O \quad (2.17)$$

Photo-Fenton reaction is a process where sunlight, ultraviolet (UV), or visible light is used in order to enhance the degradation rate by converting Fe (II) to Fe (III) [9, 59]. H_2O_2 and appropriate light wavelength are the main contributors in the formation of hydroxyl radicals. The photo-Fenton reaction is as follow [59]:

$$H_2O_2 + hv \rightarrow 2OH^{\bullet} \quad (2.18)$$

$$Fe(OH)^{2+} + hv \rightarrow Fe^{2+} + OH^{\bullet} \quad (2.19)$$

$$Fe^{3+}(L^-) + hv \rightarrow Fe^{2+} + L^{\bullet} \text{(L is an organic ligand)} \quad (2.20)$$

Effective Fenton reaction depends on several factors: the pH level and temperature of the aqueous contaminants, H_2O_2 concentration, H_2O_2/Fe ratio, and also reaction time [58, 60-61]. Low pH level of the aqueous contaminant solutions ranging from 2 to 4 will effectively initiate Fenton reaction. Fenton reaction becomes inefficient when the pH

level is high, neutral to basic condition, due to the precipitation generation of ferric iron salts.

Fenton reaction only uses a small amount of energy, and is cost effective in operation compared to other AOPs. The pH control is very important since pH level changes during Fenton reaction. Secondary contamination and formation of iron sludge from the ferrous iron are main concerns, but despite these disadvantages, Fenton reaction has been applied in many industrial waste water treatments [62].

2.3.3 Ozonation

In this process, ozone, O_3, is decomposed in water which then generates oxygen containing radicals. O_3 itself has a relatively high oxidation potential of 2.7 eV, thus it can degrade target organic contaminants directly and indirectly through hydroxyl radicals generation [5, 36, 63-64]. Overall reaction of $OH^{\bullet}$ radicals generation is as follow [36]:

$$3O_3 + H_2O \rightarrow 2OH^{\bullet} + 4O_2 \qquad (2.21)$$

Figure 2.3 shows the oxidation processes of ozone with inorganic or organic contaminants (S). Oxygen atom is transferred from O_3 to S via two-electron oxidation.

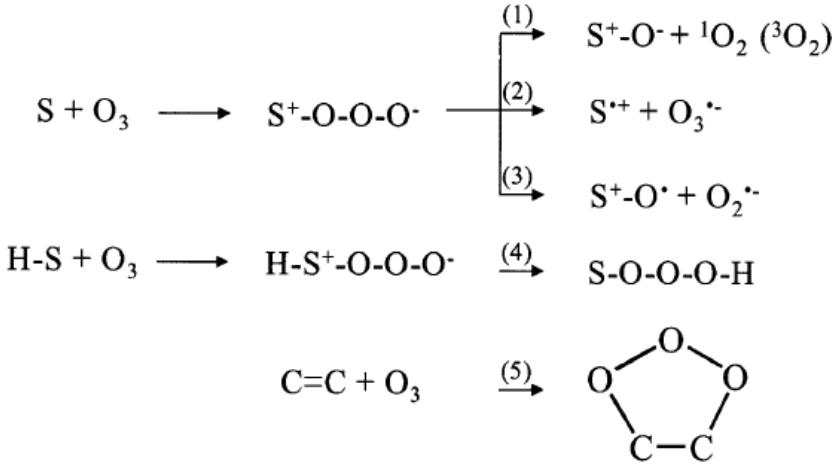

Figure 2.3. Oxidation process of ozone (O_3) with S (any inorganic and organic contaminant) [65]

Efficient ozonation occurs when the pH level of the aqueous contaminant is higher than 10, however in neutral and acid conditions, this process becomes inefficient [66]. Ozonation process might form intermediate compounds that are more toxic than the

original target contaminant. Its chemical kinetics are also slow [67]. **Figure 2.4** shows the schematic diagram of desired and undesired effects of ozonation processes. More research has been done to make ozonation more efficient and also to reduce the ozone and energy consumption which results in reducing operating costs.

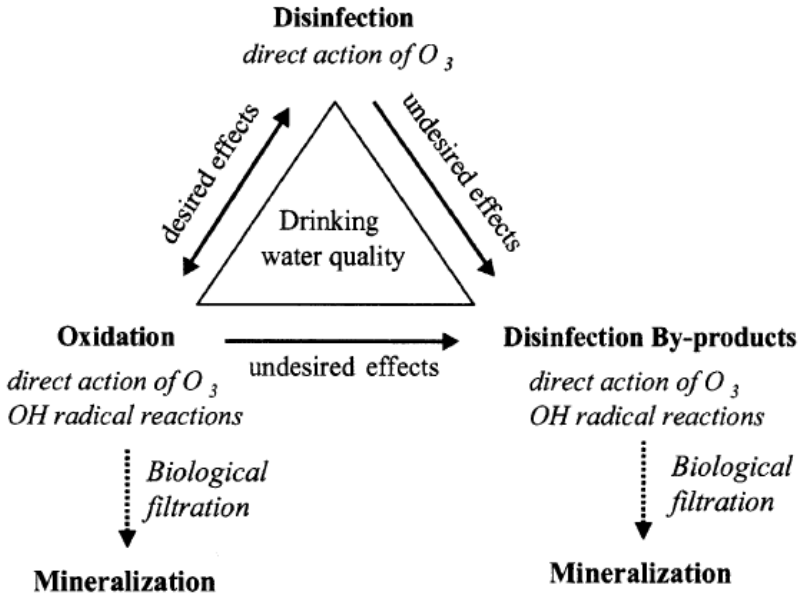

Figure 2.4. Desired and undesired effects of Ozonation processes [65]

H_2O_2 can be applied to the ozonation reaction in order to enhance the effectiveness of the process. $OH^{\bullet}$ generation is increased when O_3 reacts with H_2O_2, and then oxidizes the target contaminants. The O_3/ H_2O_2 reaction mechanism is as follow [36]:

$$H_2O_2 \rightarrow HO_2^- + H^+ \qquad (2.22)$$

$$HO_2^- + O_3 \rightarrow OH^{\bullet} + O_2^- + O_2 \qquad (2.23)$$

$OH^{\bullet}$ radical generation can be also further enhanced by the photolysis of ozone using ultraviolet (UV) light. Any UV source can be used in the O_3/ UV process due to ozone maximum absorption at 254 nm [9]. This process produces H_2O_2, which then generate $OH^{\bullet}$ radicals. The reactions are as follow [36]:

$$O_3 + H_2O + h\nu \rightarrow H_2O_2 + O_2 \qquad (2.24)$$

$$H_2O_2 + h\nu \rightarrow 2OH^{\bullet} \qquad (2.25)$$

The combination of O_3 and UV degrades the target contaminants through the reactions with $OH^{\bullet}$ radicals and the absorption of UV irradiation, making this process more effective than ozonation only [68].

2.4 Binary and ternary systems for pollutant degradation

Many studies have been carried out to investigate the efficiency of common oxidants (e.g. chlorine, ozone, hydrogen peroxide, peroxomonosulfate (PMS) and persulfate (PDS)) for chemical degradation of environmental pollutants. The advanced oxidation processes (AOPs) are generally based on the generation of highly reactive oxidizing hydroxyl and sulfate radicals [69-70]. Generally, sulfate radicals are more selective for oxidation than the hydroxyl radicals [71]. At neutral pH, sulfate radicals have a higher standard potential than that of hydroxyl radicals. At acidic pH, both of the radicals have almost the same reduction potentials. Hydrogen peroxide, PMS and PDS can be activated to generate hydroxyl radicals or sulfate radicals or both by thermal (heat), UV light, transition metals, activated carbon, nano carbons, microwave and integrated techniques.

The abilities of the two radicals in degradation of environmental pollutants lie in the right combination of the pollutant, oxidant, and activation techniques as mentioned above. The combination of pollutant and either oxidant or catalyst is assigned to the binary pollutant degradation system; whereas, the combination of pollutant and oxidant activated by thermal (heat), UV light, transition metal, activated carbon, nano-carbons techniques is assigned to the ternary pollutant degradation system.

Throughout the past decades, the binary system of organic pollutant with activation of strong oxidants such as PMS and PDS have gained many attraction. As seen in Table 2.7, the degradation of various different organic pollutants with PMS/PDS activation is almost negligible. Even though the pollutant degradation is insignificant, previous studies have shown that radical and non-radical paths were observed for pollutant degradation for the binary system (nitrobenzene and PDS), (phenol and PMS or PDS), and (sulfamethoxazole (SMX) and PMS) [72-74]. These studies were carried out at reaction temperature, 25 °C. According to Huang et al, the degradation of methyl tert-butyl ether (MTBE) with heat assisted PDS activation has improved significantly [11].

Various factors have to be considered in order to improve the degradation of the target pollutant using a binary system, such as reaction temperature, pH level, pollutant initial concentration, oxidant concentration and the type of radicals generated.

For a ternary system, the degradation of pollutants is mostly due to the presence of sulfate radical ($SO_4^{\bullet-}$) or hydroxyl radical ($^{\bullet}OH$), as seen in **Table 2.7**. The mechanism of the electron transfer can be seen in **Eq. 2.26** to **Eq. 2.31**.

$$HSO_5^- + e^- \rightarrow {}^{\bullet}OH + SO_4^{2-} \quad (2.26)$$

$$HSO_5^- + e^- \rightarrow SO_4^{\bullet-} + OH^- \quad (2.27)$$

$$HSO_5^- - e^- \rightarrow SO_5^{\bullet-} + H^+ \quad (2.28)$$

$${}^{\bullet}OH + SO_4^{2-} \rightarrow SO_4^{\bullet-} + OH^- \quad (2.29)$$

$$SO_4^{\bullet-} + OH^- \rightarrow SO_4^{2-} + {}^{\bullet}OH \quad (2.30)$$

$$\text{Phenol} + SO_4^{\bullet-} ({}^{\bullet}OH) \rightarrow \text{several steps} \rightarrow CO_2 + H_2O + SO_4^{2-} \quad (2.31)$$

It is to be noted in recent studies, both the non-radical and radical paths for degradation of pollutant were observed for the ternary systems (phenol, PMS and nitrogen doped CNT) and (phenol, PMS and nano Diamond) [75-77]. In the ternary system (phenol, PMS and rGO-900), the degradation of pollutant was dominated by the non-radical path [75] .

As seen from **Table 2.7**, negligible degradation does not necessarily mean no radicals were involved in the degradation process. Furthermore, the generation of radicals might not contribute to the improvement of degradation process, depending on the type of pollutant.

Table 2.7. Examples of binary and ternary degradation systems [75-76, 78-82]

Pollutant	Oxidant	Radical	Catalyst	Degradation
AO7	NaOH	-	-	Negligible
AO7	PMS	-	-	Negligible
AO7	PMS	Superoxide	NaOH	Significant
AO7	PDS	-	NaOH	Negligible
AO7	H_2O_2	-	NaOH	Negligible
Phenol	PMS	$SO_4^{\bullet-}$	NaOH	Significant

Bisphenol A	PMS	-	NaOH	Significant
Furfuryl alcohol	PMS	-	NaOH	Moderate
Surfamethoxazole	PMS	-	NaOH	Moderate
4-chlorophenol	PMS	-	NaOH	Negligible
Nitrobenzene	H_2O_2	$^{\bullet}OH$	Schwertzmanite	Significant
Atrazine	PMS	$SO_4^{\bullet-}$, $^{\bullet}OH$	$CuFe_2O_4$	Significant
Atrazine	PMS	-	-	Negligible
Atrazine	-	-	$CuFe_2O_4$	Negligible
Nitrobenzene	PMS	-	-	Negligible
Nitrobenzene	-	-	$CuFe_2O_4$	Negligible
Nitrobenzene	PMS	$^{\bullet}OH$	$CuFe_2O_4$	Moderate
Atrazine	PDS	-	$CuFe_2O_4$	Negligible
Atrazine	H_2O_2	-	$CuFe_2O_4$	Negligible
AO7	PMS	-	-	Negligible
AO7	-	-	PBS	Negligible
AO7	PMS	$SO_4^{\bullet-}$, $^{\bullet}OH$ (depend on pH)	PBS	Significant
AO7	PDS	-	PBS	Negligible
AO7	H_2O_2	-	PBS	Negligible
Rh B	PDS	-	PBS	Negligible
Rh B	H_2O_2	-	PBS	Negligible
2, 4, 6 TCP	PDS	-	PBS	Negligible
2, 4, 6 TCP	H_2O_2	-	PBS	Negligible
Phenol	PDS	-	-	Little
Phenol	PMS	-	-	Little
Phenol	PDS	-	UV	Moderate
Phenol	PMS	-	UV	Moderate
Phenol	PDS	-	ZnO	Little
Phenol	PMS	-	ZnO	Moderate
Phenol	PMS	Radical and non-radical	N-CNT	Significant
Phenol	PMS	Radical and non-radical	Nano diamond	Significant
Phenol	PMS	Dominated by non-radical	rGO-900	Significant

2.5 Development of carbon nanomaterials

Carbon nanomaterials have become the centre of attention recently due to their extensive applications and excellent properties. Among many carbon materials, graphene oxide has become a promising alternative to graphene because of the large scale production and manipulation.

2.5.1 Synthesis of graphene oxide

Several preparation methods have been used to prepare graphene oxide. The main methods for the preparation of graphite oxide are the Brodie, Staudenmaier and Hummers-Offeman methods. The Hummers-Offeman method is the most commonly used method where graphite powder is used to synthesize graphene oxide (GO) by $KMnO_4$ oxidation in concentrated hydrochloric acid (H_2SO_4) followed by hydrolysis, washing and centrifugation [83]. Partially oxidized graphene is also favourable in most cases for its tunable optical, conductive, and chemical properties [84]. GO can be obtained by graphite salts (nitrate or bisulphate) oxidation, either with strong oxidizing agents (potassium chlorate, permanganate bichromate, chlorine dioxide) or electrochemically [83]. The over oxygenated graphite salts are then treated to hydrolysis. Aqueous colloidal dispersion was formed after washing the salts with water. The solid GO can be obtained by drying the dispersion either in a high vacuum at room temperature, by lyophilisation, or heating in air to low temperatures (45-50° C) to prevent oxygen functional groups decomposition in GO that may take place at a high temperature. However being hydrophilic and due to the low drying temperature, not only powder-like and film-like solid GO always contains some residual water, but also GO disperses readily in water and breaking into macroscopic flakes (one layer thick). A suspension of graphene flakes will be formed by the chemical reduction.

Reduction of graphene oxide to graphene like materials is the most important chemical transformation. Reduction can be achieved not only chemically through the use of strong reductants thermally or electrochemically, but also can be performed at room temperature without chemical solutions.

2.5.1.1 Non-metal doped graphene

One of the most popular methods to change the physical properties of graphene is by boron or nitrogen doping [85]. Studies have shown promising properties of the nitrogen doped graphene. By doping the carbon network of graphene with nitrogen, it not only establishes electrocatalytic active sites but also enhances the electrical conductivity and surface hydrophilicity to help charge transfer and electrolyte-electrode interactions [86]. Previous research has shown that the electro conductivity of graphene can be improved through nitrogen doping [87]. Therefore, nitrogen doping is commonly utilized to enhance the performance of graphene based electrochemical applications such as lithium ion battery, fuel cells, and supercapacitor. Moreover, nitrogen doping can also construct new properties such as selective sensitivity for adsorbents and electrochemical catalytic activity [86].

Different carbon-nitrogen bonding configurations in nitrogen doped graphene have different electron structures, physical and chemical properties. However, scientists have not discovered which type of carbon-nitrogen bonding configurations that are responsible for the improvement of catalytic activity of nitrogen doped graphene [88].

The common nitrogen doping methods are the plasma, arch-discharge, hydrothermal, and chemical vapour deposition process (CVD). These methods are high cost and complicated due to the unreliable control of the doping structure. These methods are not safe due to the involvement of toxic and corrosive reagents and precursors. Also, they have to be done very carefully for the materials that are atmosphere sensitive.

According to Zheng et al [88], hydrothermal process is a simple method to synthesize nitrogen doped graphene. By using a synthesis route of hydrothermal reaction followed by an annealing process, the nitrogen doped graphene with different proportions of nitrogen configurations was investigated. Results showed that nitrogen doped graphene materials possessing high percentage of graphitic-N demonstrate significantly improved oxygen reduction reaction activity, which shows that graphitic-N may play an important role in electrocatalysis.

2.5.1.2. Metal doped graphene

Another way to enhance the physical and chemical properties of graphene is with metal nanoparticles doping. Metal elements that are commonly used are noble metals such as: palladium, platinum, gold, silver, rutile [89]. Due to the rarity, high cost and low availability of noble metals, transition metals such as copper, iron, manganese and nickel have been developed as an alternative dopant for metal doped graphene [90-91]. Metal nanoparticles have promising physical and chemical properties that are different from their bulk materials [90]. Doping graphene with metal nanoparticles can increase the selectivity, sensitivity, detection limit, and combination of these properties [92].

The common metal doping methods are electrochemical reduction, chemical vapour deposition (CVD), Suzuki coupling reaction, using external power sources such microwaves, or chemical-physical-or electro deposition [93-94].

Metal doped graphene have been applied as electro chemical sensors, renewable energy, substrates for surface enhanced Raman spectra, high performance catalysts for chemical reactions and oxygen reduction reactions [89, 91, 95-96].

Many previous studies focused on metal doped graphene with promising capabilities in electro catalysis [89-90, 95]. Previous research has shown improved kinetic oxygen reduction in alkaline conditions by the electrocatalytic activities of the transition metal doped graphene [90]. Good electrocatalytic activity toward methanol oxidation has been showed by Pt doped graphene [97]. Wen et al reported that MnO_2 doped graphene is a good alternative cathode catalyst to Pt in microbial fuel cells [98].

With all these unique and excellent properties of metal doped graphene, secondary contamination might occur during the catalytic oxidation processes due to the metal contents. Therefore, non-metal doped graphene or carbon catalysts have become an emerging material and attracted more researchers for waste water treatment.

2.6 Characterization techniques

Characterization is used to study the properties of the carbon catalysts and the presence of radicals. In these studies, the catalysts are various dimensions of nano-carbons under doped and undoped conditions. There are many characterisation techniques, such as X-ray diffraction (XRD), scanning electron microscopy (SEM), thermogravimetric-differential scanning calorimetry (TG-DSC), the Brunauer-Emmet-Teller (BET), Raman analysis, Fourier transform infrared spectroscopy (FTIR) and X-ray photoelectron spectroscopy (XPS). Electron paramagnetic resonance (EPR) is used to study the mechanism of pollutant degradation by super oxidants only or with the addition of a catalyst. This technique is applied to characterize the presence of different radicals with unpaired electrons that are resulted from the activation of super oxidants. These various characterization techniques will be explained briefly in this chapter.

2.6.1 Scanning electron microscopy

Scanning electron microscopy (SEM) is one of the most frequently used techniques for material characterization. It is also enhanced the capability of optical microscope for characterizing samples that require higher magnification, large depth of field and high resolution. Optical microscopy can provide specimen resolution in the range of 200 nm, magnification about 1500X [99]. In order to achieve higher resolution, an electron source is required instead of light as the illumination source. The electron illumination can produce resolution about 10 nm and magnification about 20,000X. The depth of field of the SEM can be 300X of the optical microscope.

As seen in **Figure 2.5**, SEM utilizes the interaction of primary electron beam from an electron gun with the sample surface which results in the generation of secondary electrons for image formation with a three dimensional surface topography [100]. Here, images are formed because the primary beam is made to scan a square region (a raster) on the sample surface [101]. At the same time a square raster that produces secondary electron emission is traced out simultaneously on a cathode-ray tube (CRT). The interaction of primary electron beam and specimen surface also produces variety energetic emissions, such as backscattered electron, Auger electron and characteristic X-ray [100-101]. These energetic emissions can be used to obtain

information regarding characteristics at and near the surface of a specimen.

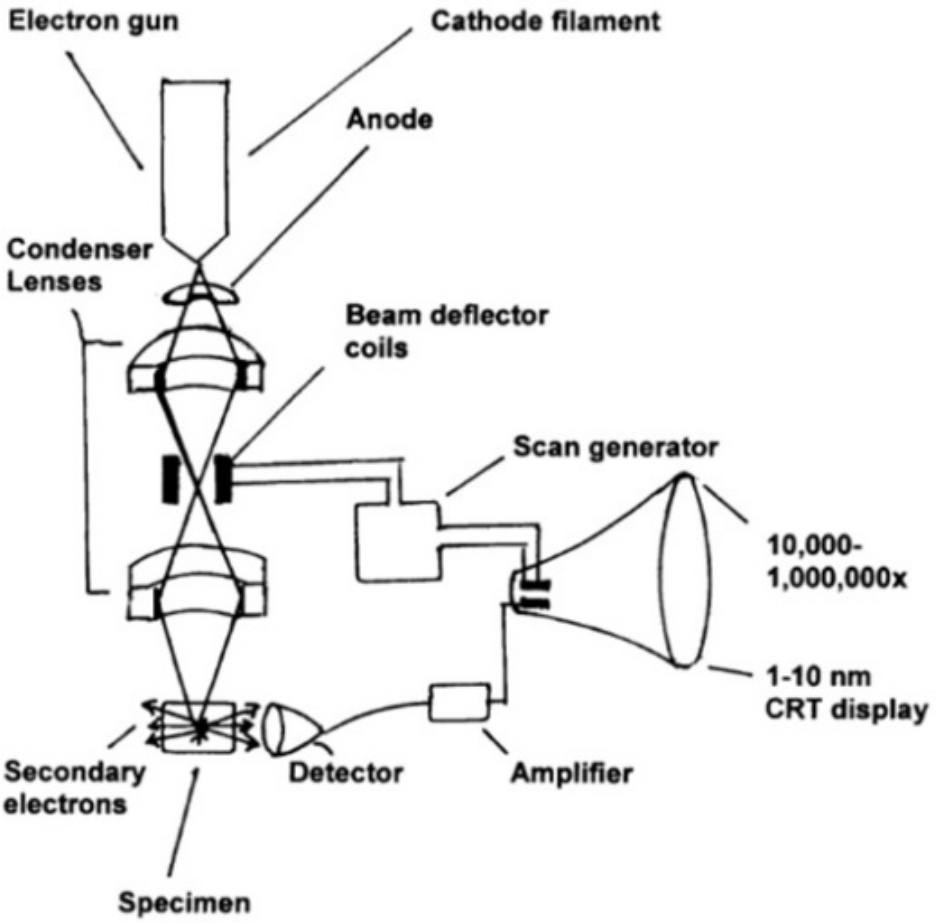

Figure 2.5. Schematic diagram of SEM [99]

In SEM, the image formation can be obtained from the signals of secondary electron or backscattered electron [102]. It is to be noted that the secondary and backscattered electrons are produced from two different types of interaction. Secondary electrons are a result of inelastic collision and scattering of incident electrons (20 keV) with the specimen electrons [100]. These secondary electrons are characterized with the emitted energy less than 50 eV and travel in trajectory [103]. The intensity of these secondary electrons is a function of the angel of the incident beam with the specimen surface. The image of a surface will be brighter on CRT screen due to the more secondary electrons reach the detector [101]. This image of a surface is a result of secondary electrons generated from 5-50 nm thickness of the surface (10 A =1 nm) [104].

Backscattered electrons are generated due to an elastic collision and scattering of incident electrons and the specimen nuclei or electrons. These backscattered electrons have almost the same emitted energy as the primary electron beam (slightly less than 20 keV) and travel in straight lines [101]. The signal of backscattered electrons is a result from the interaction of primary beam and specimen surface from the thickness more than 50 nm. It is to be noted, the number of backscattered electron is a function of Z (the atomic number of a material). Increasing the atomic number Z results in the increase of the number of backscattered electrons [103, 105]. Here, backscattered electrons can be used to form a topographic contrast from various regions of the specimen with different atomic numbers [106].

The X-ray signal is generated from the recombination interactions between free electrons and positive electron holes from the thickness deeper than that of the region of backscattered electrons. This characteristic signal is used to determine the elemental compositions of the surface through the energy dispersive x-ray spectroscopy (EDS). **Figure 2.6** shows a cross section diagram for the regions of various signals generated from the interaction of primary beam and specimen surface as a function of specimen thickness.

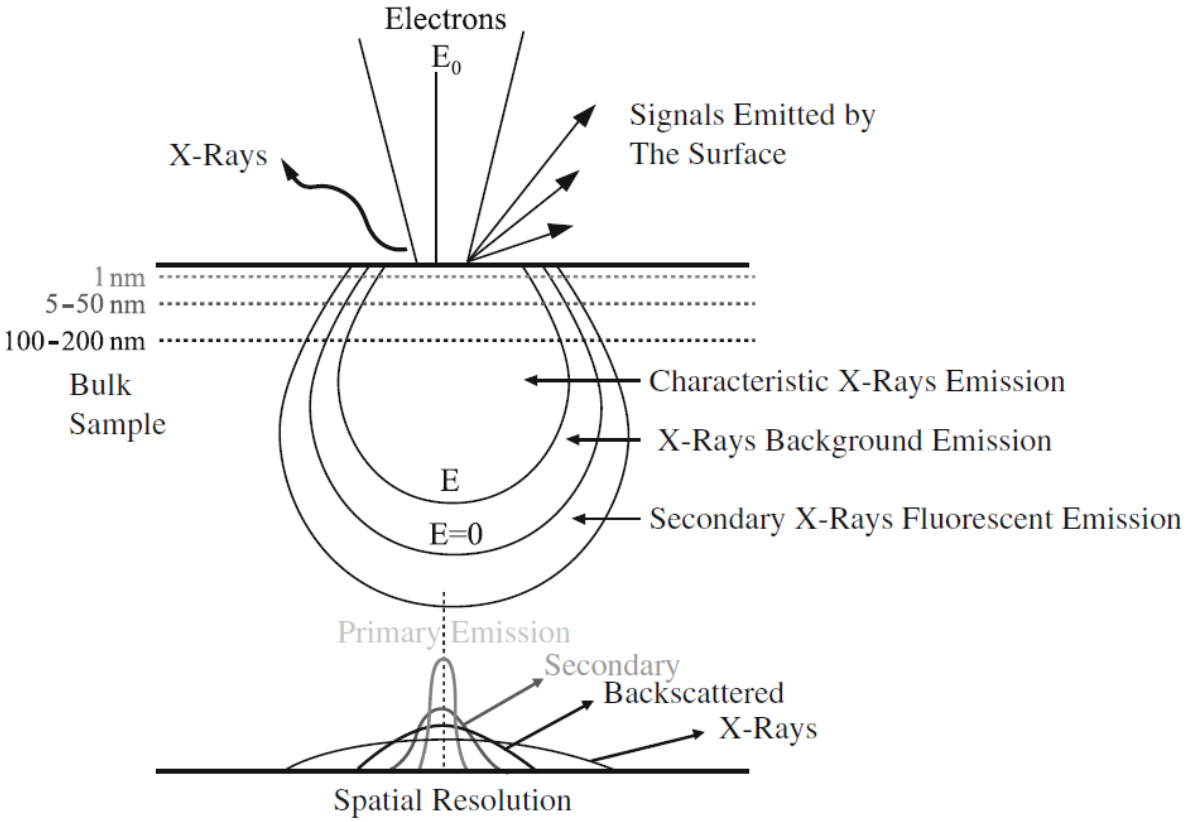

Figure 2.6. Various signals generated as a function of specimen thickness [104]

Table 2.8 lists the advantages and disadvantages of SEM and **Figure 2.7** shows example of SEM images.

Table 2.8. Advantages and Disadvantages of SEM [102, 106-107]

Advantages	Disadvantages
Direct surface analysis	Sample preparation has to be done thoroughly
Analysis time is very quick	Analysis has to be done under vacuum condition and no contamination
Can analyse samples with any thickness	Require training in order to operate it
High resolution and 3D SEM images	

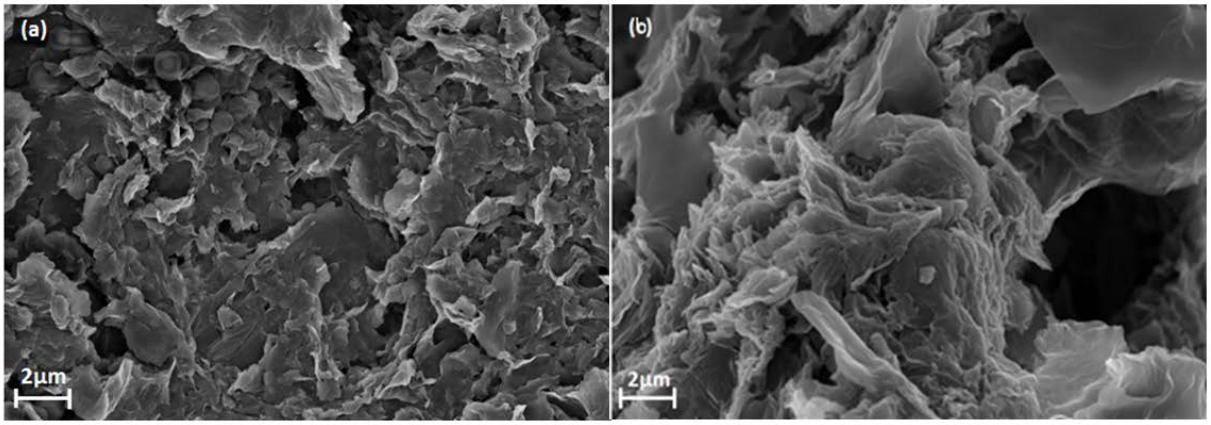

Figure 2.7. SEM images of (a) GO, and (b) N-rGO [108]

2.6.2 Fourier transform infrared spectroscopy

Infrared spectroscopy is a transmission of molecular vibration through infrared radiation as a function of wavelength (frequency). Fourier transform infrared spectroscopy (FTIR) is the commonly used IR spectroscopy method to detect the presence of certain functional groups. The materials that can be analysed using FTIR are powdered solid samples, nano materials, liquids, gases and thin films.

FTIR is used to determine [109-110]:

(a) compound identification,
(b) quantitative analysis,
(c) measurement of molecules properties, and
(d) structural interpretation.

In the electromagnetic radiation, infrared falls in the region of 0.7µm – 1000 µm. **Figure 2.8** shows the electromagnetic radiation with an expansion of infrared region. Infrared region is categorized further into three regions, which are near infrared, mid infrared, and far infrared [111]. **Table 2.9** shows the wavelength, frequency and wavenumber of UV, visible, infrared and microwave.

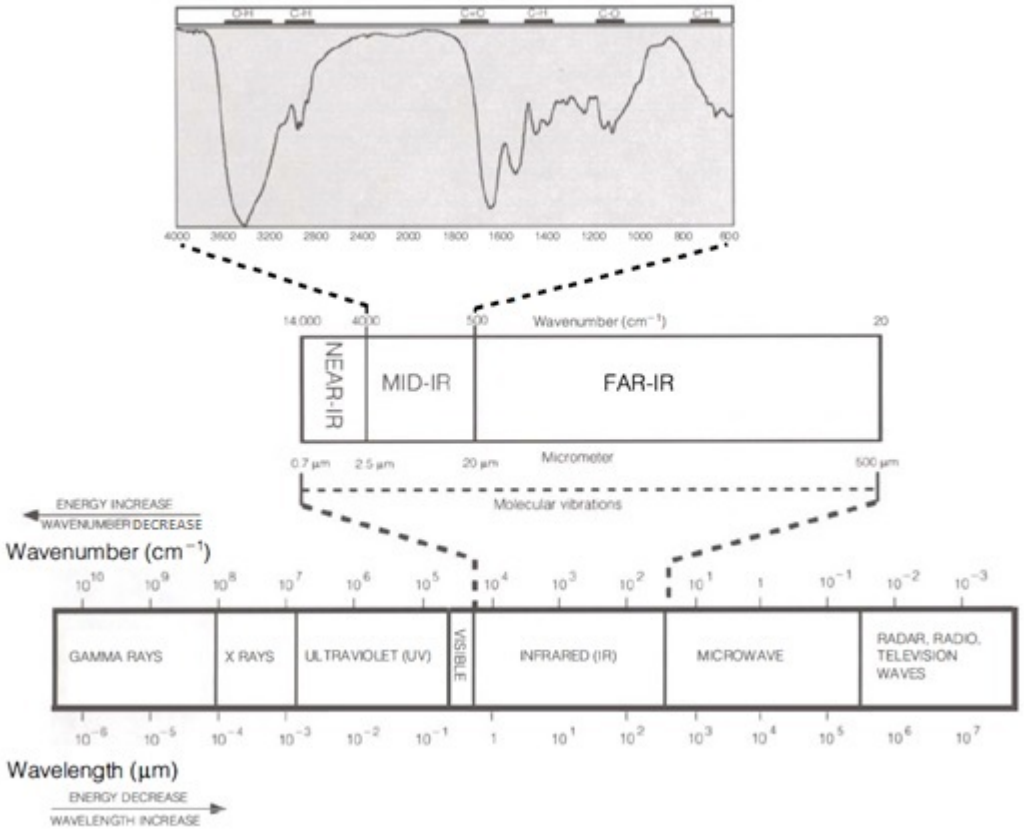

Figure 2.8. Spectral regions of electromagnetic radiation with an expansion of infrared region [112]

Table 2.9. List of common spectral region of electromagnetic radiation [110]

Region	Wavelength, λ (nm)	Frequency, v (Hz)	Wavenumber, $\ddot{v}$ (cm^{-1})
Ultraviolet (UV)	0.01-0.38	$3x10^{16}$-$7.9x10^{14}$	1,000,000-26,300
Visible	0.38-0.78	$7.9x10^{14}$-$3.8x10^{14}$	26,300-12,800
Near infrared	0.78-3	$3.8x10^{14}$-$1.2x10^{14}$	12,800-4000
Mid infrared	3-50	$1.2x10^{14}$-$6x10^{12}$	4000-200
Far infrared	50-1000	$6x10^{12}$-$3x10^{11}$	200-10
Microwave	1000-1,000,000	$3x10^{11}$-$3x10^{8}$	10-0.01

The relationship between wavelength, frequency and wavenumber is described in below equation [113]:

$$\ddot{v} = \frac{1}{\lambda} = \frac{v}{(c/n)} \qquad (2.32)$$

Where n is the refractive index of the medium and c is the speed of light.

FTIR measured the absorption of different infrared frequencies when a sample is 'shot' with an infrared beam, in which photon energy is transferred into the molecule. **Figure 2.9** shows the schematic diagram of FTIR spectrometer. The sample absorbed some of the infrared beam and photon energy, while some beams are passing through or transmitted. Below equation shows the relationship between photon energy and photon frequency [113]:

$$E = hv \qquad (2.33)$$

Where E is the photon energy, h is Planck's constant (6.6256 x 10^{-27} erg sec), and v is the photon frequency.

The transmittance and absorbance results will give us what functional groups the sample has. Functional groups are combination of two or three atoms bonded together through the infrared absorption. Examples of some functional groups can be seen in **Table 2.10** and example FTIR spectrum can be seen in **Figure 2.10**.

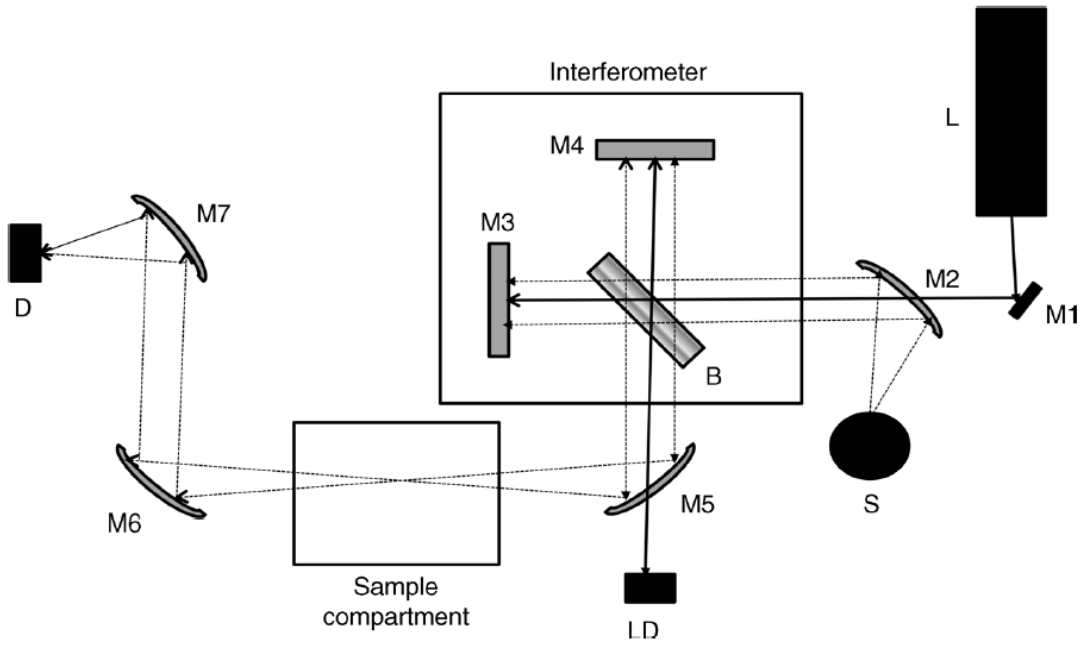

Figure 2.9. Schematic diagram of FTIR spectrometer (S= source, D= detector, L= HeNe laser, LD= laser detector, B= beam splitter, M1= beam directing plane mirror, M2, M5, M6 and M7= beam directing off axis parabolic mirrors, M3= fixed interferometer mirror, M4= moving interferometer mirror [110]

Table 2.10. Examples of functional groups and their absorption wavenumber [114]

Functional groups	Species	Wavenumber (cm^{-1})
O-H	Hydroxyls	3700-3250, 1070
C-OOH	Carboxyls	1750-1650
C=C	Alkenes	1680-1630
C≡C	Alkynes	2260-2000
C=O	Carbonyls	1870-1650
C=O	Aldehydes	1740-1720
C=O	Ketones	1720-1700
N-H	Amines	3400-3300
C-H	Alkanes	3000-2800
O-C=O	Carboxylic acids	700-590
O-C-O	Esters	645-575
C-O-C	Epoxide	1320-1230

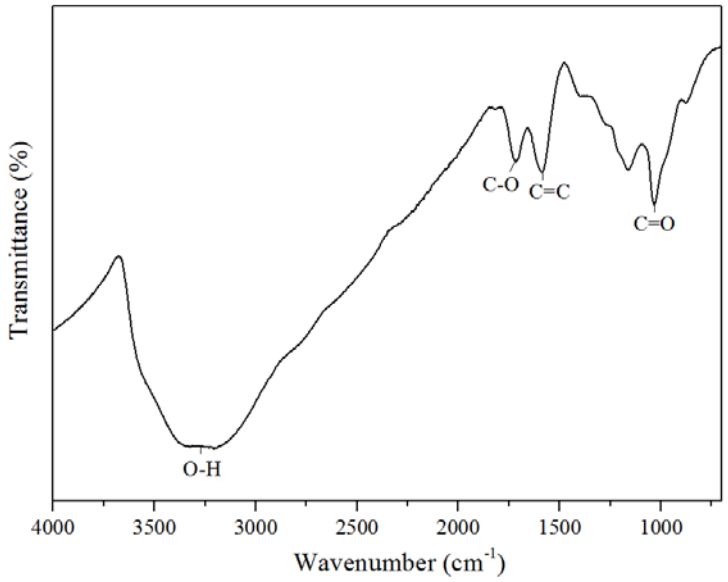

Figure 2.10. FTIR spectrum of graphene oxide [108]

FTIR is one the most popular characterisation techniques and has many advantages as listed in **Table 2.11**.

Table 2.11. List of advantages and disadvantages of FTIR analysis [109, 115]

Advantages	Disadvantages
Gas, solid, and liquid samples can be analysed Self- calibrating No sample preparation Speed (very quick to get the result) Very easy to operate Sensitivity Doesn't destroy the samples	Only have single beam (compared to Raman spectroscopy where it has double beams)

2.6.3 Raman scattering spectroscopy

Raman scattering spectroscopy is another important method of vibrational spectroscopy besides FTIR. Raman spectroscopy can be used to analyse solid, liquid and gaseous samples. Raman spectroscopy can determine [116-117]:

1. Molecular orientation
2. Chemical nature
3. Structure and properties of molecules
4. Crystallinity ratios and polymorph content

Raman spectroscopy measures the photon energy and wavelength that are inelastically and elastically scattered when monochromatic light (UV, infrared, visible) passed through a sample [118]. **Figure 2.11** shows the schematic diagram of Raman spectroscopy.

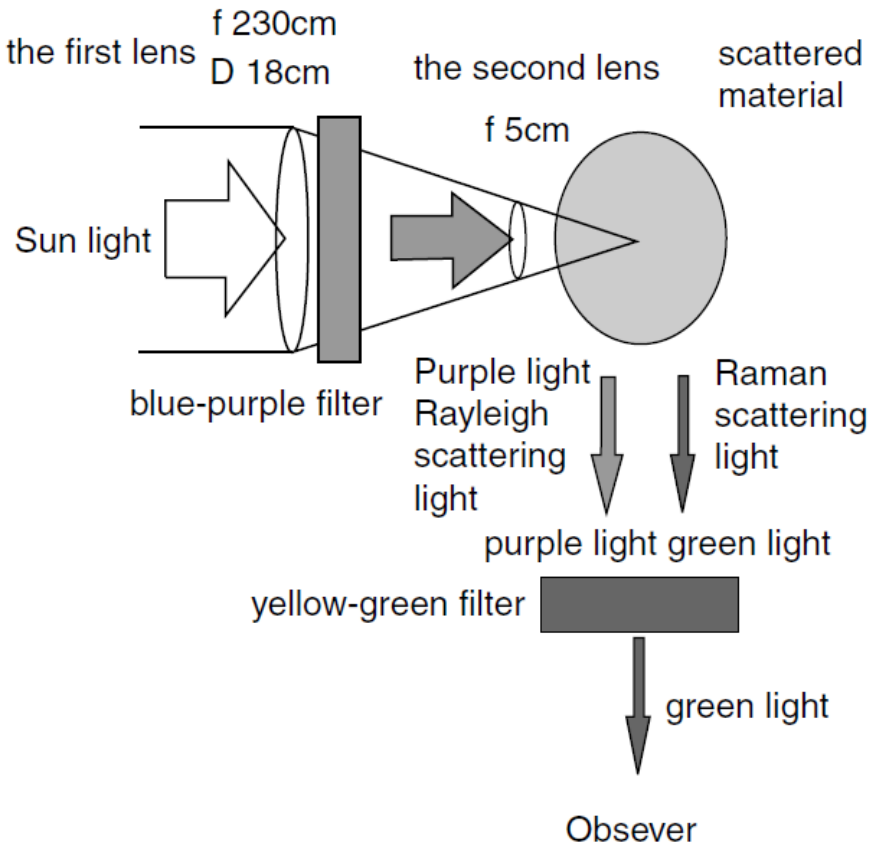

Figure 2.11. Schematic diagram of Raman spectroscopy [119]

Scattering happens due to the interaction between the particle/ molecule and the target causing changes in the direction and energy. The light scattered photons consist of Rayleigh scattering and Raman scattering [113]. Rayleigh scattering represents elastically light scattering, presence for any molecule and no energy change [117]. On the other hand, Raman scattering or Raman effect represents inelastic light scattering due to the difference in energy and incident light. It occurs when the molecule's vibration and energy change. Raman scattering changes some energy due to the sample's specific vibrational coordinates, and is categorized into two: Stokes (stronger, longer wavelength) and anti-Stokes scattering (weaker, shorter wavelength) [120]. **Figure 2.12** shows the energy level diagram of Rayleigh and Raman scattering.

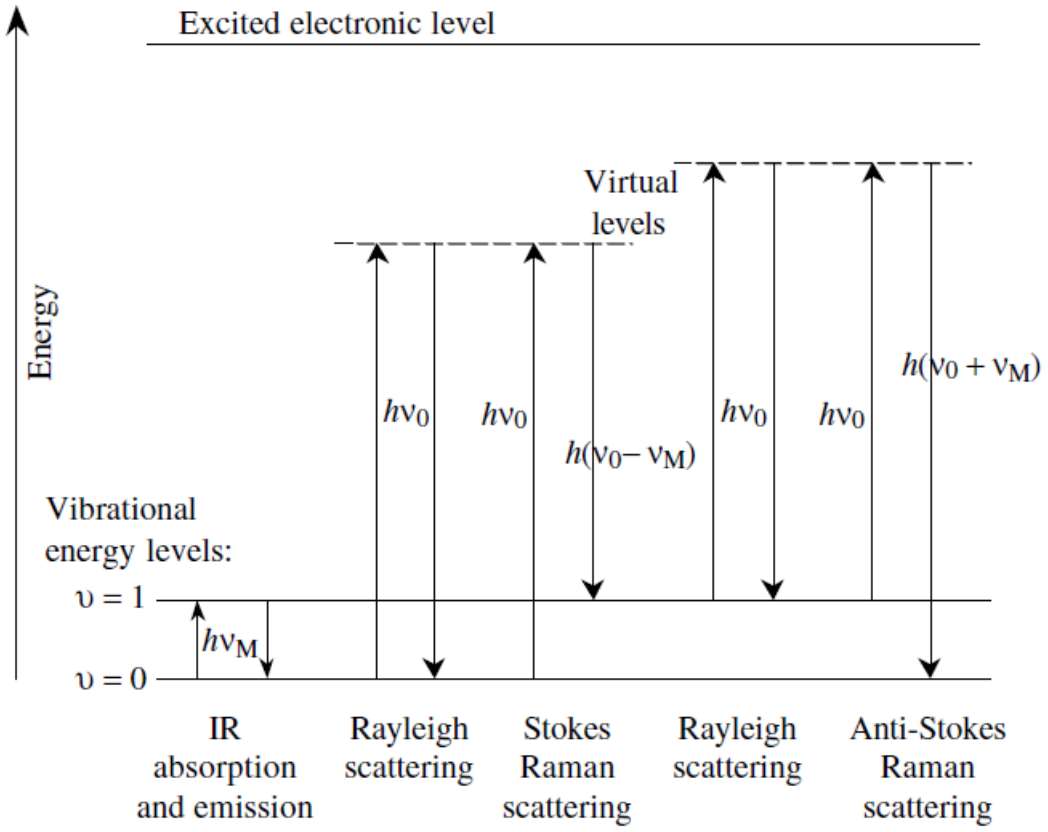

Figure 2.12. Energy level diagram of Rayleigh, Raman scattering processes and infrared absorption and emission [121]

Raman spectroscopy is widely used in carbon material characterisation. It can determine the defects, doping, presence of sp2-sp3 hybridization, crystallite size, chemical impurities, optical energy gap, edge structure, and many more [122]. Generally in the analysis of carbon materials, D-band and G-band are detected in the Raman spectrum. D-band (disorder) is ascribed for an amorphous character related to the edges, defects, and structurally disordered carbon. G-band (graphite) is ascribed for crystalline character originated from in-plane vibrations of sp^2 carbon. I_D/I_G ratio represents the degree of defects/ disorder of the carbon material. **Figure 2.13** shows an example of carbon material Raman spectrum.

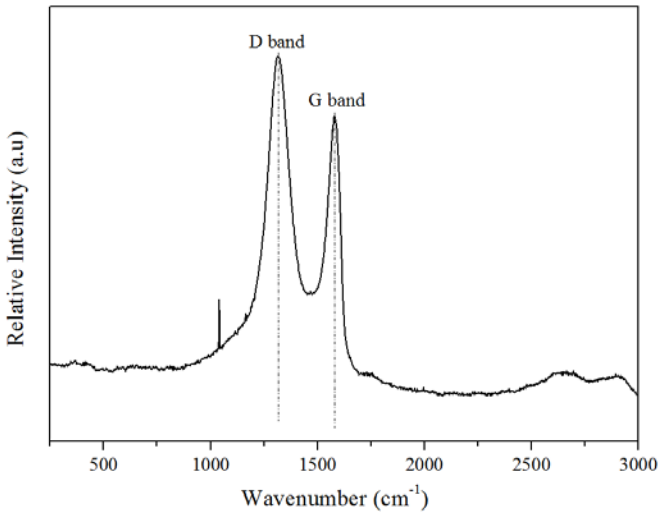

Figure 2.13. Raman spectrum of graphene oxide [108]

Table 2.12 lists the advantages and disadvantages of Raman spectroscopy.

Table 2.12. Advantages and disadvantages of Raman spectroscopy [116-117, 123]

Advantages	Disadvantages
No sample preparation	Fluorescence (impurities) interference
Doesn't destroy the sample	Slow imaging
Highly selective	
Qualitative and quantitative analysis	
Speed (quick to analyse)	

2.6.4 Thermal analysis

Thermal analysis is an analysis of a material based on its thermal behaviour and properties. It is able to analyse solid and liquid samples.

Thermal analysis can be used to determine [124]:

- materials composition, purity and crystallinity
- organic and inorganic contents
- melting point
- phase transitions
- thermal and mechanical histories and stability
- specific heat capacity
- chemical reactions kinetics

Few factors affecting thermal analysis accuracy:

- heating rate
- sample sizes, mass, shapes
- purge gas composition

Table 2.13 lists various thermal analysis techniques [125-126]. Thermogravimetric analysis (TGA) and differential scanning calorimetry (DSC) are the most popular thermal analysis techniques. In this chapter, TGA and DSC will be explained further.

Table 2.13. Thermal analysis techniques [127]

Technique	Abbreviation	Property measured
Thermomechanical analysis	TMA	Length or volume
Thermogravimetric analysis	TGA	Mass
Dynamic mechanical analysis	DMA	Viscoelastic
Differential thermal analysis	DTA	Temperature
Differential scanning calorimetry	DSC	Temperature and heat
Dielectric analysis	DEA	Dielectric
Micro/Nano-thermal analysis	μ/n-TA	Temperature and penetration
Thermometry		Temperature
Calorimetry		Heat
Dilatometry		Volume

2.6.4.1 Thermogravimetric analysis

Thermogravimetric analysis (TGA) measures the mass changes of the sample as a function of temperature, usually increasing temperature up to 1000 °C. This mass loss is due to adsorption, desorption, oxidation, reduction, decomposition, sublimation, evaporation, and chemical reaction [128].

Factors affecting the TGA results are listed below [126]:

Factors affecting mass

- Electronic drift
- Atmospheric turbulence
- Electrostatic and magnetic forces
- Buoyancy and thermal expansion
- Condensation and reaction

Factors affecting temperature

- Electronic drift
- Heating rate
- Sample/furnace sensor location
- Thermal conductivity
- Enthalpy of the processes

The materials of the crucibles used in TGA analysis also influence the TGA curves. Commonly used crucibles are made of aluminium, platinum, and ceramic. Purge gases used in the TGA sample chamber are argon, nitrogen, hydrogen, helium, carbon dioxide, and air or oxygen. Gas flow rate is very important in regards the sample heat transfer. The most important component in TGA is the thermobalance. Thermobalance is the one that measure the mass and temperature difference of the sample. **Figure 2.14** shows the schematic diagram of the thermobalance in the TGA.

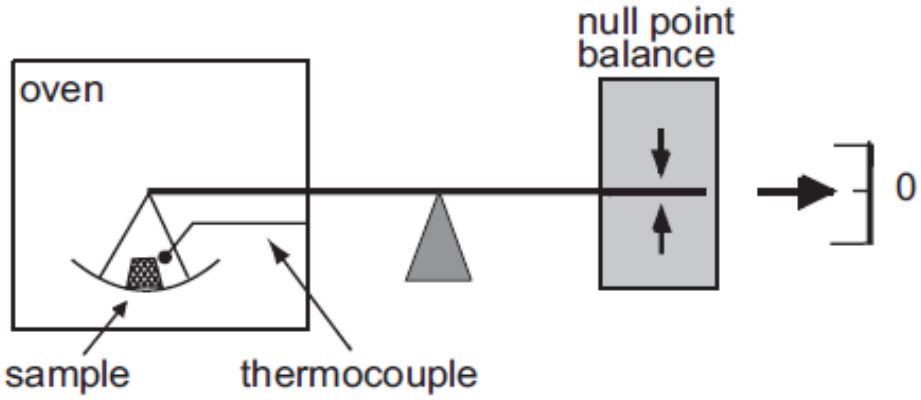

Figure 2.14. Schematic diagram of a horizontal thermobalance [128]

The percentage loss or increase of the sample mass can be calculated using below equation:

$$M = \frac{m_s - m_f}{m_s} \times 100\ (\%) \qquad (2.34)$$

Where M is the mass loss or gain, m_s is the original mass, and m_f is the final end mass.

Chemical or reaction kinetics investigates how fast the chemical reaction occurs and what it influences it. The Arrhenius rate equation is as follow:

$$k = Ae^{\left(\frac{-E}{RT}\right)} \qquad (2.35)$$

Where R is the gas constant, T is the temperature, A and E are Arrhenius constant. Using the Arrhenius equation and TGA curves, the activation energy can be estimated along with the life time.

2.6.4.2 Differential scanning calorimetric

Differential scanning calorimetric (DSC) measures the heat flow changes along with increasing temperature. It determines the heat or energy absorbed or released through a chemical change, hence changing the internal energy (enthalpy). Below equation is applied for enthalpy change [128]:

$$\Delta H = \int c_p . dT \qquad (2.36)$$

Where H is the enthalpy and c_p is the heat capacity.

Examples of endothermic reactions (corresponds to increasing enthalpy) are evaporation and melting; while example of exothermic (corresponds to decreasing enthalpy) are decomposition and crystallization. DSC measures the enthalpy changes in respect to heating rate and mass; this relationship is illustrated in below equation [128]:

$$\frac{\dot{Q}}{m} = v . c_p \qquad (2.37)$$

Where m is the mass, v is the heating rate, and $\dot{Q}$ is the heat flux. **Figure 2.15** shows the schematic diagram of instruments that is used to detect enthalpy changes where **Figure 2.16** shows an example of TGA and DSC curves.

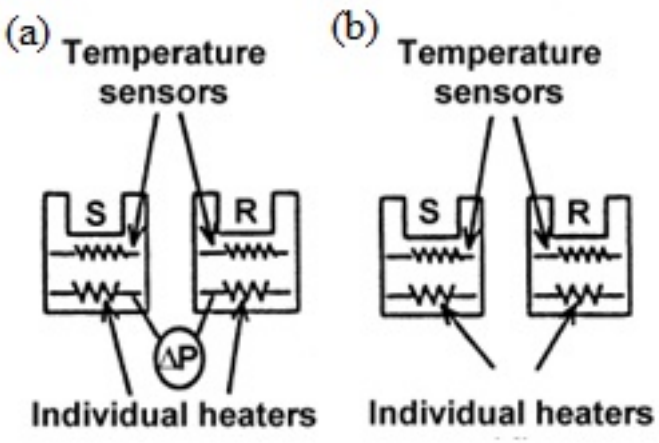

Figure 2.15. Schematic diagrams of instruments that is used to detect the enthalpy changes in DSC (a) power-compensation DSC, (b) heat-flux DSC [127]

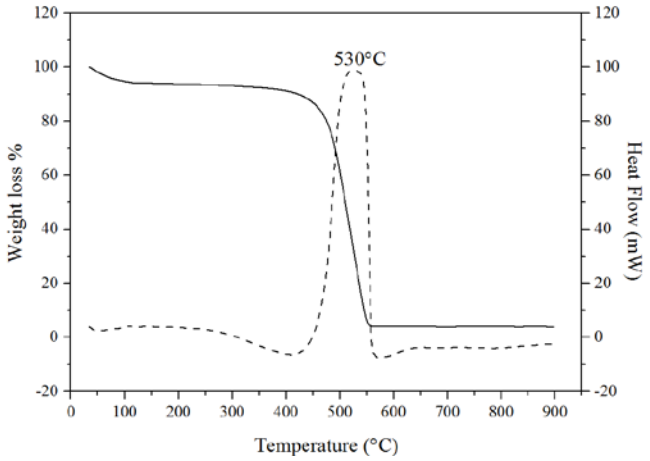

Figure 2.16. TGA/DSC graph of N-rGO 400 °C [108]

Table 2.14 lists several advantages and disadvantages of TGA and DSC.

Table 2.14. Advantages and disadvantages of TGA/DSC

Advantages	Disadvantages
Easy to operate	Very small samples are used (has to be able to fit into the pan)
Easy sample preparation	Only provide meaningful data when a change in mass occurs
Accurate and reliable data	Not all samples can be analysed
	Sensitive to heating rate and sample mass
	Requires good thermal contact with the bottom of sample crucible
	Destroy the samples
	Slow analysis (time consuming)

2.6.5 Brunauer-Emmet-Teller

Specific surface area (SSA) of carbon catalysts is one of the most important factors in influencing the degradation performance of organic pollutant. SSA is important due to the large number of atoms residing at the surface of the catalysts or materials [129-130]. Brunauer-Emmet-Teller (BET) is a gas adsorption method onto a solid surface at reduced pressure and temperature. It is the most commonly used to analyse the SSA of the catalysts [131]. It can be used to determine the pore area and specific pore

volume by nitrogen sorption (adsorption and desorption). Among other gases, liquid nitrogen is the most suitable adsorbate gas due to its unique properties.

As discussed in the previous section, there are two types of adsorption: chemisorption physisorption. In this gas adsorption BET analysis, the process is physisorption due to the weak Van der Waals forces between the gas and the solid surface. The SSA is measured by calculating the amount of gas adsorbed physically as a function of pressure and the monomolecular layer on the surface. Using a volumetric flow technique this amount of gas adsorbed can be calculated. Below is the BET equation in relation to the adsorption isotherm equation [132]:

$$\frac{P}{V_a(P_o-P)} = \frac{1}{V_m C} + \frac{C-1}{V_m C}\left(\frac{P}{P_o}\right) \qquad (2.38)$$

Where P is the equilibrium gas pressure, P_o is the saturation gas pressure, V_a is the amount of gas adsorbed, V_m is the amount of gas that covers the surface with a monolayer, and C is a constant.

V_m and constant C can be calculated from the slope and intercept obtained by plotting $\frac{P}{V_a(P_o-P)}$ versus $\frac{P}{P_o}$. Therefore, the SSA can be calculated using below equation [133]:

$$S_{BET} = \frac{N_A V_m A_N}{V_o} \qquad (2.39)$$

Where V_o is the gas molar volume, N_A is the Avogadro constant, and A_N is the surface area occupied by single adsorbed gas molecule.

BET can also analyzed the pore size distribution using the obtained adsorption and desorption curves. **Figure 2.17** shows the pore size distribution and nitrogen sorption curves of graphene nanoplate (GNP).

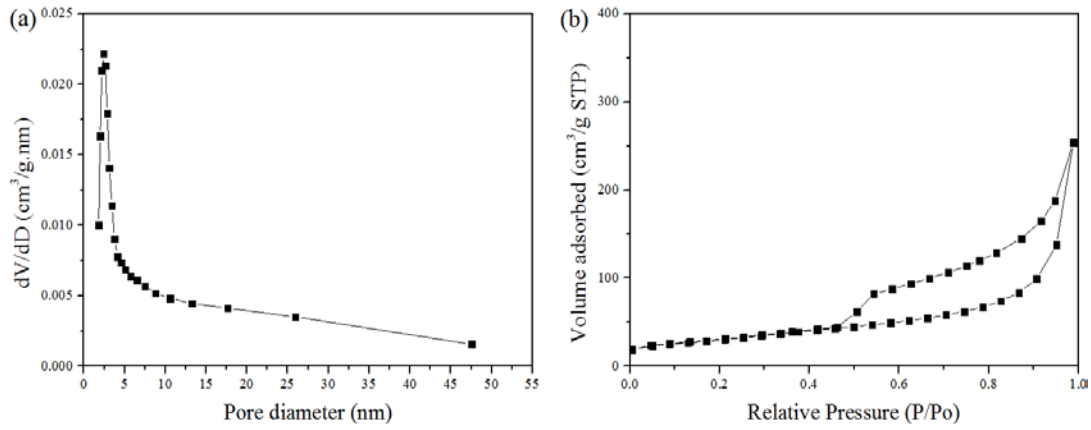

Figure 2.17. (a) pore size distribution of GNP, and (b) nitrogen sorption of GNP [134]

Sample preparation is needed to get more accurate SSA results. In this process, gas, vapour and other impurities are removed from the sample without physically and chemically change the sample. This is done in a vacuum system where dry gas flows through the sample and heat it for several hours before it can be analysed by BET.

Important factors affecting BET analysis are samples size, morphology and porosity. Non-porous and mesoporous samples with wide pore diameter are suitable for BET analysis; while this method is not suitable to analyse microporous samples. This is due to micropore excellent adsorption abilities. Hence it is hard to separate the mono-multilayer adsorption from the micropore filling [132]. **Table 2.15** shows the advantages and disadvantages of BET analysis.

Table 2.15. Advantages and disadvantages of BET analysis

Advantages	Disadvantages
Inexpensive	Only for dry samples
Fast	Sensitive to sample sizes (agglomerate samples will resulted in lower SSA values)
Abundant liquid nitrogen	Not applicable for micropores sample

2.6.6 X-ray photoelectron spectroscopy

X-ray photoelectron spectroscopy (XPS) is one of the most commonly used methods for surface analysis. XPS measures the electrons (photoelectrons) that are excited or emitted when an X-ray beam is applied to a sample/ material, as shown in **Figure**

2.18. The most commonly used X-rays are magnesium Kα with energy 1253.6 eV and aluminium Kα with energy 1486.7 eV [135].

These photoelectrons tell us the atomic composition, chemical oxidation state, and electronic surface of the sample [136]. Important characteristics of the photoelectron are the spin orientation, kinetic energy, and emission direction to the sample and the exciting radiation [137]. Photoelectrons' name is based on the orbital (s, p, d, f) and spin (±1/2) quantum numbers of the core levels. XPS spectrometer can detect all elements except hydrogen and helium, due to low photoelectron cross section [138]. In the case of overlapping orbital, XPS can identify different excitation that occurs from the same element.

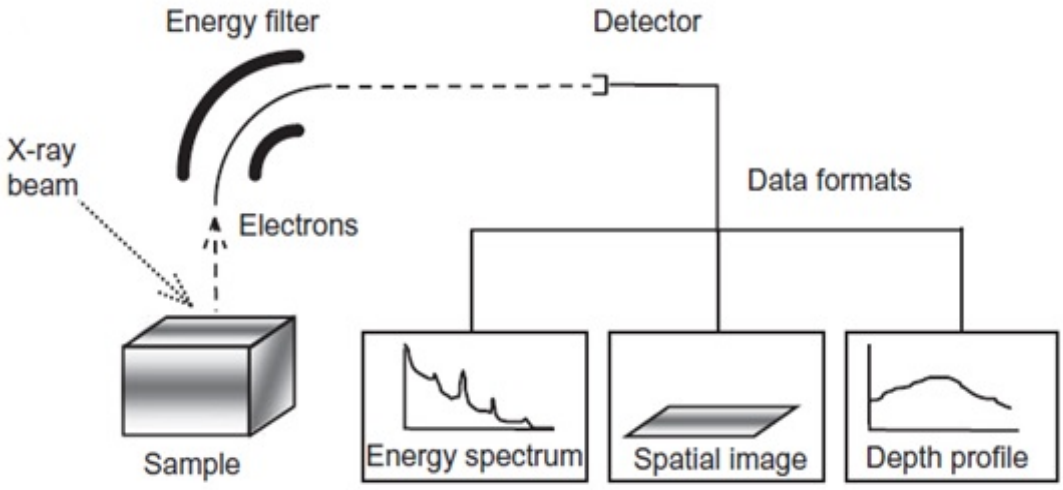

Figure 2.18. Schematic diagram of XPS spectrometer [138]

Figure 2.19 shows the photoemission process. In this process XPS detects and measures the energy that is being discharged when the X-ray photon (with energy hv) is absorbed by the sample's atom, which is shown from below reaction [136, 139]:

$$A + hv \rightarrow A^{+*} + e^{-} \qquad (2.40)$$

Where e^- is photoelectron, A is a neutral atom and A^{+*} is the excited ion.

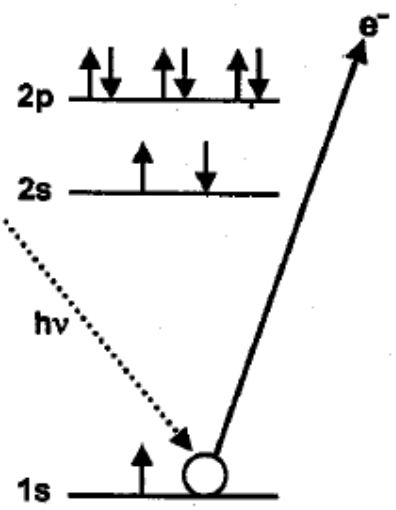

Figure 2.19. Schematic diagram of photoemission process

The X-ray photon creates the photoelectron with kinetic energy (E_k) that is relative to the vacuum level (E_v). Below is an equation to determine the kinetic energy [136-137]:

$$E_k = E_k^1 - (\varphi_{spec} - \varphi_s) \qquad (2.41)$$

Where E_k is electron kinetic energy, E_k^1 is electron kinetic energy at the sample surface, φ_{spec} is the spectrometer energy required to remove electron from Fermi to vacuum levels, and φ_s is the sample energy required to remove electron from Fermi to vacuum levels.

The relationship between the X-ray photons and kinetic energy can be described using below equation [136-137]:

$$hv = E_b + E_k + \varphi_{spec} \qquad (2.42)$$

Where E_b is the binding energy. Element and chemical structure are the parameters that affecting the binding energy [140]. Besides X-ray photon (high energy), Auger electron (low energy) is also emitted caused by the remaining excited ions [135-136]:

$$A^{+*} \rightarrow A^{+} + hv'(X - ray\ photon) \qquad (2.43)$$

$$A^{+*} \rightarrow A^{++} + e^{-}\ (Auger\ electron) \qquad (2.44)$$

The most common orbitals that XPS can detect in the survey scan are C 1s, O1 s, N1 s, and Si 2p, which have a higher binding energy and background. Each element has different binding energy. **Table 2.16** lists the functional groups and their binding

energy in XPS, while an example of XPS survey and C1s convolution of graphene nanoplate can be seen in **Figure 2.20**. Survey scan in XPS is done for binding energy between 0 to 1200 eV to detect what elements are present.

Table 2.16. Functional groups and their binding energy [140]

Element			E_b (eV)
Carbon	C=C	Double bond	285
	C_6H_6	Phenyl group	
	$-CH_2-$	Saturated	
Oxygen	-CHR-OH	Alcohol	532-534
	$-CO_2H$	Acid	
	COR	Ketone	
	-CHO	Aldehyde	
	$-CO_2R$	Ester	
Nitrogen	R_2N	Amine	400-401
	R-CH	Nitrile	
	$-CO-NR_2$	Amide	
	C_5H_5N	Heterocycle	

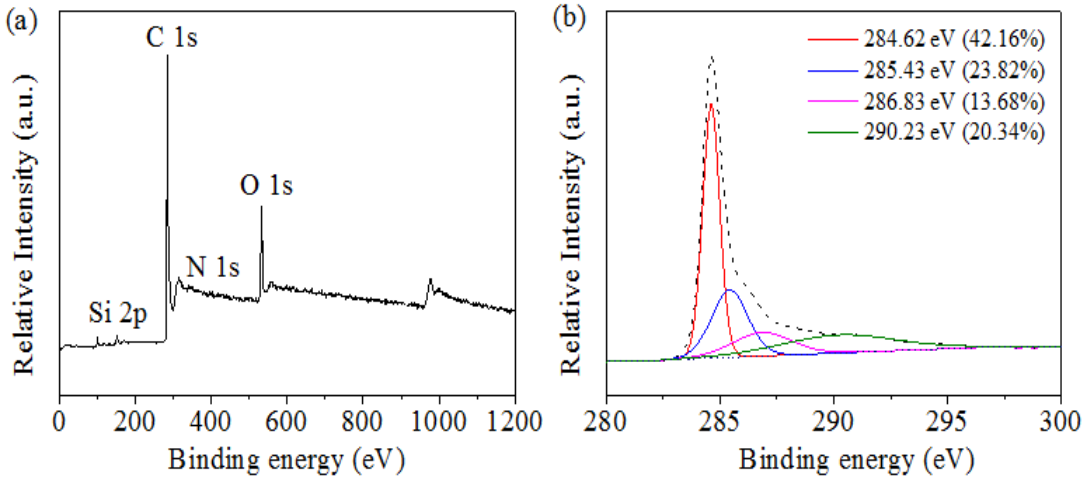

Figure 2.20. (a) XPS survey of GNP, and (b) C1s convolution of GNP [134]

There are several factors affecting the XPS curves, such as [136]:

- Produced photons energy
- X-rays energy resolution
- Samples' ability to an anode surface

Table 2.17 shows the list of some advantages and disadvantages of XPS.

Table 2.17. Advantages and Disadvantages of XPS [136, 138]

Advantages	Disadvantages
Quantitative and qualitative elemental analysis	Binding energy calibration
Able to detect all elements (except H and He)	Sample preparation
Surface specificity (< 10 nm)	De-convolution of XPS peaks is not accurate
Sensitive (concentrations < 0.1% a.t.)	

2.6.7 X-ray diffraction

X-ray diffraction (XRD) is a diffraction method to characterize and determine the crystallographic size, structure and orientation of the material or sample. X-rays are diffracted assuming they are being reflected from crystal planes. The X-ray detector is rotated at a speed twice as fast as the specimen is being rotated [141]. The detector is always at the angle of 2θ° if the specimen surface is at θ° from the incident radiation (see **Figure 2.21**).

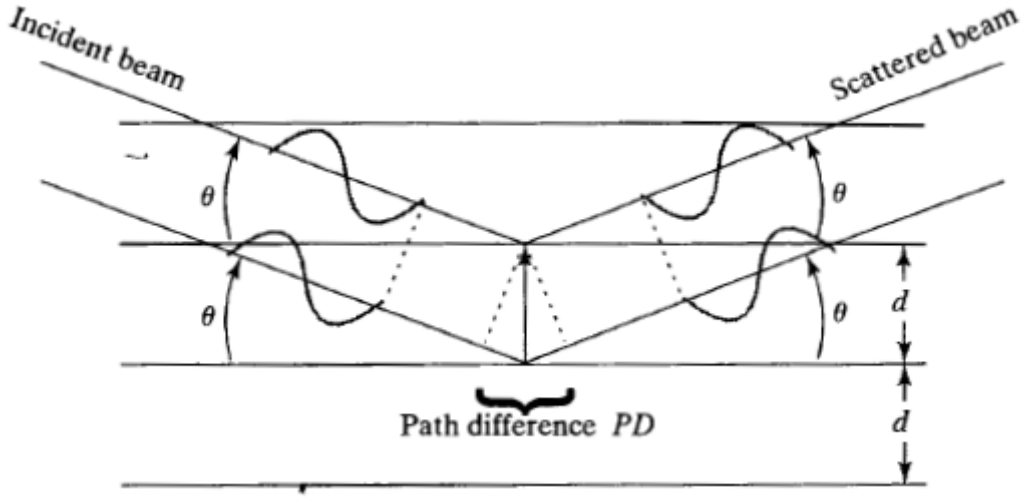

Figure 2.21. Diffraction of X-rays by a crystal [142]

The basic geometry requires that X-rays are diffracted assuming they were being reflected from specimen flat surface. At specific values of θ°, diffraction occurs (**Figure 2.22**).

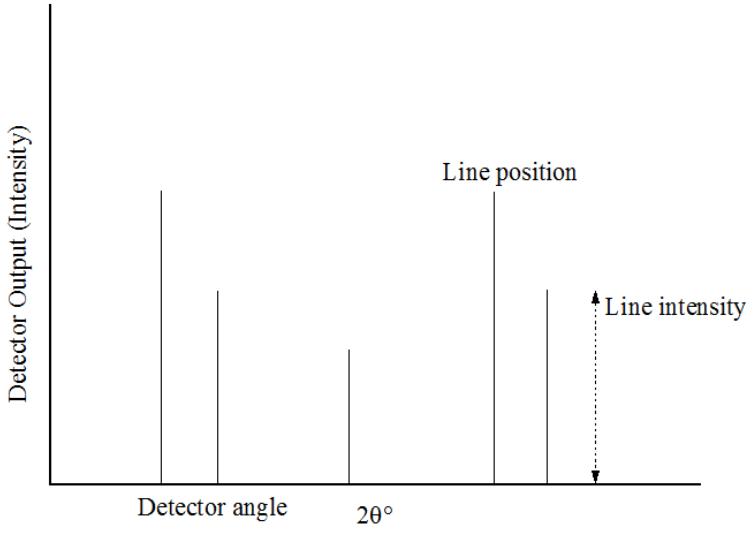

Figure 2.22. Diffractometer pattern

The two important features of diffractometer pattern are line intensity and line position [143]. Line intensity is determined by the structure factor; whereas line position is determined by the Bragg equation [143-145]:

$$F = \int_{j=1}^{n} f_j e^{2\pi i(hu_j + kv_j + lw_j)} \ (line\ intensity) \qquad (2.45)$$

$$\lambda = 2d_{hkl} sin\theta \ (line\ position) \qquad (2.46)$$

Where F is the structure factor, f_j is the atomic scattering factor, h, k, l are the line indices, u_j, v_j, w_j are the point indices, and λ is the monochromatic wavelength.

It is to be noted that the pattern of lines is exclusive to a particular crystalline structure. For example, we take the simplest possible structure the simple cubic material containing only atom A, as is seen in **Figure 2.23**.

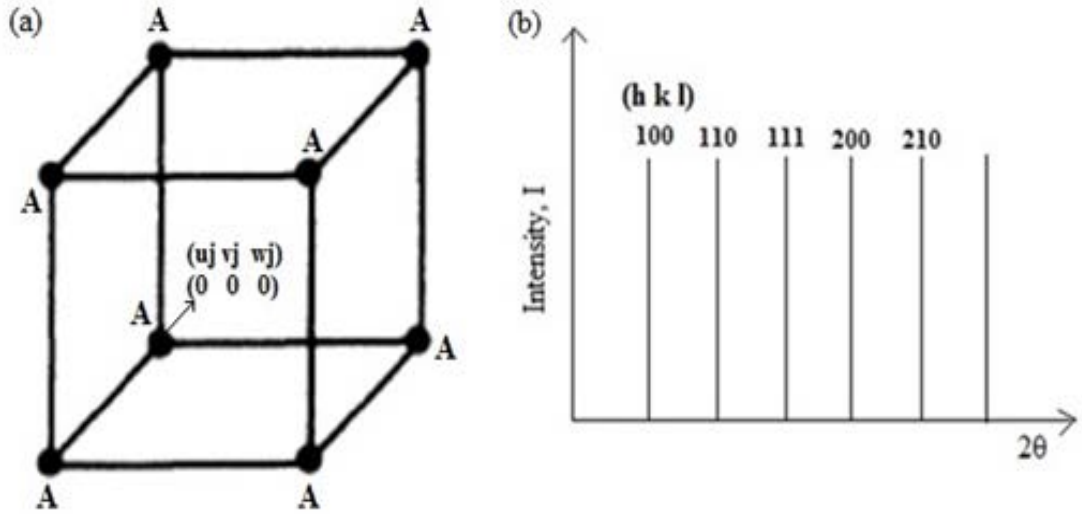

Figure 2.23. (a) simple cubic structure with atom A (b) Diffraction pattern of simple cubic structure with atoms A [144]

The atoms of A are located at specific points in the unit cell. The indices of the points are given u_j, v_j, and w_j. There is only one atom per unit cell. This atom is at the point u_j=0, y_j=0 and w_j=0, hence for the structure factor we have [144, 146-147]:

$$F = \int_{j=1}^{n=1} f_A e^{2\pi i(hu_j + kv_j + lw_j)} \quad (2.47)$$

Because $u_j = v_j = w_j = 0$, we have $F = f_A$ (2.48)

I (intensity of XRD line) is proportional to F^2 (f_A^2), which means that all of the possible diffraction lines will occur. For this simple cubic structure we will have diffraction lines with all possible values of h, k, and l [143]. The observed diffraction pattern contains all possible lines as is seen in **Figure 2.23b**. For other crystal structure, body-centred cubic, face-centred cubic, diamond and hexagonal closed-packed, the diffraction can be seen from **Figure 2.24**. In reality, XRD patterns are different in two important respects: the intensities if the different hkl lines are not the same and the lines are not lines but are profiles [144]. While the observed variation of

intensities depends on a number of factors, such as: structure (F), Lorentz-Polarisation factor (LP), multiplicity (m), Debye Waller temperature formula (e^{-2m}), absorption (A(θ)), and constant K. The intensity of an XRD line becomes [144]:

$$I = KF^2LPme^{-2m}A(\theta) \qquad (2.49)$$

The width of intensity profile increases as the thickness of crystal structure decreases. The interlayer thickness can be calculated following the Scherrer formula [148-150]:

$$L = \frac{0.9\lambda}{B\cos\theta_B} \qquad (2.50)$$

Where L is the interlayer thickness, B is the width measured at intensity equal to half the maximum intensity, and θ_B is the angle of detected intensity. Functionalize of graphene, such as nitrogen doping may result in decreasing the intensity and broadening the half peak width (B). **Figure 2.25** shows example of XRD patterns and **Table 2.18** lists the advantages and disadvantages of XRD technique.

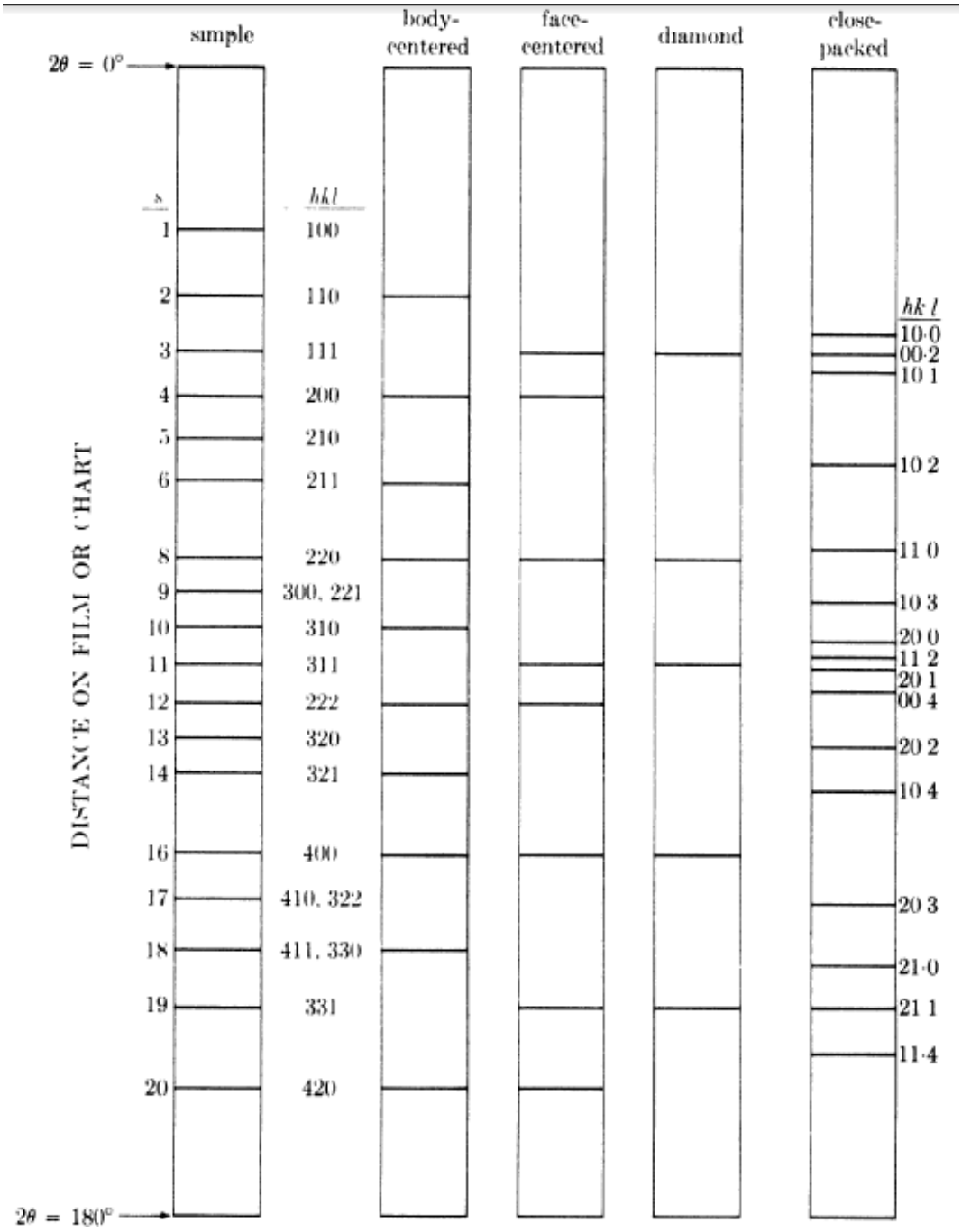

Figure 2.24. Diffraction pattern of other crystal structure [144]

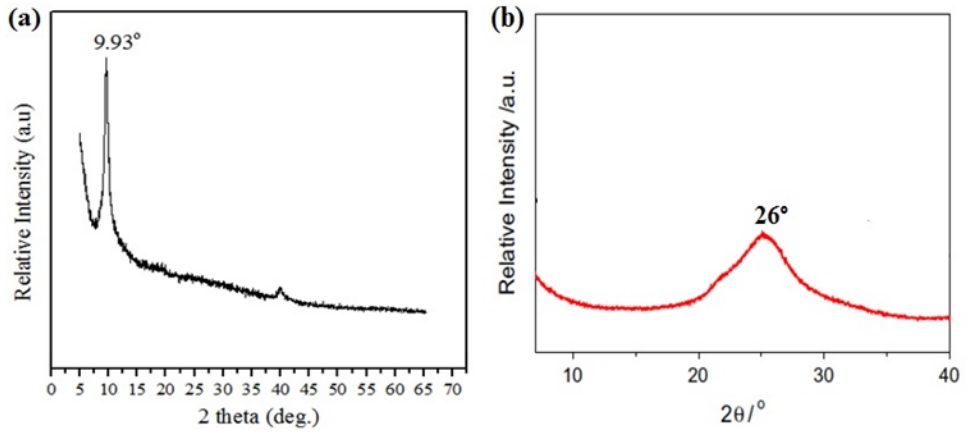

Figure 2.25. XRD pattern of (a) GO [108], and (b) rGO [3]

Table 2.18. Advantages and Disadvantages of XRD [144, 146, 151]

Advantages	Disadvantages
Quantitative and qualitative analysis	Training is needed to operate the machine
Easy sample preparation	Can only analyse solid powder samples
Simple data interpretation	Overlaying peaks might occur in a complex sample
Quick analysis	

2.6.8 Electron paramagnetic resonance

Electron paramagnetic resonance (EPR) is one of spectroscopy analysis that studies catalysts surfaces. It can be used to detect [152-155]:

1. Surface defects in solid
2. Free radicals in liquid, solid and gaseous state
3. Two, three or more unpaired electrons
4. Transition-metal ions and rare-earth ions

This is done by producing EPR spectra with well-defined spin Hamiltonian parameters. Particle sizes, surface species location, and the presence of other species in the catalytic system can affect the spin Hamiltonian parameters and therefore modified EPR spectra.

EPR spectrometer works with microwave frequency while static magnetic field scans the EPR spectrum, by adjusting the magnetic field [153]. It observes the difference between two energy levels of the molecule which are split by the magnetic field. Below equation shows the relationship between the resonance condition and the transition of the two energy levels:

$$E = hv = g\beta H \qquad (2.51)$$

Where H is the magnetic field, h is the Planck's constant (6.63 x 10^{-27} erg sec), and β is the Bohr frequency (9.27 x 10^{-21} erg/G), and g is the g-factor (for free electron, g factor is estimated to be 2)[153, 156]. Normally, the x-band microwave frequency is 9.5 GHz with magnetic field strength of 3400 G [156]. From the relation v and H, there are infinite pairs of v and H combinations which fit **Eq. 2.51**. These appropriate v and H combinations is not a unique "Fingerprint" of a species (transition metal ions, organic free radicals and ions). The fingerprint of a species is the g value that consists of the interaction information of the free electron and the electronic structure of a species.

In addition to determine the g-factor of a species from EPR spectra, the unpaired electrons can interact with an atom that has a nucleus with a magnetic moment and spin (I) to produce the hyperfine interaction [152, 157]. Here, the energy level of the unpaired electron is a function of a, the hyperfine coupling constant. For sulfate radical $SO_4^{\bullet-}$, a^N=13.82 G, a_β^H = 10.10 G, a_γ^H = 0.83 G, a_γ^H=1.42 G and g=2.0059. For hydroxyl radical $^{\bullet}OH$, $a^N = a_\beta^H$ =14.9 G [157]. The number of lines (L) resulted from hyperfine interaction can be determined by the following equation,

$$L = 2NI + 1 \qquad (2.52)$$

Where N is the number of equivalent nuclei, and I is the spin of nuclei.

Figure 2.26 shows the schematic diagram of EPR spectrometer. These coefficients are the ratio of the line peak intensities in EPR spectra as is shown in an example of EPR spectrum of N-SWCNT in **Figure 2.27a**.

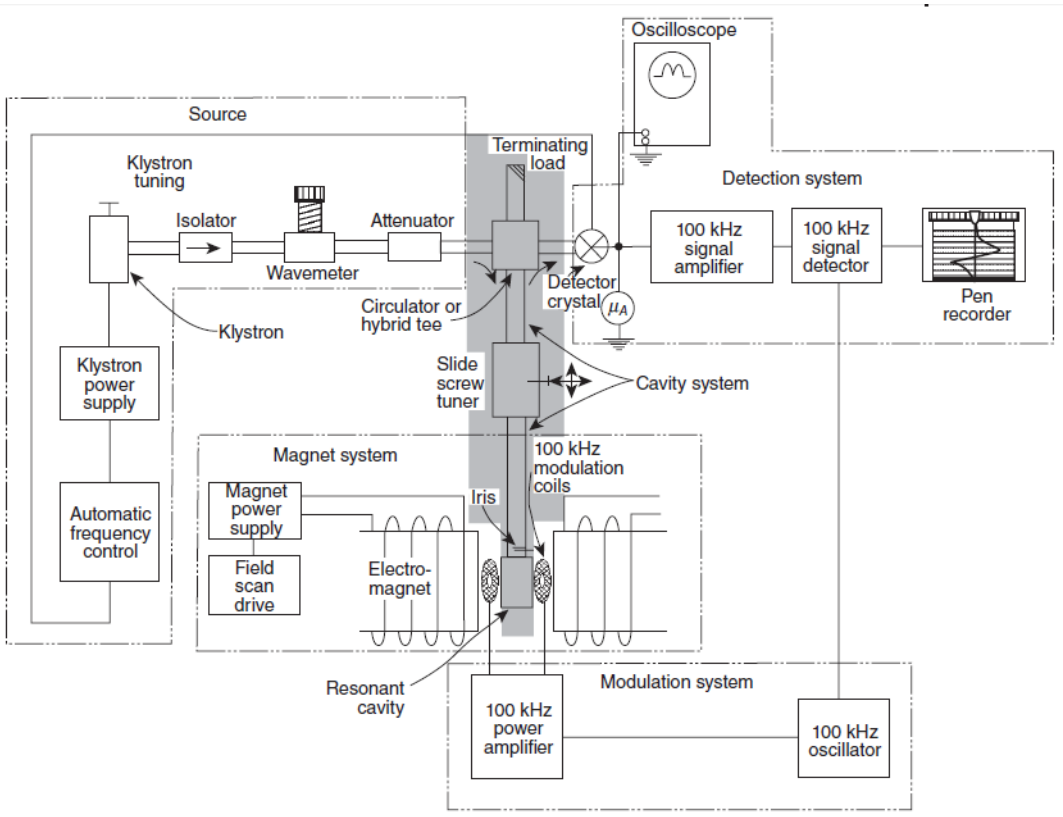

Figure 2.26. Schematic diagram of x-band EPR spectrometer with 100 kHz phase-sensitive detector [153]

Pascals triangle (**Table 2.19**) is used to determine the increasing n-coefficient from the binomial expansion $(1+x)^n$. This n represents the number of equivalent protons. This coefficients are the ratio in which the intensity of the peaks line in EPR spectra; shown in an example of EPR spectrum of N-SWCNT in **Figure 2.27**.

Table 2.19. Coefficients for the binomial expansion $(1+x)^n$ [152-153]

n	Pattern	Coefficients
0		1
1	Doublet	1 1
2	Triplet	1 2 1
3	Quartet	1 3 3 1
4	Pentet	1 4 6 4 1
5	Sextet	1 5 10 10 5 1
6	Septet	1 6 15 20 15 6 1
7	Octet	1 7 21 35 35 21 7 1
8	Nonet	1 8 28 56 70 56 28 8 1

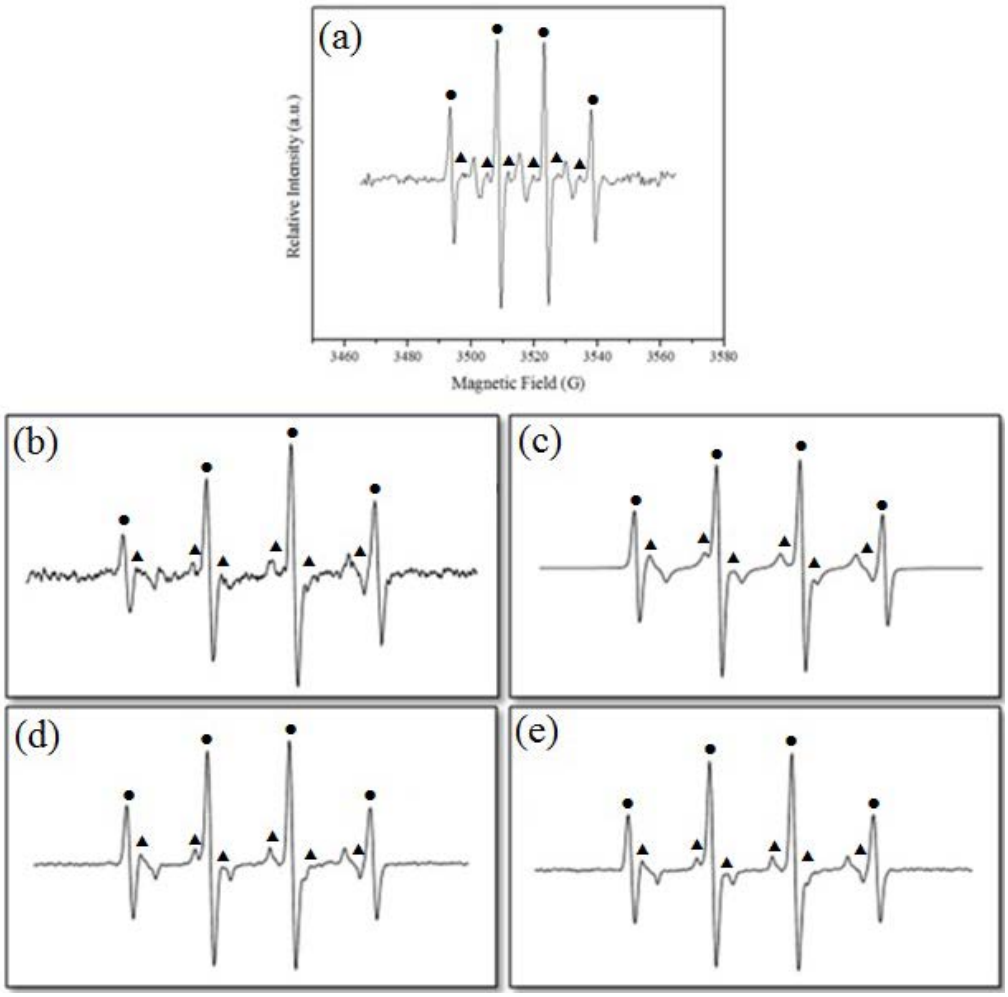

Figure 2.27. (a) EPR spectrum of N-SWCNT in 25 °C nitrobenzene aqueous solution with the addition of PMS. Spectra of DMPO (100 mM) and $(NH_4)_2S_2O_8$ (100 mM) under 254 nm light taken at (b) t = 0 min, (c) simulation of E ($DMPO^{\bullet}-SO_4$, a_N = 13.66, $a_{\beta\text{-}H}$ =9.97, $a_{\gamma\text{-}H1}$ = 1.55, $a_{\gamma\text{-}H2}$ = 0.73; $DMPO^{\bullet}-OH$, a_N = 15.02, $a_{\beta\text{-}H}$ = 14.72), (d) at t = 5 min, and (e) at t = 10 min [158]. ((▲) DMPO- SO_4 (●) DMPO-OH)

Researchers have found that free radicals such as sulfate radicals ($SO_4^{\bullet-}$) and hydroxyl radicals ($^{\bullet}OH$) were the prime factors in catalytic oxidation [158-161], therefore producing different EPR spectra for various radical adducts as is seen in **Figure 2.22b-e**. EPR is the best method in order to detect, determine and characterized these free radicals. Free radicals are normally short lived, but it lives longer by reacting it with a spin trap agent [162-163]. There are many spin trapping agents that can be used, such as: EMPO, DIPPMPO, BMPO, PBN, POBN, DMPO, DMSO [164]. The commonly used spin trapping agent is DMPO (5,5-dimethyl-1-pyrroline N-oxide);

because DMPO is very redox inert, therefore producing different EPR spectra compare to the radical adducts.

Table 2.20 shows several advantages and disadvantages of EPR [153].

Table 2.20. Advantages and Disadvantages of EPR

Advantages	Disadvantages
Provide valuable information regarding the symmetry of paramagnetic defects Sensitive Very quick to analyse	Can only detects paramagnetic centres such as free radicals and unpaired electrons

2.7 Conclusions

Among various water purification techniques, AOPs have been found to be the most suitable method to degrade aqueous contaminants which are persistent and difficult to degrade biologically into simpler end products. AOPs consume lower energy and chemical and also involve faster reaction rate, simple design, and in-situ treatment. But the technique itself is not the only factor that needs to be considered in improving waste water remediation. Several factors may affect the successful occurrence for pollutant degradation, such as the oxidants, catalysts, reaction temperature, aqueous pH level and the types of radicals generated. The combination and manipulation of these factors may enhance or hinder the pollutant degradation.

Choosing the right catalysts would be one of the major factors in order to improve the pollutant degradation. Past studies have developed and synthesise many types of catalysts. For metal based catalysts, it was found that they show very significant pollutant degradation and faster reaction rate. However, metal based catalysts, due to the metals may cause secondary contamination. Thus, green metal-free catalysts are more suitably used in the waste water remediation. Among many metal-free catalysts, carbon nano materials especially graphene, have gained many attractions. Graphene is a material with extraordinary electronic properties and as a promising catalyst for degradation of aqueous contaminants. However, graphene is costly and it is still an emerging and developed material. More research has to be done to develop modified

graphene and better catalysts that are not only cost effective but also efficient for catalysis. With the right combination of catalyst, the mechanism of oxidant‘s activation process and characterisation techniques, a novel binary or ternary system may be developed in order to enhance pollutant degradation in the waste water.

References

1. H. Liang, Y. Y. T., H. Sun, H.M. Ang, M.O. Tade, and S. Wang, Solution combustion synthesis of Co oxide-based catalysts for phenol degradation in aqueous solution. *J. Colloid Interface Sci.* **2012,** *372*, 58-62.
2. Rashed, M. N., *Adsorption technique for the removal of organic pollutants from water and wastewater*. INTECH Open Access Publisher: **2013**.
3. Sun, H. Q.; Wang, Y. X.; Liu, S. Z.; Ge, L.; Wang, L.; Zhu, Z. H.; Wang, S. B., Facile synthesis of nitrogen doped reduced graphene oxide as a superior metal-free catalyst for oxidation. *Chem. Commun.* **2013,** *49* (85), 9914-9916.
4. Shukla, P.; Wang, S. B.; Sun, H. Q.; Ang, H. M.; Tade, M., Adsorption and heterogeneous advanced oxidation of phenolic contaminants using Fe loaded mesoporous SBA-15 and H2O2. *Chem. Eng. J.* **2010,** *164* (1), 255-260.
5. Rao, D. G.; Senthilkumar, R.; Byrne, J. A.; Feroz, S., *Wastewater Treatment: Advanced Processes and Technologies*. Taylor & Francis: **2012**.
6. Pera-Titus, M.; Garcia-Molina, V.; Banos, M. A.; Gimenez, J.; Esplugas, S., Degradation of chlorophenols by means of advanced oxidation processes: a general review. *Appl. Catal. B-Environ.* **2004,** *47* (4), 219-256.
7. Sun, H.; Liu, S.; Zhou, G.; Ang, H. M.; Tadé, M. O.; Wang, S., Reduced Graphene Oxide for Catalytic Oxidation of Aqueous Organic Pollutants. *ACS Applied Materials & Interfaces* **2012,** *4* (10), 5466-5471.
8. Liang, H. W.; Sun, H. Q.; Patel, A.; Shukla, P.; Zhu, Z. H.; Wang, S. B., Excellent performance of mesoporous Co3O4/MnO2 nanoparticles in heterogeneous activation of peroxymonosulfate for phenol degradation in aqueous solutions. *Appl. Catal. B-Environ.* **2012,** *127*, 330-335.
9. Parsons, S., *Advanced Oxidation Processes for Water and Wastewater Treatment*. IWA Publishing: **2004**.
10. Suty, H.; De Traversay, C.; Cost, M., Applications of advanced oxidation processes: present and future. *Water Science and Technology* **2004,** *49* (4), 227-233.

11. Huang, K.-C.; Couttenye, R. A.; Hoag, G. E., Kinetics of heat-assisted persulfate oxidation of methyl tert-butyl ether (MTBE). *Chemosphere* **2002,** *49* (4), 413-420.

12. Saputra, E.; Muhammad, S.; Sun, H. Q.; Ang, H. M.; Tade, M. O.; Wang, S. B., Different Crystallographic One-dimensional MnO2 Nanomaterials and Their Superior Performance in Catalytic Phenol Degradation. *Environ. Sci. Technol.* **2013,** *47* (11), 5882-5887.

13. Saputra, E.; Muhammad, S.; Sun, H. Q.; Ang, H. M.; Tade, M. O.; Wang, S. B., Shape-controlled activation of peroxymonosulfate by single crystal alpha-Mn2O3 for catalytic phenol degradation in aqueous solution. *Appl. Catal. B-Environ.* **2014,** *154*, 246-251.

14. Zhou, G.; Tian, H.; Sun, H.; Wang, S.; Buckley, C. E., Synthesis of carbon xerogels at varying sol–gel pHs, dye adsorption and chemical regeneration. *Chem. Eng. J.* **2011,** *171* (3), 1399-1405.

15. Lofrano, G., *Emerging Compounds Removal from Wastewater: Natural and Solar Based Treatments*. Springer Netherlands: **2012**.

16. Worch, E., *Adsorption Technology in Water Treatment: Fundamentals, Processes, and Modeling*. De Gruyter: **2012**.

17. Hu, A.; Apblett, A., *Nanotechnology for Water Treatment and Purification*. Springer International Publishing: **2014**.

18. Adamson, A. W., *Physical chemistry of surfaces*. Wiley: **1990**.

19. Suzuki, M., *Adsorption engineering*. Kodansha: **1990**.

20. Agarwal, A. K.; Kadu, M. S.; Pandhurnekar, C. P.; Muthreja, I. L., Langmuir, Freundlich and BET Adsorption Isotherm Studies for Zinc ions onto coal fly ash. *International Journal of Application or Innovation in Engineering & Management* **2012,** *3* (1), 64-71.

21. Desta, M. B., Batch Sorption Experiments: Langmuir and Freundlich Isotherm Studies for the Adsorption of Textile Metal Ions onto Teff Straw (Eragrostis tef) Agricultural Waste. *Journal of Thermodynamics* **2013,** *2013*, 6.

22. Iakovleva, E.; Sillanpaa, M., The use of low-cost adsorbents for wastewater purification in mining industries. *Environmental Science and Pollution Research* **2013,** *20* (11), 7878-7899.

23. Dąbrowski, A., Adsorption — from theory to practice. *Advances in Colloid and Interface Science* **2001,** *93* (1–3), 135-224.

24. Dabrowski, A.; Podkoscielny, P.; Hubicki, Z.; Barczak, M., Adsorption of phenolic compounds by activated carbon - a critical review. *Chemosphere* **2005,** *58* (8), 1049-1070.

25. Velasco, L. F.; Ania, C. O., Understanding phenol adsorption mechanisms on activated carbons. *Adsorpt.-J. Int. Adsorpt. Soc.* **2011,** *17* (1), 247-254.

26. László, K.; Podkościelny, P.; Dąbrowski, A., Heterogeneity of Polymer-Based Active Carbons in Adsorption of Aqueous Solutions of Phenol and 2,3,4-Trichlorophenol. *Langmuir* **2003,** *19* (13), 5287-5294.

27. Mattson, J. A.; Mark, H. B.; Malbin, M. D.; Weber, W. J.; Crittenden, J. C., Surface chemistry of active carbon: Specific adsorption of phenols. *Journal of Colloid and Interface Science* **1969,** *31* (1), 116-130.

28. Coughlin, R. W.; Ezra, F. S., Role of surface acidity in the adsorption of organic pollutants on the surface of carbon. *Environ. Sci. Technol.* **1968,** *2* (4), 291-297.

29. Gao, Z. M.; Bandosz, T. J.; Zhao, Z. B.; Han, M.; Qiu, J. S., Investigation of factors affecting adsorption of transition metals on oxidized carbon nanotubes. *Journal of Hazardous Materials* **2009,** *167* (1-3), 357-365.

30. Seco, A.; Marzal, P.; Gabaldon, C.; Ferrer, J., Study of the adsorption of Cd and Zn onto an activated carbon: Influence of pH, cation concentration, and adsorbent concentration. *Separation Science and Technology* **1999,** *34* (8), 1577-1593.

31. Otker, H. M.; Akmehmet-Balcioglu, I., Adsorption and degradation of enrofloxacin, a veterinary antibiotic on natural zeolite. *Journal of Hazardous Materials* **2005,** *122* (3), 251-258.

32. Bekci, Z.; Seki, Y.; Yurdakoc, M. K., Equilibrium studies for trimethoprim adsorption on montmorillonite KSF. *Journal of Hazardous Materials* **2006,** *133* (1-3), 233-242.

33. Cesaro, A.; Naddeo, V.; Belgiorno, V., Wastewater treatment by combination of advanced oxidation processes and conventional biological systems. *Journal of Bioremediation & Biodegradation* **2013,** *2013*.

34. Pereira, M. C.; Oliveira, L. C. A.; Murad, E., Iron oxide catalysts: Fenton and Fenton-like reactions - a review. *Clay Min.* **2012,** *47* (3), 285-302.

35. Sharma, S.; Ruparelia, J.; Patel, M. L. In *A general review on Advanced Oxidation Processes for waste water treatment*, Nirma University International Conference, Ahmedabad, Gujarat, **2011**.

36. Deng, Y.; Zhao, R., Advanced Oxidation Processes (AOPs) in Wastewater Treatment. *Current Pollution Reports* **2015,** *1* (3), 167-176.

37. Howe, K. J.; Hand, D. W.; Crittenden, J. C.; Trussell, R. R.; Tchobanoglous, G., *Principles of Water Treatment*. Wiley: **2012**.

38. Oturan, M. A.; Aaron, J. J., Advanced Oxidation Processes in Water/Wastewater Treatment: Principles and Applications. A Review. *Crit. Rev. Environ. Sci. Technol.* **2014,** *44* (23), 2577-2641.

39. S. D. Choi, J. H. L., D. M. Park, and G. J. Kim, Fabrication of CNT/ CMK3 Carbon Composites with High Electrical/ Thermal Conductive Properties. *Bull. Korean Chem. Soc.* **2013,** *34* (7), 2155-2161.

40. Anandan, S.; Ikuma, Y.; Niwa, K., An Overview of Semi-Conductor Photocatalysis: Modification of TiO(2) Nanomaterials. In *Solid State Chemistry and Photocatalysis of Titanium Dioxide*, Nowotny, M. K.; Nowotny, J., Eds. **2010**, pp 239-260.

41. Li, J. T.; Wu, N. Q., Semiconductor-based photocatalysts and photoelectrochemical cells for solar fuel generation: a review. *Catalysis Science & Technology* **2015,** *5* (3), 1360-1384.

42. Gupta, S. M.; Tripathi, M., An Overview of Commonly Used Semiconductor Nanoparticles in Photocatalysis. *High Energy Chemistry* **2012,** *46* (1), 1-9.

43. Hoffmann, M. R.; Martin, S. T.; Choi, W. Y.; Bahnemann, D. W., ENVIRONMENTAL APPLICATIONS OF SEMICONDUCTOR PHOTOCATALYSIS. *Chemical Reviews* **1995,** *95* (1), 69-96.

44. Zhao, Y.; Zhou, X.; Ye, L.; Tsang, S. C. E., Nanostructured Nb2O5 catalysts. *Nano Reviews* **2012**.

45. Rajeshwar, K.; Osugi, M. E.; Chanmanee, W.; Chenthamarakshan, C. R.; Zanoni, M. V. B.; Kajitvichyanukul, P.; Krishnan-Ayer, R., Heterogeneous photocatalytic treatment of organic dyes in air and aqueous media. *Journal of Photochemistry and Photobiology C-Photochemistry Reviews* **2008,** *9* (4), 171-192.

46. Xu, C.; Rangaiah, G. P.; Zhao, X. S., Photocatalytic Degradation of Methylene Blue by Titanium Dioxide: Experimental and Modeling Study. *Ind. Eng. Chem. Res.* **2014,** *53* (38), 14641-14649.

47. Wang, S. B.; Ang, H. M.; Tade, M. O., Volatile organic compounds in indoor environment and photocatalytic oxidation: State of the art. *Environ. Int.* **2007,** *33* (5), 694-705.

48. Cao, L. X.; Spiess, F. J.; Huang, A. M.; Suib, S. L.; Obee, T. N.; Hay, S. O.; Freihaut, J. D., Heterogeneous photocatalytic oxidation of 1-butene on SnO2 and TiO2 films. *Journal of Physical Chemistry B* **1999,** *103* (15), 2912-2917.

49. Houas, A.; Lachheb, H.; Ksibi, M.; Elaloui, E.; Guillard, C.; Herrmann, J. M., Photocatalytic degradation pathway of methylene blue in water. *Appl. Catal. B-Environ.* **2001,** *31* (2), 145-157.

50. Konstantinou, I. K.; Albanis, T. A., TiO2-assisted photocatalytic degradation of azo dyes in aqueous solution: kinetic and mechanistic investigations - A review. *Appl. Catal. B-Environ.* **2004,** *49* (1), 1-14.

51. Matthews, R. W., PHOTOCATALYTIC OXIDATION OF ORGANIC CONTAMINANTS IN WATER - AN AID TO ENVIRONMENTAL PRESERVATION. *Pure and Applied Chemistry* **1992,** *64* (9), 1285-1290.

52. Bhatkhande, D. S.; Pangarkar, V. G.; Beenackers, A., Photocatalytic degradation for environmental applications - a review. *Journal of Chemical Technology and Biotechnology* **2002,** *77* (1), 102-116.

53. Ahmed, S.; Rasul, M. G.; Martens, W. N.; Brown, R.; Hashib, M. A., Heterogeneous photocatalytic degradation of phenols in wastewater: A review on current status and developments. *Desalination* **2010,** *261* (1-2), 3-18.

54. Ahmed, S.; Rasul, M. G.; Martens, W. N.; Brown, R.; Hashib, M. A., Advances in Heterogeneous Photocatalytic Degradation of Phenols and Dyes in Wastewater: A Review. *Water Air and Soil Pollution* **2011,** *215* (1-4), 3-29.

55. Lucking, F.; Koser, H.; Jank, M.; Ritter, A., Iron powder, graphite and activated carbon as catalysts for the oxidation of 4-chlorophenol with hydrogen peroxide in aqueous solution. *Water Res.* **1998,** *32* (9), 2607-2614.

56. Pignatello, J. J.; Oliveros, E.; MacKay, A., Advanced oxidation processes for organic contaminant destruction based on the Fenton reaction and related chemistry. *Crit. Rev. Environ. Sci. Technol.* **2006,** *36* (1), 1-84.

57. Che, H.; Bae, S.; Lee, W., Degradation of trichloroethylene by Fenton reaction in pyrite suspension. *Journal of Hazardous Materials* **2011,** *185* (2-3), 1355-1361.

58. Wang, S., A comparative study of Fenton and Fenton-like reaction kinetics in decolourisation of wastewater. *Dyes and Pigments* **2008,** *76* (3), 714-720.

59. Tarr, M. A., *Chemical Degradation Methods for Wastes and Pollutants: Environmental and Industrial Applications*. CRC Press: **2003**.

60. Neyens, E.; Baeyens, J., A review of classic Fenton's peroxidation as an advanced oxidation technique. *Journal of Hazardous Materials* **2003,** *98* (1-3), 33-50.

61. Barbusinski, K., FENTON REACTION - CONTROVERSY CONCERNING THE CHEMISTRY. *Ecological Chemistry and Engineering S-Chemia I Inzynieria Ekologiczna S* **2009,** *16* (3), 347-358.

62. Stasinakis, A. S., USE OF SELECTED ADVANCED OXIDATION PROCESSES (AOPs) FOR WASTEWATER TREATMENT - A MINI REVIEW. *Global Nest Journal* **2008,** *10* (3), 376-385.

63. Tian, G. P.; Wu, Q. Y.; Li, A.; Wang, W. L.; Hu, H. Y., Enhanced decomposition of 1,4-dioxane in water by ozonation under alkaline condition. *Water Science and Technology* **2014,** *70* (12), 1934-1940.

64. Majumdar, S. B.; Sproul, O. J., Technical and economic aspects of water and wastewater ozonation: A critical review. *Water Res.* **1974,** *8* (5), 253-260.

65. von Gunten, U., Ozonation of drinking water: Part I. Oxidation kinetics and product formation. *Water Res.* **2003,** *37* (7), 1443-1467.

66. Rodriguez, E. M.; Marquez, G.; Leon, E. A.; Alvarez, P. M.; Amat, A. M.; Beltran, F. J., Mechanism considerations for photocatalytic oxidation, ozonation and photocatalytic ozonation of some pharmaceutical compounds in water. *Journal of Environmental Management* **2013,** *127*, 114-124.

67. Medellin-Castillo, N. A.; Ocampo-Pérez, R.; Leyva-Ramos, R.; Sanchez-Polo, M.; Rivera-Utrilla, J.; Méndez-Díaz, J. D., Removal of diethyl phthalate from water solution by adsorption, photo-oxidation, ozonation and advanced oxidation process (UV/H2O2, O3/H2O2 and O3/activated carbon). *Science of The Total Environment* **2013,** *442*, 26-35.

68. Gurol, M. D.; Vatistas, R., Oxidation of phenolic compounds by ozone and ozone + u.v. radiation: A comparative study. *Water Res.* **1987,** *21* (8), 895-900.

69. Buxton, G. V.; Greenstock, C. L.; Helman, W. P.; Ross, A. B., CRITICAL-REVIEW OF RATE CONSTANTS FOR REACTIONS OF HYDRATED ELECTRONS, HYDROGEN-ATOMS AND HYDROXYL RADICALS (.OH/.O-) IN AQUEOUS-SOLUTION. *J. Phys. Chem. Ref. Data* **1988,** *17* (2), 513-886.

70. Xu, X.-R.; Li, X.-Z., Degradation of azo dye Orange G in aqueous solutions by persulfate with ferrous ion. *Separation and Purification Technology* **2010,** *72* (1), 105-111.

71. Anipsitakis, G. P.; Dionysiou, D. D., Radical generation by the interaction of transition metals with common oxidants. *Environ. Sci. Technol.* **2004,** *38* (13), 3705-3712.

72. Ahmad, M.; Teel, A. L.; Watts, R. J., Mechanism of Persulfate Activation by Phenols. *Environ. Sci. Technol.* **2013,** *47* (11), 5864-5871.

73. Lee, H.; Lee, H.-J.; Jeong, J.; Lee, J.; Park, N.-B.; Lee, C., Activation of persulfates by carbon nanotubes: Oxidation of organic compounds by nonradical mechanism. *Chem. Eng. J.* **2015,** *266*, 28-33.

74. Zhou, Y.; Jiang, J.; Gao, Y.; Ma, J.; Pang, S. Y.; Li, J.; Lu, X. T.; Yuan, L. P., Activation of Peroxymonosulfate by Benzoquinone: A Novel Nonradical Oxidation Process. *Environ. Sci. Technol.* **2015,** *49* (21), 12941-12950.

75. Duan, X. G.; Ao, Z. M.; Zhou, L.; Sun, H. Q.; Wang, G. X.; Wang, S. B., Occurrence of radical and nonradical pathways from carbocatalysts for aqueous and nonaqueous catalytic oxidation. *Appl. Catal. B-Environ.* **2016,** *188*, 98-105.

76. Duan, X. G.; Sun, H. Q.; Wang, Y. X.; Kang, J.; Wang, S. B., N-Doping-Induced Nonradical Reaction on Single-Walled Carbon Nanotubes for Catalytic Phenol Oxidation. *ACS Catal.* **2015,** *5* (2), 553-559.

77. Duan, X. G.; Ao, Z. M.; Sun, H. Q.; Zhou, L.; Wang, G. X.; Wang, S. B., Insights into N-doping in single-walled carbon nanotubes for enhanced activation of superoxides: a mechanistic study. *Chem. Commun.* **2015,** *51* (83), 15249-15252.

78. Qi, C.; Liu, X.; Ma, J.; Lin, C.; Li, X.; Zhang, H., Activation of peroxymonosulfate by base: Implications for the degradation of organic pollutants. *Chemosphere* **2016,** *151*, 280-288.

79. Duan, H. T.; Liu, Y.; Yin, X. H.; Bai, J. F.; Qi, J., Degradation of nitrobenzene by Fenton-like reaction in a H2O2/schwertmannite system. *Chem. Eng. J.* **2016,** *283*, 873-879.

80. Guan, Y. H.; Ma, J.; Ren, Y. M.; Liu, Y. L.; Xiao, J. Y.; Lin, L. Q.; Zhang, C., Efficient degradation of atrazine by magnetic porous copper ferrite catalyzed peroxymonosulfate oxidation via the formation of hydroxyl and sulfate radicals. *Water Res.* **2013,** *47* (14), 5431-5438.

81. Lou, X.; Wu, L.; Guo, Y.; Chen, C.; Wang, Z.; Xiao, D.; Fang, C.; Liu, J.; Zhao, J.; Lu, S., Peroxymonosulfate activation by phosphate anion for organics degradation in water. *Chemosphere* **2014,** *117*, 582-585.

82. Sun, H.; Feng, X.; Wang, S.; Ang, H. M.; Tadé, M. O., Combination of adsorption, photochemical and photocatalytic degradation of phenol solution over supported zinc oxide: Effects of support and sulphate oxidant. *Chem. Eng. J.* **2011,** *170* (1), 270-277.

83. Titelman, G. I.; Gelman, V.; Bron, S.; Khalfin, R. L.; Cohen, Y.; Bianco-Peled, H., Characteristics and microstructure of aqueous colloidal dispersions of graphite oxide. *Carbon* **2005,** *43* (3), 641-649.

84. Chen, C.; Cai, W. M.; Long, M. C.; Zhou, B. X.; Wu, Y. H.; Wu, D. Y.; Feng, Y. J., Synthesis of Visible-Light Responsive Graphene Oxide/TiO2 Composites with p/n Heterojunction. *Acs Nano* **2010,** *4* (11), 6425-6432.

85. An, Y.; Wei, X.; Yang, Z., Improving electronic transport of zigzag graphene nanoribbons by ordered doping of B or N atoms. *Physical Chemistry Chemical Physics* **2012,** *14* (45), 15802-15806.

86. H. Sun, Y. W., S. Liu, L. Gei, L. Wang, Z. Zhu, and S. Wang, Facile synthesis of nitrogen doped reduced graphene oxide as a superior metal-free catalyst for oxidation. *RSC. Chem. Comm.* **2013,** *10*.

87. T.N.Huan, T. V. K., Y. Kang, K.B.Shim, and H. Chung, Enhancement of quarternary nitrogen doping of graphene oxide via chemical reduction prior to thermal annealing and an investigation of its electrochemical properties. *J. Mat. Chem.* **2012,** *22*, 14756-14762.

88. B. Zheng, J. W., F. B. Wang, and X. H. Xia, Synthesis of nitrogen doped graphene with high electrocatalytic activity toward oxygen reduction reaction. *Electrochem. Commun.* **2013,** *28*, 24-26.

89. Giovanni, M.; Poh, H. L.; Ambrosi, A.; Zhao, G.; Sofer, Z.; Sanek, F.; Khezri, B.; Webster, R. D.; Pumera, M., Noble metal (Pd, Ru, Rh, Pt, Au, Ag) doped graphene hybrids for electrocatalysis. *Nanoscale* **2012,** *4* (16), 5002-5008.

90. Toh, R. J.; Poh, H. L.; Sofer, Z.; Pumera, M., Transition Metal (Mn, Fe, Co, Ni)-Doped Graphene Hybrids for Electrocatalysis. *Chemistry – An Asian Journal* **2013,** *8* (6), 1295-1300.

91. Fu, X.; Liu, Y.; Cao, X.; Jin, J.; Liu, Q.; Zhang, J., FeCo–Nx embedded graphene as high performance catalysts for oxygen reduction reaction. *Applied Catalysis B: Environmental* **2013,** *130–131*, 143-151.

92. Gutes, A.; Hsia, B.; Sussman, A.; Mickelson, W.; Zettl, A.; Carraro, C.; Maboudian, R., Graphene decoration with metal nanoparticles: Towards easy integration for sensing applications. *Nanoscale* **2012,** *4* (2), 438-440.

93. Vadahanambi, S.; Jung, J. H.; Oh, I. K., Microwave syntheses of graphene and graphene decorated with metal nanoparticles. *Carbon* **2011,** *49* (13), 4449-4457.

94. Li, Y.; Fan, X. B.; Qi, J. J.; Ji, J. Y.; Wang, S. L.; Zhang, G. L.; Zhang, F. B., Palladium nanoparticle-graphene hybrids as active catalysts for the Suzuki reaction. *Nano Res.* **2010,** *3* (6), 429-437.

95. Wei, G.; Miao, Y. E.; Zhang, C.; Yang, Z.; Liu, Z. Y.; Tjiu, W. W.; Liu, T. X., Ni-Doped Graphene/Carbon Cryogels and Their Applications As Versatile Sorbents for Water Purification. *Acs Applied Materials & Interfaces* **2013,** *5* (15), 7584-7591.

96. Dubey, S. P.; Nguyen, T. T. M.; Kwon, Y. N.; Lee, C., Synthesis and characterization of metal-doped reduced graphene oxide composites, and their application in removal of Escherichia coli, arsenic and 4-nitrophenol. *Journal of Industrial and Engineering Chemistry* **2015,** *29*, 282-288.

97. Liu, X. W.; Mao, J. J.; Liu, P. D.; Wei, X. W., Fabrication of metal-graphene hybrid materials by electroless deposition. *Carbon* **2011,** *49* (2), 477-483.

98. Wen, Q.; Wang, S. Y.; Yan, J.; Cong, L. J.; Pan, Z. C.; Ren, Y. M.; Fan, Z. J., MnO2-graphene hybrid as an alternative cathodic catalyst to platinum in microbial fuel cells. *J. Power Sources* **2012,** *216*, 187-191.

99. Verma, A. R.; Srivastava, O. N., *Crystallography Applied to Solid State Physics*. Wiley Eastern Limited: **1991**.

100. Reed, S. J. B., *Electron Microprobe Analysis and Scanning Electron Microscopy in Geology*. Cambridge University Press: **2005**.

101. Abbaschian, R.; Reed-Hill, R. E., *Physical Metallurgy Principles - SI Version*. Cengage Learning: **2009**.

102. Echlin, P., *Handbook of Sample Preparation for Scanning Electron Microscopy and X-Ray Microanalysis*. Springer US: **2011**.

103. Lloyd, G. E., ATOMIC-NUMBER AND CRYSTALLOGRAPHIC CONTRAST IMAGES WITH THE SEM - A REVIEW OF BACKSCATTERED ELECTRON TECHNIQUES. *Mineralogical Magazine* **1987,** *51* (359), 3-19.

104. Ayache, J.; Beaunier, L.; Boumendil, J.; Ehret, G.; Laub, D., *Sample Preparation Handbook for Transmission Electron Microscopy: Methodology*. Springer New York: **2010**.

105. Sanchez, E.; Deluigi, M. T.; Castellano, G., Mean Atomic Number Quantitative Assessment in Backscattered Electron imaging. *Microsc. microanal.* **2012,** *18* (6), 1355-1361.

106. Lyman, C. E.; Newbury, D. E.; Goldstein, J.; Williams, D. B.; Romig, A. D.; Armstrong, J.; Echlin, P.; Fiori, C.; Joy, D. C.; Lifshin, E., *Scanning Electron Microscopy, X-Ray Microanalysis, and Analytical Electron Microscopy: A Laboratory Workbook*. Springer US: **2012**.

107. Joy, D. C., THE THEORY AND PRACTICE OF HIGH-RESOLUTION SCANNING ELECTRON-MICROSCOPY. *Ultramicroscopy* **1991,** *37* (1-4), 216-233.

108. Indrawirawan, S.; Sun, H. Q.; Duan, X. G.; Wang, S. B., Low temperature combustion synthesis of nitrogen-doped graphene for metal-free catalytic oxidation. *J. Mater. Chem. A* **2015,** *3* (7), 3432-3440.

109. Griffiths, P. R.; De Haseth, J. A.; Winefordner, J. D., *Fourier Transform Infrared Spectrometry*. Wiley: **2007**.

110. Kaufmann, E. N., *Characterization of materials*. Wiley-Interscience: **2003**.

111. Chalmers, J. M.; Edwards, H. G. M.; Hargreaves, M. D., *Infrared and Raman Spectroscopy in Forensic Science*. Wiley: **2012**.

112. Derrick, M. R.; Stulik, D.; Landry, J. M., *Infrared Spectroscopy in Conservation Science*. Getty Conservation Institute: **2000**.

113. Larkin, P., *Infrared and Raman Spectroscopy: Principles and Spectral Interpretation*. Elsevier Science: **2011**.

114. Meyers, R. A., *Encyclopedia of Analytical Chemistry*. Wiley: **2012**.

115. Colthup, N. B.; Daly, L. H.; Wiberley, S. E., *Introduction to Infrared and Raman Spectroscopy*. Academic Press: **1964**.

116. Zoubir, A., *Raman Imaging: Techniques and Applications*. Springer Berlin Heidelberg: **2012**.

117. Krafft, C.; Dietzek, B.; Schmitt, M.; Popp, J., Raman and coherent anti-Stokes Raman scattering microspectroscopy for biomedical applications. *J. Biomed. Opt.* **2012,** *17* (4), 15.

118. Harris, D. C.; Bertolucci, M. D., *Symmetry and Spectroscopy: An Introduction to Vibrational and Electronic Spectroscopy*. Dover Publications: **1978**.

119. Zhang, S. L., *Raman Spectroscopy and its Application in Nanostructures*. Wiley: **2012**.

120. Smith, E.; Dent, G., *Modern Raman Spectroscopy: A Practical Approach*. Wiley: **2013**.

121. Keresztury, G., Raman Spectroscopy: Theory. In *Handbook of Vibrational Spectroscopy*, John Wiley & Sons, Ltd: **2006**.

122. Dresselhaus, M. S.; Jorio, A.; Hofmann, M.; Dresselhaus, G.; Saito, R., Perspectives on Carbon Nanotubes and Graphene Raman Spectroscopy. *Nano Letters* **2010,** *10* (3), 751-758.

123. Bumbrah, G. S.; Sharma, R. M., Raman spectroscopy – Basic principle, instrumentation and selected applications for the characterization of drugs of abuse. *Egyptian Journal of Forensic Sciences*.

124. Pyramides, G.; Robinson, J. W.; William Zito, S., The combined use of DSC and TGA for the thermal analysis of atenolol tablets. *Journal of Pharmaceutical and Biomedical Analysis* **1995,** *13* (2), 103-110.

125. Wunderlich, B., *Thermal Analysis of Polymeric Materials*. Springer: **2005**.

126. Menczel, J. D.; Prime, R. B., *Thermal Analysis of Polymers: Fundamentals and Applications*. Wiley: **2009**.

127. Ramachandran, V. S.; Paroli, R. M.; Beaudoin, J. J.; Delgado, A. H., *Handbook of Thermal Analysis of Construction Materials*. Elsevier Science: **2002**.

128. Ehrenstein, G. W.; Riedel, G.; Trawiel, P., *Thermal Analysis of Plastics: Theory and Practice*. Carl Hanser Verlag GmbH & Company KG: **2012**.

129. Baalousha, M.; Lead, J., *Characterization of Nanomaterials in Complex Environmental and Biological Media*. Elsevier Science: **2015**.

130. Dollimore, D.; Spooner, P.; Turner, A., The bet method of analysis of gas adsorption data and its relevance to the calculation of surface areas. *Surface Technology* **1976,** *4* (2), 121-160.

131. Karamalidis, A. K.; Dzombak, D. A., *Surface Complexation Modeling: Gibbsite*. Wiley: **2011**.

132. Lowell, S.; Shields, J. E., *Powder Surface Area and Porosity*. Springer Netherlands: **1991**.

133. Scrivener, K.; Snellings, R.; Lothenbach, B., *A Practical Guide to Microstructural Analysis of Cementitious Materials*. Taylor & Francis: **2016**.

134. Indrawirawan, S.; Sun, H. Q.; Duan, X. G.; Wang, S. B., Nanocarbons in different structural dimensions (0-3D) for phenol adsorption and metal-free catalytic oxidation. *Appl. Catal. B-Environ.* **2015,** *179*, 352-362.

135. Kerber, S. J.; Barr, T. L.; Mann, G. P.; Brantley, W. A.; Papazoglou, E.; Mitchell, J. C., The complementary nature of x-ray photoelectron spectroscopy and angle-resolved x-ray diffraction - Part I: Background and theory. *Journal of Materials Engineering and Performance* **1998,** *7* (3), 329-333.

136. Meyers, R. A., *Encyclopedia of physical science and technology*. Academic Press: **2002**.

137. Brundle, C. R.; Baker, A. D., *Electron Spectroscopy: Theory, Techniques and Applications*. Academic Press: **1977**.

138. van der Heide, P., *X-ray Photoelectron Spectroscopy: An introduction to Principles and Practices*. Wiley: **2011**.

139. Winograd, N.; Gaarenstroom, S. W., X-Ray Photoelectron Spectroscopy A2 - KUWANA, THEODORE. In *Physical Methods in Modern Chemical Analysis*, Academic Press: **1980**, pp 115-169.

140. Miller, D. R.; Peppas, N. A., THE USE OF X-RAY PHOTOELECTRON SPECTROSCOPY FOR THE ANALYSIS OF THE SURFACE OF BIOMATERIALS. *Journal of Macromolecular Science, Part C* **1986,** *26* (1), 33-66.

141. Jaensson, B., A PRINCIPAL DISTINCTION BETWEEN DIFFERENT KINDS OF X-RAY-EQUIPMENT FOR RESIDUAL-STRESS MEASUREMENT. *Materials Science and Engineering* **1980,** *43* (2), 169-176.

142. Van Holde, K. E.; Johnson, W. C.; Ho, P. S., *Principles of Physical Biochemistry*. Prentice Hall: **1998**.

143. Fultz, B.; Howe, J. M., *Transmission Electron Microscopy and Diffractometry of Materials*. Springer Berlin Heidelberg: **2012**.

144. Cullity, B. D.; Stock, S. R., *Elements of X-ray Diffraction*. Prentice Hall: **2001**.

145. Birkholz, M., *Thin Film Analysis by X-Ray Scattering*. Wiley: **2006**.

146. Klug, H. P.; Alexander, L. E., *X-Ray Diffraction Procedures: For Polycrystalline and Amorphous Materials*. Wiley: **1974**.

147. Barrante, J. R., *Applied Mathematics for Physical Chemistry: Third Edition*. **2016**.

148. Alexander, L.; Klug, H. P., Determination of Crystallite Size with the X-Ray Spectrometer. *Journal of Applied Physics* **1950,** *21* (2), 137-142.

149. Monshi, A.; Foroughi, M. R.; Monshi, M. R., Modified Scherrer equation to estimate more accurately nano-crystallite size using XRD. *World Journal of Nano Science and Engineering* **2012,** *2* (03), 154.

150. Qazi, S. J. S.; Rennie, A. R.; Cockcroft, J. K.; Vickers, M., Use of wide-angle X-ray diffraction to measure shape and size of dispersed colloidal particles. *Journal of Colloid and Interface Science* **2009,** *338* (1), 105-110.

151. Chauhan, A.; Chauhan, P., Powder XRD technique and its applications in science and technology. *Journal of Analytical & Bioanalytical Techniques* **2014,** *2014*.

152. Jackson, S. D.; Hargreaves, J. S. J., *Metal Oxide Catalysis*. Wiley: **2009**.

153. Weil, J. A.; Bolton, J. R.; Wertz, J. E., *Electron Paramagnetic Resonance: Elementary Theory and Practical Applications*. Wiley: **1994**.

154. Lancaster, G., Electron paramagnetic resonance (a review). *Journal of Materials Science* **1967,** *2* (5), 489-495.

155. Elias, R. J.; Andersen, M. L.; Skibsted, L. H.; Waterhouse, A. L., Identification of Free Radical Intermediates in Oxidized Wine Using Electron Paramagnetic Resonance Spin Trapping. *Journal of Agricultural and Food Chemistry* **2009,** *57* (10), 4359-4365.

156. Harriman, J. E., *Theoretical foundations of electron spin resonance*. Academic Press: **1978**.

157. Kirino, Y.; Ohkuma, T.; Kwan, T., Spin Trapping with 5, 5-Dimethylpyrroline-N-oxide in Aqueous Solution. *CHEMICAL & PHARMACEUTICAL BULLETIN* **1981,** *29* (1), 29-34.

158. Zamora, P. L.; Villamena, F. A., Theoretical and Experimental Studies of the Spin Trapping of Inorganic Radicals by 5,5-Dimethyl-1-pyrroline N-Oxide (DMPO). 3. Sulfur Dioxide, Sulfite, and Sulfate Radical Anions. *The Journal of Physical Chemistry A* **2012,** *116* (26), 7210-7218.

159. Sun, H.; Wang, S., Chapter 6 Catalytic oxidation of organic pollutants in aqueous solution using sulfate radicals. In *Catalysis: Volume 27*, The Royal Society of Chemistry: **2015**, pp 209-247.

160. Sun, H.; Kwan, C.; Suvorova, A.; Ang, H. M.; Tadé, M. O.; Wang, S., Catalytic oxidation of organic pollutants on pristine and surface nitrogen-modified carbon nanotubes with sulfate radicals. *Applied Catalysis B: Environmental* **2014,** *154–155*, 134-141.

161. Saputra, E.; Muhammad, S.; Sun, H.; Patel, A.; Shukla, P.; Zhu, Z. H.; Wang, S., α-MnO2 activation of peroxymonosulfate for catalytic phenol degradation in aqueous solutions. *Catalysis Communications* **2012,** *26*, 144-148.

162. Floyd, R. A.; Soong, L. M., Spin trapping in biological systems. Oxidation of the spin trap 5,5-dimethyl-1-pyrroline-1-oxide by a hydroperoxide-hematin system. *Biochemical and Biophysical Research Communications* **1977,** *74* (1), 79-84.

163. Davies, M. J.; Gilbert, B. C.; Stell, J. K.; Whitwood, A. C., NUCLEOPHILIC-SUBSTITUTION REACTIONS OF SPIN ADDUCTS - IMPLICATIONS FOR THE CORRECT IDENTIFICATION OF REACTION INTERMEDIATES BY EPR SPIN TRAPPING. *Journal of the Chemical Society-Perkin Transactions 2* **1992,** (3), 333-335.

164. Zalibera, M.; Rapta, P.; Stasko, A.; Brindzova, L.; Brezova, V., Thermal generation of stable image omitted spin trap adducts with super-hyperfine structure in their EPR spectra: An alternative EPR spin trapping assay for radical scavenging capacity determination in dimethylsulphoxide. *Free Radical Research* **2009,** *43* (5), 457-U19.

CHAPTER 3

Low temperature combustion synthesis of nitrogen-doped graphene for metal-free catalytic oxidation

Abstract

Nitrogen-doped reduced graphene oxide (N-rGO) was prepared by a simple process of simultaneous reduction and nitrogen doping on graphene oxide (GO) at low temperatures using ammonium nitrate as a N precursor. Characterization techniques indicated that N-rGO materials with high N loading (5-8 at.%) can be easily produced and that the crystal-/micro- structures and chemical compositions of N-rGO materials are dependent on the calcination conditions. The metal-free catalysis of N-rGO was investigated in catalytic activation of peroxymonosulfate (PMS) for phenol oxidative degradation in water. It was found that N-rGO samples are promising green catalysts for phenol degradation. Kinetic studies showed that phenol degradation follows first order reaction kinetics on N-rGO-350 with activation energy of 31.6 kJ/mol. The mechanism of PMS activation and phenol oxidation was elucidated by employing both electron paramagnetic resonance (EPR) studies and quenching tests with ethanol and tert-butanol.

3.1. Introduction

One of the most critical issues in industrialization is the discharge of polluted water that largely contains particles, organics, and heavy metal ions.[1] Many water treatment technologies have been established, such as adsorption, filtration, evaporation, and membrane separation, to remediate the organic contaminations. [2] Advanced oxidation processes (AOPs) using metal-based materials as catalysts have attracted more attention over those physical processes due to the complete decomposition of organic pollutants. [3-4]

As an excellent alternative to hydroxyl radicals ($^{\bullet}OH$), sulfate radicals ($SO_4^{\bullet-}$) have been widely applied to decompose organic pollutants. [5-8] However, metal-based catalysts, such as cobalt and manganese oxides, are expensive and sometimes toxic metal leaching in either homogeneous or heterogeneous catalysis can lead to secondary contamination.[4, 6-7] Therefore, metal-free catalysts are highly recommended for environmental remediation. [9]

Graphene is a single sheet of graphite and has impressive theoretical surface area of 2630 m^2/g, chemical stability, and high electrical conductivity.[10-11] Therefore, it can be a promising candidate of metal-free catalysts. In a previous study, reduced graphene oxide (rGO) was firstly discovered to be effective for activation of peroxymonosulfate (PMS) to produce sulfate radicals. The catalytic activity of rGO can be improved by increased porosity and specific surface area (SSA) and manipulated surface functional groups. [10, 12-13] Structural modification was conducted by CO_2 activation to obtain highly porous rGO (A-rGO-25, A-rGO-60 and A-rGO-75). It was found that 100% MB removal would be achieved in 4 h for rGO, and that the same efficiency would be obtained in 1.5 h on A-rGO-25 after CO_2 activation, 1.0 h on A-rGO-60 and 2 h on A-rGO-75. [10] Physical and chemical activation of rGO using different reagents, CO_2, $ZnCl_2$ and $CO_2/ZnCl_2$, were further carried out to obtain highly porous metal-free carbonaceous materials for adsorption and catalytic oxidation. The study showed that specific surface area and oxygen containing groups are two important factors determining the adsorptive and catalytic performances. [12]

It was also reported that the performances of graphene can be improved by doping with other elements such as nitrogen, boron, halogen, sulphur or metals.[13-18] Qu et

al.[19] reported that nitrogen-doped graphene can show much better electrocatalytic activity for oxygen reduction in fuel cells than platinum. The superior catalytic activity of nitrogen-doped graphene was also demonstrated in aerobic selective oxidation of benzylic alcohols, and the graphitic nitrogen was suggested to be the active sites.[20] Gao et al.[21] examined the catalytic performances of nitrogen doped graphene and concluded that graphitic nitrogen is effective for activation of C-H bonds in selective oxidation by changing the electronic structure of sp^2 carbon atoms. A recent study has discovered that nitrogen doped reduced graphene oxide (N-rGO) showed an enhanced activity for aqueous organic oxidation by activation of peroxymonosulfate (PMS or oxone) in phenol solution. [17] The performance of this N-rGO as a green catalyst has been studied under the thermal annealing temperature at 350 °C. Such a condition was also found to be effective for nitrogen modification of carbon nanotubes, which were able to activate both PMS and PDS (persulfate). [22] In this chapter, we report further investigation on the effect of the thermal annealing temperature on the physicochemical properties of N-rGO and their performances in aqueous oxidation of phenol solutions.

3.2. Experimental section

3.2.1. Materials and catalyst preparation

All chemicals were obtained from Chem-Supply. Synthesis of graphene oxide (GO) was carried out using a modified Hummers' method. [23] In a typical synthesis, graphite powder was mixed with a strong oxidizer of concentrated H_2SO_4 and then $KMnO_4$ was slowly added. The mixture was stirred at 35 °C for 5 h. Deionized (DI) water was then slowly added into the mixed solution and the temperature was kept carefully below 98 °C. The suspension was then treated by H_2O_2 to reduce the residual permanganate. The obtained GO slurry was separated by centrifugation and washed using HCl and DI water three times. The final product was ground after drying in an oven at 60 °C for at least 48 h.

The reduction process and nitrogen doping were conducted simultaneously using ammonium nitrate as the N precursor. [17] GO and ammonium nitrate at 1.0 g each were mixed in 50 mL ethanol at room temperature for 30 min, then the temperature was increased to 50 °C and stirred for a few hours until the ethanol was completely

evaporated. The dried mixture was thermally annealed at different temperatures in the range of 300 to 400 °C for 1 h. The N-rGO was obtained after being washed using ethanol and DI water three times, and drying in the oven at 60 °C. The obtained samples were denoted as N-rGO-n and n is referring to the annealing temperature. In addition, further thermal annealing of N-rGO-350 was carried out by employing nitrogen gas atmosphere at 400 °C for 1 h to obtain another sample, N-rGO-350-400.

3.2.2. Characterization of the catalysts

X-ray diffraction (XRD) patterns were acquired on a Bruker D8-Advanced X-ray instrument using Cu-Kα radiation with λ at 1.5418 Å. Nitrogen sorption isotherms were obtained using a Tristar II 3020 after degassing the samples at 110 °C for 4 h. The Brunauer-Emmett-Teller (BET) equation and Barrett-Joyner-Halenda (BJH) method were utilized to evaluate the specific surface area, and pore size distribution of the samples, respectively. Fourier transform infrared spectra (FTIR) were obtained from a Bruker instrument with ATR correction mode. X-ray photoelectron spectroscopy (XPS) was carried out to determine the chemical states of elements using a Thermo Escalab 250 with Al-Kα X-ray. Thermogravimetric-differential thermal analysis (TG-DTA) was carried out by heating the samples in an air flow at a rate of 100 mL/min using a Perkin Elmer Diamond TGA/DTA thermal analyzer with a heating rate of 10 °C/min. Scanning electron microscopy (SEM) was applied to investigate the morphology of the catalysts on Zeiss Neon 40 EsB FIBSEM. Raman analysis was performed on an ISA dispersive Raman spectrometer using argon ion lasers (514 nm). Electron paramagnetic resonance (EPR) spectra were obtained on a Bruker EMS-plus to detect the free radicals generated during activation of PMS.

3.2.3. Catalytic activity tests

The catalytic oxidation of phenol was carried out in a 500 mL conical flask with phenol solution (20 ppm), catalyst (0.2 g/L) and PMS (2.0 g/L) in a constant-temperature controlled water bath for the kinetic studies. At each time interval, 1 mL solution was withdrawn by a syringe, filtered by a 0.45 μm Millipore film, and injected into a vial. Then 0.5 mL of methanol as a quenching reagent was also injected into the reaction solution. The mixed solution was analyzed by a high

performance liquid chromatography (HPLC, Varian) with a C-18 column and a UV detector set at 270 nm.

3.3. Results and Discussion

3.3.1. Characterization of materials

After oxidization of graphite by the modified Hummers' method, [23] the peak in XRD pattern at 2θ = 9.9° (002 plane) clearly indicated the formation of graphene oxide (GO) from the oxidation of graphite (**Figure 3.1a**), which has a typical peak at around 2θ = 26°.

Figure 3.2 shows XRD patterns of N-rGO samples. The peak at 2θ = 9.9° (002 plane) disappeared and a new peak at 2θ = 25.5° (corresponding to the interplanar spacing of 0.35 nm) was observed on all N-doped samples. The changes in XRD patterns suggested the successful reduction of GO to rGO along with nitrogen doping process. [24]

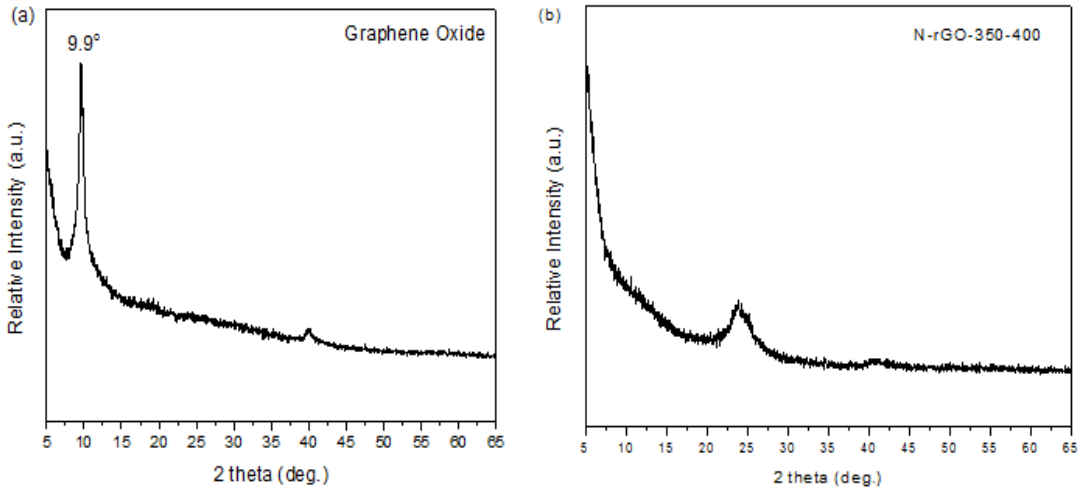

Figure 3.1. XRD patterns of (a) graphene oxide and (b) N-rGO-350-400.

In general, graphene has three types of ordered crystal structures dependent on the stacking sequences of graphene sheets. These three different stacking sequences are simple hexagonal (AAA), hexagonal (Bernal stacking, ABAB) and rhombohedral (ABC).[25] For graphene with hexagonal AB and ABC stacking, the interlayer spacing is 0.335 and 0.337 nm, respectively.[26] In this study, the interlayer spacing of N-rGO was about 0.35 nm. The interplanar spacing of N-rGO was slightly larger than that of graphite (0.34 nm) for (002) plane due to the presence of oxygen functional groups and water molecules. [27] The peak (2θ = 25.5°) broadening might

be attributed to the large strain in the lattice induced by the presence of hydroxyl and epoxide groups on both sides of rGO layers.[28] The large strain is related to the distortion of lattice periodicity of the carbon-carbon distance. Further annealing N-rGO-350 in N_2 at 400 ^{o}C would decrease the intensity of the characteristic peak at around 2θ =25.5°, as shown in **Figure 3.1b**.

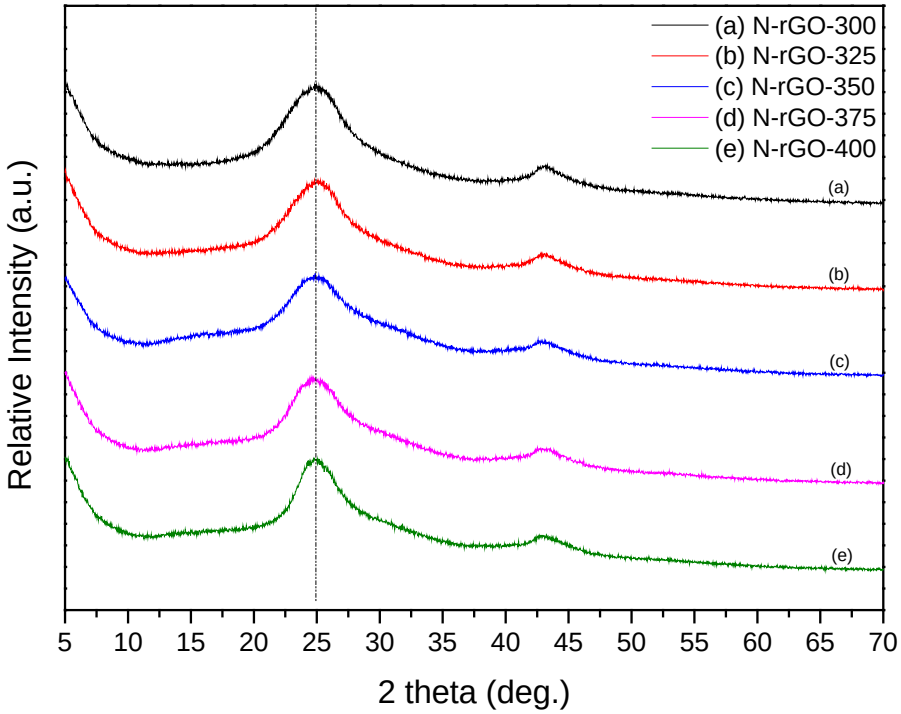

Figure 3.2. XRD patterns of N-rGO via different thermal annealing temperatures.

The detailed information of crystal structures of N-rGO samples are shown in **Table 3.1**. Peak broadening at different thermal annealing temperatures can be compared by the half peak width (HPW, B). Thermal treatment and associated reduction process would reduce the half peak width compared to that of GO. Moreover, HPW decreased with the increased temperature. Also, HPW of N-rGO-350-400 (3.4 ^{o}) was much narrower than that N-rGO-35 (5.6 ^{o}). The changes of HPW values indicated the degree of reduction, removal of oxygen functional groups, and distortion of the lattice periodicity. The origin of the B changes may be due to the increase of the interlayer thickness, L,[29] as shown in **Table 3.1**.

Table 3.1. Crystal- and micro-structures of N-rGO samples.

Sample	Half peak width (B, ^{o})	Interlayer material thickness (L, nm)	D band (cm^{-1})	G band (cm^{-1})	I_D/I_G ratio	SSA (m^2/g)
N-rGO-300	5.8	3.12	1323	1589	1.32	53
N-rGO-325	5.6	3.23	1323	1580	1.40	58
N-rGO-350	5.6	3.23	1323	1577	1.26	99
N-rGO-350-400	3.4	5.33	1335	1583	1.21	91
N-rGO-375	5.1	3.55	1329	1586	1.38	127
N-rGO-400	4.4	4.11	1329	1580	1.41	159

Figure 3.3 shows Raman spectra of GO and N-rGO prepared at different thermal annealing temperatures. The G bands (originated from in-plane vibrations of sp^2 carbon in rGO domains) appear at about 1580 cm^{-1} and strong D bands (related to the edges, defects, and structurally disordered carbon) occur at about 1320 cm^{-1}. These results are consistent with previous Raman investigations on GO. [30-32] The I_D/I_G ratio (intensity ratio of D band to G band) of the GO was 1.18, and those ratios of N-rGO via different thermal annealing temperatures are tabulated in **Table 3.1**. The I_D/I_G ratio shows the degree of defects in rGO materials. [24]

As seen in **Table 3.1**, the I_D/I_G ratios of N-rGO via different calcination conditions significantly increased after the thermal annealing, compared with that of GO. The increased I_D/I_G ratio by thermal annealing indicates the enhanced defective edges, and declined sp^2 carbon of rGO structure. [32] However, among the N-rGO samples, no temperature dependent I_D/I_G ratio was observed, indicating the complicated processes of simultaneous reduction and nitrogen doping, as nitrogen doping might be able to adjust the defective structure as well.

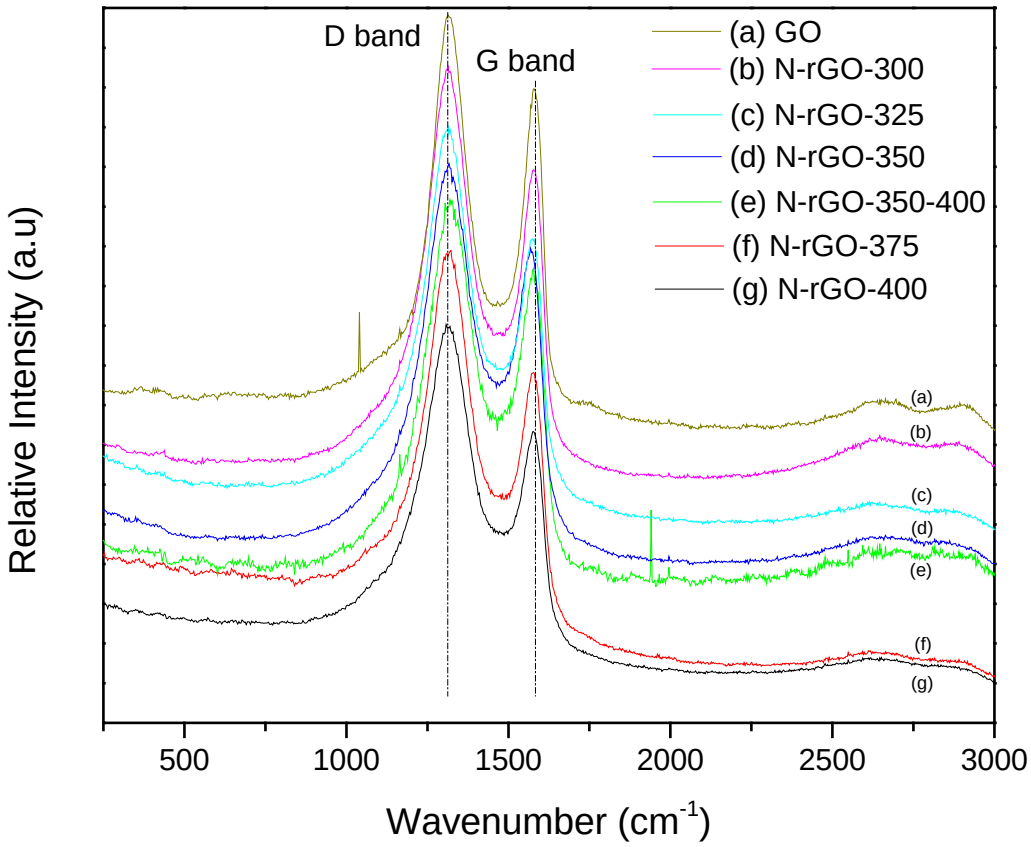

Figure 3.3. Raman spectra of GO and N-rGO samples.

The morphologies of GO, N-rGO-300 and N-rGO-400 were observed by SEM imaging. As shown in **Figure 3.4a** GO had a wrinkled and sponge-like structure due to the exfoliation and restacking process. For N-rGO-300 and -400 (**Figure 3.4b and Figure 3.4c**), SEM micrographs show irregularly enfolding and layered structures tangled with each other due to the exfoliation. These results confirm that thermal annealing was able to exfoliate the stacked layers of GO, and improve the microstructure, resulting in a higher specific surface area (SSA) as shown in **Table 3.1**.

In atomic scope of the structures of GO and rGO, both sides of the basal plane have randomly intermixed oxygen groups, such as hydroxyl and epoxide groups[33-34]. Meanwhile, carbonyl and carboxylic groups are attached at the sheet edges. It was reported that decompositions of the hydroxyl and epoxy sites would occur in thermal treatment and result in a build-up of pressure between adjacent graphene oxide sheets.[35] Therefore, thermal exfoliation may occur when the pressure exceeds the van der Waals interlayer attraction.

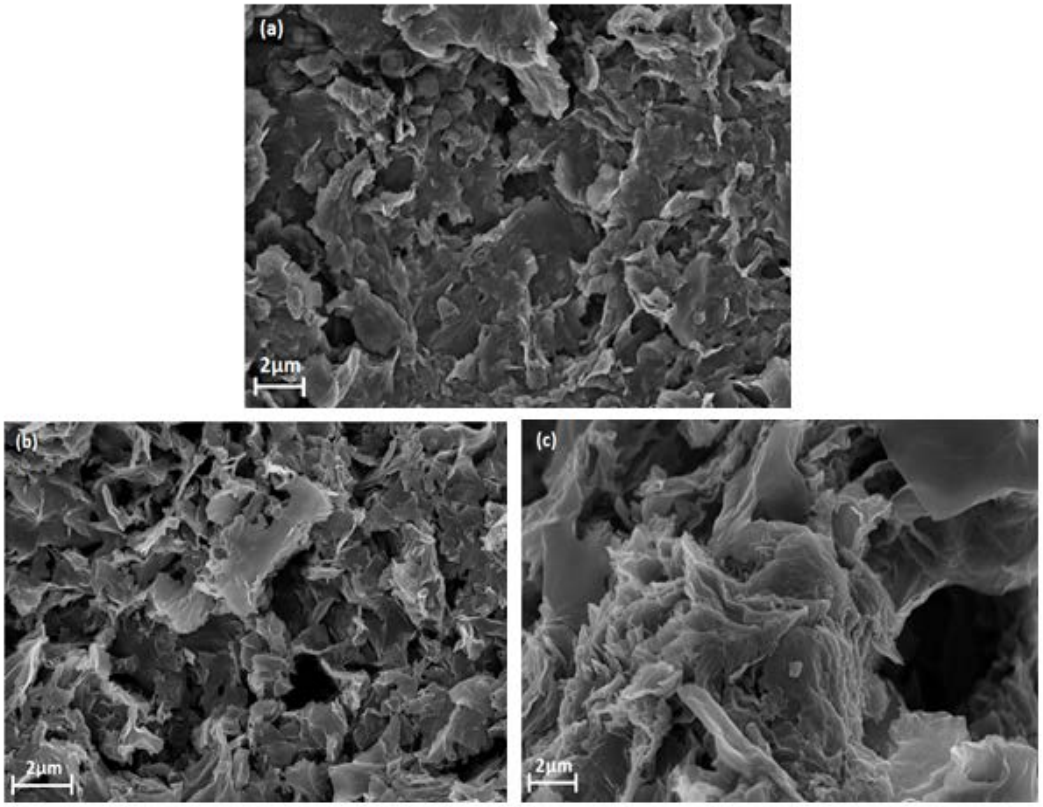

Figure 3.4. SEM images of (a) GO, (b) N-rGO-300 and (c) N-rGO-400

The textural information of N-rGO samples were investigated by N_2 sorption isotherms, as shown in **Figure 3.5**. The SSA values of N-rGO samples prepared at different temperatures are tabulated in **Table 3.1**. In general, nitrogen doping and thermal treatment at 300 -400 °C imposed a significant effect on SSA values. Surface area increased with increasing calcination temperature. At 350 ^{o}C, a rather significant exfoliation occurred as indicated by the increased SSA value from about 58 to 99 m^2/g. At the thermal annealing temperatures of 375 and 400 °C, the SSA values are 127 and 159 m^2/g, respectively. While further annealing the sample of N-rGO-350 at 400 °C in nitrogen would slightly decrease the SSA of N-rGO-350-400.

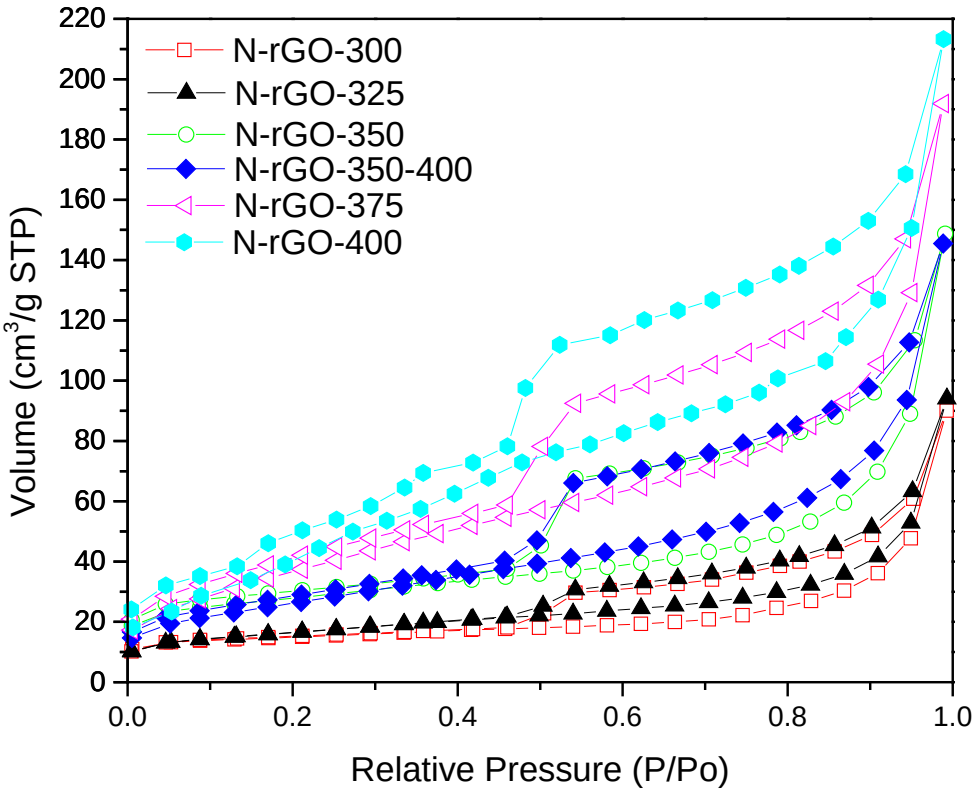

Figure 3.5. N_2 sorption isotherms of N-rGO samples.

The thermal behaviors of GO and N-rGO-400 were investigated by TGA-DTA. The curves of GO and N-rGO-400 are presented in **Figure 3.6a** and **b**, respectively. The analysis was performed in air at a heating rate of 10 °C/min.

Figure 3.6a shows that the weight loss of GO occurs from starting temperature to 100 °C primarily due to the evaporation of thermally unstable water molecules. [36-37] Further weight loss was observed from 100 up to 450 °C due to the removal of the oxygen functional groups. [35, 38-39] It was also found that from 100 to 450 °C, the DTA curve shows a characteristic step or peak at 180 °C. From 450 to 540 °C, the DTA curve also shows a characteristic step or peak at 520 °C corresponding to the thermal decomposition of carbon structure. These two peaks are corresponding to the strong exothermal peaks and in good agreement with previous studies. [37] There was no further weight loss of GO after reaching the temperature of 540 °C.

Figure 3.6b indicates that there are three regions on N-rGO-400 weight loss process. First, a minor weigh loss occurs from room temperature to about 110 °C which may be due to the evaporation of adsorbed water molecules. Second, another minor weight loss occurs from 110 to 450 °C attributed to the removal of residue oxygenated functional groups generating CO_2 and H_2O. [35, 38-39] Finally, a major weight loss can be observed between 450 and 550 °C. The TGA and DTA curves show a characteristic step or strong exothermal peak at 530 °C due to the carbon combustion and decomposition. [11, 39] No further weight loss of N-rGO-400 can be observed after 550 °C. In this study, the weight losses of N-rGO-400 and GO before 450 °C are about 5% and 54%, respectively. These results suggested that a substantial amount of water and oxygen functional groups were removed by simultaneous process of reduction and nitrogen doping using ammonium nitrate as N precursor.

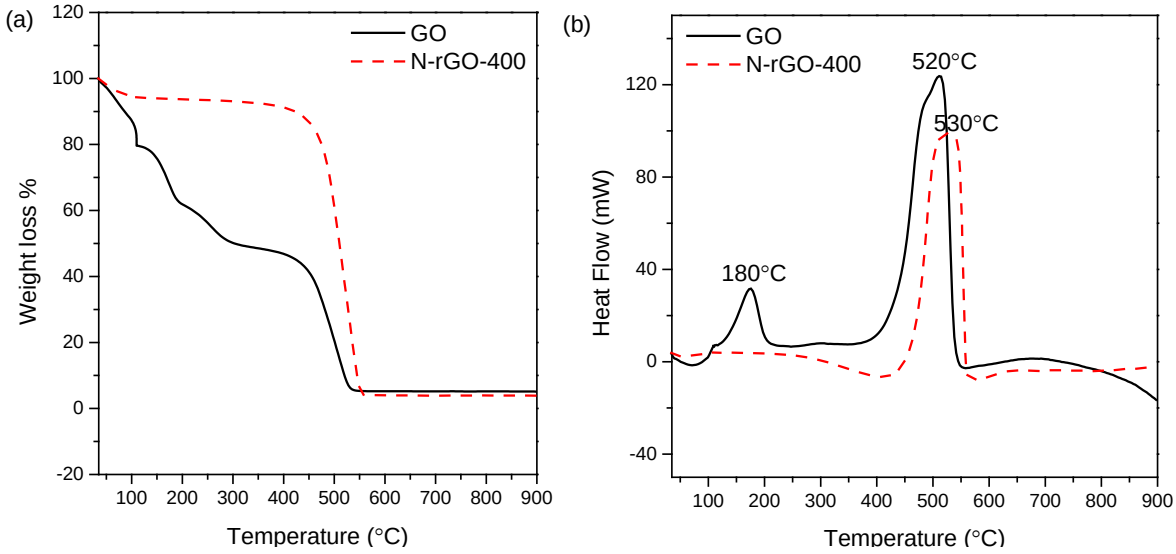

Figure 3.6. (a) TGA and (b) DTA curves of GO and N-rGO-400 in air atmosphere.

Figure 3.7 displays FTIR spectra of N-rGO samples. The spectrum of GO displays several characteristic peaks, such as O-H group (hydroxyl) at 3323 cm^{-1} , C=O group (carbonyl) at 1715 cm^{-1}, C=C group (aromatic) at 1586 cm^{-1} and C-O group (epoxy or alkoxy) at 1035 cm^{-1}. These results are consistent with reported values. [12, 40-41] Compared to GO, the signals of oxygen functional groups of N-rGO are very weak indicating the presence of less oxygen groups attached to the surface. For N-rGO, the absorption bands at approximate 1560 and 1200 cm^{-1} are attributed to the C=C/C=N groups and C-N groups, respectively [42].

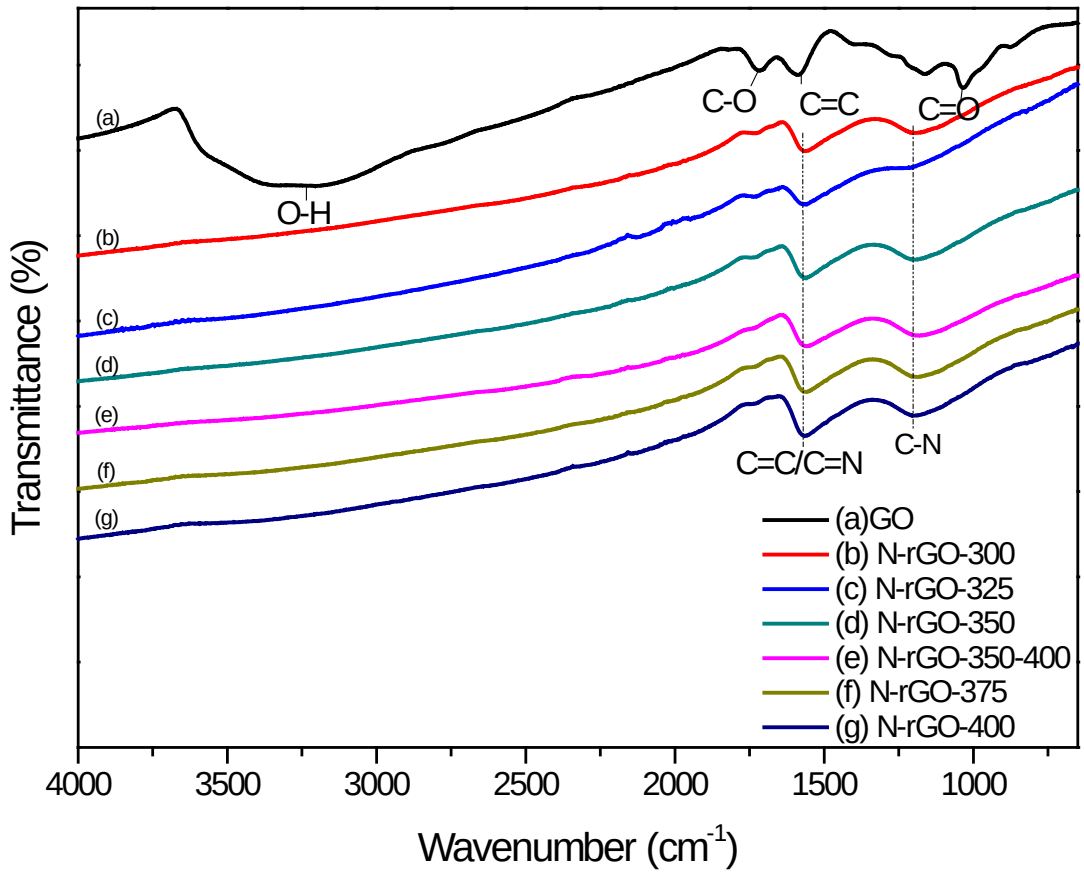

Figure 3.7. FTIR spectra of GO and N-rGO materials.

Figure 3.8 shows XPS studies of the different N-rGO samples. The XPS analysis was carried out to investigate atomic concentration (at.%) of nitrogen contents in N-rGO via different calcination temperatures. The O/C (oxygen versus carbon) and N/C (nitrogen versus carbon) ratios are tabulated in **Table 3.2**.

Table 3.2. Chemical compositions of various N-rGO materials.

Sample	N level, at. %	N/C ratio	Pyridinic N, at. %	Pyrrolic N, at. %	Graphitic N, at. %	O/C ratio
N-rGO-300	5.8	0.078	1.9	3.1	0.8	0.28
N-rGO-325	7.2	0.085	2.4	4.2	0.6	0.11
N-rGO-350	6.4	0.075	2.2	3.7	0.5	0.10
N-rGO-375	7.0	0.081	2.5	3.8	0.7	0.08
N-rGO-400	6.7	0.079	2.3	3.5	0.9	0.10

Figure 3.8a shows XPS surveys of the N-doped rGO samples prepared at different temperatures. The corresponding C 1s, O 1s and N 1s peaks are centred at 284.6, 531, and 399.5 eV, respectively.[43-45] Based on the compositional information of carbon,

oxygen and nitrogen, it can be found that treatment temperature has varying effect on the nitrogen and oxygen levels of the samples.

High resolution of XPS N 1s spectra of N-rGO can be found in **Figure 3.8b**. Three types of nitrogen species can be identified from the de-convolution of XPS N 1s spectra: pyridinic (N-6) at 398.3 eV, pyrrolic (N-5) at 399.8 eV, and graphitic N at 401.8 eV [45-49]. **Table 3.2** shows that the contents of pyridinic N, pyrrolic N, and graphitic N vary from 1.5%-2.5%, 3%-4.5%, and 0-1%, respectively. For all the N-rGO samples, the content of pyrrolic N was generally higher than the pyridinic N and graphitic N.

Figure 3.9 shows the de-convolution C1s XPS spectra of N-rGO samples. A broad C 1s peak indicated five different C species in the range of 281 - 291 eV. For N-rGO-400, the C-C bond, C-N bond, C=N bond, C=O bond, and O-C=O bond occur at 284.6, 285.8, 286.8, 288, and 290.5 eV, respectively. [24, 50-53]

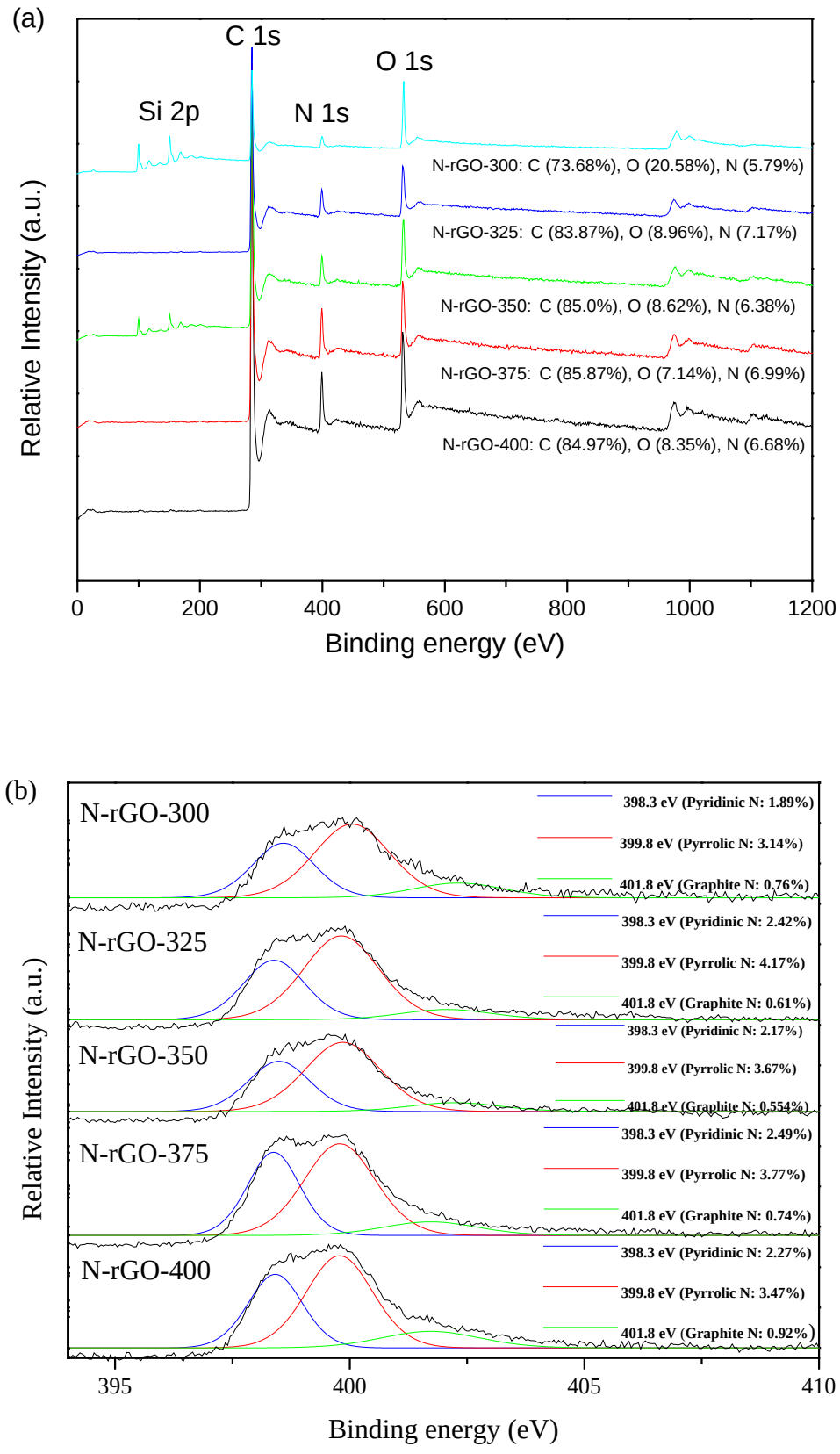

Figure 3.8. (a) XPS survey and (b) N 1s of N-rGO samples.

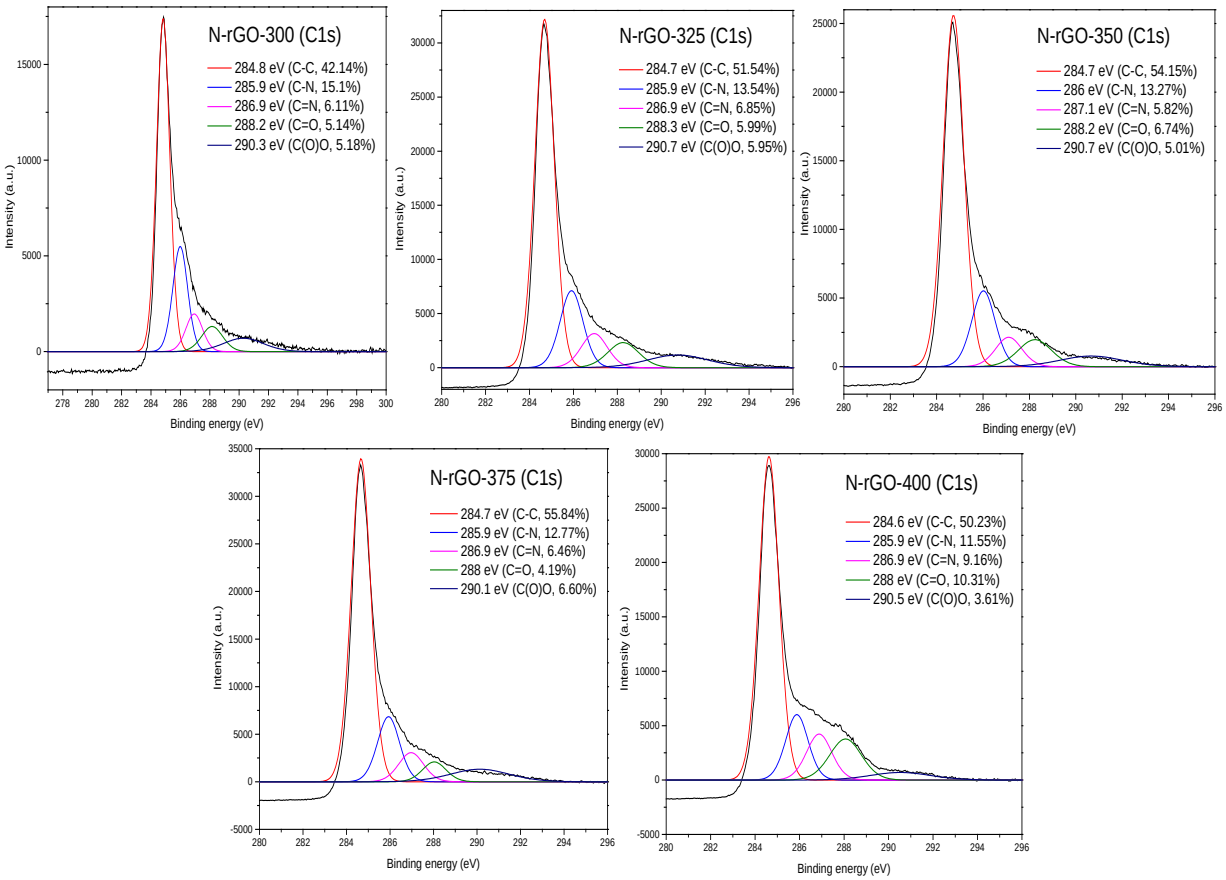

Figure 3.9. XPS C 1s spectra of N-rGO synthesized at different thermal annealing temperatures.

Previous studies showed that N-doping can occur at temperature as low as 80 °C and up to 1100 °C for reduced graphene oxide by thermal or hydrothermal treatment of GO with ammonia or urea or hydrazine and that ammonia can produce the highest nitrogen doping level at 500 °C.[43, 49, 54] The nitrogen doping level will decrease significantly when the temperature is above 500 °C. Thermal treatment at 900 °C and above would result in breaking up of C-N bonds and removing off of the nitrogen from N-rGO. In general, the nitrogen atoms will be assigned to pyridinic-N, pyrrolic-N and graphitic-N forms. At low calcination temperatures, the C-N bond formations occur predominantly on the defect sites (zigzag or armchair) in the plane, where the C atoms are more chemically reactive than those in the perfect lattice. The concentration of graphitic N was found to increase with increasing annealing temperature, whereas the concentration of pyridinic-N will decrease with increasing annealing temperature.[20, 43, 45] In a recent study, for the mixture of GO and

ammonium nitrate annealed at 350 °C, the N-rGO contains 5.61 at.% nitrogen with the compositional nitrogen ratio of graphitic: pyridinic: pyrrolic at 1: 1.46 : 2.45.[17] For GO, carbocyclic and lactone groups begin to decompose at about 250 °C, whereas carbonyl and -COOH groups are decomposed at about 450 °C. Therefore, it is suggested that these oxygen functional groups in the GO are mostly responsible for reaction with ammonia to form C-N bonds.[43] In this study, the mixture of ammonium nitrate and GO was thermally annealed between 300-400 °C to produce nitrogen doped rGO. The temperature was high enough for the decomposition of certain oxygen functional groups with ammonium nitrate to form the C-N bonds. As seen in **Table 3.2**, it appeared that no direct correlation between the nitrogen doping level and the temperature could be derived.

3.3.2. Catalytic oxidation performance of phenol

The effect of calcination temperature on the performance of catalytic phenol oxidation on rGO and various N-rGO is shown in **Figure 3.10**. For rGO without nitrogen doping, 50% phenol degradation was achieved in 2 h.[17] The performance of phenol degradation on N-rGO-300 showed a significant improvement compared to rGO and 95% phenol degradation was achieved within 2 h on the N-rGO-300.

Further improvement can be seen on N-rGO-325 and, 100% phenol degradation was observed in 1 h. Comparison of rGO with N-rGO-300 and N-rGO-325, it was suggested that SSA contributes less significantly than nitrogen doping to the enhanced performance of catalytic oxidation of phenol. The SSA values of N-rGO-300 (58 m^2/g) and N-rGO-325 (53 m^2/g) were lower than rGO (301 m^2/g). N-rGO-350, -375 and -400 had SSA values lower than unmodified rGO and showed very significant improvement in the performance of phenol degradation. Therefore, nitrogen doping might play the dominant role in phenol degradation on rGO-based catalysts. The doped nitrogen would change the electronic structure of carbon atoms nearby, and thus accelerate the electron transfer for the catalytic processes[17, 21]. The performance of N-rGO-350 was in good agreement with that of the previous study.[17]

In this study, further annealing (two-step thermal annealing) of the N-rGO-350 at 400 °C in N_2 had very little effect on the improvement of the performance of phenol degradation. This result is consistent with those of the occurrence 2θ peaks, the SSA

values, and the I_D/I_G ratios although decreasing B values or increasing L values. The effects of SSA and defective structure of rGO on the phenol degradation were not significant, evidenced by that rGO (301 m^2/g) had a much lower activity than N-rGO 300-400 with SSAs of 53 – 153 m^2/g.

Meanwhile, nitrogen doping would play a dominant role in activation of PMS for phenol oxidation and resulted in much higher phenol degradation efficiency. N-rGO-400 (SSA= 159 m^2/g) shows the best performance by reducing the phenol concentration from 100% to 0 within 15 min. Furthermore, no direct correlation between nitrogen dopants, including doping level and different nitrogen contents, and catalytic phenol oxidation was observed. This result suggests that in terms of nitrogen doping, a relatively high SSA value may still contribute to the improved phenol degradation.

Further kinetic studies were carried out to investigate the effect of reaction temperature on phenol oxidation over N-rGO-350. **Figure 3.11** shows that phenol degradation almost follows linear correlation between Ln (phenol concentration) versus time, suggesting phenol degradation follows first order kinetics on N-rGO by activation of PMS.

Figure 3.10b shows that the activation energy was estimated to be 31.6 kJ/mol using the Arrhenius equation.

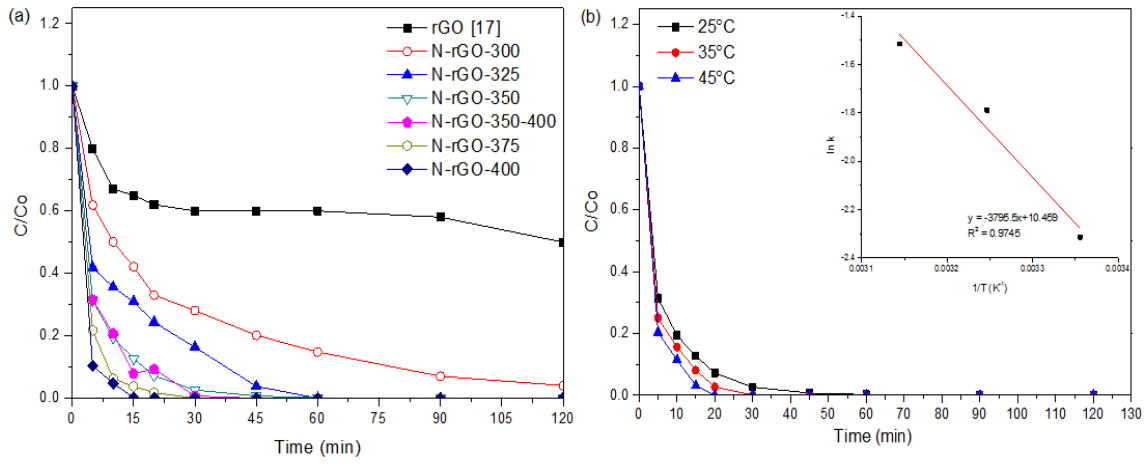

Figure 3.10. Catalytic degradation of phenol vs time on N-rGO at different thermal annealing temperatures by activation of PMS. (a) Phenol removal profiles on N-rGO, (b) Phenol removal profiles on N-rGO-350 at varying temperatures.

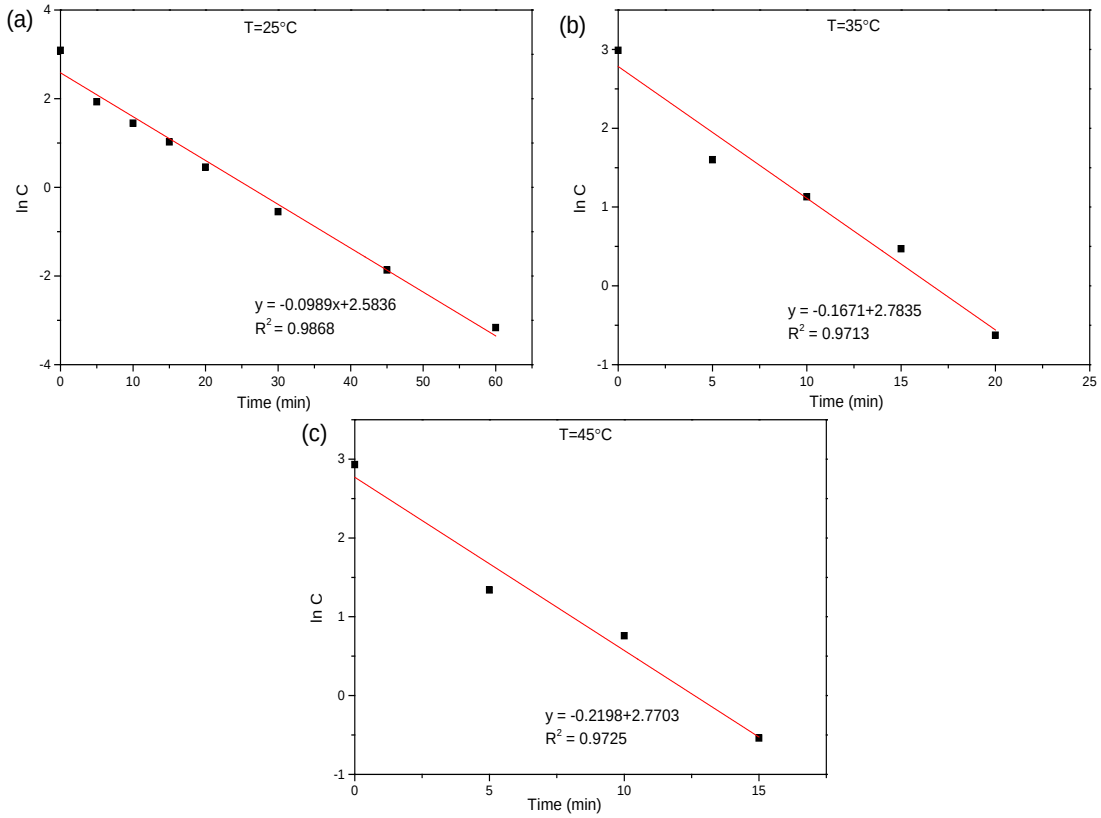

Figure 3.11. First order kinetics of N-rGO-350 at 25, 35 and 45 °C.

3.3.3. Mechanism of PMS activation and phenol oxidation

It was known that both $^{\bullet}OH$ and $SO_4^{\bullet-}$ radicals are generated during PMS activation by metal-based catalysts.[55-56] $SO_4^{\bullet-}$ has been suggested to be the major radical for degradation of typical organic pollutants. In this study, rapid removal of phenol was obtained by PMS activation on N-rGO, especially on N-rGO-375 and N-rGO-400. In order to elucidate the mechanism of PMS activation on N-rGO for phenol degradation, electron paramagnetic resonance (EPR) studies were carried out, in which 5, 5-dimethyl-pyrroline-oxide (DMPO) was used as the spin trapping reagent for $^{\bullet}OH$ and $SO_4^{\bullet-}$ radicals.

Figure 3.12a shows the time-dependent radical generation at different reaction time (3, 5, 10, and 20 min). In all time, $^{\bullet}OH$ and $SO_4^{\bullet-}$ radicals were detected by EPR spectra. At 3 min, $^{\bullet}OH$ radicals occurred as the major species. This might indicate that $^{\bullet}OH$ radicals play a major role in catalytic phenol oxidation at initial stage.

It was known that $^{\bullet}OH$ and $SO_4^{\bullet-}$ radicals show different reaction rates with two radical scavengers, ethanol (EtOH) and tert-butyl alcohol (TBA) as the quenching agents.[56] EtOH can capture both $^{\bullet}OH$ and $SO_4^{\bullet-}$ while TBA prefers capturing $^{\bullet}OH$ radicals rather than $SO_4^{\bullet-}$ radicals.

Figure 3.12b and c display the changes of reactive radicals generated by N-rGO activation of PMS with different quenching reagents. Both radicals and their changes upon addition of classical quenching reagents were identified.

Figure 3.12d shows the variation of the peak intensities of DMPO-HO and DMPO-SO_4 adducts during the reaction time (3, 5, 10 and 20 min) with and without the presence of the two scavengers, EtOH and TBA. It can be seen that, without scavengers, the DMPO-OH intensity increased significantly (N-rGO-350 DMPO-OH curve) within the reaction time of 3 min and decreased afterward (5-20 min). On the other hand, the DMPO-SO_4 intensity remained stable at a low level, which might be due to the great consumption of sulfate radicals in phenol oxidation. In the presence of EtOH, DMPO-OH intensity reduced and the peak occurred at 5 min. Meanwhile, in the presence of TBA, DMPO-OH intensity was much lower. However, DMPO-SO_4 intensity did not show much difference with or without the scavengers. The above results suggest that both radicals are important in phenol degradation.

With the combination of EPR studies and classical quenching tests, it was confirmed that $^{\bullet}OH$ and $SO_4^{\bullet-}$ radicals are present in PMS activation for phenol oxidation on N-rGO catalysis. N-rGO would contribute to the electron transfer processes and facilitate below reactions.

$$HSO_5^- + e^- \rightarrow {}^{\bullet}OH + SO_4^{2-} \quad (3.1)$$

$$HSO_5^- + e^- \rightarrow SO_4^{\bullet-} + OH^- \quad (3.2)$$

$$HSO_5^- - e^- \rightarrow SO_5^{\bullet-} + H^+ \quad (3.3)$$

$$^{\bullet}OH + SO_4^{2-} \rightarrow SO_4^{\bullet-} + OH^- \quad (3.4)$$

$$SO_4^{\bullet-} + OH^- \rightarrow SO_4^{2-} + {}^{\bullet}OH \quad (3.5)$$

$$\text{Phenol} + SO_4^{\bullet-} (\ ^{\bullet}OH\ ) \rightarrow \text{several steps} \rightarrow CO_2 + H_2O + SO_4^{2-} \quad (3.6)$$

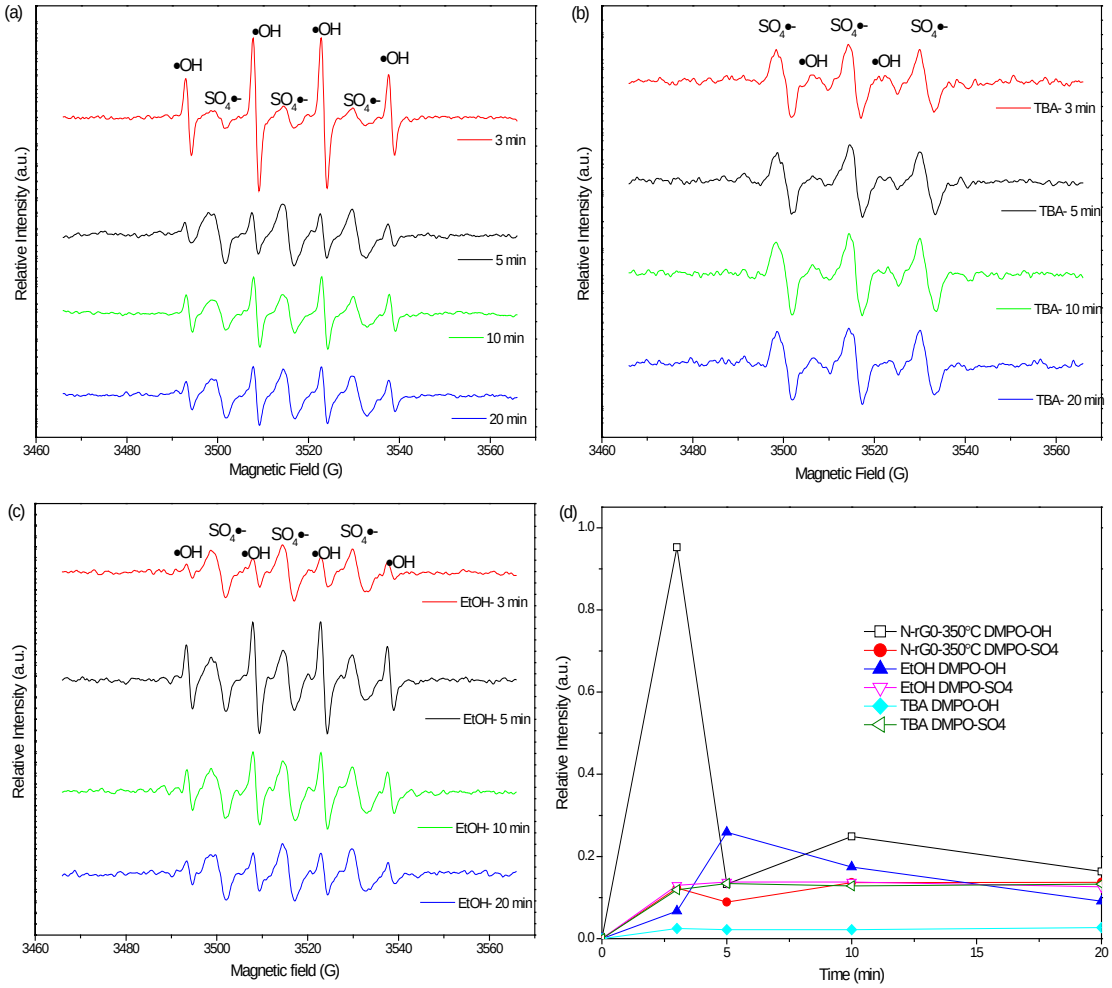

Figure 3.12. EPR spectra in various conditions, (a) PMS activation on N-rGO-350, (b) with addition of TBA, (c) with addition of EtOH, and (d) Comparison of hydroxyl and sulfate radicals dependence on time.

3.4. Conclusions

In this chapter, a simple method was used to successfully prepare nitrogen-doped reduced graphene oxide (N-rGO) by a simultaneous reduction and nitrogen doping of GO at low temperatures ranging from 300 to 400 °C. Comprehensive studies by a variety of characterization techniques suggested that significant crystal, structural and compositional modifications could be achieved by simply varying the calcination temperature for synthesis of highly efficient metal-free catalysts. These N-rGO materials were demonstrated to be efficient in catalytic activation of PMS for phenol degradation in water. For N-rGO via thermal annealing temperatures between 300 to 325 °C, the improvement of phenol degradation may be primarily due to the nitrogen

dopant. Whereas for N-rGO from thermal annealing temperatures between 350 to 400 °C, the improvement of phenol degradation may be due to both nitrogen dopants and relatively high SSA. Combination of EPR studies and quenching tests indicated that N-rGO can activate PMS to produce both hydroxyl and sulfate radicals, which induce phenol degradation.

References

1. Liang, H. W.; Ting, Y. Y.; Sun, H. Q.; Ang, H. M.; Tade, M. O.; Wang, S. B., Solution combustion synthesis of Co oxide-based catalysts for phenol degradation in aqueous solution. *Journal of Colloid and Interface Science* **2012,** *372*, 58-62.
2. Shukla, P.; Sun, H. Q.; Wang, S. B.; Ang, H. M.; Tade, M. O., Nanosized Co3O4/SiO2 for heterogeneous oxidation of phenolic contaminants in waste water. *Separation and Purification Technology* **2011,** *77* (2), 230-236.
3. Shukla, P. R.; Wang, S. B.; Sun, H. Q.; Ang, H. M.; Tade, M., Activated carbon supported cobalt catalysts for advanced oxidation of organic contaminants in aqueous solution. *Applied Catalysis B-Environmental* **2010,** *100* (3-4), 529-534.
4. Sun, H. Q.; Liang, H. W.; Zhou, G. L.; Wang, S. B., Supported cobalt catalysts by one-pot aqueous combustion synthesis for catalytic phenol degradation. *Journal of Colloid and Interface Science* **2013,** *394*, 394-400.
5. Saputra, E.; Muhammad, S.; Sun, H. Q.; Ang, H. M.; Tade, M. O.; Wang, S. B., Shape-controlled activation of peroxymonosulfate by single crystal alpha-Mn2O3 for catalytic phenol degradation in aqueous solution. *Appl. Catal. B-Environ.* **2014,** *154*, 246-251.
6. Saputra, E.; Muhammad, S.; Sun, H. Q.; Ang, H. M.; Tade, M. O.; Wang, S. B., Different Crystallographic One-dimensional MnO2 Nanomaterials and Their Superior Performance in Catalytic Phenol Degradation. *Environ. Sci. Technol.* **2013,** *47* (11), 5882-5887.
7. Sun, H. Q.; Zhou, G. L.; Liu, S. Z.; Ang, H. M.; Tade, M. O.; Wang, S. B., Nano-Fe-0 Encapsulated in Microcarbon Spheres: Synthesis, Characterization, and Environmental Applications. *Acs Applied Materials & Interfaces* **2012,** *4* (11), 6235-6241.
8. Liang, H. W.; Sun, H. Q.; Patel, A.; Shukla, P.; Zhu, Z. H.; Wang, S. B., Excellent performance of mesoporous Co3O4/MnO2 nanoparticles in heterogeneous

activation of peroxymonosulfate for phenol degradation in aqueous solutions. *Appl. Catal. B-Environ.* **2012,** *127*, 330-335.

9. Sun, H. Q.; Liu, S. Z.; Zhou, G. L.; Ang, H. M.; Tade, M. O.; Wang, S. B., Reduced Graphene Oxide for Catalytic Oxidation of Aqueous Organic Pollutants. *Acs Applied Materials & Interfaces* **2012,** *4* (10), 5466-5471.

10. Peng, W. C.; Liu, S. Z.; Sun, H. Q.; Yao, Y. J.; Zhi, L. J.; Wang, S. B., Synthesis of porous reduced graphene oxide as metal-free carbon for adsorption and catalytic oxidation of organics in water. *Journal of Materials Chemistry A* **2013,** *1* (19), 5854-5859.

11. Yao, Y. J.; Miao, S. D.; Liu, S. Z.; Ma, L. P.; Sun, H. Q.; Wang, S. B., Synthesis, characterization, and adsorption properties of magnetic Fe3O4@graphene nanocomposite. *Chemical Engineering Journal* **2012,** *184*, 326-332.

12. Liu, S. Z.; Peng, W. C.; Sun, H. Q.; Wang, S. B., Physical and chemical activation of reduced graphene oxide for enhanced adsorption and catalytic oxidation. *Nanoscale* **2014,** *6* (2), 766-771.

13. W. Peng, S. L., H. Sun, Y. Yao, L. Zhi, and S. Wang, Synthesis of porous reduced graphene oxide as metal-free carbon for adsorption and catalytic oxidation of organics in water. *J. Mat. Chem.* **2013,** *1*, 5854-5859.

14. Huan, T. N.; Khai, T. V.; Kang, Y.; Shim, K. B.; Chung, H., Enhancement of quaternary nitrogen doping of graphene oxide via chemical reduction prior to thermal annealing and an investigation of its electrochemical properties. *Journal of Materials Chemistry* **2012,** *22* (29), 14756-14762.

15. Lv, R.; Li, Q.; Botello-Mendez, A. R.; Hayashi, T.; Wang, B.; Berkdemir, A.; Hao, Q. Z.; Elias, A. L.; Cruz-Silva, R.; Gutierrez, H. R.; Kim, Y. A.; Muramatsu, H.; Zhu, J.; Endo, M.; Terrones, H.; Charlier, J. C.; Pan, M. H.; Terrones, M., Nitrogen-doped graphene: beyond single substitution and enhanced molecular sensing. *Scientific Reports* **2012,** *2*.

16. Jiang, J.; Turnbull, J.; Lu, W. C.; Boguslawski, P.; Bernholc, J., Theory of nitrogen doping of carbon nanoribbons: Edge effects. *Journal of Chemical Physics* **2012,** *136* (1).

17. Sun, H. Q.; Wang, Y. X.; Liu, S. Z.; Ge, L.; Wang, L.; Zhu, Z. H.; Wang, S. B., Facile synthesis of nitrogen doped reduced graphene oxide as a superior metal-free catalyst for oxidation. *Chem. Commun.* **2013,** *49* (85), 9914-9916.

18. Liu, S. Z.; Sun, H. Q.; Liu, S. M.; Wang, S. B., Graphene facilitated visible light photodegradation of methylene blue over titanium dioxide photocatalysts. *Chemical Engineering Journal* **2013,** *214*, 298-303.

19. Qu, L. T.; Liu, Y.; Baek, J. B.; Dai, L. M., Nitrogen-Doped Graphene as Efficient Metal-Free Electrocatalyst for Oxygen Reduction in Fuel Cells. *Acs Nano* **2010,** *4* (3), 1321-1326.

20. Long, J. L.; Xie, X. Q.; Xu, J.; Gu, Q.; Chen, L. M.; Wang, X. X., Nitrogen-Doped Graphene Nanosheets as Metal-Free Catalysts for Aerobic Selective Oxidation of Benzylic Alcohols. *Acs Catalysis* **2012,** *2* (4), 622-631.

21. Gao, Y. J.; Hu, G.; Zhong, J.; Shi, Z. J.; Zhu, Y. S.; Su, D. S.; Wang, J. G.; Bao, X. H.; Ma, D., Nitrogen-Doped sp2-Hybridized Carbon as a Superior Catalyst for Selective Oxidation. *Angewandte Chemie-International Edition* **2013,** *52* (7), 2109-2113.

22. Sun, H. Q.; Kwan, C.; Suvorova, A.; Ang, H. M.; Tade, M. O.; Wang, S. B., Catalytic oxidation of organic pollutants on pristine and surface nitrogen-modified carbon nanotubes with sulfate radicals. *Applied Catalysis B-Environmental* **2014,** *154*, 134-141.

23. Hummers, W. S.; Offeman, R. E., Preparation of Graphitic Oxide. *Journal of the American Chemical Society* **1958,** *80* (6), 1339-1339.

24. Perera, S. D.; Mariano, R. G.; Nijem, N.; Chabal, Y.; Ferraris, J. P.; Balkus, K. J., Alkaline deoxygenated graphene oxide for supercapacitor applications: An effective green alternative for chemically reduced graphene. *Journal of Power Sources* **2012,** *215*, 1-10.

25. Charlier, J. C.; Gonze, X.; Michenaud, J. P., First-principles study of the stacking effect on the electronic properties of graphite(s). *Carbon* **1994,** *32* (2), 289-299.

26. Haering, R. R., BAND STRUCTURE OF RHOMBOHEDRAL GRAPHITE. *Canadian Journal of Physics* **1958,** *36* (3), 352-362.

27. Park, S.; An, J.; Potts, J. R.; Velamakanni, A.; Murali, S.; Ruoff, R. S., Hydrazine-reduction of graphite- and graphene oxide. *Carbon* **2011,** *49* (9), 3019-3023.

28. Wilson, N. R.; Pandey, P. A.; Beanland, R.; Rourke, J. P.; Lupo, U.; Rowlands, G.; Romer, R. A., On the structure and topography of free-standing chemically modified graphene. *New Journal of Physics* **2010,** *12*, 21.

29. H. P. Klug, a. L. E. A., *X-Ray Diffraction Procedures: For Polycrystalline and Amorphous Materials* John Wiley and Sons, Inc: New York, **1974**; p 966.

30. Kudin, K. N.; Ozbas, B.; Schniepp, H. C.; Prud'homme, R. K.; Aksay, I. A.; Car, R., Raman spectra of graphite oxide and functionalized graphene sheets. *Nano Letters* **2008,** *8* (1), 36-41.

31. Yang, D.; Velamakanni, A.; Bozoklu, G.; Park, S.; Stoller, M.; Piner, R. D.; Stankovich, S.; Jung, I.; Field, D. A.; Ventrice, C. A.; Ruoff, R. S., Chemical analysis of graphene oxide films after heat and chemical treatments by X-ray photoelectron and Micro-Raman spectroscopy. *Carbon* **2009,** *47* (1), 145-152.

32. Wilson, N. R.; Pandey, P. A.; Beanland, R.; Young, R. J.; Kinloch, I. A.; Gong, L.; Liu, Z.; Suenaga, K.; Rourke, J. P.; York, S. J.; Sloan, J., Graphene Oxide: Structural Analysis and Application as a Highly Transparent Support for Electron Microscopy. *Acs Nano* **2009,** *3* (9), 2547-2556.

33. Cai, W.; Piner, R. D.; Stadermann, F. J.; Park, S.; Shaibat, M. A.; Ishii, Y.; Yang, D.; Velamakanni, A.; An, S. J.; Stoller, M.; An, J.; Chen, D.; Ruoff, R. S., Synthesis and Solid-State NMR Structural Characterization of 13C-Labeled Graphite Oxide. *Science* **2008,** *321* (5897), 1815-1817.

34. Gomez-Navarro, C.; Weitz, R. T.; Bittner, A. M.; Scolari, M.; Mews, A.; Burghard, M.; Kern, K., Electronic transport properties of individual chemically reduced graphene oxide sheets. *Nano Letters* **2007,** *7* (11), 3499-3503.

35. McAllister, M. J.; Li, J. L.; Adamson, D. H.; Schniepp, H. C.; Abdala, A. A.; Liu, J.; Herrera-Alonso, M.; Milius, D. L.; Car, R.; Prud'homme, R. K.; Aksay, I. A., Single sheet functionalized graphene by oxidation and thermal expansion of graphite. *Chemistry of Materials* **2007,** *19* (18), 4396-4404.

36. R. Bissessur, P. K. Y. L., W. White, and S. F. Scully, Encapsulation of Polyanilines into Graphite Oxide. *Langmuir* **2006,** *22*, 1729-1734.

37. Xu, C.; Wang, X.; Zhu, J. W.; Yang, X. J.; Lu, L., Deposition of Co(3)O(4) nanoparticles onto exfoliated graphite oxide sheets. *Journal of Materials Chemistry* **2008,** *18* (46), 5625-5629.

38. Herrera-Alonso, M.; Abdala, A. A.; McAllister, M. J.; Aksay, I. A.; Prud'homme, R. K., Intercalation and stitching of graphite oxide with diaminoalkanes. *Langmuir* **2007,** *23* (21), 10644-10649.

39. Bourlinos, A. B.; Gournis, D.; Petridis, D.; Szabo, T.; Szeri, A.; Dekany, I., Graphite oxide: Chemical reduction to graphite and surface modification with primary aliphatic amines and amino acids. *Langmuir* **2003,** *19* (15), 6050-6055.

40. Yao, Y. J.; Miao, S. D.; Yu, S. M.; Ma, L. P.; Sun, H. Q.; Wang, S. B., Fabrication of Fe3O4/SiO2 core/shell nanoparticles attached to graphene oxide and its use as an adsorbent. *Journal of Colloid and Interface Science* **2012,** *379*, 20-26.

41. Guo, P. P.; Xiao, F.; Liu, Q.; Liu, H. F.; Guo, Y. L.; Gong, J. R.; Wang, S.; Liu, Y. Q., One-Pot Microbial Method to Synthesize Dual-Doped Graphene and Its Use as High-Performance Electrocatalyst. *Scientific Reports* **2013,** *3*, 6.

42. Boncel, S.; Pattinson, S. W.; Geiser, V.; Shaffer, M. S. P.; Koziol, K. K. K., En route to controlled catalytic CVD synthesis of densely packed and vertically aligned nitrogen-doped carbon nanotube arrays. *Beilstein Journal of Nanotechnology* **2014,** *5*, 219-233.

43. Li, X. L.; Wang, H. L.; Robinson, J. T.; Sanchez, H.; Diankov, G.; Dai, H. J., Simultaneous Nitrogen Doping and Reduction of Graphene Oxide. *Journal of the American Chemical Society* **2009,** *131* (43), 15939-15944.

44. Guo, B. D.; Liu, Q. A.; Chen, E. D.; Zhu, H. W.; Fang, L. A.; Gong, J. R., Controllable N-Doping of Graphene. *Nano Letters* **2010,** *10* (12), 4975-4980.

45. Lai, L. F.; Potts, J. R.; Zhan, D.; Wang, L.; Poh, C. K.; Tang, C. H.; Gong, H.; Shen, Z. X.; Jianyi, L. Y.; Ruoff, R. S., Exploration of the active center structure of nitrogen-doped graphene-based catalysts for oxygen reduction reaction. *Energy & Environmental Science* **2012,** *5* (7), 7936-7942.

46. Zheng, B.; Wang, J.; Wang, F. B.; Xia, X. H., Synthesis of nitrogen doped graphene with high electrocatalytic activity toward oxygen reduction reaction. *Electrochemistry Communications* **2013,** *28*, 24-26.

47. Luo, Z. Q.; Lim, S. H.; Tian, Z. Q.; Shang, J. Z.; Lai, L. F.; MacDonald, B.; Fu, C.; Shen, Z. X.; Yu, T.; Lin, J. Y., Pyridinic N doped graphene: synthesis, electronic structure, and electrocatalytic property. *Journal of Materials Chemistry* **2011,** *21* (22), 8038-8044.

48. Jeon, I. Y.; Yu, D. S.; Bae, S. Y.; Choi, H. J.; Chang, D. W.; Dai, L. M.; Baek, J. B., Formation of Large-Area Nitrogen-Doped Graphene Film Prepared from Simple Solution Casting of Edge-Selectively Functionalized Graphite and Its Electrocatalytic Activity. *Chemistry of Materials* **2011,** *23* (17), 3987-3992.

49. Long, D. H.; Li, W.; Ling, L. C.; Miyawaki, J.; Mochida, I.; Yoon, S. H., Preparation of Nitrogen-Doped Graphene Sheets by a Combined Chemical and Hydrothermal Reduction of Graphene Oxide. *Langmuir* **2010,** *26* (20), 16096-16102.
50. Stankovich, S.; Dikin, D. A.; Piner, R. D.; Kohlhaas, K. A.; Kleinhammes, A.; Jia, Y.; Wu, Y.; Nguyen, S. T.; Ruoff, R. S., Synthesis of graphene-based nanosheets via chemical reduction of exfoliated graphite oxide. *Carbon* **2007,** *45* (7), 1558-1565.
51. Wei, D. C.; Liu, Y. Q.; Wang, Y.; Zhang, H. L.; Huang, L. P.; Yu, G., Synthesis of N-Doped Graphene by Chemical Vapor Deposition and Its Electrical Properties. *Nano Letters* **2009,** *9* (5), 1752-1758.
52. Bag, S.; Roy, K.; Gopinath, C. S.; Raj, C. R., Facile Single-Step Synthesis of Nitrogen-Doped Reduced Graphene Oxide-Mn3O4 Hybrid Functional Material for the Electrocatalytic Reduction of Oxygen. *Acs Applied Materials & Interfaces* **2014,** *6* (4), 2691-2698.
53. Singh, G.; Sutar, D. S.; Botcha, V. D.; Narayanam, P. K.; Talwar, S. S.; Srinivasa, R. S.; Major, S. S., Study of simultaneous reduction and nitrogen doping of graphene oxide Langmuir-Blodgett monolayer sheets by ammonia plasma treatment. *Nanotechnology* **2013,** *24* (35), 11.
54. Li, X. J.; Yu, X. X.; Liu, J. Y.; Fan, X. D.; Zhang, K.; Cai, H. B.; Pan, N.; Wang, X. P., Synthesis of Nitrogen-Doped Graphene via Thermal Annealing Graphene with Urea. *Chinese Journal of Chemical Physics* **2012,** *25* (3), 325-329.
55. Huang, Z. F.; Bao, H. W.; Yao, Y. Y.; Lu, W. Y.; Chen, W. X., Novel green activation processes and mechanism of peroxymonosulfate based on supported cobalt phthalocyanine catalyst. *Applied Catalysis B-Environmental* **2014,** *154*, 36-43.
56. Wang, Y.; Sun, H.; Ang, H. M.; Tadé, M. O.; Wang, S., 3D-hierarchically structured MnO2 for catalytic oxidation of phenol solutions by activation of peroxymonosulfate: Structure dependence and mechanism. *Applied Catalysis B: Environmental* **2015,** *164* (0), 159-167.

CHAPTER 4

Nanocarbons in different structural dimensions (0–3D) for phenol adsorption and metal-free catalytic oxidation

Abstract

Metal-free nanocarbon materials in different structural dimensions, such as 0D fullerene (C_{60}), 1D single-walled carbon nanotubes (SWCNTs), 2D graphene nanoplate (GNP), 3D hexagonally-ordered mesoporous carbon (CMK-3) and cubically-ordered ***mesoporous carbon*** *(CMK-8) were investigated for adsorption and catalytic oxidation of phenol in water solutions. A variety of characterisation techniques were used to investigate the properties of the carbon samples. It was found that structural dimension and heat treatment would significantly affect the performance of the nanocarbons in adsorption and catalysis. Both GNP and CMK-3 showed better phenol adsorption with around 40% phenol removal in 500 mL of 20 ppm solutions. The nanocarbons were also used for metal-free activation of peroxymonosulfate (PMS) to produce sulfate radicals for catalytic phenol oxidation. Efficient catalysis was observed on CMK-3, CMK-8 and SWCNTs. Thermal treatment of the nanocarbons at 350 ^{o}C in nitrogen was conducted to modulate the crystal- and micro-structures and surface functional groups of the different nanocarbons. Enhancement at 2-fold in adsorption on SWCNTs and 7.5-fold in catalysis on CMK-8 were observed after the heat treatments. Mechanisms of adsorption and catalytic oxidation of phenol were discussed. This study contributes to the development of green materials for sustainable remediation of aqueous organic pollutants.*

4.1. Introduction

Severe air, water and soil pollutions from the rapid developments in industrialisation, population expansion and urbanisation have posed detrimental effects on the eco-environment and human life [1]. Toxic gases, heavy metals, organics and bio-toxics are the major contributors to the pollution. A variety of chemical, physical and biological treatments have been employed to tackle the issues [2], among which adsorption and catalytic oxidation processes have been proven to be effective for removal of aqueous contaminants [3-4]. For efficient adsorption and degradation, many porous materials have been developed and employed [5]. Pillared clays, zeolites, mesoporous metal oxides, polymers and metal-organic frameworks have shown varying effectiveness in removing toxic pollutants [6]. However, most traditional adsorbents and catalysts are metal-based materials [7-10] and the demerits of high-cost, scarcity in nature and metal leaching of those materials were experienced [11]. Metal-free carbon materials for adsorption and catalytic oxidation are expected to overcome the issues.

Carbonaceous-based adsorbents including activated carbon, carbon nanotubes (CNTs), fullerene (C_{60}), graphene oxide (GO), and graphene have demonstrated high adsorption capacities and thermal stabilities [12-13]. Also for catalytic oxidation, reduced graphene oxide (rGO) was recently demonstrated to be an effective catalyst for activation of peroxymonosulfate (PMS) [11], which was previously achieved only on homogeneous or heterogeneous metal-based catalysts [3, 7, 14-19]. Physical CO_2 activation at a high temperature and chemical activation using $ZnCl_2$ were applied to improve the porous structure and surface features of rGO samples, and enhanced adsorption and catalysis were then achieved [4, 20]. It was suggested that three important parameters such as specific surface area (SSA), porous structure and proper functional groups can enhance the performance of the green catalysts [4, 13, 20-22].

Previously, nanoscaled materials in different dimensional structures have been synthesised. However, few investigations have focused on the dimension-dependent effects [7, 9]. In this study, several nanocarbons in different dimensions, such as 0D C_{60}, 1D single-wall carbon nanotubes (SWCNTs), 2D GNP, and 3D CMK-3 and CMK-8, were employed for adsorptive and catalytically oxidative removal of organic pollutants in water. In addition, thermal treatment at a low temperature of 350 ^{o}C in nitrogen was applied to tune the physicochemical properties of the nanocarbons. As a

result, enhanced adsorption and catalysis in phenol removal on some nanocarbons were observed. The mechanism of the enhanced performances for removing organic pollutants in water was discussed.

4.2. Experimental section

4.2.1. Materials and catalyst preparation

All chemicals were obtained from Sigma-Aldrich. Nanocarbons in different dimensions, such as 0D C_{60}, 1D single-wall carbon nanotubes (SWCNTs), 2D GNP, and 3D CMK-3 and CMK-8 were thermally annealed in a tube furnace under nitrogen atmosphere at temperature of 350 ^{o}C for 1 hour and cooled down naturally. The obtained nanocarbons were washed with ethanol and DI water three times each, and dried in an oven at 60 °C.

4.2.2. Characterization of catalysts

X-ray diffraction (XRD) patterns were acquired on a Bruker D8-Advanced X-ray instrument using Cu-Kα radiation with λ at 1.5418 Å. Nitrogen sorption isotherms were obtained on a Micrometrics Tristar 3000 and the Brunauer-Emmet-Teller (BET) and Barrett-Joyner-Halenda (BJH) methods were applied to evaluate the specific surface area (SSA) and pore size distribution, respectively, of the samples. Fourier transform infrared spectra (FTIR) were recorded on a Bruker instrument with an ATR correction mode. X-ray photoelectron spectroscopy (XPS) was used to determine the chemical states of elements using a Thermo Escalab 250 with Al-Kα X-ray. Thermogravimetric-differential scanning calorimetry (TG-DSC) was carried out in an air flow at a flowrate of 100 mL/min using a Perkin-Elmer Diamond thermal analyser. Scanning electron microscopy (SEM) was applied to investigate the morphology of the carbons on Zeiss Neon 40 EsB FIBSEM. Raman analysis was performed on an ISA dispersive Raman spectroscopy using argon ion laser with a wavelength at 514 nm. The points of zero charge (PZC) of the carbon samples were measured using a Malvern Zetasizer Nano ZS.

4.2.3. Adsorption and catalytic activity tests

The adsorption test were carried out in a 500 mL conical flask with phenol solution (20 ppm) and carbon adsorbents (0.2 g/L) in a temperature-controlled water bath

keeping the temperature at 25 °C. The catalytic oxidation of phenol was carried out in the same condition with addition of PMS (2.0 g/L). During each time interval, 1 mL solution was withdrawn by a syringe, filtered by a 0.45 μm Millipore film, and injected into a vial. Then 0.5 mL of methanol was injected into the reaction solution as a quenching reagent to immediately stop further oxidation in the vial. The mixed solution was analysed by a high performance liquid chromatography (HPLC, Varian) with a C-18 column and a UV detector set at 270 nm. The initial solution pH was 6.5 – 7.0, and during the catalytic oxidation, the solution pH had been almost constant at 2.5 – 3.0. Electron paramagnetic resonance (EPR) spectroscopy (Bruker EMX-E spectrometer, Germany) was applied for *in situ* investigation of the generation of reactive radicals, using 5, 5-dimethyl-pyrroline-oxide (DMPO) as the spin trapping reagent.

4.3. Results and Discussion

4.3.1. Characterization of carbon samples

XRD technique was applied to investigate the crystal structures and the potential effects of thermal treatment on various dimensional nanocarbons. **Figure 4.1a** shows XRD patterns of 0D nanocarbons of C_{60} and C_{60}-T. Several strong peaks were observed on C_{60}, and the peaks at 10.9, 17.8, 20.9, 21.0, 27.5, 28.2, 31.0 and 32.9^o are corresponding to specific (hkl) planes of (002), (110), (112), (004), (210), (114), (300) and (006), respectively [23]. It is noted that the absence of the strong (101) diffraction peak suggested that the order of hexagonal close-packed structure was not perfect. Compared to the pristine C_{60}, no obvious changes in XRD pattern were observed after annealing at 350 ^{o}C for 1 h under nitrogen atmosphere.

Figure 4.1b shows XRD patterns of 1D SWCNTs and SWCNTs-T. Two characteristic peaks were found approximately at 2θ= 26° and 43°, corresponding to (002) and (100) planes, respectively [24-25]. XRD characteristic peaks of GNP were consistent well with those of graphene. The 2θ peak can be observed at approximate 26.5° corresponding to (002) plane of graphite with *d* spacing of 0.34 nm.

For CMK-3 and CMK-8, XRD patterns (**Figure 4.1c**) showed a very weak signal at about 2θ = 23°. As seen, there were no additional peaks of other crystalline structures (guest species) for all the carbon nanomaterials, indicating the high purity of these

carbons. Half peak width (B) and interlayer thickness (L) of nanocarbons and nanocarbon-Ts are listed in **Table 4.1**.

Generally, thermal annealing at 350 °C did not produce significant effects on crystalline structures of the carbon materials.

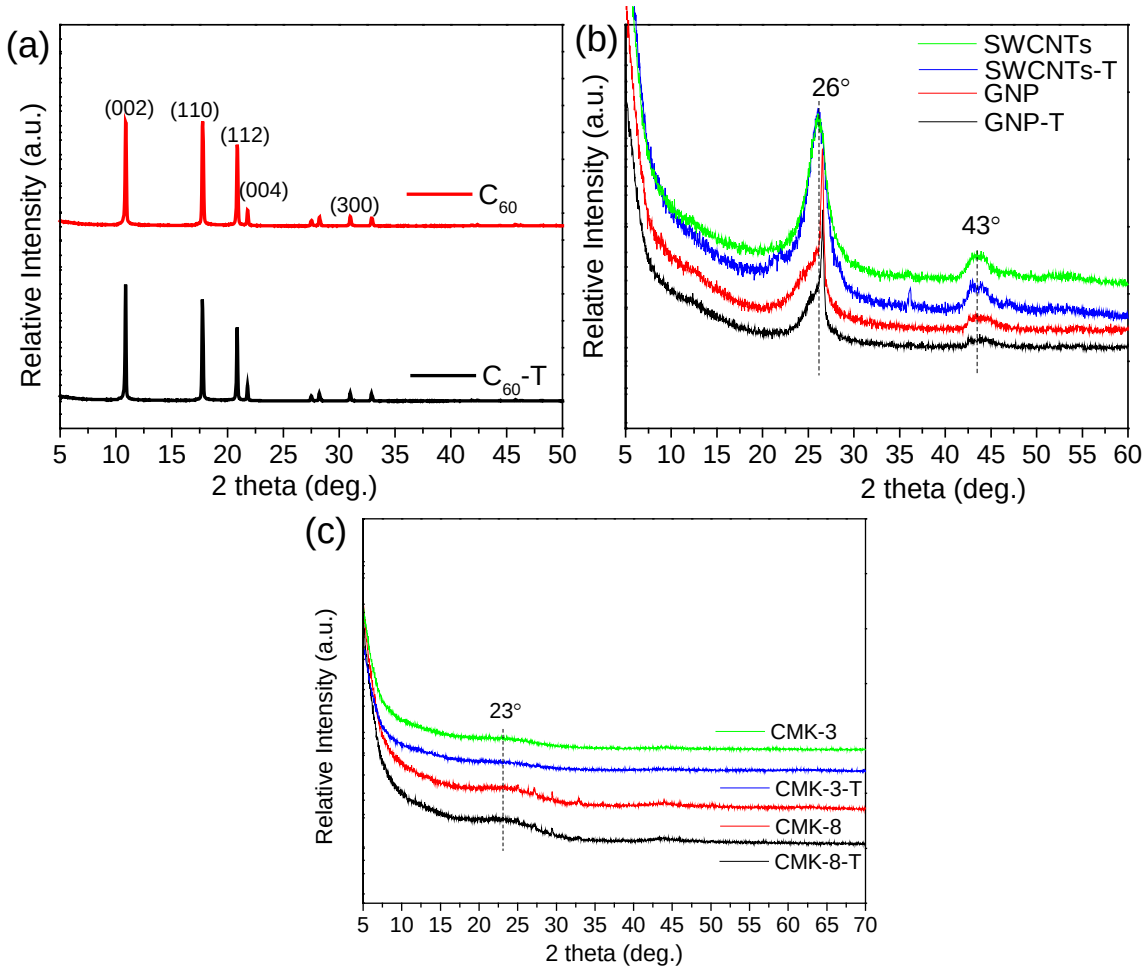

Figure 4.1. XRD patterns of (a) C_{60} and C_{60}-T, (b) SWCNTs, SWCNTs-T, GNP, and GNP-T, (c) CMK-3, CMK-3-T, CMK-8, and CMK-8-T.

Table 4.1. Crystal- and micro-structures of different carbon nanomaterials.

Sample	Half peak width (B, ^{o})	Interlayer material thickness (L, nm)	D band (cm^{-1})	G band (cm^{-1})	I_D/I_G ratio	SSA (m^2/g)	Pore size (nm)
C_{60}	-	-	-	-	-	5.0	5.3
C_{60}-T	-	-	-	-	-	6.0	5.9
SWCNTs	3.1	5.9	1332	1615	0.46	366	8.7
SWCNTs-T	2.9	6.3	1311	1572	0.43	442	8.8
GNP	1.0	18.2	1320	1569	1.28	103	13.5
GNP-T	0.7	25.9	1320	1569	1.27	129	14.5
CMK-3			1311	1583	1.17	1129	4.1
CMK-3-T	-	-	1311	1575	1.15	1246	4.1
CMK-8	-	-	1308	1577	1.49	1040	5.6
CMK-8-T	-	-	1308	1575	1.55	1167	5.9

Figure 4.2 shows the Raman spectra of different carbon nanomaterials before and after thermal treatments. The D band and G band of these different carbon nanomaterials before the thermal annealing are consistent with previous studies [24, 26-28]. The I_D/I_G ratios of different carbon nanomaterials are listed in **Table 4.1**. As seen, I_D/I_G ratio of CMK-8 slightly increased after thermal treatment. On the other hand, the I_D/I_G ratios of SWCNTs, GNP and CMK-3 slightly decreased. There was no significant effect of thermal annealing on the defective structures as indicated by the I_D/I_G ratios.

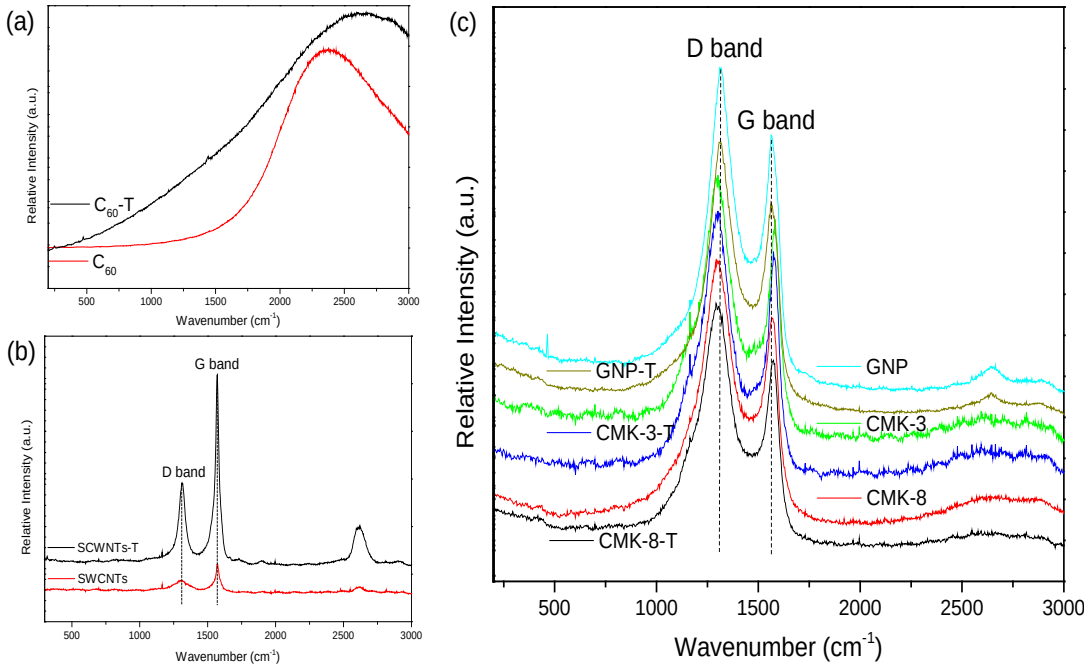

Figure 4.2. Raman spectra of (a) C_{60} and C_{60}-T, (b) SWCNTs, SWCNTs-T, (c) GNP, GNP-T, CMK-3, CMK-3-T, CMK-8, and CMK-8-T.

Figure 4.3 shows pore size distribution and nitrogen sorption isotherms of the nanocarbons. 1D SWCNTs and 2D GNP showed good nitrogen adsorption, and 3D mesoporous carbons of CMK-3 and CMK-8 demonstrated much higher nitrogen adsorption volumes. Hysteresis loops between P/P_0 at 0.5 – 0.9 were observed on all the samples, indicating mesoporous structures of the nanocarbons. The specific surface areas (SSAs) of C_{60}, SWCNTs, GNP, CMK-3 and CMK-8 were estimated to be 5.0, 366, 103, 1129, and 1040 m^2/g, respectively. After thermal treatment at 350 ^oC for 1 h, nitrogen adsorption was generally enhanced on the samples and the SSAs were increased to 6.0, 442, 129, 1246 and 1167 m^2/g, accordingly. The SSA of SWCNTs (366 m^2/g) was in good agreement with the as-received value (380 m^2/g) [29-30]. For CMK-3 and CMK-8, the SSA values were slightly higher than the data provided by the supplier [24, 31-32].

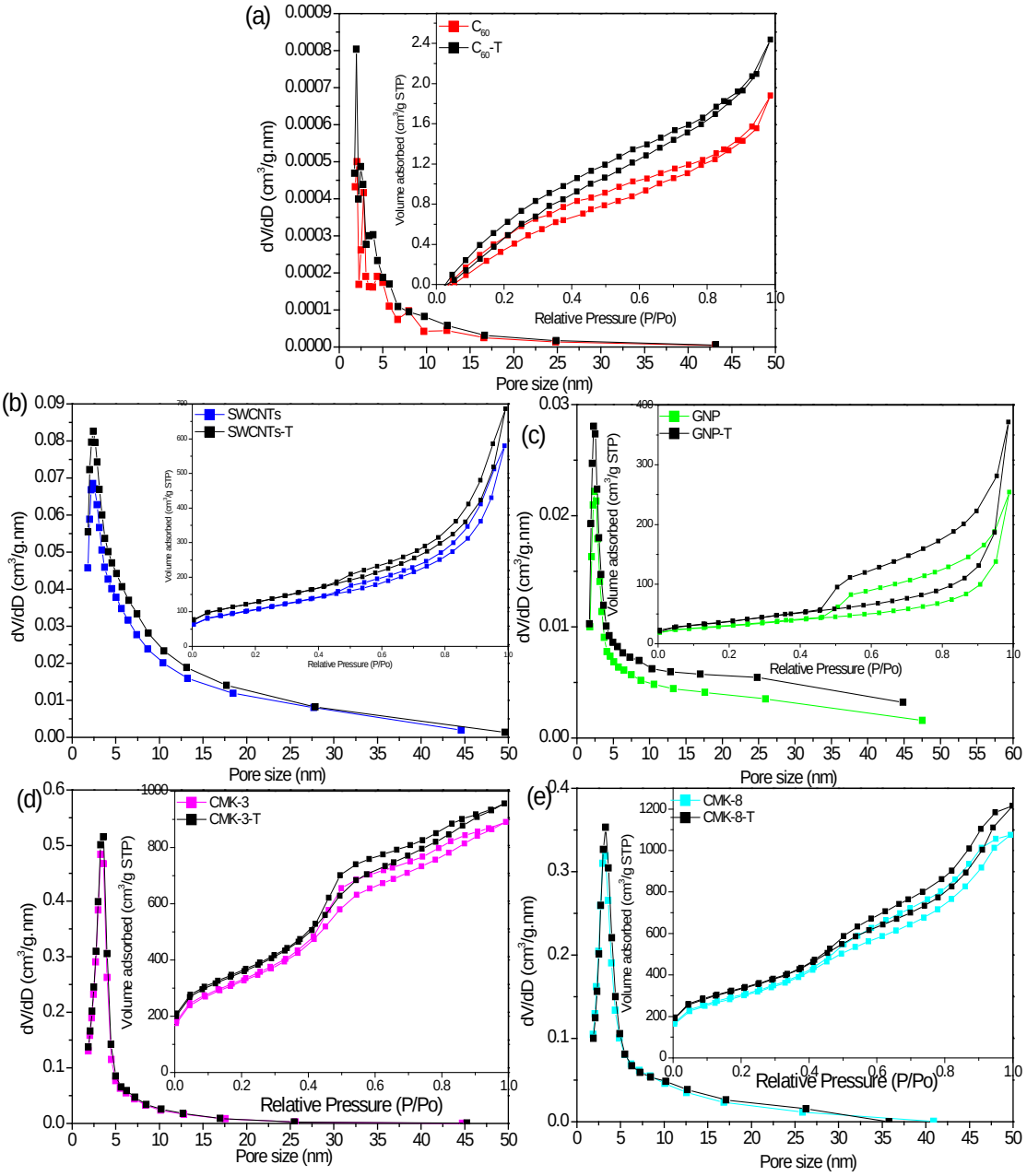

Figure 4.3 Pore size distribution of various nanocarbons. Insets: Nitrogen sorption isotherms.

The morphologies of different carbon nanomaterials are shown in SEM images (**Figure 4.4**). Thermal treatments in this study would not result in any changes in the morphology.

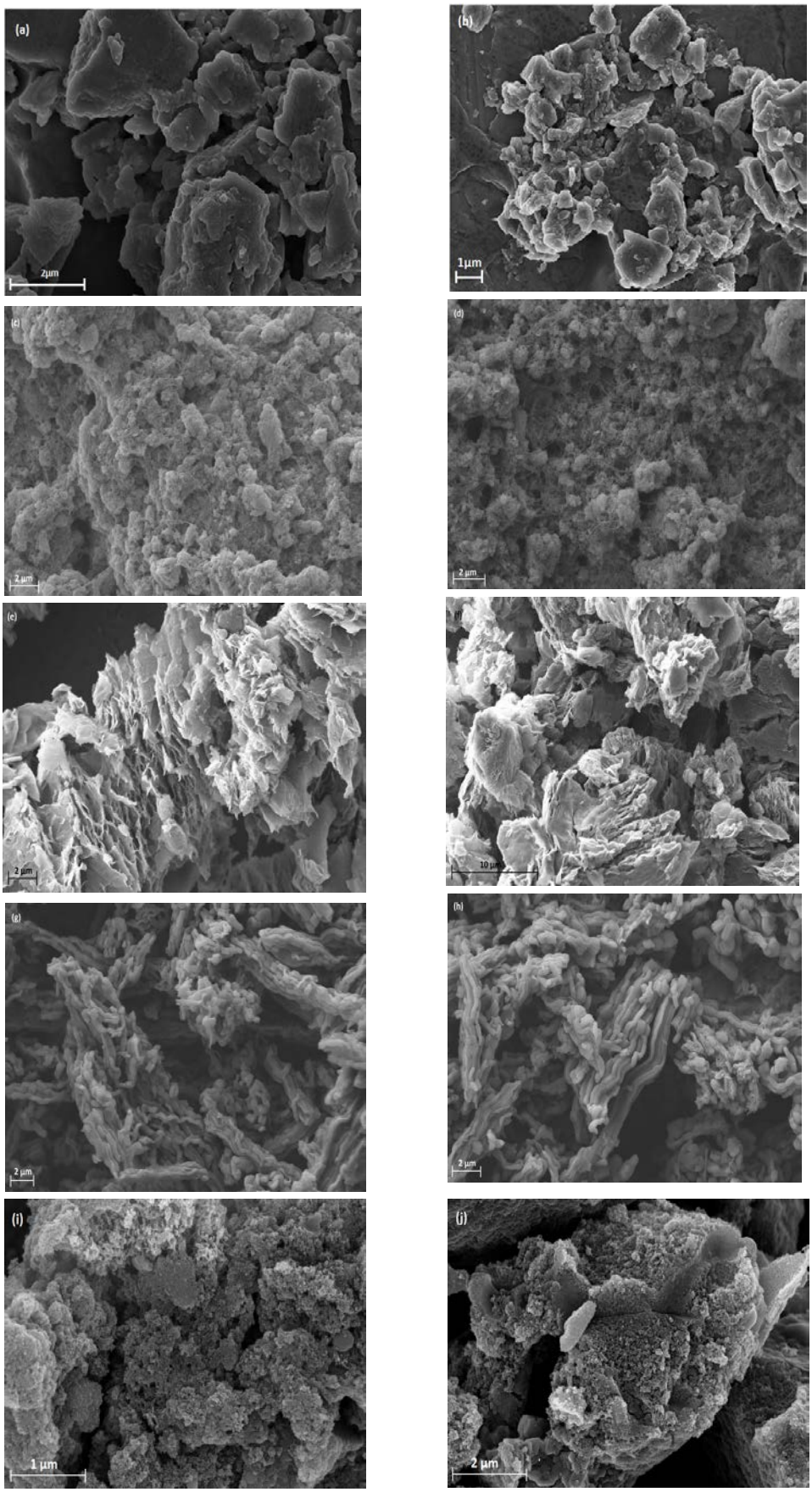

Figure 4.4. SEM images of (a) C_{60}, (b) C_{60}-T, (c) SWCNT, (d) SWCNT-T, (e) GNP, (f) GNP-T, (g) CMK-3, (h) CMK-3-T, (i) CMK-8, and (j) CMK-8-T

The non-microporous surface areas were determined using the t-plot method. **Figure 4.5** shows the comparison of total surface area SSA with microporous surface area and non-microporous surface area. Non-microporous area of C_{60}, SWCNT, GNP, CMK-3 and CMK-8 were 5, 352, 91, 1086 and 977 m^2/g, respectively. After thermal treatment, the non- microporous area were increased to 6, 408, 126, 1131 and 993 m^2/g, accordingly. From these results, the mesopore contents of C_{60}, SWCNT, GNP, CMK-3 and CMK-8 were estimated to be 100, 96, 89, 96 and 94%, respectively, of the total surface area (SSA); and 100, 92, 98, 91, and 85% were determined for the carbon materials after thermal treatment.

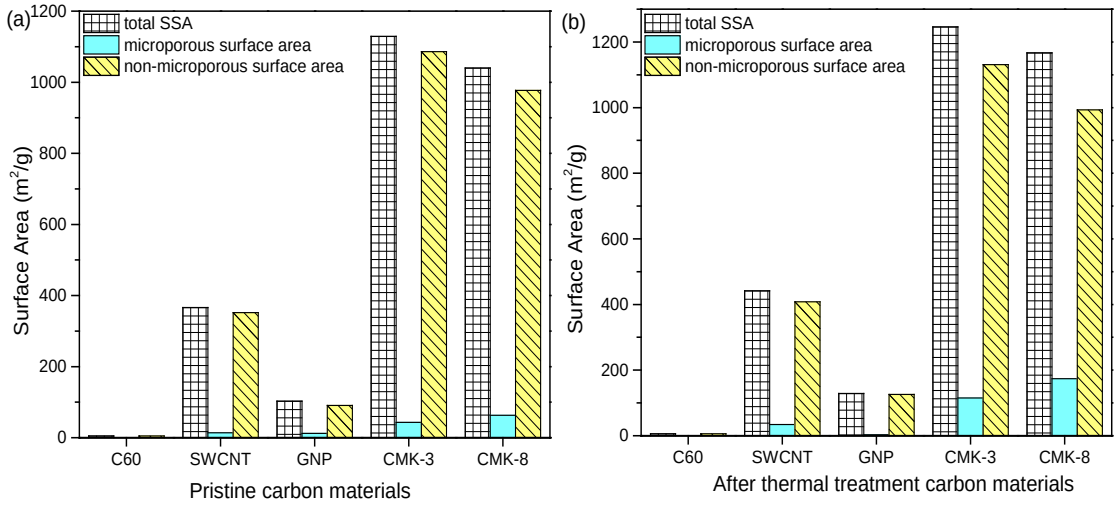

Figure 4.5. Comparison of SSA, microporous surface area and non-microporous surface area for (a) pristine carbon materials, (b) carbon materials after thermal treatment.

The functional groups of the carbon materials were investigated by FTIR (**Figure 4.6**). Two modes of T_{1u} (3) at 1181 cm^{-1} and T_{1u} (4) at 1427 cm^{-1} can be observed on C_{60} [33-34], corresponding to the tangential motion of the carbon atoms. It was also observed that fullerene has a stable carbon structure [35-36].

For SWCNTs, three main groups such as O-H group (hydroxyl) at 3336 cm^{-1}, C-H group (methyl) at 2911 cm^{-1}, and C=C group at 1575 cm^{-1} were appearing [37-38]. However, the C-H and O-H groups were absent after thermal annealing, which indicated the lack of hydrogen and oxygen groups due to thermal desorption. On the other hand, the aromatic group (C=C) at 1565 cm^{-1} remained with a decreased intensity.

Only C=C group at 1555 cm^{-1} can be observed on GNP, which was slightly shifted to 1562 cm^{-1} after thermal treatment. That suggested a very low oxygen content on GNP.

A few carbon groups, such as C-H groups at 2880 cm^{-1}, C=O group at 1700 cm^{-1}, C=C group at 1573 cm^{-1}, C-O group at 1428 cm^{-1} and 1135 cm^{-1} can be observed on CMK-3 [39]. After thermal treatment, the C=C group at 1562 cm^{-1} remained strong and other peaks became pale, due to the removal of hydrogen and oxygen groups [40-41]. Meanwhile, C=C group at 1559 cm^{-1} and C-O group at 1052 cm^{-1} can be seen on CMK-8, which showed slight changes to 1560 cm^{-1} and 1055 cm^{-1} after annealing.

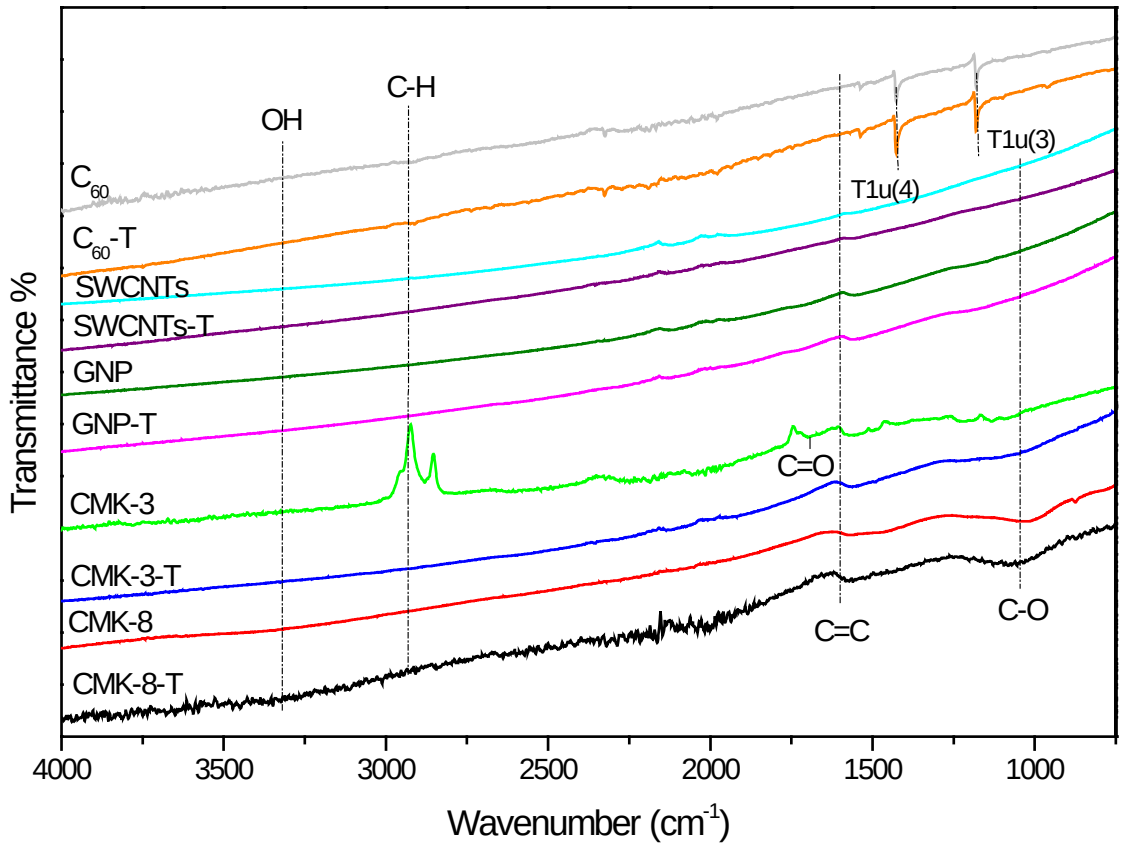

Figure 4.6. FTIR spectra of different nanocarbons before and after thermal treatment in nitrogen.

Figure 4.7 shows the thermal analysis results of the nanocarbon samples. It can be found that before 400 ^{o}C, all the raw carbon materials are stable in air. Therefore, thermal treatment at 350 ^{o}C in nitrogen would only modulate the functional groups without any significant combustion or decomposition.

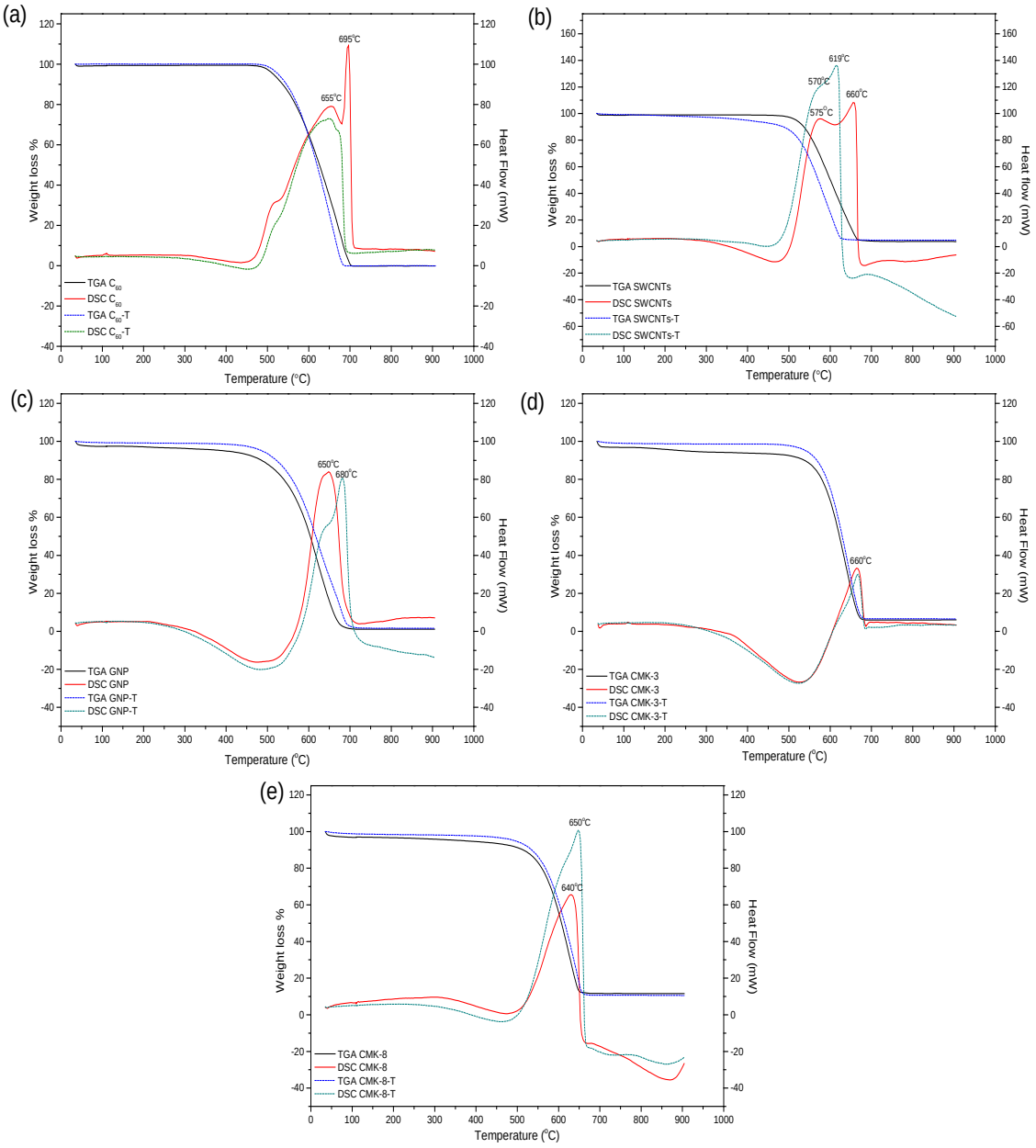

Figure 4.7. TGA/DSC curves of different nanocarbons.

Figure 4.8 shows XPS studies of different carbon nanomaterials. **Figure 4.8a** shows that C 1s and O 1s peaks are centred at 284.7 and 532.2 eV, respectively [42-44]. The changes in oxygen contents for different carbon nanomaterials before and after thermal treatment were tabulated in **Table 4.2**. The changes in oxygen contents would adjust the surface features of the nanocarbons and therefore influence the adsorption and catalytic behaviour.

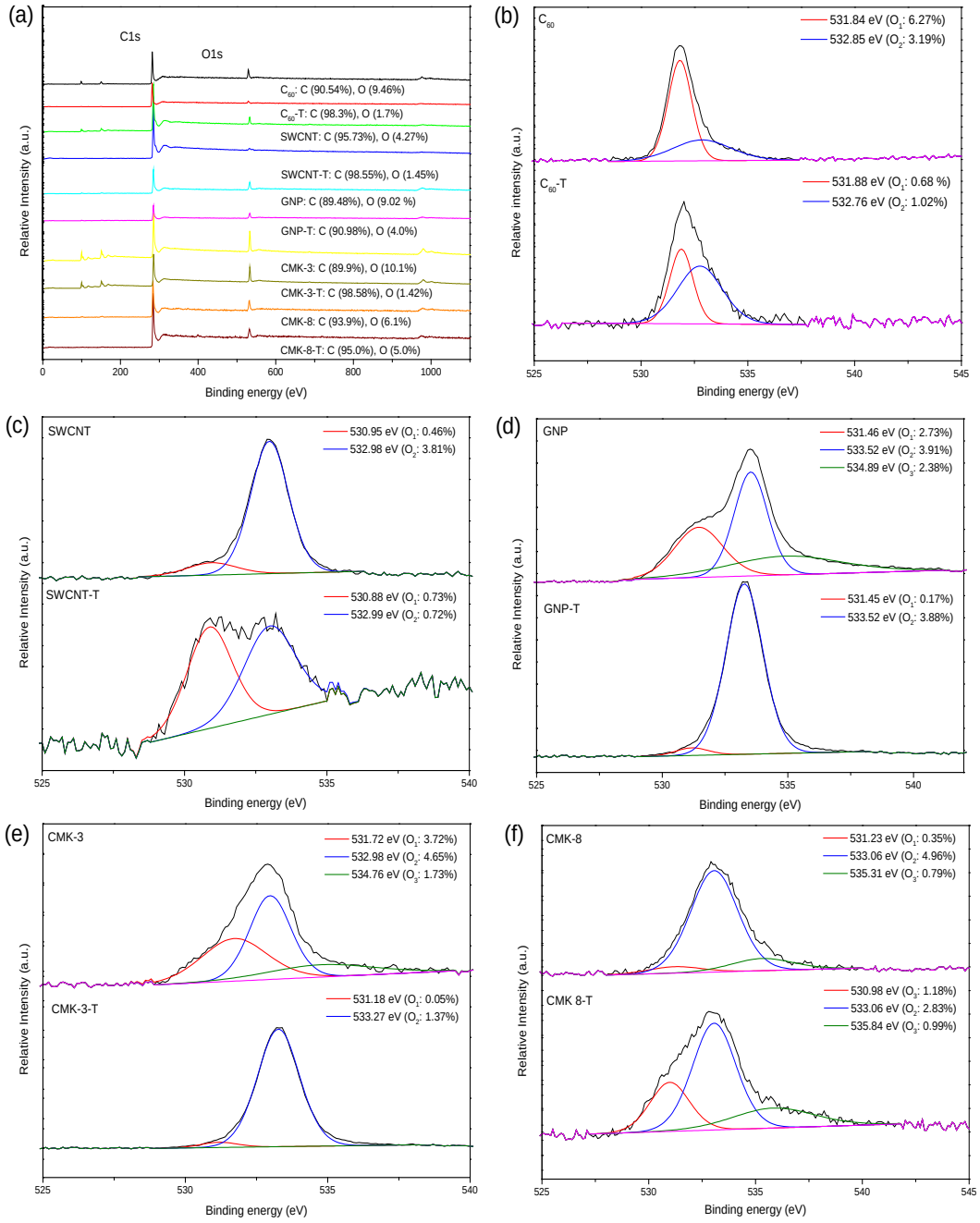

Figure 4.8. (a) XPS survey; O1s of (b) C_{60} and C_{60}-T, (c) SWCNT and SWCNT-T, (d) GNP and GNP-T, (e) CMK-3 and CMK-3-T, and (f) CMK-8 and CMK-8-T.

Figure 4.8b to f show high resolution XPS O 1s spectra of different carbon nanomaterials. Two types of oxygen species can be seen from the de-convolution of XPS O 1s spectra in C_{60}, C_{60}-T, SWCNT, SWCNT-T, GNP-T and CMK-3-T: O_1 (C=O) at 530.84 - 531.88 eV and O_2 (C-O-C) at 532.76-533.0 eV [42].

Three types of oxygen species can be seen from the de-convolution of XPS O 1s spectra in GNP, CMK-3, CMK-8 and CMK-8-T: O_1 (C=O) at 530.98-531.8 eV, O_2

(C-O-C) at 532.9-533.6 eV, and O_3 (chemisorbed oxygen and adsorbed water) at 534.7-535.84 eV [39, 43-45].

The O/C (oxygen versus carbon) ratios and levels of different oxygen-containing groups are listed in **Table 4.2**. The overall oxygen contents were decreased after thermal treatment in nitrogen. For the specific oxygen groups, such as C=O, C-O-C, and chemisorbed groups/water showed different trends after thermal treatment. And the oxygen levels of specific groups (such as C=O or chemisorbed groups/water) might increase due to the transformation of C-O-C/C-O-H. The changes of the contents of specific groups may also affect the catalytic performances of the carbon materials.

Table 4.2. Chemical compositions of different nanocarbons before and after oxidation reactions.

Sample	O level, at. %	O/C ratio	O_1, at. %,	O_2, at. %,	O_3, at. %,
C_{60}	9.46	0.104	6.27	3.19	-
C_{60}-T	1.70	0.017	0.68	1.02	-
SWCNT	4.27	0.045	0.46	3.81	-
SWCNT-T	1.45	0.015	0.73	0.72	-
GNP	9.02	0.101	2.73	3.91	2.38
GNP-T	4.00	0.044	0.17	3.88	-
CMK-3	10.1	0.112	3.72	4.65	1.73
CMK-3-T	1.42	0.014	0.05	1.37	-
CMK-8	6.10	0.065	0.35	4.96	0.79
CMK-8-T	5.00	0.053	1.18	2.83	0.99
Used SWCNT (2^{nd} run)	2.3	0.024	0.43	1.87	-
Used SWCNT (3^{rd} run)	6.72	0.072	1.39	5.33	-
Used CMK-8 (2^{nd} run)	12	0.14	1.28	6.91	3.82
Used CMK-8 (3^{rd} run)	13.14	0.15	2.78	6.06	4.3

Figure 4.9 shows the de-convolution XPS C1s spectra of different carbon nanomaterials.

A broad C1s peak can be divided into four sections indicating four different C species for C_{60} and C_{60}-T in the range of 284 – 291 eV. For C_{60} and C_{60}-T, C=C, C-O-C/ C-O-H, COOH bond and π-π* shake up occurred at 284.5, 285.5, 288.5 and 290.3 eV, respectively [43-44].

A broad C1s peak indicated three different C species on SWCNT and SWCNT-T in the range of 284 – 289 eV: C=C, C-O-C, and COOH bond occurred at 284.5, 285.1 and 288.7 eV, respectively.

A broad C1s peak indicated four different C species for GNP and GNP-T in the range of 284 – 291 eV: C=C, C-O-C, C=O and π-π* shake up bond occurred at 284.6, 285.4, 286.8 and 290.2 eV, respectively.

A broad C1s peak indicated three different C species for CMK-3 and CMK-3-T in the range of 284 – 291 eV: C=C, C-O-C and π-π* shake up occurred at 284.3, 285.3 and 289 eV, respectively.

A broad C1s peak indicated five different C species for CMK-8 and CMK-8-T in the range of 284 – 291 eV. For CMK-8 and CMK-8-T, C=C, C-O-C, C=O, COOH bond and π- π* shake up occurred at 284.5, 285.5, 286.6, 288.3, and 290.4 eV, respectively [39, 45]. The results confirmed the different oxygen functional groups on the surfaces of the nanocarbons.

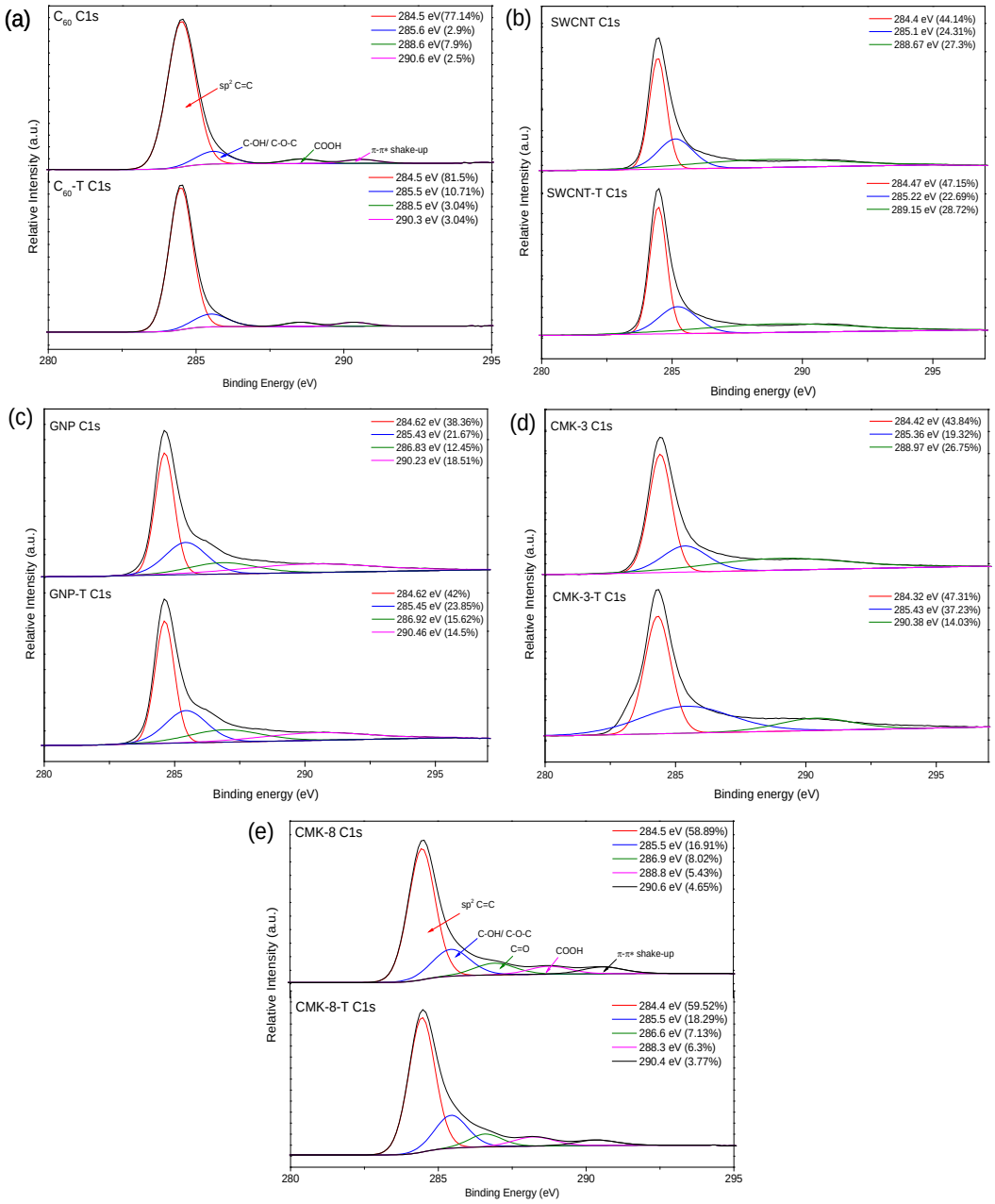

Figure 4.9. (a) XPS C1s spectra of (a) C_{60} and C_{60}-T (b) SWCNT and SWCNT-T, (c) GNP and GNP-T, (d) CMK-3 and CMK-3-T, and (e) CMK-8 and CMK-8-T.

4.3.2. Adsorption performance of nanocarbons

Figure 4.10a shows dynamic phenol adsorption profiles on different unmodified carbons.

All carbons exhibited fast adsorption and reached equilibrium quickly in 40 min. In 180 min, around 10% phenol was removed by C_{60}. Ballesteros et al. [46] also observed

the poor adsorption of phenol on fullerene, which was attributed to the inferior interactions of C_{60} and polar functional groups of phenol.

SWCNTs had a better adsorptive performance than C_{60}, providing around 20% phenol adsorption in 180 min. It was reported that carbon nanotubes are made of cylindrical graphitic sheets, which are of super hydrophobicity and very large van der Waals index, and that they have sp^2-hybridized carbon atoms with high electronic polarizability showing significant interaction with aromatic compounds via π-π coupling/stacking [47].

GNP had a lower SSA than SWCNTs, while it showed a much better adsorption at around 40% phenol removal in 180 min.

The phenol adsorption of GNP was much higher than reported rGO samples [11, 22]. The π-π bonds and flat structure of graphene might significantly contribute to the better adsorptive performance of GNP [13].

For the two mesoporous carbons, CMK-3 showed comparable adsorption to GNP, and higher than CMK-8. Their adsorption was attributed to the much high SSAs.

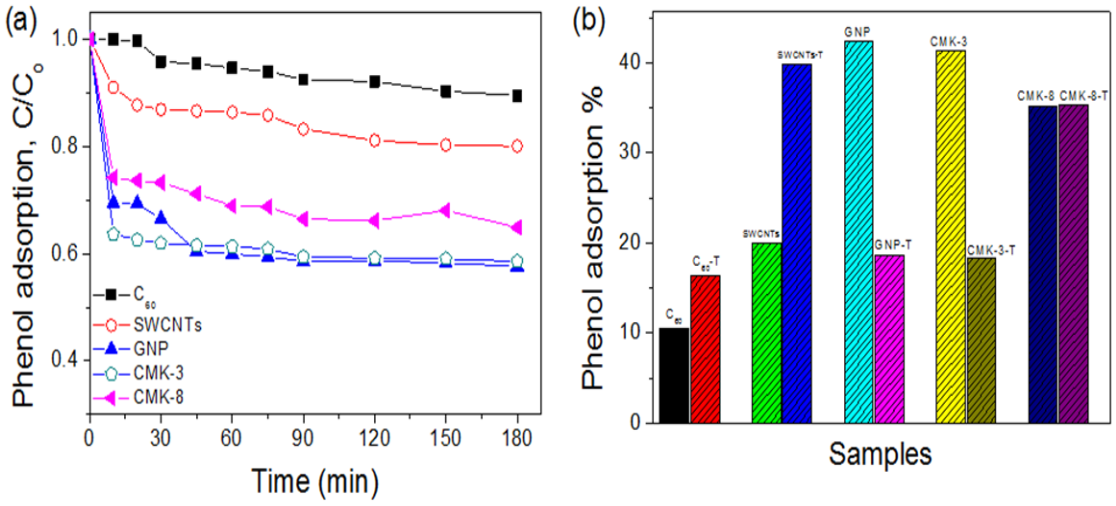

Figure 4.10. (a) Adsorption of phenol on different pristine carbon nanomaterials, and (b) effect of thermal treatment in nitrogen on phenol adsorption in 180 min.

The effect of thermal treatment on phenol adsorption is shown in **Figure 4.10b**, in which phenol adsorption at 180 min on the materials before and after thermal treatment was compared. Enhanced adsorption was observed for C_{60} and SWCNTs

after thermal treatment and phenol removal was increased from 10.5% and 20% to 16.3% and 39.8%, respectively.

Significant decline in phenol adsorption was observed on GNP and CMK-3 after thermal treatment, which showed decreased phenol removal from 42.4% and 41.4% to 18.6% and 18.4%, respectively.

On the other hand, adsorption of CMK-8 was remained almost unchanged after thermal treatment. Thermal treatment in nitrogen slightly increased SSA and removed the surface oxygen groups. The varied effect of thermal treatment on adsorption was due to the different adsorption mechanisms on different carbon materials.

Phenol adsorption on carbon materials has been generally classified as physisorption and chemisorption [48]. Physisorption of phenol depends strictly on the porosity (surface geometrical heterogeneity), whereas chemisorption depends on the availability of the basal planes (surface chemical heterogeneity). The presence of surface oxygen sites on carbon surface was suggested to have a capacity of chemisorption for binding phenol [49]. Three possible interactions between phenol and carbon surfaces were proposed: (a) a donor-acceptor complex interaction between the negatively charged aromatic ring of phenol and the positively charged basal plane of carbon containing oxygen functional groups [50], (b) a dispersive interaction between the phenol aromatic rings and the π-electrons of the graphitic carbon basal planes [51] and, (c) an electrostatic attraction and repulsion when ions are present [52]. In general, the practical phenol adsorption on the nanocarbons was a result of combined interactions as indicated above.

For pristine nanomaterials in this study, the adsorption performance at 180 min shows GNP (2D with SSA of 103 m^2/g) ~ CMK-3 (3D with SSA of 1129 m^2/g) > CMK-8 (3D with SSA of 1040 m^2/g) > SWCNTs (1D with SSA of 366 m^2/g) > C_{60} (0D with SSA of 5 m^2/g).

After thermal annealing at 350 °C, the adsorption performance at 180 min shows SWCNTs-T (1D with SSA of 442 m^2/g) > CMK-8-T (3D with SSA of 1167 m^2/g) > GNP-T (2D with SSA of 129 m^2/g) ~ CMK-3-T (3D with SSA of 1246 m^2/g) > C_{60}-T (0D with SSA of 6 m^2/g).

It appeared that phenol adsorption and dimensional structure of carbons are not in the same order. However, 2D and 3D nanocarbons show higher adsorption than 1D and 0D nanocarbons due to more porous structure for physisorption and the presence of edge defects with certain oxygen functional groups for chemisorption. After thermal treatment by removal of oxygen functional groups, phenol adsorption will be affected depending on structural dimension. Phenol adsorption will be enhanced on 0D and 1D, while phenol adsorption will be reduced for 2D and 3D nanocarbons. This suggest that phenol adsorption via sp^2 hybridized structure with porosity will play a significant role to enhance physisorption and that oxygen functional groups on the nanocarbon edge defects will influence carbon surface polarity to interact with phenol for chemisorption process. In this study, the chemisorption process for phenol adsorption may be due to the donor-acceptor complex interaction and the dispersive interaction without any preference.

C_{60} and C_{60}-T showed low adsorption capacity of phenol, which might be due to the low SSA for physisorption with very little contribution of chemisorption because of the minor edge defects. The improvement of phenol adsorption after thermal annealing was mainly due to the increased SSA.

SWCNT and SWCNT-T show better phenol adsorption compared to C_{60} and C_{60}-T, due to the increase of SSA value and increase of mesopore content for physisorption with porosity pore size (8.7-8.8 nm) along with the moderate contribution of chemisorption because of edge defects (I_D/I_G = 0.46 and 0.43) with certain oxygen functional groups. After thermal annealing and the decomposition of certain oxygen functional groups, SWCNT-T showed an increase of phenol adsorption owing to the enhanced physisorption.

GNP showed the best phenol adsorption, which was mainly due to the dominant chemisorption because of the presence of edge defects (I_D/I_G = 1.28) with certain oxygen functional groups along with the moderate physisorption (SSA= 103 m^2/g) by porosity of pore size 13.5 nm. After thermal annealing, the phenol adsorption of GNP-T decreased significantly due to the lowered chemisorption because of the decomposition of certain oxygen functional groups.

CMK-3 showed the second best phenol adsorption that might be due to the

significant chemisorption from the presence of edge defects (I_D/I_G = 1.17) with certain oxygen functional groups. After thermal annealing, the phenol adsorption of CMK-3-T significantly decreased due to the decomposition of certain oxygen functional groups.

CMK-8 showed the third best phenol adsorption. After thermal annealing, CMK-8-T showed almost similar phenol adsorption because the insignificant decrease of oxygen concentrations from 6.1% to 5% for chemisorption was compensated by the increase of SSA value from 1040 to 1167 m^2/g for physisorption.

Phenols have weak acidic properties and are preferable to be adsorbed on the basic surface. Some of the oxygen groups, such as carbonyl, carboxyl, phenolic hydroxyl and lactonic are acidic, while some groups, for example, pyrone, chromene and quinone are basic [48-49]. The points of zero charge of the carbon materials were evaluated to investigate the surface charges. The PZCs of C_{60} (C_{60}-T), GNP (GNP-T), SWCNT (SWCNT-T), CMK-3 (CMK-3-T), and CMK-8 (CMK-8-T) were determined to be 5.06 (5.33), 2.21 (2.41), 4.97 (4.29), 5.33 (5.10), and 4.08 (3.92), respectively. There was no direct correlation between PZCs and phenol adsorption that can be made for the pristine carbon materials. However, the changes of increased or decreased phenol adsorption after thermal treatments were consistent to the increased or decreased PZCs. The PZC changes were ascribed to the decomposition and evolution of oxygen groups before and after thermal treatment. Therefore, the almost unchanged phenol adsorption on CMK-8 and CMK-8-T could be explained by the minor effect on oxygen levels by the thermal treatment.

4.3.3. Catalytic oxidation performance of phenol

Figure 4.11a shows the catalytic oxidation of phenol on different carbons by activation of PMS. For C_{60}, 15% phenol removal was rapidly achieved in 5 min, and then further 7% phenol removal occurred very slowly in 240 min. The phenol removal profile indicated an adsorption characteristic rather than effective catalysis.

Continuous and effective phenol degradation was observed on SWCNTs, and around 100% phenol removal was achieved in 90 min. The efficient PMS activation on

multi-walled carbon nanotubes was reported recently, showing around 65% phenol removal in 90 min [21], and a lower activity than SWCNTs in this study.

On GNP, continuous phenol degradation was found in first 120 min providing around 50% phenol removal, and then the removal curve became flat. As GNP showed around 40% phenol removal in adsorption tests, the catalysis on GNP was not effective. The catalysis on GNP was not as good as rGO [4, 11, 20, 22], which might be due to the different functional groups and defective structures.

For the first time, this study observed the effective catalytic activation of PMS on CMK-3 and CMK-8. Complete phenol removal was achieved in 40 min on 3D hexagonally-ordered mesoporous carbon (CMK-3), while the reaction time for complete phenol decomposition was 210 min on cubically ordered **mesoporous carbon** (CMK-8). It has been reported that an activated carbon shows a similar activity [53].

A first-order kinetics was used to evaluate the rate constants in phenol degradation on the carbons. **Figure 4.11b** shows the rate constants before and after thermal treatments. For pristine samples, the rate constants followed an order of CMK-3 > SWCNTs > CMK-8 > C_{60} ~ GNP. A varied effect of thermal treatment on catalysis of nanocarbons was also observed.

Significant enhanced catalysis was achieved on C_{60}-T, GNP-T and CMK-8-T, but decreased catalysis was found on SWCNTs-T and CMK-3-T. It was very interesting to find that a 7.5-fold enhancement was found on CMK-8 after thermal treatment. As indicated before, the adsorption and SSA were not changed much after thermal treatment. XPS suggested that C=O groups was increased from 0.35 at.% to 1.18 at.%. In previous studies [11, 20, 22], the C=O was proposed to be one of the active sites for PMS activation. Yet such a case was not applied to C_{60}, due to the much high oxygen species, which is similar to GO [11]. However, a decrease in C=O groups was observed on CMK-3 and CMK-3-T from 3.72 at.% to 0.05 at.%. This was one of the reasons for the decreased phenol degradation on CMK-3 after thermal treatment, apart from the significant drop of adsorption ability.

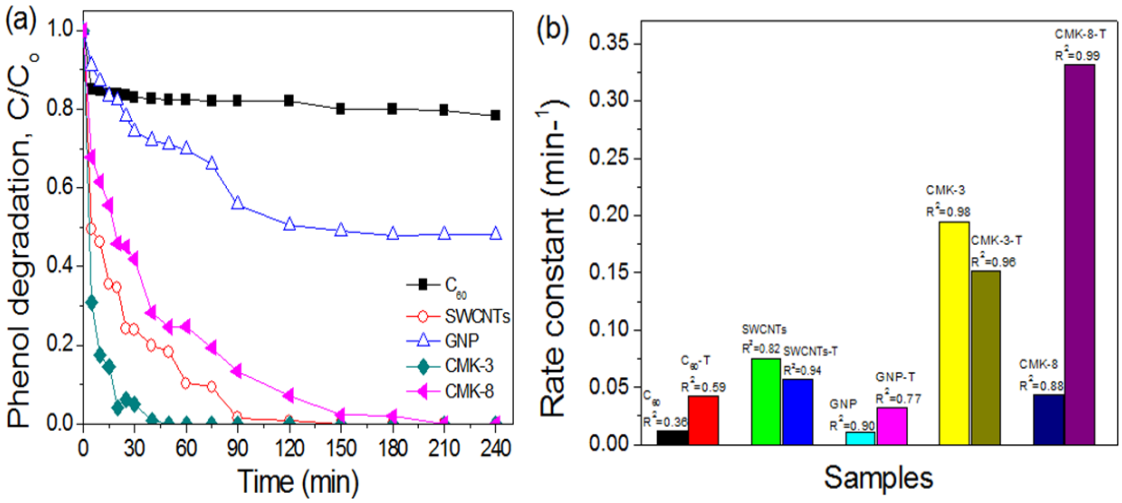

Figure 4.11. (a) Catalytic degradation of phenol on pristine carbons, and (b) rate constants of phenol degradation on carbons before and after thermal treatment.

In general, thermal annealing at 350°C has the effect of the restoration of the pristine nanocarbon surfaces through the elimination of oxygen functional groups, increasing SSA values [4, 13, 20] and improving the performance of phenol degradation of 0D fullerene (C_{60}), and 1D SWCNTs. The catalytic phenol removal at 60 min for the 0D (C_{60}) increased from 17% to 52% after thermal annealing. This might be due to the restoration of C_{60} structure which resulted in a lower oxygen content and a higher conductivity [54].

For 1D SWCNTs and SWCNTs-T, the phenol removals by catalytic oxidation at 60 min were 90% and 97%, respectively. In comparison with C_{60}, the better performance of 1D SWCNTs can be attributed to the presence of edge defects (zigzag or armchair) as indicated by the I_D/I_G ratios (0.46-0.43) and the contribution of rather high SSAs (366 and 442 m^2/g) [30, 55].

For 2D GNP, phenol oxidation at 60 min increased from 30% to 62 % after thermal annealing. This improvement might also be due to the restoration of GNP structure which led to a lower oxygen content and a higher conductivity, the presence of edge defects and a slight increase of SSA values from 103 to 128 m^2/g [4, 20]. In comparison with the 1D SWCNTs, a lower phenol catalytic oxidation can be ascribed to their lower SSA.

For 3D CMK-3 and CMK-3-T, phenol removals by catalytic oxidation at 60 min were 100%. It was suggested that 3D hexagonally-ordered mesoporous structure has

provided sufficient edged defects with the contribution of high SSA of 1129 m^2/g even in the pristine condition [24, 56].

For the 3D CMK-8 and CMK-8-T, catalytic oxidation of phenol at 60 min was 76% and 100%, respectively. The enhancement was possibly attributed to the restoration of CMK-8 surface resulting in a lower oxygen content and a higher conductivity (which increases the electron transfer between carbon and PMS for a fast activation), and the presence of edge defects [31, 57].

Further first-order kinetics was used to evaluate the rate constants in phenol degradation on SWCNT and CMK-8. **Figure 4.12** shows the rate constants and phenol catalytic oxidation on SWCNT and CMK-8, with 20, 30 and 50 ppm as the initial phenol concentration. The higher the initial phenol concentration, the lower the efficiency of the phenol degradation, as shown in **Figure 4.12a and b**.

Figure 4.12c and d show that the reaction rate constants decreased from 0.038 (20 ppm) to 0.0068 (30 ppm) and 0.0035 min^{-1} (50 ppm) for SWCNT; and from 0.0213 (20 ppm) to 0.0115 (30 ppm) and 0.003 min^{-1} (50 ppm) for CMK-8, respectively.

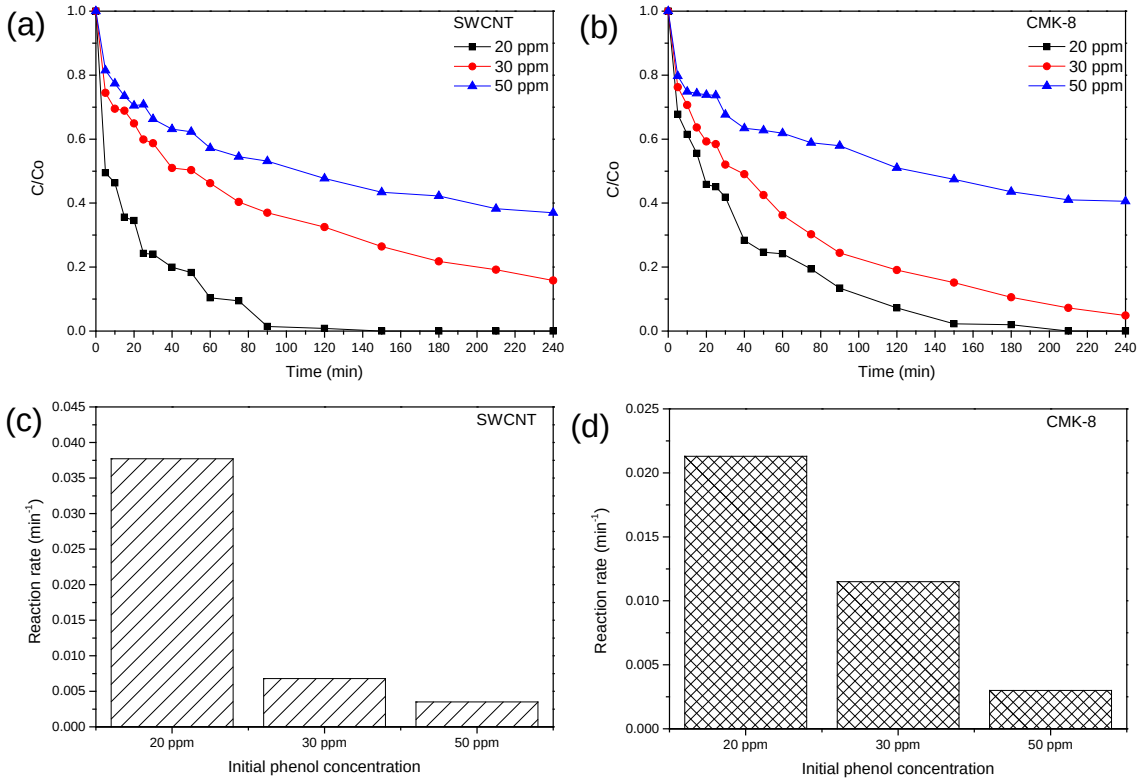

Figure 4.12. Effects of initial concentration and rate constants for phenol degradation on (a, c) SWCNT, and (b, d) CMK-8.

Total organic carbon (TOC) after catalytic phenol oxidation for 180 min on different nanocarbons was measured. In general, TOC removal was slower than phenol degradation. It was found that CMK-3 was able to reduce 50.5% of TOC. Other TOC removals were determined to be 18.1%, 19.5%, 3.8% and 26.7% on CMK-8, GNP, C_{60}, and SWCNT, respectively.

One of the metal-free nanocarbons, CMK-3-T, was employed to check the catalyst stability, as shown in **Figure 4.13**. It was seen that in the second run, 80% phenol removal was achieved within 240 min. In the third run, CMK-3-T was no longer efficient in catalytic oxidation which only removed phenol about 20% in 240 min. The poor catalytic stability of nanocarbons still needs improvement in future studies [11, 21, 58].

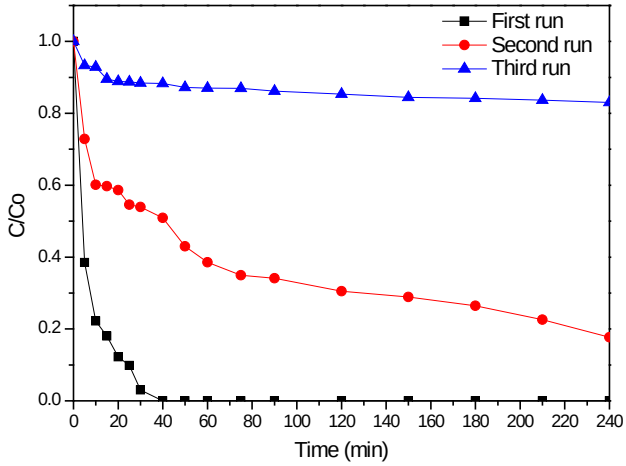

Figure 4.13. Stability tests of CMK-3-T for phenol oxidation

Figure 4.14 shows the XPS analysis of the used catalysts. **Figure 4.14b and c** show high resolution XPS O 1s spectra of used SWCNT and CMK-8. Two types of oxygen species can be seen from the de-convolution of XPS O 1s spectra in used SWCNT (2^{nd} and 3^{rd} run): O_1 (C=O) at 530.88 and 531.5 eV and O_2 (C-O-C) at 533.0 and 533.28 eV.

Three types of oxygen species can be identified from the de-convolution of XPS O 1s spectra in used CMK-8 (2^{nd} and 3^{rd} run): O_1 (C=O) at 531.43 and 531.72 eV, O_2 (C-O-C) at 533.06 and 533.25 eV, and O_3 (chemisorbed oxygen and adsorbed water) at 536 and 535.5 eV. The O/C (oxygen versus carbon) ratios and levels of different oxygen-containing groups are listed in Table 2.

The overall oxygen contents for SWCNT (4.27%) were decreased to 2.3% after undergoing 240 min oxidation reaction (2nd run) and were increased to 6.72% after the 3rd run. The overall oxygen contents for CMK-8 (6.1%) were increased to 12% after undergoing 240 min oxidation reaction (2nd run) and were increased to 13.14% after the 3rd run.

Figure 4.14d and e show the de-convolution XPS C1s spectra of used SWCNT and CMK-8. Changes related to oxygen functional groups were also observed.

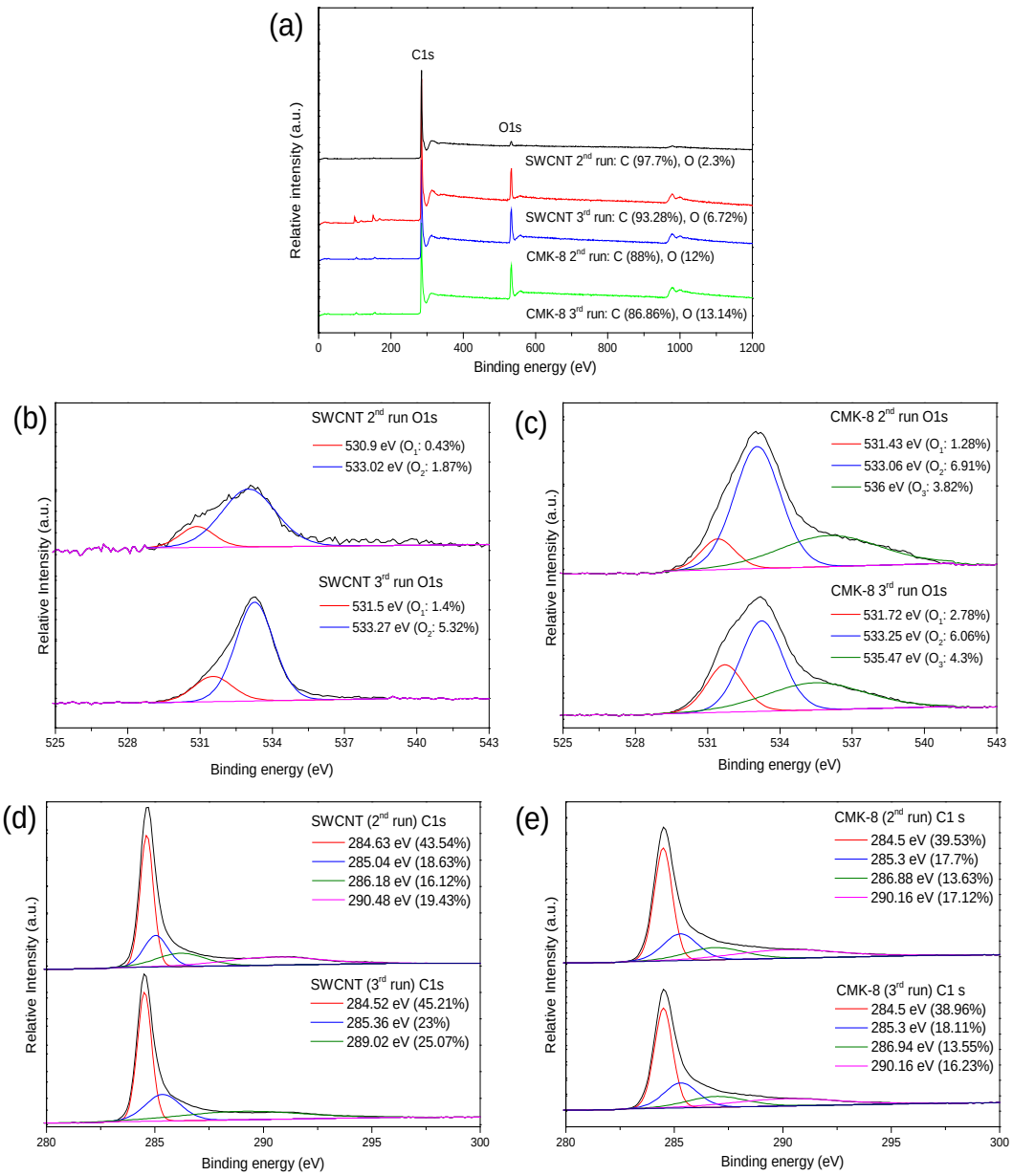

Figure 4.14. (a) XPS survey, O1s of (b) used SWCNT, (c) used CMK-8; and C1s of (d) used SWCNT, (e) used CMK-8.

4.3.4. Mechanism of PMS activation and phenol oxidation

It was discovered that PMS can be activated by either metal-based or metal-free catalysts to generate both hydroxyl radicals ($^{\bullet}OH$) and sulfate radicals ($SO_4^{\bullet-}$) [19, 21]. Electron paramagnetic resonance (EPR) spectroscopy can be used to monitor the generation and evolution of the reactive radicals by catalytic activation of PMS [58-60]. In this study, the time-dependent evolutions of hydroxyl and sulfate radicals were monitored by EPR. The results obtained from the two efficient catalysts of SWCNT and CMK-8 and their derivatives were shown in **Figure 4.15**.

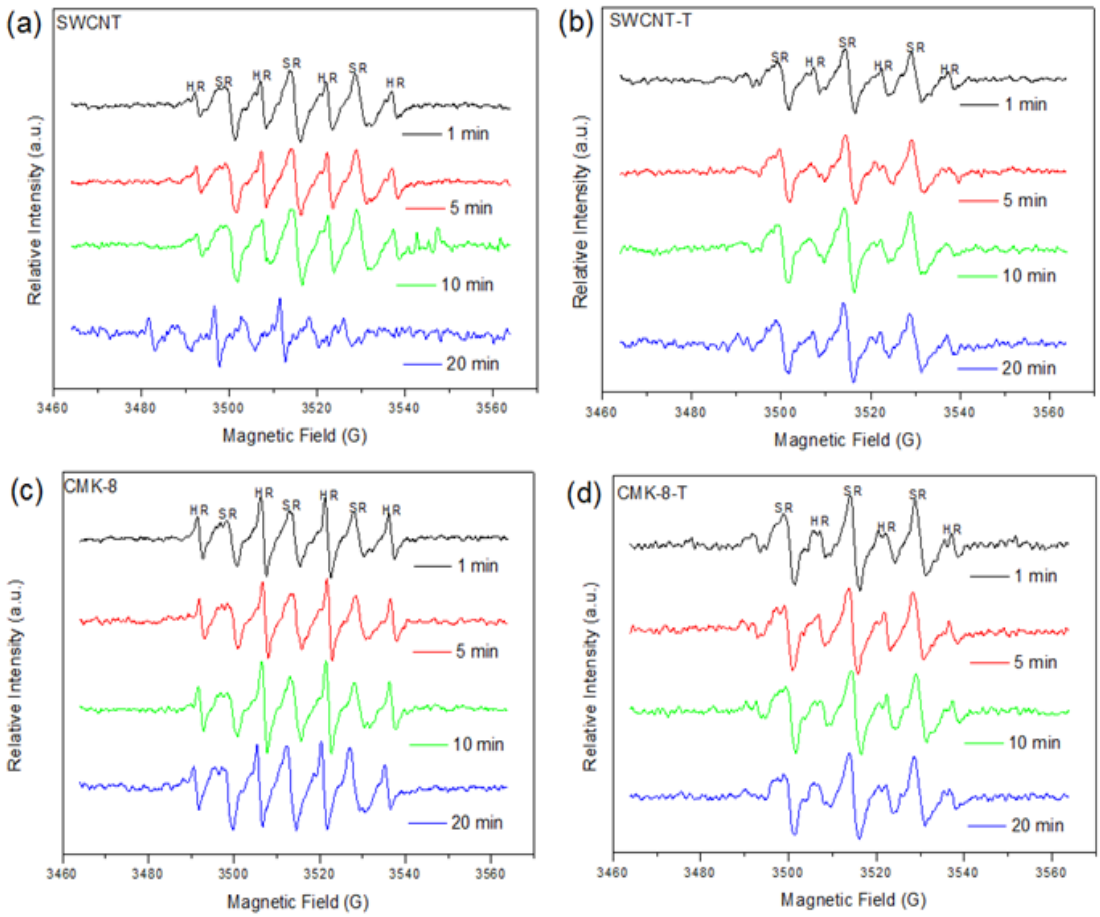

Figure 4.15. EPR spectra of time-dependent generation and evolution of reactive radicals on (a) SWCNT, (b) SWCNT-T, (c) CMK-8, and (d) CMK-8-T. HR: hydroxyl radicals; SR: sulfate radicals.

EPR spectra from other carbon materials can be found in **Figure 4.16**. It can be seen that both hydroxyl radicals ($^{\bullet}OH$) and sulfate radicals ($SO_4^{\bullet-}$) were present in the

catalytic oxidation processes. Then the roles of the reactive radicals were further studied by competitive radical tests.

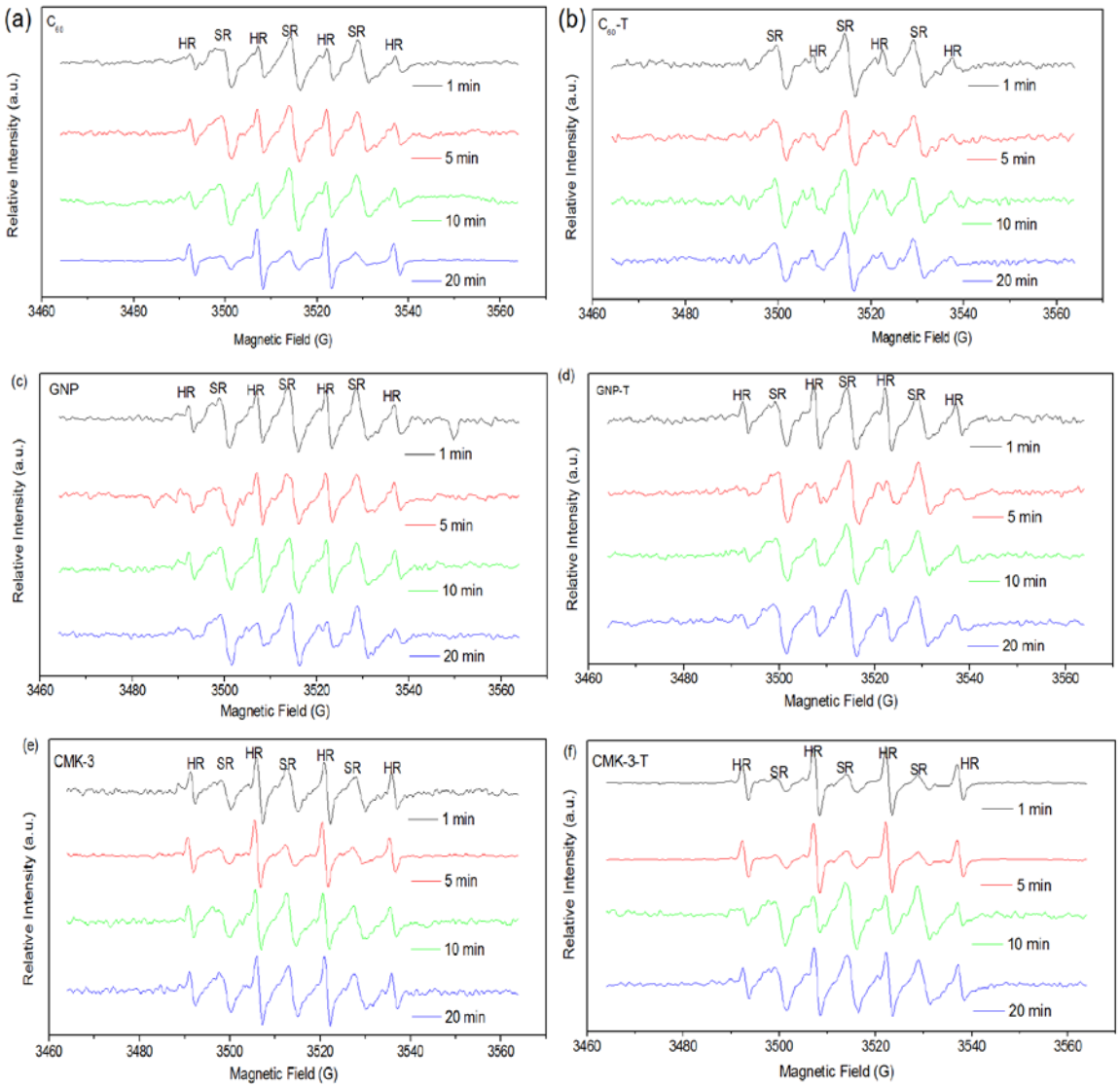

Figure 4.16. ERP spectra of generation and evolution of reactive radicals on (a) C_{60}, (b) C_{60}-T, (c) GNP, (d) GNP-T, (e) CMK-3 and (f) CMK-3-T. HR: hydroxyl radicals; SR: sulfate radicals.

It was known that $^{\bullet}OH$ and $SO_4^{\bullet-}$ radicals show different reaction rates with two radical scavengers, ethanol (EtOH) and tert-butyl alcohol (TBA). The quenching agent of EtOH can capture both $^{\bullet}OH$ and $SO_4^{\bullet-}$ while TBA prefers capturing $^{\bullet}OH$ radicals rather than $SO_4^{\bullet-}$ radicals [58].

Figure 4.17 displays the changes of reactive radicals generated by SWCNT and CMK-8 activation of PMS with different quenching reagents. Both radicals and their changes upon addition of classical quenching reagents were identified.

The associated EPR spectra are shown in **Figure 4.18**. Without the scavengers, the DMPO-OH intensities remained stable (SWCNT and CMK-8 DMPO-OH curves) within first 5 min and decreased afterwards. The DMPO-SO_4 intensities remained stable at a low level, which might be due to the great consumption of sulfate radicals in phenol oxidation. In the presence of EtOH, DMPO-OH intensities reduced and the peak occurred at 5 min. Meanwhile, in the presence of TBA, DMPO-OH intensities were similar to that with the presence of EtOH. However, DMPO-SO_4 intensities did not show much difference with or without the scavengers. The above results suggest that both radicals are important for phenol degradation.

With the combination of EPR studies and classical quenching tests, $^{\bullet}OH$ and $SO_4^{\bullet-}$ radicals were confirmed to be present in PMS activation for phenol oxidation on different carbon nanomaterials. The electron transfer processes facilitated by carbon catalysis for phenol degradation can be described in below reactions [58].

$$HSO_5^- + e^- \rightarrow {}^{\bullet}OH + SO_4^{2-} \quad (4.1)$$

$$HSO_5^- + e^- \rightarrow SO_4^{\bullet-} + OH^- \quad (4.2)$$

$$HSO_5^- - e^- \rightarrow SO_5^{\bullet-} + H^+ \quad (4.3)$$

$${}^{\bullet}OH + SO_4^{2-} \rightarrow SO_4^{\bullet-} + OH^- \quad (4.4)$$

$$SO_4^{\bullet-} + OH^- \rightarrow SO_4^{2-} + {}^{\bullet}OH \quad (4.5)$$

$$\text{Phenol} + SO_4^{\bullet-} ({}^{\bullet}OH) \rightarrow \text{several steps} \rightarrow CO_2 + H_2O + SO_4^{2-} \quad (4.6)$$

The different phenol degradation efficiencies were suggested to be controlled by the above processes, which were indeed determined by the nature of the carbon catalysts, for example, the electron transfer rate, the selective production of the reactive radicals, and the ability for carrying out surface reactions.

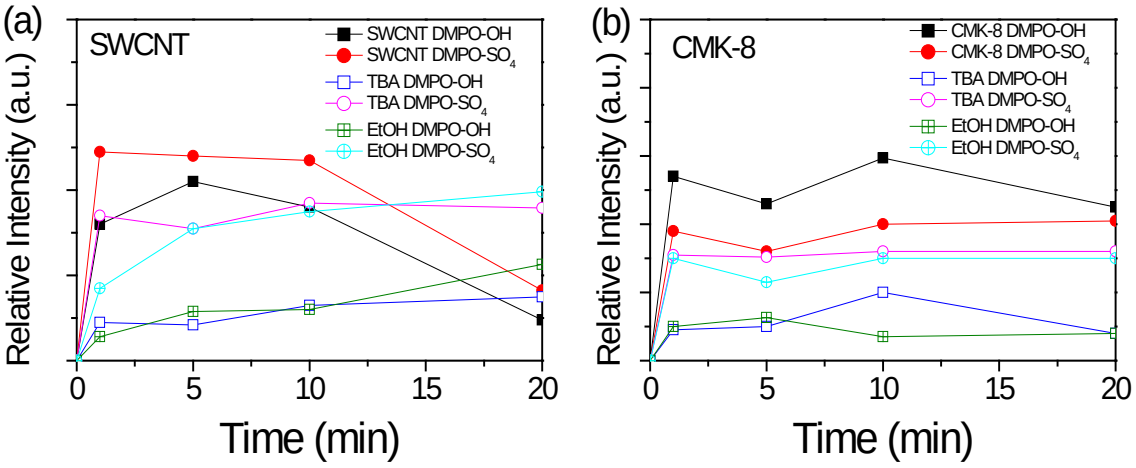

Figure 4.17. Time-dependent evolutions of reactive radicals on (a) SWCNT and (b) CMK-8 with addition of quenching reagents. TAB: tert-butanol; EtOH: ethanol.

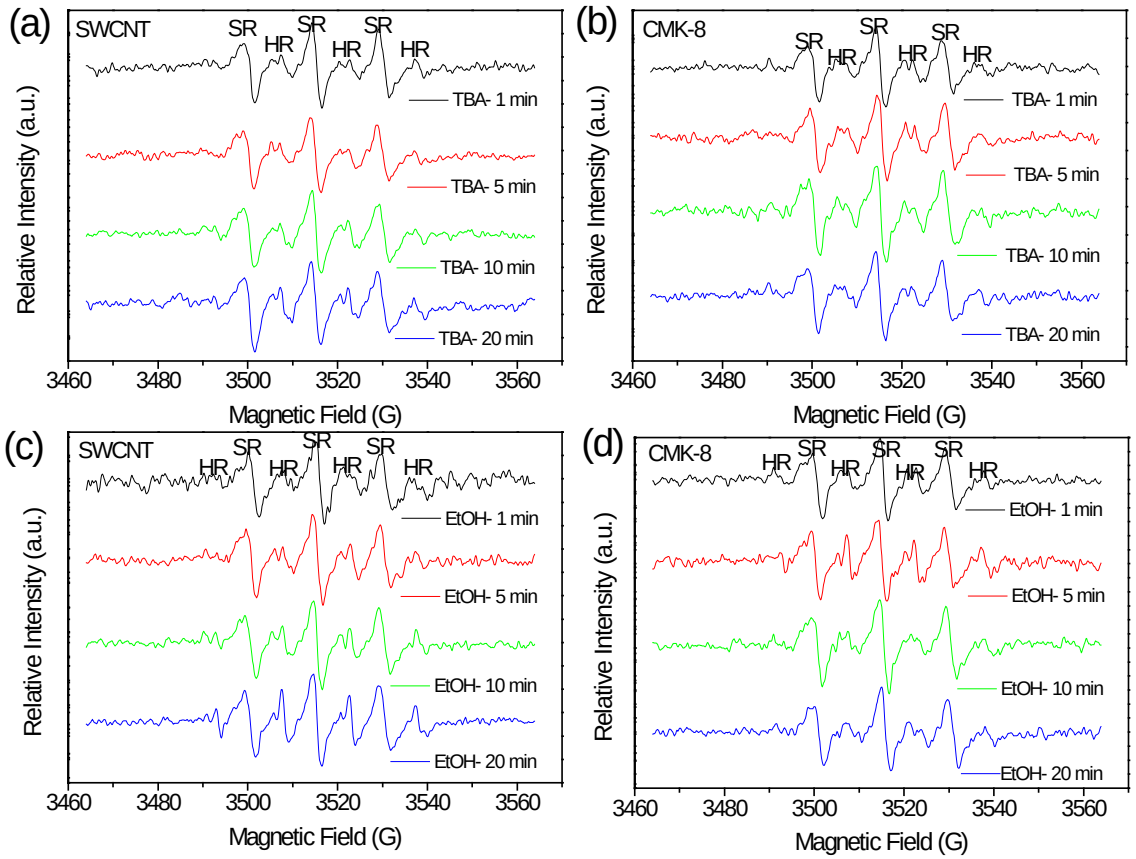

Figure 4.18. EPR spectra of reactive radicals on SWCNT and CMK-8 with addition of quenching reagents. TBA: ter-butanol; EtOH: ethanol. HR: hydroxyl radicals; SR: sulfate radicals.

4.4. Conclusions

In conclusion, properties of carbon nanomaterials in different structural dimensions (0-3D) before and after thermal annealing employing nitrogen gas at 350 °C were investigated and used for phenol adsorption and metal-free catalytic oxidation. The materials are C_{60}, SWCNTs (single wall carbon nanotubes), GNP (graphene nanoplate), CMK-3 and CMK-8 (ordered mesoporous carbon). Pristine nanocarbons showed varied phenol adsorption and the adsorptive performances followed the order of GNP ~ CMK-3 > CMK-8 > SWCNTs > C_{60}, while the catalysis followed another order of CMK-3 > SWCNTs > CMK-8 > GNP > C_{60}. Thermal treatment at a lower temperature would not significantly change the SSA and crystal structure but could dramatically modify the surface functional groups. As a result, enhanced adsorption was found on SWCNTs by 2-fold and superior catalysis was achieved on CMK-8 by 7.5-fold after thermal treatment. Structural dimension can influence nanocarbon performance in adsorption and catalysis and surface oxygen functionality can also affect the adsorption and catalysis. 0D C_{60} exhibited the lowest adsorption capacity and catalytic activity while 3D CMK-3 generally presented higher adsorption capacity and catalytic activity than 1D SWCNT and 2D GNP. The adsorption and catalysis were controlled by the integrated effects of structure, surface and chemical composition of the different nanocarbons.

References

1. Liang, H. W.; Ting, Y. Y.; Sun, H. Q.; Ang, H. M.; Tade, M. O.; Wang, S. B., Solution combustion synthesis of Co oxide-based catalysts for phenol degradation in aqueous solution. *Journal of Colloid and Interface Science* **2012,** *372*, 58-62.
2. Gadd, G. M., Biosorption: critical review of scientific rationale, environmental importance and significance for pollution treatment. *Journal of Chemical Technology and Biotechnology* **2009,** *84* (1), 13-28.
3. Shukla, P. R.; Wang, S. B.; Sun, H. Q.; Ang, H. M.; Tade, M., Activated carbon supported cobalt catalysts for advanced oxidation of organic contaminants in aqueous solution. *Applied Catalysis B-Environmental* **2010,** *100* (3-4), 529-534.
4. Peng, W. C.; Liu, S. Z.; Sun, H. Q.; Yao, Y. J.; Zhi, L. J.; Wang, S. B., Synthesis of porous reduced graphene oxide as metal-free carbon for adsorption and

catalytic oxidation of organics in water. *Journal of Materials Chemistry A* **2013,** *1* (19), 5854-5859.

5. Liang, C. D.; Li, Z. J.; Dai, S., Mesoporous carbon materials: Synthesis and modification. *Angewandte Chemie-International Edition* **2008,** *47* (20), 3696-3717.

6. Haque, E.; Khan, N. A.; Talapaneni, S. N.; Vinu, A.; Jegal, J.; Jhung, S. H., Adsorption of Phenol on Mesoporous Carbon CMK-3: Effect of Textural Properties. *Bulletin of the Korean Chemical Society* **2010,** *31* (6), 1638-1642.

7. Saputra, E.; Muhammad, S.; Sun, H. Q.; Ang, H. M.; Tade, M. O.; Wang, S. B., Shape-controlled activation of peroxymonosulfate by single crystal alpha-Mn2O3 for catalytic phenol degradation in aqueous solution. *Appl. Catal. B-Environ.* **2014,** *154*, 246-251.

8. Sun, H. Q.; Zhou, G. L.; Liu, S. Z.; Ang, H. M.; Tade, M. O.; Wang, S. B., Visible light responsive titania photocatalysts codoped by nitrogen and metal (Fe, Ni, Ag, or Pt) for remediation of aqueous pollutants. *Chemical Engineering Journal* **2013,** *231*, 18-25.

9. Saputra, E.; Muhammad, S.; Sun, H. Q.; Ang, H. M.; Tade, M. O.; Wang, S. B., Different Crystallographic One-dimensional MnO2 Nanomaterials and Their Superior Performance in Catalytic Phenol Degradation. *Environ. Sci. Technol.* **2013,** *47* (11), 5882-5887.

10. Zhou, G. L.; Tian, H. Y.; Sun, H. Q.; Wang, S. B.; Buckley, C. E., Synthesis of carbon xerogels at varying sol-gel pHs, dye adsorption and chemical regeneration. *Chemical Engineering Journal* **2011,** *171* (3), 1399-1405.

11. Sun, H. Q.; Liu, S. Z.; Zhou, G. L.; Ang, H. M.; Tade, M. O.; Wang, S. B., Reduced Graphene Oxide for Catalytic Oxidation of Aqueous Organic Pollutants. *Acs Applied Materials & Interfaces* **2012,** *4* (10), 5466-5471.

12. Yang, Y. X.; Chiang, K.; Burke, N., Porous carbon-supported catalysts for energy and environmental applications: A short review. *Catalysis Today* **2011,** *178* (1), 197-205.

13. Wang, S. B.; Sun, H. Q.; Ang, H. M.; Tade, M. O., Adsorptive remediation of environmental pollutants using novel graphene-based nanomaterials. *Chemical Engineering Journal* **2013,** *226*, 336-347.

14. Saputra, E.; Muhammad, S.; Sun, H. Q.; Ang, H. M.; Tade, M. O.; Wang, S. B., Manganese oxides at different oxidation states for heterogeneous activation of

peroxymonosulfate for phenol degradation in aqueous solutions. *Applied Catalysis B-Environmental* **2013,** *142*, 729-735.

15. Ling, S. K.; Wang, S. B.; Peng, Y. L., Oxidative degradation of dyes in water using Co2+/H2O2 and Co2+/peroxymonosulfate. *Journal of Hazardous Materials* **2010,** *178* (1-3), 385-389.

16. Chan, K. H.; Chu, W., Degradation of atrazine by cobalt-mediated activation of peroxymonosulfate: Different cobalt counteranions in homogenous process and cobalt oxide catalysts in photolytic heterogeneous process. *Water Research* **2009,** *43* (9), 2513-2521.

17. Yang, Q. J.; Choi, H.; Chen, Y. J.; Dionysiou, D. D., Heterogeneous activation of peroxymonosulfate by supported cobalt catalysts for the degradation of 2,4-dichlorophenol in water: The effect of support, cobalt precursor, and UV radiation. *Applied Catalysis B-Environmental* **2008,** *77* (3-4), 300-307.

18. Anipsitakis, G. P.; Dionysiou, D. D.; Gonzalez, M. A., Cobalt-mediated activation of peroxymonosulfate and sulfate radical attack on phenolic compounds. Implications of chloride ions. *Environmental Science & Technology* **2006,** *40* (3), 1000-1007.

19. Anipsitakis, G. P.; Dionysiou, D. D., Degradation of organic contaminants in water with sulfate radicals generated by the conjunction of peroxymonosulfate with cobalt. *Environ. Sci. Technol.* **2003,** *37* (20), 4790-4797.

20. Liu, S. Z.; Peng, W. C.; Sun, H. Q.; Wang, S. B., Physical and chemical activation of reduced graphene oxide for enhanced adsorption and catalytic oxidation. *Nanoscale* **2014,** *6* (2), 766-771.

21. Sun, H. Q.; Kwan, C.; Suvorova, A.; Ang, H. M.; Tade, M. O.; Wang, S. B., Catalytic oxidation of organic pollutants on pristine and surface nitrogen-modified carbon nanotubes with sulfate radicals. *Applied Catalysis B-Environmental* **2014,** *154*, 134-141.

22. Sun, H.; Wang, Y.; Liu, S.; Ge, L.; Wang, L.; Zhu, Z.; Wang, S., Facile synthesis of nitrogen doped reduced graphene oxide as a superior metal-free catalyst for oxidation. *Chemical Communications* **2013,** *49* (85), 9914-9916.

23. Kratschmer, W.; Lamb, L. D.; Fostiropoulos, K.; Huffman, D. R., Solid C60: a new form of carbon. *Nature* **1990,** *347* (6291), 354-358.

24. Choi, S. D.; Lee, J. H.; Park, D. M.; Kim, G. J., Fabrication of CNT/CMK3 Carbon Composites with High Electrical/Thermal Conductive Properties. *Bulletin of the Korean Chemical Society* **2013,** *34* (7), 2155-2161.

25. Wang, Z.; Ba, D. C.; Liu, F.; Cao, P. J.; Yang, T. Z.; Gu, Y. S.; Gao, H. J., Synthesis and characterization of large area well-aligned carbon nanotubes by ECR-CVD without substrate bias. *Vacuum* **2005,** *77* (2), 139-144.

26. Ciobotaru, C. C.; Damian, C. M.; Iovu, H., Single-wall carbon nanotubes purification and oxidation. *UPB Scientific Bulletin, Series B: Chemistry and Materials Science* **2013,** *75* (2), 55-66.

27. Lu, S. C.; Yao, M. G.; Yang, X. G.; Li, Q. J.; Xiao, J. P.; Yao, Z.; Jiang, L. H.; Liu, R.; Liu, B.; Chen, S. L.; Zou, B.; Cui, T.; Liu, B. B., High pressure transformation of graphene nanoplates: A Raman study. *Chemical Physics Letters* **2013,** *585*, 101-106.

28. Ignat, M.; Popovici, E., SYNTHESIS OF MESOPOROUS CARBON MATERIALS via NANOCASTING ROUTE-COMPARATIVE STUDY OF GLYCEROL AND SUCROSE AS CARBON SOURCES. *Revue Roumaine De Chimie* **2011,** *56* (10-11), 947-952.

29. Ye, Y.; Ahn, C. C.; Witham, C.; Fultz, B.; Liu, J.; Rinzler, A. G.; Colbert, D.; Smith, K. A.; Smalley, R. E., Hydrogen adsorption and cohesive energy of single-walled carbon nanotubes. *Applied Physics Letters* **1999,** *74* (16), 2307-2309.

30. Chakraborty, S.; Chattopadhyay, J.; Peng, H. Q.; Chen, Z. Y.; Mukherjee, A.; Arvidson, R. S.; Hauge, R. H.; Billups, W. E., Surface area measurement of functionalized single-walled carbon nanotubes. *Journal of Physical Chemistry B* **2006,** *110* (49), 24812-24815.

31. Lezanska, M.; Wloch, J.; Szymanski, G.; Szpakowska, I.; Kornatowski, J., Properties of CMK-8 carbon replicas obtained from KIT-6 and pyrrole at various contents of ferric catalyst. *Catalysis Today* **2010,** *150* (1-2), 77-83.

32. Zolfaghari, G.; Esmaili-Sari, A.; Anbia, M.; Younesi, H.; Amirmahmoodi, S.; Ghafari-Nazari, A., Taguchi optimization approach for Pb(II) and Hg(II) removal from aqueous solutions using modified mesoporous carbon. *Journal of Hazardous Materials* **2011,** *192* (3), 1046-1055.

33. Rymarczyk, J.; Kaminska, A.; Keczkowska, J.; Kozlowski, M.; Czerwosz, E., Morphological, topographical and FTIR characterizations of Pd-C films. *Optica Applicata* **2013,** *43* (1), 123-132.

34. Wadayama, T.; Ohta, T.; Hatta, A., Enhanced Infrared Absorption of C60 on Thin Evaporated Pd Island Films. *Israel Journal of Chemistry* **2006,** *46* (3), 257-263.

35. Bethune, D. S.; Meijer, G.; Tang, W. C.; Rosen, H. J.; Golden, W. G.; Seki, H.; Brown, C. A.; Devries, M. S., VIBRATIONAL RAMAN AND INFRARED-SPECTRA OF CHROMATOGRAPHICALLY SEPARATED C60 AND C70 FULLERENE CLUSTERS. *Chemical Physics Letters* **1991,** *179* (1-2), 181-186.

36. Thomas, S.; Kalarikkal, N.; Stephan, A. M.; Raneesh, B., *Advanced Nanomaterials: Synthesis, Properties, and Applications*. Apple Academic Press: **2014**.

37. Park, H. M.; Kim, K. H.; Lee, S. H.; Park, D. H.; Hong, Y. K.; Joo, J., Electrochemical polymerization of polypyrrole (PPy) and poly(3-hexylthiophene) (P3HT) using functionalized single-wall carbon nanotubes. *Colloids and Surfaces a-Physicochemical and Engineering Aspects* **2008,** *313*, 72-76.

38. Meyers, R. A., *Encyclopedia of Analytical Chemistry*. Wiley: **2012**.

39. Su, D. S.; Delgado, J. J.; Liu, X.; Wang, D.; Schlogl, R.; Wang, L. F.; Zhang, Z.; Shan, Z. C.; Xiao, F. S., Highly Ordered Mesoporous Carbon as Catalyst for Oxidative Dehydrogenation of Ethylbenzene to Styrene. *Chemistry-an Asian Journal* **2009,** *4* (7), 1108-1113.

40. Yuan, D. S.; Zeng, J.; Chen, J.; Liu, Y., Highly Ordered Mesoporous Carbon Synthesized via in Situ Template for Supercapacitors. *International Journal of Electrochemical Science* **2009,** *4* (4), 562-570.

41. Zou, W.-j.; Mo, S.-s.; Zhou, S.-l.; Zhou, T.-x.; Xia, N.-n.; Yuan, D.-s., Preparation of mesoporous carbon/polypyrrole composite materials and their supercapacitive properties. *Journal of Electrochemical Science and Engineering* **2011**.

42. Briggs, D., *Surface Analysis of Polymers by XPS and Static SIMS*. Cambridge University Press: **1998**.

43. Xie, Y. M.; Sherwood, P. M. A., X-RAY PHOTOELECTRON-SPECTROSCOPIC STUDIES OF CARBON-FIBER SURFACES .9. THE EFFECT OF MICROWAVE PLASMA TREATMENT ON CARBON-FIBER SURFACES. *Applied Spectroscopy* **1989,** *43* (7), 1153-1158.

44. Xie, Y. M.; Sherwood, P. M. A., X-RAY PHOTOELECTRON SPECTROSCOPIC STUDIES OF CARBON-FIBER SURFACES .11. DIFFERENCES IN THE SURFACE-CHEMISTRY AND BULK STRUCTURE OF

DIFFERENT CARBON-FIBERS BASED ON POLY(ACRYLONITRILE) AND PITCH AND COMPARISON WITH VARIOUS GRAPHITE SAMPLES. *Chem. Mat.* **1990,** *2* (3), 293-299.

45. Darmstadt, H.; Roy, C.; Kaliaguine, S.; Choi, S. J.; Ryoo, R., Surface chemistry of ordered mesoporous carbons. *Carbon* **2002,** *40* (14), 2673-2683.

46. Ballesteros, E.; Gallego, M.; Valcarcel, M., Analytical potential of fullerene as adsorbent for organic and organometallic compounds from aqueous solutions. *Journal of Chromatography A* **2000,** *869* (1-2), 101-110.

47. Ji, L. L.; Shao, Y.; Xu, Z. Y.; Zheng, S. R.; Zhu, D. Q., Adsorption of Monoaromatic Compounds and Pharmaceutical Antibiotics on Carbon Nanotubes Activated by KOH Etching. *Environmental Science & Technology* **2010,** *44* (16), 6429-6436.

48. Velasco, L. F.; Ania, C. O., Understanding phenol adsorption mechanisms on activated carbons. *Adsorpt.-J. Int. Adsorpt. Soc.* **2011,** *17* (1), 247-254.

49. Dabrowski, A.; Podkoscielny, P.; Hubicki, Z.; Barczak, M., Adsorption of phenolic compounds by activated carbon - a critical review. *Chemosphere* **2005,** *58* (8), 1049-1070.

50. Laszlo, K.; Podkoscielny, P.; Dabrowski, A., Heterogeneity of polymer-based active carbons in adsorption of aqueous solutions of phenol and 2,3,4-trichlorophenol. *Langmuir* **2003,** *19* (13), 5287-5294.

51. Mattson, J. A.; Mark Jr, H. B.; Malbin, M. D.; Weber Jr, W. J.; Crittenden, J. C., Surface chemistry of active carbon: Specific adsorption of phenols. *Journal of Colloid and Interface Science* **1969,** *31* (1), 116-130.

52. Coughlin, R. W.; Ezra, F. S., Role of surface acidity in the adsorption of organic pollutants on the surface of carbon. *Environ. Sci. Technol.* **1968,** *2* (4), 291-297.

53. Saputra, E.; Muhammad, S.; Sun, H. Q.; Wang, S. B., Activated carbons as green and effective catalysts for generation of reactive radicals in degradation of aqueous phenol. *Rsc Advances* **2013,** *3* (44), 21905-21910.

54. Gomez-Navarro, C.; Burghard, M.; Kern, K., Elastic properties of chemically derived single graphene sheets. *Nano Letters* **2008,** *8* (7), 2045-2049.

55. Huang, S. M.; Cai, X. Y.; Liu, J., Growth of millimeter-long and horizontally aligned single-walled carbon nanotubes on flat substrates. *Journal of the American Chemical Society* **2003,** *125* (19), 5636-5637.

56. Nsabimana, A.; Bo, X. J.; Zhang, Y. F.; Li, M.; Han, C.; Guo, L. P., Electrochemical properties of boron-doped ordered mesoporous carbon as electrocatalyst and Pt catalyst support. *Journal of Colloid and Interface Science* **2014,** *428*, 133-140.

57. Maiyalagan, T.; Nassr, A. A.; Alaje, T. O.; Bron, M.; Scott, K., Three-dimensional cubic ordered mesoporous carbon (CMK-8) as highly efficient stable Pd electro-catalyst support for formic acid oxidation. *Journal of Power Sources* **2012,** *211*, 147-153.

58. Wang, Y. X.; Sun, H. Q.; Ang, H. M.; Tade, M. O.; Wang, S. B., 3D-hierarchically structured MnO2 for catalytic oxidation of phenol solutions by activation of peroxymonosulfate: Structure dependence and mechanism. *Appl. Catal. B-Environ.* **2015,** *164*, 159-167.

59. Indrawirawan, S.; Sun, H. Q.; Duan, X. G.; Wang, S. B., Low temperature combustion synthesis of nitrogen-doped graphene for metal-free catalytic oxidation. *Journal of Materials Chemistry A* **2015,** *3* (7), 3432-3440.

60. Duan, X. G.; Sun, H. Q.; Wang, Y. X.; Kang, J.; Wang, S. B., N-Doping-Induced Nonradical Reaction on Single-Walled Carbon Nanotubes for Catalytic Phenol Oxidation. *ACS Catal.* **2015,** *5* (2), 553-559.

CHAPTER 5

Temperature-dependent radical generation in peroxymonosulfate activation for catalytic oxidation of nitrobenzene

Abstract

Nitrogen doped single-walled carbon nanotubes (N-SWCNTs) were prepared using urea as the N precursor via pyrolysis at 700 °C. Superb nitrobenzene removal in water solutions via advanced oxidation processes using peroxymonosulfate (PMS) as the oxidant and N-SWCNT was observed in a range of 5 – 75 °C. The results showed that nitrobenzene degradation was enhanced with increasing reaction temperatures. It was found that ˙OH radicals play a dominant role in the process of nitrobenzene degradation at higher reaction temperatures. The mechanism of PMS activation with/without N-SWCNT for nitrobenzene degradation was elucidated by employing both in situ electron paramagnetic resonance (EPR) and classical radical quenching tests with methanol and tert-butanol (TBA). Nitrobenzene degradation kinetic studies using PMS only and PMS/N-SWCNT shows activation energies of 49.9 and 16.6 kJ/mol, respectively.

5.1. Introduction

Due to the rapid civilization, polluted water discharged from households and industries has become a major environmental issue in human health, balance of water eco-system and re-utilization of water. Various techniques for water purification have been developed based on advanced oxidation processes (AOPs) such as photocatalysis, ozonation, and Fenton reaction to oxidize complex organic contaminants into mineralized acids, carbon dioxide and water. AOPs in metal-based systems generally involve highly reactive radicals as a strong oxidant to degrade compounds that cannot be oxidized by conventional oxidants such as oxygen, ozone and chlorine [1-3]. In general metal-based systems would result in secondary contamination due to potential metal leaching. The relative redox potential of hydroxyl radicals ($^{\bullet}OH$) in Fenton reactions is about 2.7 V, and the effective oxidation requires an acidic condition of pH 2 to 5. As an alternative to hydroxyl radicals, sulfate radicals ($SO_4^{\bullet-}$) possesses a higher potential (2.5-3.1 V) and have been applied to decompose organic pollutants in a wider pH range [4-5].

In the pioneering studies, reduce graphene oxide (rGO) can effectively promote peroxymonosulfate (PMS) activation to generate reactive radicals ($^{\bullet}OH$ and $SO_4^{\bullet-}$) for oxidation of phenol, 2,4-dichlorophenol and methylene blue in aqueous solutions [6]. Nitrogen-doped graphene (N-rGO) synthesized by direct annealing of graphene oxide (GO) with a nitrogen precursor (melamine) demonstrated outstanding performances in PMS activation for phenol degradation, which was superior to other carbon allotropes (fullerene and carbon nanotubes) and a classical metal-based catalyst Co_3O_4 [7]. Both $^{\bullet}OH$ and $SO_4^{\bullet-}$ radicals were discovered during the activation processes. Surface modified single-wall carbon nanotubes have shown an extraordinary catalytic performance for activating PMS toward phenol decomposition. It was found that both radical and non-radical pathways contribute to the phenol oxidation. In a radical process, $^{\bullet}OH$ and $SO_4^{\bullet-}$ attacked the phenol via a series of hydrogen abstraction and addition reactions in the homogeneous phase. Whereas in the non-radical process, the PMS is first bonded with N-doped sp^2-hybridized system and then will be activated to react with the adsorbed phenol via outer-shell electron transfer [8]. Nanocarbons with varying carbon-conjugation structures and functional groups showed that radical and non-radical oxidations

could occur on different pristine carbocatalysts depending on the carbon structure [9]. Radical oxidation occurs particularly on MWCNT and CMK-3, while both radical and non-radical oxidations occur in annealed nanodiamond and rGO. In general, the $^{\bullet}OH$ and $SO_4^{\bullet-}$ radicals generation from PMS can be enhanced via structural and compositional modifications of the carbocatalysts. However, the previous studies are practically carried out at room temperature and the effect of reaction temperature on PMS activation with carbocatalysts has not reported yet.

In this chapter, nitrobenzene ($C_6H_5NO_2$, NB), a biologically non-degradable organic compound, was chosen as the target organic to estimate the oxidative efficiency. NB is a highly toxic aromatic compound for human health and widely used in chemical industries for anilines, explosives, dyes and pesticide productions. Schwertmannite has been utilized as a heterogeneous catalyst in Fenton reaction for effective degradation of nitrobenzene [10]. The performance of nitrobenzene degradation with nanocrystalline TiO_2 under UV light irradiation was better than that of Degussa P-25 [11]. Functionalized multi-walled carbon nanotubes (MWCNTs) with O_3 also exhibited a good catalytic activity for nitrobenzene oxidation [12]. In the process of nitrobenzene decomposition, it is generally accepted that $^{\bullet}OH$ radicals react with benzene and its derivatives by electrophilic addition [13]. However, the reactions of nitrobenzene and $SO_4^{\bullet-}$ radicals are negligible due to the low reaction rate constants ($k_{^{\bullet}OH, NB} = 3.9 \times 10^9\ M^{-1}s^{-1}$, $k_{SO4^{\bullet-}, NB} < 10^6\ M^{-1}s^{-1}$) [5, 14-15]. Therefore, catalytic NB oxidation is rarely reported in PMS-based systems.

Herein, nitrogen-doped single-walled carbon nanotubes were prepared by a simple process of annealing with urea as a N precursor at 700 ^{o}C. We further investigate the nitrobenzene degradation in water by using PMS only and PMS with N-SWCNT in the temperature range of 5 – 75 ^{o}C under acidic condition (pH 3). The purpose for varying temperatures is to study the temperature-dependent generation of the reactive radicals ($^{\bullet}OH$ and $SO_4^{\bullet-}$) during the process of nitrobenzene removal. An interesting phenomenon occurs in the temperature range of 45 - 75 ^{o}C, in which even PMS only is able to degrade nitrobenzene. Besides, carbocatalysis further boosted the catalytic oxidation efficiencies.

5.2. Experimental Section

5.2.1. Materials and catalysts preparation

Single-walled carbon nanotubes were obtained from Timesnano, China. Other chemicals were obtained from Chem-Supply, Australia. The nitrogen-doped single-walled carbon nanotubes were prepared using urea as the N precursor. SWCNT (1.0 g) and urea were mixed in 50 mL ethanol at room temperature for 30 min, then the temperature was increased to 50 °C and stirred for a few hours until the ethanol was completely evaporated. The dried mixture was thermally annealed in a tube furnace under nitrogen atmosphere at 700 °C for 30 min and cooled down naturally. The obtained N-SWCNT was washed with ethanol and deionised (DI) water three times each, and dried in an oven at 60 °C.

5.2.2. Characterization of the catalysts

X-ray diffraction (XRD) patterns were acquired on a Bruker D8-Advanced X-ray instrument using Cu-Kα radiation with λ at 1.5418 Å. Nitrogen sorption isotherms were obtained on a Micrometrics Tristar 3000. The Brunauer-Emmet-Teller (BET) and Barrett-Joyner-Halenda (BJH) methods were applied to evaluate the specific surface area (SSA) and pore size distribution. Fourier transform infrared spectra (FTIR) were recorded on a Bruker instrument with an ATR correction mode. X-ray photoelectron spectroscopy (XPS) was used to determine the chemical states of elements using a Thermo Escalab 250 with Al-Kα X-ray. Thermogravimetric-differential scanning calorimetry (TG-DSC) was carried out in an air flow at a flowrate of 100 mL/min with a heating rate of 5 °C on a Perkin-Elmer Diamond thermal analyser. Scanning electron microscopy (SEM) was applied to investigate the morphology of the nanocarbons on Zeiss Neon 40 EsB FIBSEM. Raman analysis was performed on an ISA dispersive Raman spectroscopy using argon ion laser with a wavelength at 514 nm. Electron paramagnetic resonance (EPR) spectra were obtained on a Bruker EMS-plus to detect the free radicals generated during PMS activation.

5.2.3. Catalytic activity test

The catalytic oxidation of nitrobenzene was carried out in a 500 mL conical flask with nitrobenzene solution (20 ppm), catalyst (0.2 g/L) and PMS (2.0 g/L) in a constant-temperature controlled water bath for the kinetic studies. At each time interval, 1 mL solution was withdrawn by a syringe, filtered by a 0.45 μm Millipore film, and injected into a vial. Then 0.5 mL of methanol was immediately injected into the reaction solution to completely quenching the oxidation. The mixed solution was analysed on an ultrahigh performance liquid chromatograph (UHPLC, Thermal) with a C-18 column and a UV detector set at 270 nm.

5.3. Results and Discussion

5.3.1. Characterization of nitrogen-doped SWCNT

Figure 5.1 shows XRD patterns of SWCNT and N-SWCNT. Two characteristic peaks were found approximately at 2θ = 26° and 43°, corresponding to (002) and (100) planes, respectively [16]. It can be noted that the intensities of N-SWCNT at 26 and 43° decreased substantially compared to those of SWCNT. This indicates that the order of lattice periodicity of crystalline SWCNT (hexagonal ABAB and rhombohedral ABC stacking) was distorted due to the nitrogen doping and thermal treatment at 700 °C [17-18]. At 2θ = 26°, the interplanar spacing is about 0.34 nm. From the Schrerrer equation, the interlayer thicknesses (L) of SWCNT and N-SWCNT were calculated to be 5.9 nm with half peak width 3.1°, and 7.3 nm with half peak width 2.5°, respectively. As seen in **Figure 5.1**, there are no additional peaks of other crystalline structures (guest species) for SWCNT and N-SWCNT indicating the high purity of these materials.

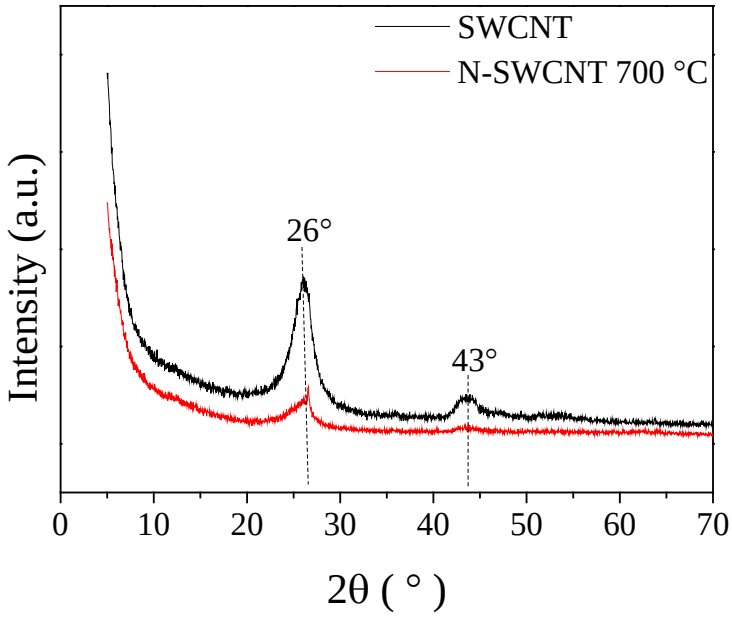

Figure 5.1. XRD patterns of SWCNT and N-SWCNT.

The morphology of N-SWCNT was observed using SEM imaging. As seen in **Figure 5.2**, SWCNT and N-SWCNT presented agglomerate and irregular morphology with thin tube-like structures. These thin tube like structures were attributed to the SWCNT and N-SWCNT [19]. It can be seen the amount of these thin tube-like structures was more pronounce in N-SWCNT. This may be due to the thermal annealing at 700 °C and nitrogen doping.

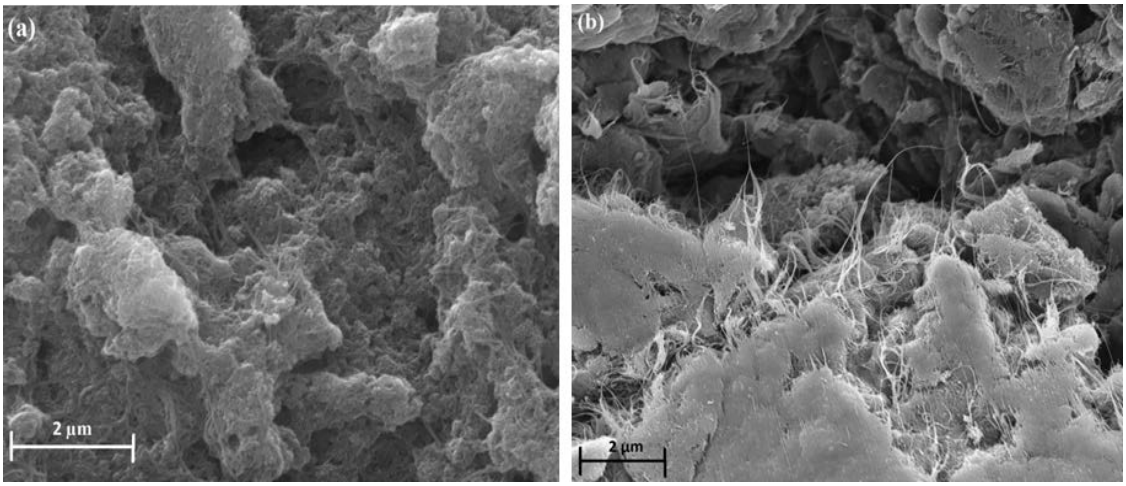

Figure 5.2. SEM images of (a) SWCNT (b) N-SWCNT.

TGA-DTA was used to investigate the thermal behaviour of SWCNT and N-SWCNT, as it is seen from **Figure 5.3**. The analysis was performed in air at a heating rate of 10°C/min.

Figure 5.3a shows that a major weight loss can be seen for both SWCNT and N-SWCNT between 500 and 680 °C due to the excess carbonaceous material oxidation or due to combustion of carbon.

The DTA curves in **Figure 5.3b** shows two characteristic peaks or strong exothermal peaks at 575 and 660 °C for SWCNT indicating that there are two different carbonaceous materials undergone thermal decomposition. For N-SWCNT, there is one exothermal peak at 620 °C suggesting only one carbonaceous material took place in thermal decomposition. There was no further weight loss of SWCNT and N-SWCNT after reaching the temperature of 660 °C. Thermal annealing at 700 °C and nitrogen doping has the effect of decreasing the number of strong exothermal peak from two peaks into one peak.

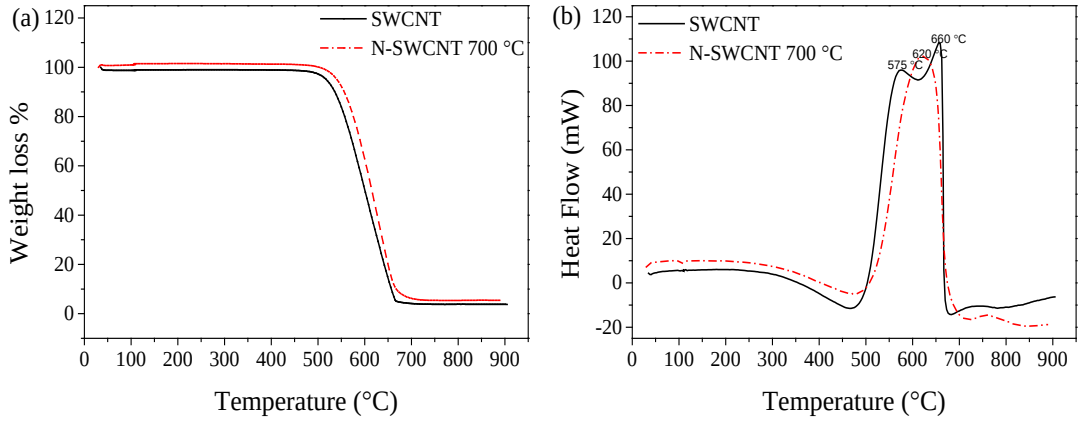

Figure 5.3. (a) TGA and (b) DTA curves of SWCNT and N-SWCNT in the air atmosphere.

Nitrogen sorption isotherms were used for the textural characteristics of SWCNT and N-SWCNT, as shown in **Figure 5.4**. The specific surface area (SSA) of SWCNT is 366 m^2/g. After nitrogen doping and thermal treatment, the SSA is increased to 516 m^2/g.

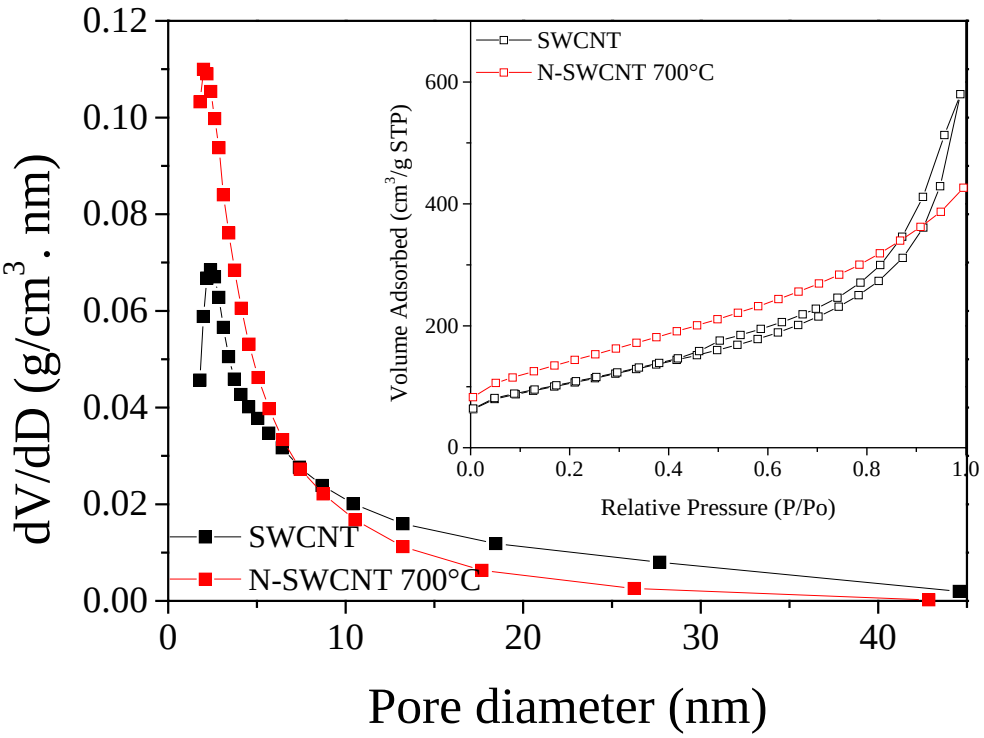

Figure 5.4. Pore size distribution of SWCNT and N-SWCNT.

FTIR was carried out to determine the presence of typical functional groups in SWCNT before and after nitrogen doping. As it is seen in **Figure 5.5**, the characteristic peaks of O-H group (hydroxyl) at 3336 cm^{-1}, C-H group (methyl) at 2911 cm^{-1}, and C=O (carbonyl) group at 1715 cm^{-1} were absent for both SWCNT and N-SWCNT. These results show that very little oxygen and hydrogen groups attached to the surface of SWCNT and N-SWCNT. A very weak characteristic peak at 1575 cm^{-1} is attributed to C=C aromatic group for SWCNT, where a similar characteristic peak may be attributed to C=N group for N-SWCNT [16, 20].

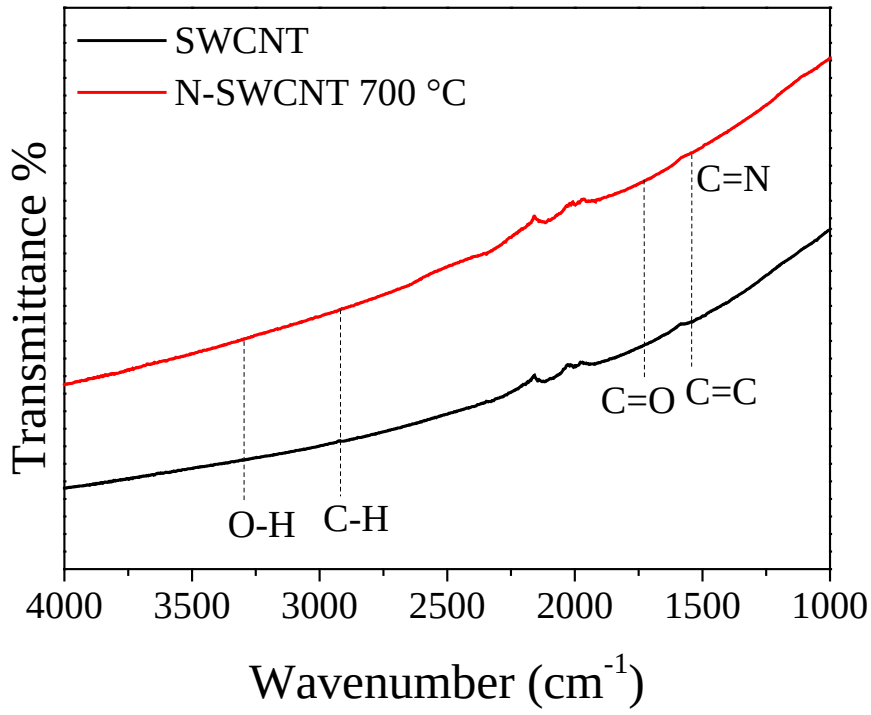

Figure 5.5. FTIR spectra of SWCNT and N-SWCNT.

The XPS studies were carried out to investigate the atomic concentration (at.%) of elemental contents in SWCNT and N-SWCNT. The corresponding C1s, O1s, and N1s peaks are centred at 284.1, 531, and 399.2 eV, respectively (**Figure 5.6a**) [21]. The elemental information of surface chemistry is summarised in **Table 5.1**. It can be seen that nitrogen doping and thermal annealing resulted in decreasing oxygen level from 4.27 at.% to 0.8 at.% and increasing nitrogen level from 0 to 0.6 at.%. A substantial amount of oxygen functional groups and water were removed due to the simultaneous process of thermal annealing and nitrogen doping with urea.

Figure 5.6b shows high resolution XPS N 1s spectra of N-SWCNT. Four types of nitrogen species can be identified from the de-convolution of XPS N 1s spectra: pyridinic (N-6) at 398.3 eV, pyrrolic (N-5) at 400.1 eV, graphitic N at 401.8 eV, and nitric oxide at 403.73 eV [22-23]. As it is seen in **Table 5.1**, the concentrations of pyridinic N, pyrrolic N, graphitic N and nitric oxide are 0.3 at.%, 0.2 at.%, 0.06 at.% and 0.05 at.%, respectively.

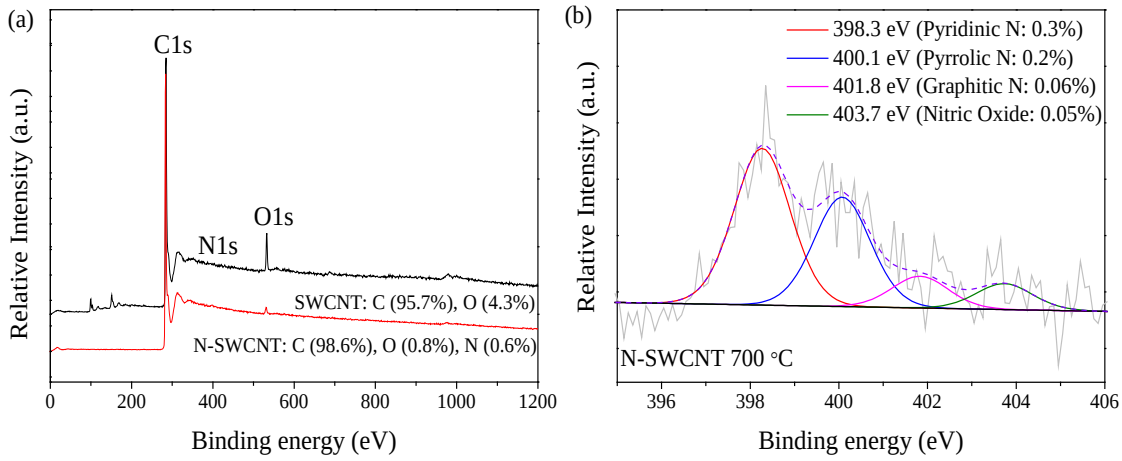

Figure 5.6. (a) XPS survey, (b) N1s of N-SWCNT.

O 1s high resolution XPS spectra of SWCNT and N-SWCNT can be seen in **Figure 5.7**. For SWCNT, two types of oxygen species can be identified from the de-convolution of XPS O 1s spectra: O_1 (C=O) at 530.95 eV and O_2 (C-O-C) at 532.98 eV [21]. For N-SWCNT 700 °C, the two types of oxygen species are O_1 (C=O) at 530.55 eV and O_3 (chemisorbed oxygen and adsorbed water) at 534.78 eV.

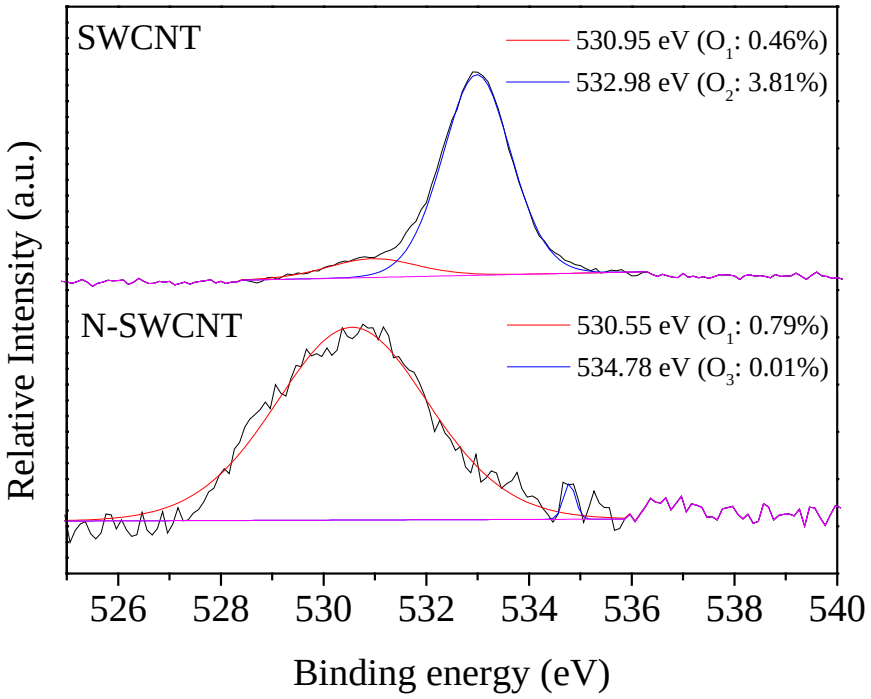

Figure 5.7. O1s of SWCNT and N-SWCNT

Table 5.1. Chemical Composition of SWCNT and N-SWCNT

Sample	N level, at. %	Pyridinic N, at. %	Pyrrolic N, at. %	Graphitic N, at. %	Nitric Oxide, at. %	O level, at.%	BET m^2/g
SWCNT	-	-	-	-	-	4.27	366
N-SWCNT	0.6	0.3	0.2	0.06	0.05	0.80	516

5.3.2. Catalytic oxidation of different organic contaminants

Figure 5.8a shows the catalytic efficiency for degradation of different organic contaminants on N-SWCNT with PMS at room temperature (25 °C). The N-SWCNT can give 45% and 60% of benzoquinone and nitrobenzene removal in 180 min, respectively [24]. Complete phenol and SCP degradation was achieved in 60 and 45 min, respectively. The effective degradation in phenol using N-SWCNT was consistent with our previous study with enhanced catalytic activity upon N-doping [25].

Figure 5.8b shows the comparison of phenol degradation for SWCNT and N-SWCNT. Pristine SWCNT can achieve 20% phenol removal in 180 min due to the adsorption process. For SWCNT/PMS, the phenol was completely degraded in 150 min. N-SWCNT shows an improved adsorption performance with 40% phenol removal in 180 min. Here, phenol can be completely oxidized in 60 min in the catalytic oxidative system with PMS. The results confirm that surface-modified SWCNT with thermal annealing and nitrogen-doping can enhance adsorption and catalytic oxidation performances compared with pristine SWCNT.

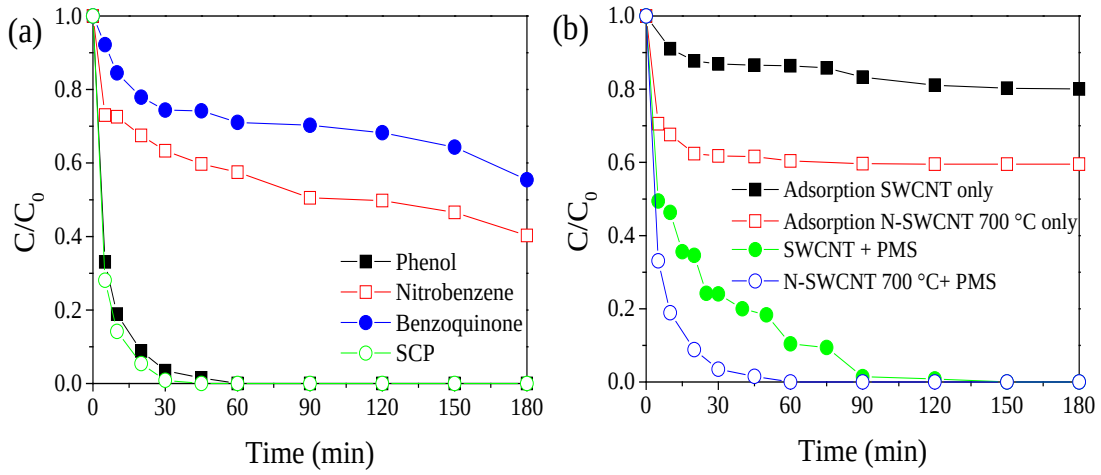

Figure 5.8. (a) Degradation of different organic contaminants (20 ppm) with PMS on N-SWCNT at room temperature 25 °C, (b) Phenol degradation using pristine SWCNT and N-SWCNT at room temperature 25 °C.

5.3.3. Adsorption and catalytic oxidation performance of nitrobenzene

In a previous study, N-SWCNT was only able to remove 10% phenol in 180 min at 25 °C due to adsorption [8]. Here, N-SWCNT at 25, 35 and 45 °C can remove 80% of nitrobenzene (NB) in 180 min due to adsorption (**Figure 5.9a**). Increasing the temperature to 75 °C, N-SWCNT can even further remove 90% NB in 180 min. As it is seen in **Figure 5.9a**, at pH of 3 and 25 °C, N-SWCNT can remove 70% of NB in 180 min due to adsorption. The different adsorption behaviours between phenol and nitrobenzene on N-SWCNT may be due to ^{-}OH as nucleophile that contributes negative charge into the benzene ring resulting in the π electron cloud of the ring more negative; whereas $^{+}NO_2$ as electrophile withdraws negative charge from the benzene ring resulting in the π electron cloud of the ring more positive. Therefore, it is expected that NB will be more preferably attracted to N-SWCNT than phenol to N-SWCNT; which is consistent with the previous studies that nitrogen doped graphene and SWCNT were possibly able to produce more electrons [7].

It is known that phenol adsorption on carbon materials has been generally attributed to physisorption and chemisorption. The temperature independent of 80% NB removal at 25, 35 and 45 °C is most likely due to the physisorption that depends strictly on the porosity, specific surface area (surface geometrical heterogeneity) with the contribution of chemisorption [26]. This chemisorption is likely due to the more

positive π electron cloud of nitrobenzene attracted to the N-SWCNT (as an electron donor). At 75 °C, the NB removal at 90% may be due to more contribution of chemisorption as expected with increasing the reaction temperature.

Bar chart comparison of nitrobenzene removal efficiency with and without N-SWCNT up to 60 min can be seen in **Figure 5.9b**. In general, increasing the solution temperatures results in an increasing of nitrobenzene removal. Here, the presence of N-SWCNT further improves the nitrobenzene removal.

Based on the results in **Figure 5.8**, nitrobenzene is chosen as a target contaminant due to its mediocre degradation performance to study the effect of temperature dependence. **Figure 5.9c** shows the effect of different reaction temperatures on nitrobenzene oxidation using PMS only (without N-SWCNT). The nitrobenzene degradation was remarkably improved with increasing reaction temperatures from 5 to 75 °C. In the range of 5 to 25 °C, nitrobenzene degradation slightly increased from less than 5 to 18% in 180 min. From 35 to 75 °C, the nitrobenzene degradation significantly improved from 26 to 100%. The results suggested that significant improvement of nitrobenzene degradation was achieved with increasing reaction temperatures.

Figure 5.9d demonstrates the effect of reaction temperature on nitrobenzene degradation by PMS activation in the presence of N-SWCNT. The oxidation performances were greatly improved with the addition of N-SWCNT. It is noted, the catalytic activity was also enhanced with the increasing reaction temperature. About 31, 48, and 60% of nitrobenzene degradations were achieved within 180 min at 5, 15, and 25 °C, respectively. Further improvement of nitrobenzene degradation occurred at higher temperatures from 35 to 75 °C. More specifically, 95% nitrobenzene was degraded at 35 °C within 180 min, while complete removal of nitrobenzene could be obtained in 120, 45, 20, and 10 min at 45, 55, 65 and 75 °C, respectively. **Figure 5.9a** suggests that N-SWCNT presents great adsorption capability of nitrobenzene. Since most heterogeneously catalytic reactions occur at the interface of the catalyst, the enhanced adsorption may synergistically contribute to the improvement of the oxidative performances.

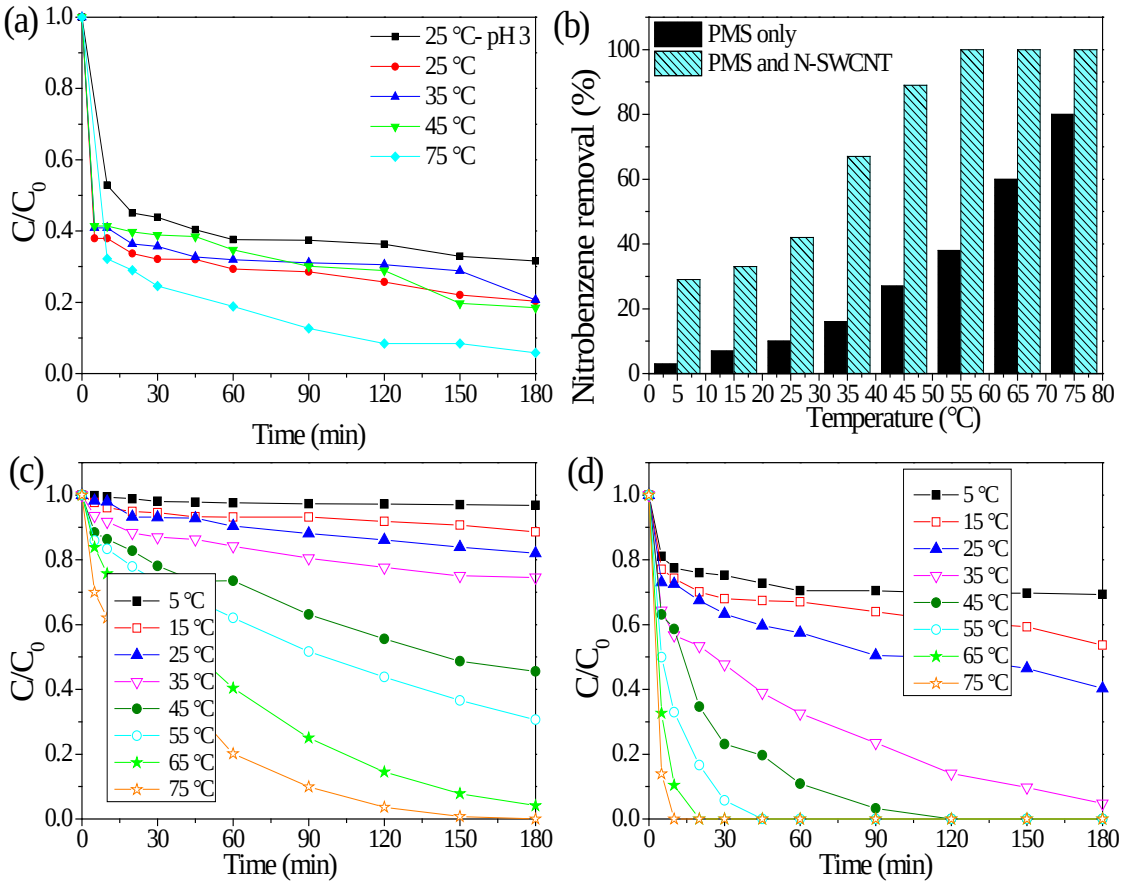

Figure 5.9. (a) Adsorption of nitrobenzene on N-SWCNT (pH level = 7), (b) Bar chart comparison of nitrobenzene removal (%) with and without N-SWCNT up to 60 min, (c) Effect of various temperatures on nitrobenzene degradation using PMS only (pH level = 3), (d) Effect of various temperatures on nitrobenzene degradation using PMS and N-SWCNT (pH level = 3).

Kinetic studies were carried out to investigate the effect of reaction temperature on nitrobenzene degradation by PMS with/without the addition of N-SWCNT from 5 to 75 °C. The overall activation energies were estimated to be 49.9 and 16.6 kJ/mol for the catalyst-free and catalytic systems using the Arrhenius equation based on the initial reaction rate (**Figure 5.10**). The activation energy decreased with the addition of the carbocatalyst. The existence of N-SWCNT works as a catalyst to lower the activation energy therefore increasing successful molecules collision. It can be seen from **Figure 5.10**, there is an indication that the degradation of NB took place into two stages for both PMS with/ without N-SWCNT. For PMS only, it appears the first stage is from 5 to 35 °C and the second stage occurs at 35 to 75 °C. For PMS with N-SWCNT, the first stage occurs at 5 to 45 °C, and second stage takes place at 45 to 75 °C. At lower temperatures, it appears the rate of degradation is not significant due

to insufficient thermal activation for the reaction to overcome the barrier of the activation energy for the first stage. At the second stage of higher temperatures, it appears the thermal activation is sufficient to overcome the barrier of activation energy for the reaction to occur which results in moderate to significant NB degradation.

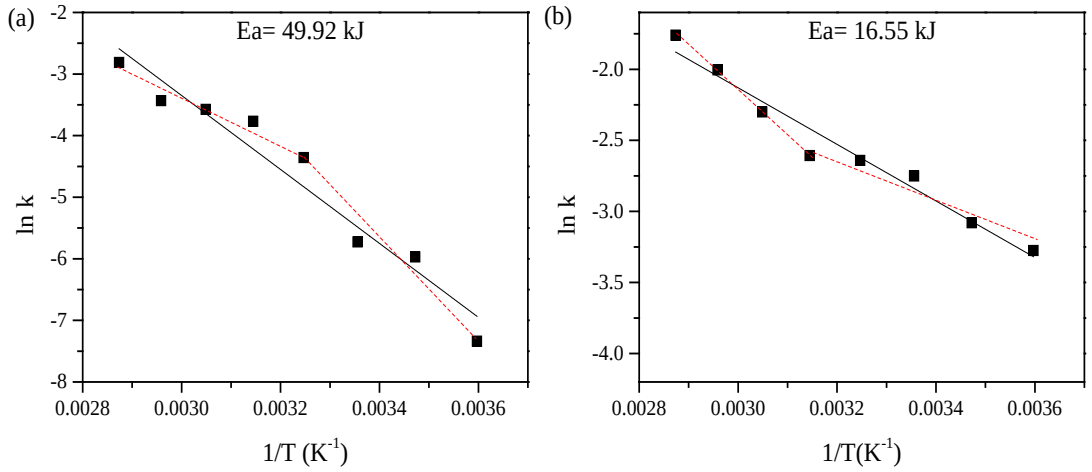

Figure 5.10. Kinetic study for nitrobenzene degradation using (a) PMS only, and (b) PMS and N-SWCNT.

5.3.4. Mechanism of PMS activation and nitrobenzene degradation

AOPs have demonstrated excellent effectiveness for complete degradation of the target organic pollutants into harmless substances. Both hydroxyl ($^{\bullet}OH$) and sulfate ($SO_4^{\bullet-}$) radicals from PMS activation have been applied to degrade various organic pollutants (nitrobenzene, phenol, SCP, acid red 1) [5, 20, 27]. It is expected that without the consideration of reaction kinetics, $SO_4^{\bullet-}$ radicals exhibit a higher oxidative potential of 2.5-3.1 V compared to 2.7 V of $^{\bullet}OH$. It is widely accepted that metals/metal oxides tend to activate peroxymonosulfate to produce sulfate radicals which play the dominant role in oxidative reactions [28]. However, the targeted nitrobenzene in this study is quite reluctant to react with sulfate radicals compared with hydroxyl radicals. Faster nitrobenzene degradation was obtained by PMS activation with/without N-SWCNT at higher reaction temperatures, suggesting that the enhanced oxidation efficiency of nitrobenzene may be ascribed to the generation of more hydroxyl radicals at higher temperatures.

Previous studies showed that graphene and carbon nanotubes were able to effectively

activate PMS to produce free radicals for removal various organic compounds [6, 16]. However, N-SWCNT could also induce both radical and non-radical pathways for phenol degradation with PMS activation [29]. In order to elucidate the mechanism of temperature-dependent PMS activation, electron paramagnetic resonance (EPR) was utilized to capture the $^{\bullet}OH$ and $SO_4^{\bullet-}$ radicals during the oxidative processes with 5, 5-dimethyl-pyrroline-oxide (DMPO) as the radical spin trapping agent.

Figure 5.11 shows the radical generation of PMS activation with the presence of nitrobenzene without N-SWCNT as the binary system at different reaction temperatures (5, 25, and 45 °C). At all times, $^{\bullet}OH$ and $SO_4^{\bullet-}$ radicals were detected by EPR spectra. Sulfate radicals are usually considered as the dominant reactive species generated in PMS-based AOP. Nevertheless, it is known that nitrobenzene will react with $^{\bullet}OH$ radical due to its high reactivity compared to $SO_4^{\bullet-}$ radical [30]. In this study, $^{\bullet}OH$ radicals appeared as the major species at all reaction temperatures. Previous study for the binary system, phenol and PMS indicated minor radicals detected from the EPR spectra [8]. In this study, the EPR spectra of the binary system, nitrobenzene and PMS, show contradictory results. Both the oxidative system and the in situ EPR suggest that the temperature-dependent PMS activation tend to activate PMS to generate hydroxyl radicals for nitrobenzene degradation.

The mechanism may be proposed as below: first, PMS is initially hydrolized to hydroperoxide (HO_2^-) and sulfate [31].

$$^{-}_{3}OS - O - O^{-} + H_2O \xrightarrow{OH^-} H - O - O^{-} + SO_4^{2-} + H^+ \quad (5.1)$$

Then, the hydroperoxide generated from the hydrolysis of PMS reduces another PMS forming sulfate radical ($SO_4^{\bullet-}$), sulfate anion and superoxide (O_2).

$$2(^{-}_{3}OS - O - O^{-}) + H - O - O^{-} \rightarrow SO_4^{\bullet-} + SO_4^{2} + H^+ + 2O_2^{\bullet-} \quad (5.2)$$

At low pH regimes, sulfate radical reacts with water to form hydroxyl radical [30].

$$SO_4^{\bullet-} + H_2O \rightarrow SO_4^{2-} + {}^{\bullet}OH + H^+ \quad (5.3)$$

Here, NB will react with $^{\bullet}OH$ radical to form intermediates [32].

$$Nitrobenzene + {}^{\bullet}OH \rightarrow intermediates \quad (5.4)$$

Finally, the intermediates react with another $^{\bullet}OH$ radical to form CO_2, H_2O and inorganic compounds.

$$Intermediates + {}^{\bullet}OH \rightarrow CO_2 + H_2O + inorganic\ compounds \quad (5.5)$$

It is noted the asymmetric of PMS structure made it easy to undergo fission of the S-

O bond (**Equation 5.1**) [33].

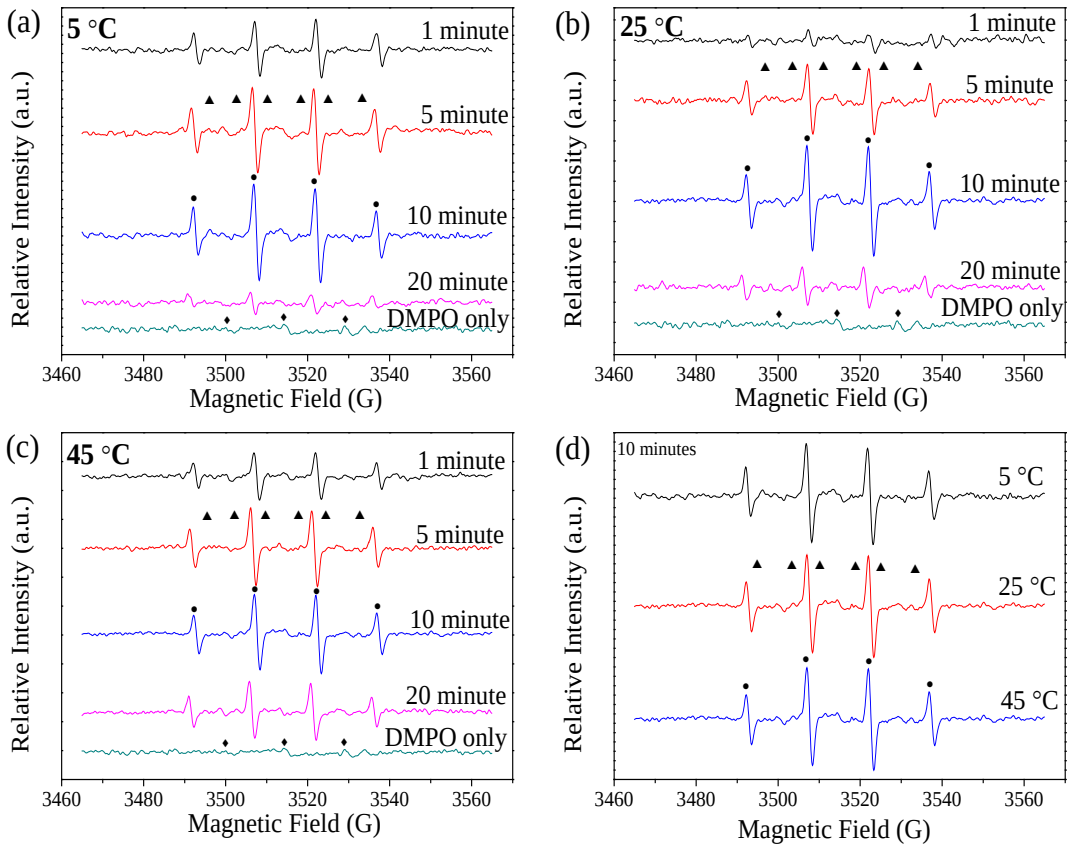

Figure 5.11. EPR spectra of PMS only in nitrobenzene degradation at different reaction temperatures (a) 5 °C, (b) 25 °C, and (c) 45 °C (♦) DMPO-X (▲) DMPO-SO_4 (●) DMPO- OH (d) Comparison of EPR spectra of PMS activation at 10 minutes without N-SWCNT at 5 °C, 25 °C, and 45 °C.

Figure 5.12 shows the radical generation of PMS activation with the presence of nitrobenzene and N-SWCNT as the ternary system at different reaction temperatures (5, 25, and 45 °C). It can be seen that •OH radicals also appeared as the major species for all reaction temperatures at all times. The existence of carbocatalyst alters the PMS activation pathway and acts as an excellent media for electron transfer. Therefore the performance for PMS activation was enhanced by producing hydroxyl radicals which was identified in the carbocatalytic systems.

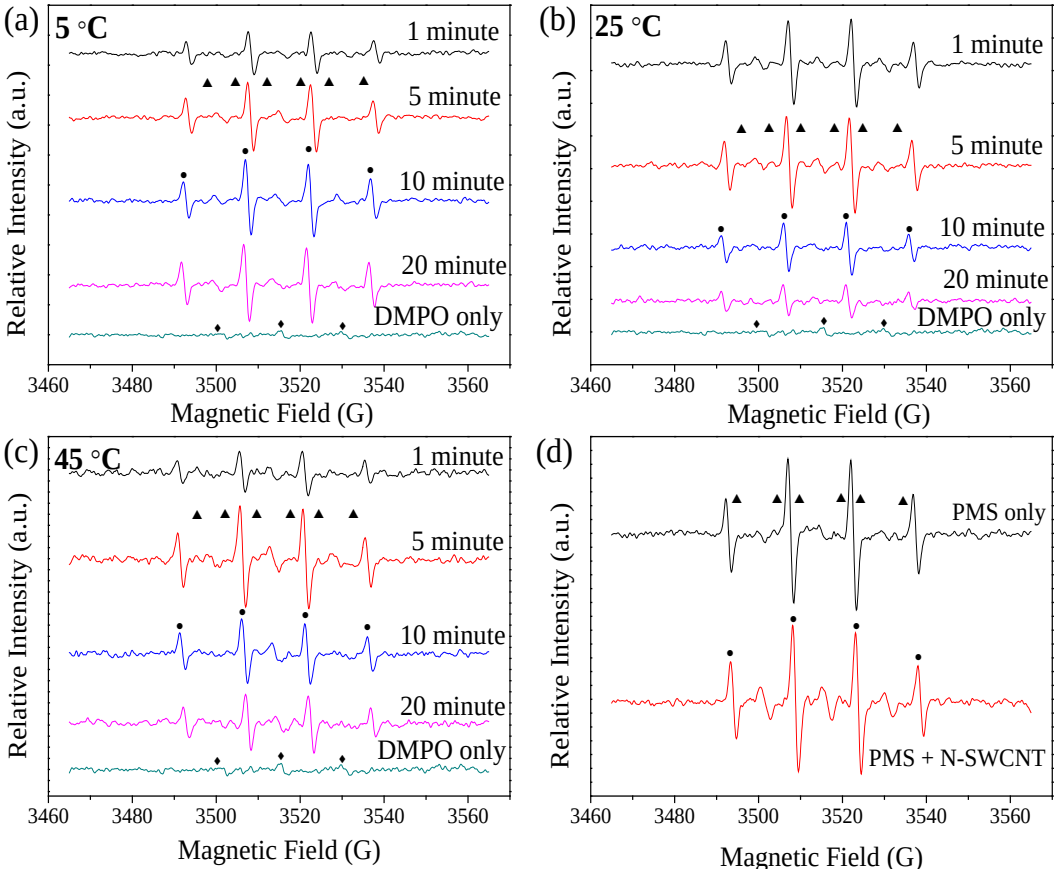

Figure 5.12. EPR spectra of PMS and N-SWCNT 700 °C in nitrobenzene degradation at different reaction temperatures (a) 5 °C, (b) 25 °C, (c) 45 °C (♦) DMPO-X (▲) DMPO- SO_4 (●) DMPO-OH and (d) Comparison of EPR spectra of PMS with and without N-SWCNT at 25 °C and 10 min.

It is well known that $^{\bullet}OH$ and $SO_4^{\bullet-}$ radicals demonstrate different reaction rates toward two radical scavengers, methanol and tert-butyl alcohol (TBA) ($k_{\bullet OH,\ methanol}$ = $9.7 \times 10^8\ M^{-1}s^{-1}$, $k_{SO4^{\bullet-},\ methanol} = 2.5 \times 10^7\ M^{-1}s^{-1}$, $k_{\bullet OH,\ TBA} = 3.8 \times 10^8$ - $7.6 \times 10^8\ M^{-1}s^{-1}$) [14, 34]. Methanol can capture both $^{\bullet}OH$ and $SO_4^{\bullet-}$ while TBA prefers to capture $^{\bullet}OH$ radicals other than $SO_4^{\bullet-}$ radicals.

Figure 5.13 displays nitrobenzene degradation by N-SWCNT activation of PMS with different quenching reagents at 45 °C. It can be seen that NB degradation is hindered with the addition of methanol or TBA; only 50% NB was degraded which is due to adsorption. It is noted, the performance of NB degradation in PMS with N-SWCNT is worse than in N-SWCNT (see **Figure 5.9a**). Both PMS and NB are electron acceptors, therefore the performance of NB degradation is hindered by the

presence of PMS which appears to be more attracted to N-SWCNT as an electron donor [26, 35]. This indicates that the hydroxyl radicals are the principal reactive species accounting for nitrobenzene degradation with N-SWCNT as an electron mediator in the ternary system.

The superior nitrobenzene degradation is most likely due to the $^{\bullet}OH$ radicals which were generated from PMS (**Equation 5.6**) or transferred from $SO_4^{\bullet-}$ radicals (**Equation 5.10**) where N-SWCNT would contribute to the electron and heat transfer processes and facilitate PMS activation processes [34].

$$HSO_5^- + e^- \rightarrow {}^{\bullet}OH + SO_4^{2-} \quad (5.6)$$

$$HSO_5^- + e^- \rightarrow SO_4^{\bullet-} + OH^- \quad (5.7)$$

$$HSO_5^- - e^- \rightarrow SO_5^{\bullet-} + H^+ \quad (5.8)$$

$$^{\bullet}OH + SO_4^{2-} \rightarrow SO_4^{\bullet-} + OH^- \quad (5.9)$$

$$SO_4^{\bullet-} + OH^- \rightarrow SO_4^{2-} + {}^{\bullet}OH \quad (5.10)$$

$$\text{Nitrobenzene} + {}^{\bullet}OH \rightarrow \text{intermediates} \rightarrow CO_2 + H_2O + \text{inorganic compounds} \quad (5.11)$$

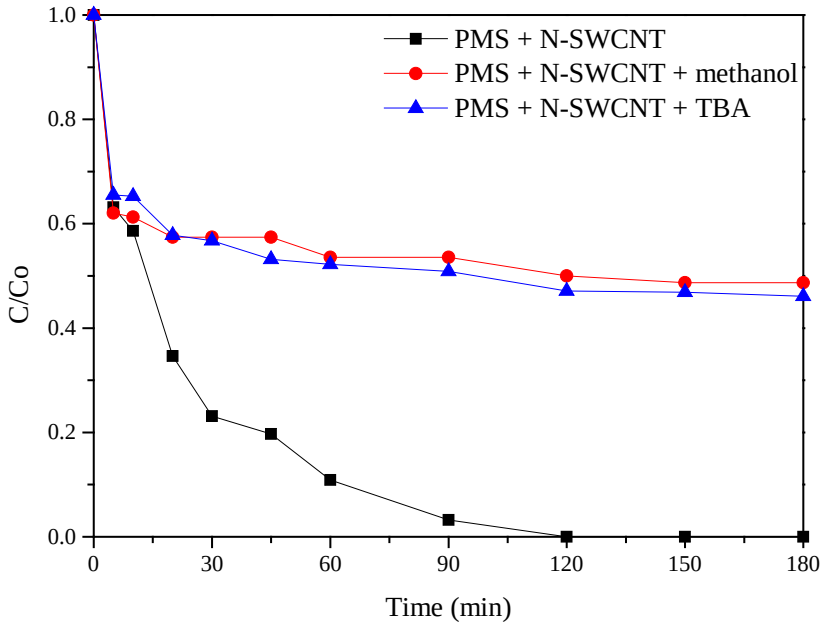

Figure 5.13. Nitrobenzene degradation using N-SWCNT by PMS activation with addition of methanol and TBA at 45 °C ($[methanol]_0$ = 0.22 M , $[TBA]_0$ = 0.2 M)

5.4. Conclusions

In this chapter, N-SWCNT was synthesized by a simple nitrogen doping of SWCNT at 700 °C. The excellent adsorption and PMS activation for nitrobenzene degradation with/without N-SWCNT were investigated at different reaction temperatures from 5 °C to 75 °C. Nitrobenzene was selected as the target organic and electron acceptor for catalytic evaluation in both binary and ternary systems. Nitrobenzene degradation, quenching test, and radical trapping method indicated that the PMS activation with/without N-SWCNT is a temperature-dependent process. The thermal activation tends to improve PMS activation to generate hydroxyl radicals and further improve the effectiveness of nitrobenzene degradation. Hydroxyl radicals contribute as the main radicals to nitrobenzene degradation on PMS with and without N-SWCNT. In the binary system (NB and PMS), the $^{\bullet}$OH radicals were generated through the hydrolysis process; whereas in the ternary system (NB, PMS and N-SWCNT), the $^{\bullet}$OH radicals were generated through the electron transfer process. These $^{\bullet}$OH radicals can react with nitrobenzene non-selectively and convert it into non-toxic inorganic compounds. In the binary system (NB and N-SWCNT), the nitrobenzene removal is attributed to the physisorption and chemisorptions via π electron donor-acceptor mechanisms. Moreover, PMS as an electron acceptor and metal-free N-SWCNT catalyst as an electron donor show a promising result for removal of nitrobenzene in aqueous solution with controlled reaction temperatures. Although both PMS and NB are electron acceptors, it appears that PMS is more attracted to N-SWNCT.

References

1. H. Sun, H. L., G.Zhou, and S. Wang, Supported cobalt catalysts by one pot aqueous combustion synthesis for catalytic phenol degradation. *J. Colloid Interface Sci.* **2013,** *394*, 394-400.
2. Saputra, E.; Muhammad, S.; Sun, H.; Patel, A.; Shukla, P.; Zhu, Z. H.; Wang, S., α-MnO2 activation of peroxymonosulfate for catalytic phenol degradation in aqueous solutions. *Catalysis Communications* **2012,** *26*, 144-148.
3. Shukla, P.; Wang, S. B.; Sun, H. Q.; Ang, H. M.; Tade, M., Adsorption and heterogeneous advanced oxidation of phenolic contaminants using Fe loaded mesoporous SBA-15 and H2O2. *Chem. Eng. J.* **2010,** *164* (1), 255-260.

4. Hu, P. D.; Long, M. C., Cobalt-catalyzed sulfate radical-based advanced oxidation: A review on heterogeneous catalysts and applications. *Appl. Catal. B-Environ.* **2016,** *181*, 103-117.

5. Yang, Y.; Jiang, J.; Lu, X. L.; Ma, J.; Liu, Y. Z., Production of Sulfate Radical and Hydroxyl Radical by Reaction of Ozone with Peroxymonosulfate: A Novel Advanced Oxidation Process. *Environ. Sci. Technol.* **2015,** *49* (12), 7330-7339.

6. Sun, H.; Liu, S.; Zhou, G.; Ang, H. M.; Tadé, M. O.; Wang, S., Reduced Graphene Oxide for Catalytic Oxidation of Aqueous Organic Pollutants. *ACS Applied Materials & Interfaces* **2012,** *4* (10), 5466-5471.

7. Duan, X. G.; Ao, Z. M.; Sun, H. Q.; Indrawirawan, S.; Wang, Y. X.; Kang, J.; Liang, F. L.; Zhu, Z. H.; Wang, S. B., Nitrogen-Doped Graphene for Generation and Evolution of Reactive Radicals by Metal-Free Catalysis. *Acs Applied Materials & Interfaces* **2015,** *7* (7), 4169-4178.

8. Duan, X. G.; Sun, H. Q.; Wang, Y. X.; Kang, J.; Wang, S. B., N-Doping-Induced Nonradical Reaction on Single-Walled Carbon Nanotubes for Catalytic Phenol Oxidation. *ACS Catal.* **2015,** *5* (2), 553-559.

9. Duan, X. G.; Ao, Z. M.; Zhou, L.; Sun, H. Q.; Wang, G. X.; Wang, S. B., Occurrence of radical and nonradical pathways from carbocatalysts for aqueous and nonaqueous catalytic oxidation. *Appl. Catal. B-Environ.* **2016,** *188*, 98-105.

10. Duan, H. T.; Liu, Y.; Yin, X. H.; Bai, J. F.; Qi, J., Degradation of nitrobenzene by Fenton-like reaction in a H2O2/schwertmannite system. *Chem. Eng. J.* **2016,** *283*, 873-879.

11. Tayade, R. J.; Kulkarni, R. G.; Jasra, R. V., Photocatalytic degradation of aqueous nitirobenzene by nanocrystalline TiO2. *Ind. Eng. Chem. Res.* **2006,** *45* (3), 922-927.

12. Yang, S. X.; Sun, Y.; Yang, H. W.; Wan, J. F., Catalytic wet air oxidation of phenol, nitrobenzene and aniline over the multi-walled carbon nanotubes (MWCNTs) as catalysts. *Front. Env. Sci. Eng.* **2015,** *9* (3), 436-443.

13. Carlos, L.; Fabbri, D.; Capparelli, A. L.; Prevot, A. B.; Pramauro, E.; Einschlag, F. S. G., Intermediate distributions and primary yields of phenolic products in nitrobenzene degradation by Fenton's reagent. *Chemosphere* **2008,** *72* (6), 952-958.

14. Buxton, G. V.; Greenstock, C. L.; Helman, W. P.; Ross, A. B., CRITICAL-REVIEW OF RATE CONSTANTS FOR REACTIONS OF HYDRATED

ELECTRONS, HYDROGEN-ATOMS AND HYDROXYL RADICALS (.OH/.O-) IN AQUEOUS-SOLUTION. *J. Phys. Chem. Ref. Data* **1988,** *17* (2), 513-886.

15. Neta, P.; Madhavan, V.; Zemel, H.; Fessenden, R. W., Rate constants and mechanism of reaction of sulfate radical anion with aromatic compounds. *Journal of the American Chemical Society* **1977,** *99* (1), 163-164.

16. Indrawirawan, S.; Sun, H. Q.; Duan, X. G.; Wang, S. B., Nanocarbons in different structural dimensions (0-3D) for phenol adsorption and metal-free catalytic oxidation. *Appl. Catal. B-Environ.* **2015,** *179*, 352-362.

17. J. H. Warner, F. S., A. Bachmatiuk, and M. H. Rummeli, *Graphene: Fundamentals and Emergent Applications*. Elsevier: **2013**.

18. Cullity, B. D.; Stock, S. R., *Elements of X-ray Diffraction*. Prentice Hall: **2001**.

19. Li, J. Y.; Zhang, J. F., A simple purification for single-walled carbon nanotubes. *Physica E* **2005,** *28* (3), 309-312.

20. Indrawirawan, S.; Sun, H. Q.; Duan, X. G.; Wang, S. B., Low temperature combustion synthesis of nitrogen-doped graphene for metal-free catalytic oxidation. *J. Mater. Chem. A* **2015,** *3* (7), 3432-3440.

21. Briggs, D., *Surface Analysis of Polymers by XPS and Static SIMS*. Cambridge University Press: **1998**.

22. Vazquez-Arenas, J.; Galano, A.; Lee, D. U.; Higgins, D.; Guevara-Garcia, A.; Chen, Z., Theoretical and experimental studies of highly active graphene nanosheets to determine catalytic nitrogen sites responsible for the oxygen reduction reaction in alkaline media. *J. Mater. Chem. A* **2016,** *4* (3), 976-990.

23. Lin, Z. Y.; Waller, G. H.; Liu, Y.; Liu, M. L.; Wong, C. P., Simple preparation of nanoporous few-layer nitrogen-doped graphene for use as an efficient electrocatalyst for oxygen reduction and oxygen evolution reactions. *Carbon* **2013,** *53*, 130-136.

24. Zhou, Y.; Jiang, J.; Gao, Y.; Ma, J.; Pang, S. Y.; Li, J.; Lu, X. T.; Yuan, L. P., Activation of Peroxymonosulfate by Benzoquinone: A Novel Nonradical Oxidation Process. *Environ. Sci. Technol.* **2015,** *49* (21), 12941-12950.

25. Duan, X. G.; Ao, Z. M.; Sun, H. Q.; Zhou, L.; Wang, G. X.; Wang, S. B., Insights into N-doping in single-walled carbon nanotubes for enhanced activation of superoxides: a mechanistic study. *Chem. Commun.* **2015,** *51* (83), 15249-15252.

26. Mattson, J. A.; Mark, H. B.; Malbin, M. D.; Weber, W. J.; Crittenden, J. C., Surface chemistry of active carbon: Specific adsorption of phenols. *Journal of Colloid and Interface Science* **1969,** *31* (1), 116-130.

27. Tian, W. J.; Zhang, H. Y.; Duan, X. G.; Sun, H. Q.; Tade, M. O.; Ang, H. M.; Wang, S. B., Nitrogen- and Sulfur-Codoped Hierarchically Porous Carbon for Adsorptive and Oxidative Removal of Pharmaceutical Contaminants. *Acs Applied Materials & Interfaces* **2016,** *8* (11), 7184-7193.

28. Anipsitakis, G. P.; Dionysiou, D. D., Radical generation by the interaction of transition metals with common oxidants. *Environ. Sci. Technol.* **2004,** *38* (13), 3705-3712.

29. Duan, X. G.; Sun, H. Q.; Kang, J.; Wang, Y. X.; Indrawirawan, S.; Wang, S. B., Insights into Heterogeneous Catalysis of Persulfate Activation on Dimensional-Structured Nanocarbons. *ACS Catal.* **2015,** *5* (8), 4629-4636.

30. Ahmad, M.; Teel, A. L.; Watts, R. J., Mechanism of Persulfate Activation by Phenols. *Environ. Sci. Technol.* **2013,** *47* (11), 5864-5871.

31. Furman, O. S.; Teel, A. L.; Watts, R. J., Mechanism of Base Activation of Persulfate. *Environ. Sci. Technol.* **2010,** *44* (16), 6423-6428.

32. Celin, S. M.; Pandit, M.; Kapoor, J. C.; Sharma, R. K., Photoperoxidation of nitrobenzene in aqueous phase. *Indian J. Chem. Technol.* **2004,** *11* (2), 266-270.

33. Guan, Y. H.; Ma, J.; Ren, Y. M.; Liu, Y. L.; Xiao, J. Y.; Lin, L. Q.; Zhang, C., Efficient degradation of atrazine by magnetic porous copper ferrite catalyzed peroxymonosulfate oxidation via the formation of hydroxyl and sulfate radicals. *Water Res.* **2013,** *47* (14), 5431-5438.

34. Wang, Y. X.; Sun, H. Q.; Ang, H. M.; Tade, M. O.; Wang, S. B., 3D-hierarchically structured MnO2 for catalytic oxidation of phenol solutions by activation of peroxymonosulfate: Structure dependence and mechanism. *Appl. Catal. B-Environ.* **2015,** *164*, 159-167.

35. Anipsitakis, G. P.; Dionysiou, D. D., Degradation of organic contaminants in water with sulfate radicals generated by the conjunction of peroxymonosulfate with cobalt. *Environ. Sci. Technol.* **2003,** *37* (20), 4790-4797.

CHAPTER 6

Radicals generation in metal-free persulfate activation

Abstract

Nitrogen doped single-walled carbon nanotubes (N-SWCNTs) were prepared using urea as the N precursor via pyrolysis at 700 °C. Nitrobenzene (NB) degradation in aqueous solutions via advanced oxidation processes (AOPs) using persulfate (PDS) as the oxidant and N-SWCNT was observed in the range of 5 – 75 °C. Phenol degradation in water solutions by PDS activation was also observed in the range 55 – 75 °C. The results showed that NB and phenol degradation was enhanced by increasing reaction temperatures. The mechanism of PDS activation with/without N-SWCNT for NB degradation was elucidated by employing both in situ electron paramagnetic resonance (EPR) and classical radical quenching tests with methanol and tert-butanol (TBA). Both NB and phenol can be degraded by PDS and peroxomonosulfate (PMS). It was found that $^{\bullet}OH$ radicals play a dominant role in NB degradation, while $SO_4^{\bullet-}$ radicals play a dominant role in phenol degradation. NB degradation kinetic studies using PDS only and PDS/N-SWCNT shows activation energies of 53.4 and 9.7 kJ/mol, respectively.

6.1. Introduction

One of the most critical issues in today's industrialization era is environmental pollution. Increasing waste water has been discharged along with the expansion of industrial production. The high concentration of organic contaminants in the waste water has alarmed many people due to their toxicity. There are many water purification technologies that have been established. One of the emerging methods is advance catalytic oxidation processes (AOPs). AOPs rely on highly reactive free radicals, mainly hydroxyl radicals, $^{\bullet}OH$, which have a higher oxidation potential (2.8 eV) compared to that of ozone and hydrogen peroxide with oxidation potential of 2.07 and 1.77 eV, respectively [1-3]. In addition to hydroxyl radicals, sulfate radicals are also very effective for a wide range of pollutants with oxidation potential 2.7 eV [4]. The stronger the oxidising agent is, the easier and faster the degradation of the target pollutants will be. Commonly used oxidants in AOPs are hydrogen peroxide, peroxymonosulfate (PMS) and persulfate or peroxydisulfate (PDS). Here, PDS is chosen as an alternative strong, cheap and high stability oxidant [5-6]. It can be activated to generate hydroxyl radicals or sulfate radicals or both by homolysis process, thermal or UV light, an oxidation-reduction process with electron donors (low - valent metals such as Fe^{2+} and Ag^{+}) [7], activated carbon, nano carbons, microwave and integrated techniques.

Many previous studies have been reported focusing on PDS activation for chemical oxidation. Fang et al reported that PDS activation by magnetite nanoparticle (MNP) can degrade 2,4,4' Trichlorobiphenyl (PCB28) efficiently [8]. Zero valent iron (Fe^{0}) has been reported to be an efficient catalyst to activate PDS to degrade various organic compounds, such as: 2, 4 dinitrotoluene (DNT), methyl tert-butyl ether (MTBE), trichloroethylene (TCE), chlorobenzene, naphthalene, remazol golden yellow (RGY) [9-11]. Various forms of iron minerals such as Fe^{2+}, Fe^{3+} and Fe_2O_3 were also found to be an excellent catalyst for PDS activation for degradation of nitrobenzene, TCE, toluene [12-14]. Here, most of previous studies were carried out at room temperature and using metal catalysts. Secondary contamination might occur during the catalytic oxidation process due to the metal content. Therefore, carbon catalysts have gained more interests in waste water treatments.

Single-walled carbon nanotube (SWCNT) is a single sheet of graphene rolled up into a tubular structure. These SWCNTs have demonstrated as a promising catalyst for catalytic activation of PDS in the process of phenol degradation along with reduced graphene oxide and mesoporous carbons [15]. A recent study has discovered that nitrogen modified single- walled carbon nanotubes (N-SWCNTs) were able to effectively activate PDS for the generation active radicals such as $^{\bullet}OH$ and $SO_4^{\bullet-}$ radicals in phenol removal [16-17].

In this chapter, further investigations on the degradation of nitrobenzene in water using PDS activated by N-SWCNTs. Nitrobenzene ($C_6H_5NO_2$, NB) is chosen because it is biologically non-degradable organic compound due to the high toxicity to human health and also the wide applications in chemical industries such as anilines, explosives, dyes and pesticide productions. The purpose for varying the degradation temperatures is to study the temperature dependence of the generation of active radicals ($^{\bullet}OH$ and $SO_4^{\bullet-}$) during the process of nitrobenzene removal. An interesting phenomena occurs in the temperature ranges 45-75^{o} C, i.e., PDS only would be able to degrade nitrobenzene.

6.2. Experimental section

6.2.1. Materials and catalyst preparation

All chemicals were obtained from Sigma-Aldrich. The nitrogen-doped single-walled carbon nanotubes were prepared using urea as the N precursor. 1.0 g of SWCNT and urea were mixed in 50 mL ethanol at room temperature for 30 min, and then the temperature was increased to 50 °C. The solution was stirred for a few hours until the ethanol was completely evaporated. The dried mixture was thermally annealed in a tube furnace under nitrogen atmosphere at 700 °C for 30 min and cooled down naturally. The obtained N-SWCNT was washed with ethanol and DI water three times each, and dried in an oven at 60 °C.

6.2.2. Characterization of the catalysts

Raman analysis was performed on an ISA dispersive Raman spectroscopy using argon ion laser with a wavelength at 514 nm. Electron paramagnetic resonance (EPR)

spectra were obtained on a Bruker EMS-plus to detect the free radicals generated during PDS activation.

6.2.3. Catalytic activity tests

The catalytic oxidation of nitrobenzene was carried out in a 500 mL conical flask with nitrobenzene solution (20 ppm), catalyst (0.2 g/L) and PDS (2.0 g/L) in a constant-temperature controlled water bath for the kinetic studies. At each time interval, 1 mL solution was withdrawn by a syringe, filtered by a 0.45 μm Millipore film, and injected into a vial. Then 0.5 mL of methanol was immediately injected into the reaction solution to completely quench the oxidation. The mixed solution was analysed on an ultrahigh performance liquid chromatography (UHPLC, Thermal) with a C-18 column and a UV detector set at 270 nm.

6.3. Results and Discussion

6.3.1. Characterization of nitrogen- doped SWCNT

Figure 6.1 shows Raman spectra of SWCNT and N-SWCNT. The D bands (related to the edges, defects, and structurally disordered carbon) occur at about 1320 cm^{-1}, G bands (originated from in-plane vibrations of sp^2 carbon) at about 1570 cm^{-1} and G' bands (overtone of D-band) at 2600 cm^{-1}. These results are consistent with previous Raman investigations on SWCNT [18-20]. The I_D/I_G ratio (intensity ratio of D band to G band) of the SWCNT is 0.23, and the I_D/I_G ratio of N-SWCNT is slightly decreased to 0.21. There was no significant effect of nitrogen doped and thermal annealing on the defective structures as indicated by the similar I_D/I_G ratios.

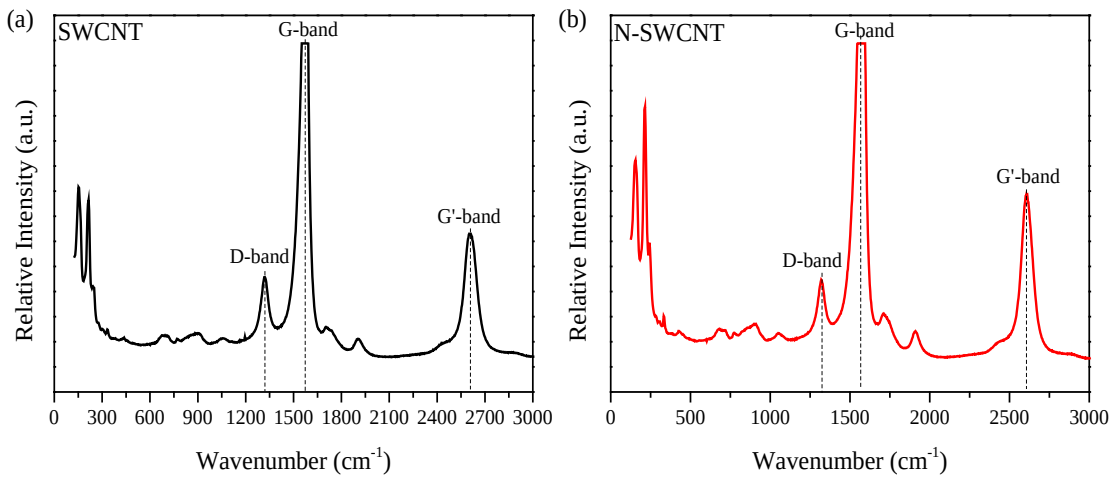

Figure 6.1. Raman spectra of (a) SWCNT and (b) N-SWCNT 700 °C.

6.3.2. Catalytic oxidation performance of nitrobenzene

Figure 6.2a shows the catalytic degradation of different organic contaminants on N-SWCNT with PDS at room temperature (25 °C). For benzoquinone and nitrobenzene, 33% and about 50% was degraded in 180 min, respectively. Complete phenol and SCP degradations were achieved in 90 min and 30 min, respectively. Based on **Figure 6.2a** results, nitrobenzene is chosen as a model contaminant due to its mediocre degradation performance to study the effect of temperature dependant on the degradation performance in the presence of both PDS and N-SWCNT 700 °C.

Bar chart comparison of % nitrobenzene degradation with and without N-SWCNT up to 60 min can be seen in **Figure 6.2b**. In general, increasing the reaction temperatures results in a reaction rate (speed) increase of nitrobenzene degradation. Moreover, the presence of N-SWCNT further improves the nitrobenzene degradation.

Figure 6.2c shows the effect of different reaction temperatures on nitrobenzene degradation using PDS only (without N-SWCNT). The performances of nitrobenzene degradation were improved by increasing the reaction temperatures from 5 to 75 °C. From 5 to 25 °C, nitrobenzene was degraded about 15% within 180 min. At 35 °C, the nitrobenzene degradations are 30% within 180 min, and complete removal within 30 min at 75 °C reaction temperature. These results indicated significant improvement on the performances of nitrobenzene degradation can be obtained by increasing reaction temperature.

Figure 6.2d shows the effect of different reaction temperatures on nitrobenzene degradation with N-SWCNT. The addition of N-SWCNT 700 °C and increasing the

reaction temperatures from 5 to 75 °C significantly improved nitrobenzene degradation performances. It is to be noted, the catalytic activity was also enhanced with the increasing reaction temperatures. The degradation of nitrobenzene was achieved 38%, 41%, 47% and 58% within 180 min for 5, 15, 25, and 35 °C respectively. Further improvement of nitrobenzene degradation performances occurred at 45 to 75 °C. At 45 °C nitrobenzene was degraded 90.5% within 180 min. Complete removals of nitrobenzene were observed in 150 min, 60 min and 30 min for reaction temperature of 55, 65 and 75 °C, respectively. In the previous chapter, it was found that N-SWCNT presents a great adsorption capability of nitrobenzene. Since most heterogeneously catalytic reactions occur at the surface of the catalyst, the enhanced adsorption may synergistically contribute to the improvement of the oxidative performances.

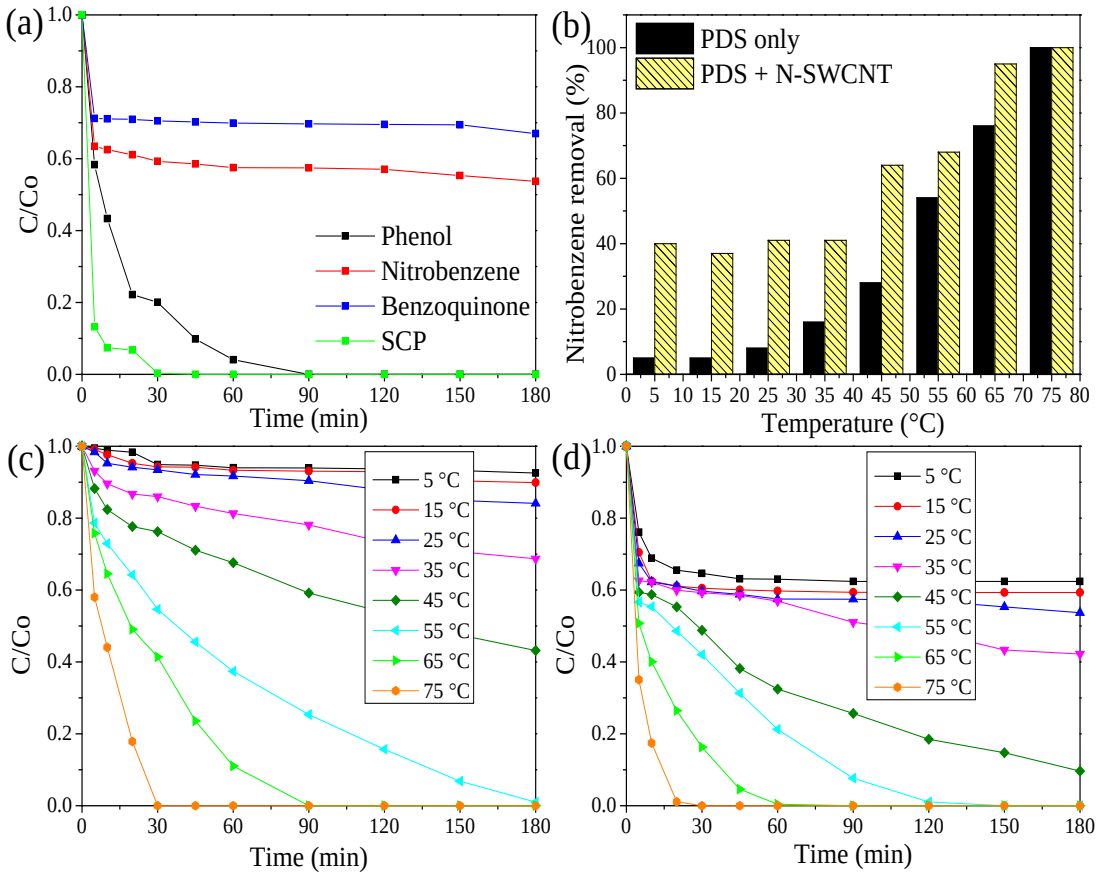

Figure 6.2. (a) Degradation of different organic contaminants (20 ppm) with PDS on N-SWCNT at room temperature 25 °C, (b) Bar chart comparison of nitrobenzene removal % with and without N-SWCNT up to 60 min, (c) Effect of various

temperatures on nitrobenzene degradation using PDS only, and (d) Effect of various temperatures on nitrobenzene degradation using PDS and N-SWCNT. ([pH]= 3).

It can be seen from **Figure 6.3** that for reaction temperatures from 55 to 75 °C the performance of nitrobenzene degradation using PDS only are more efficient than using PMS only (data of PMS only were obtained from Chapter 5). The possible explanation of this phenomenon will be discussed in section 6.3.3.

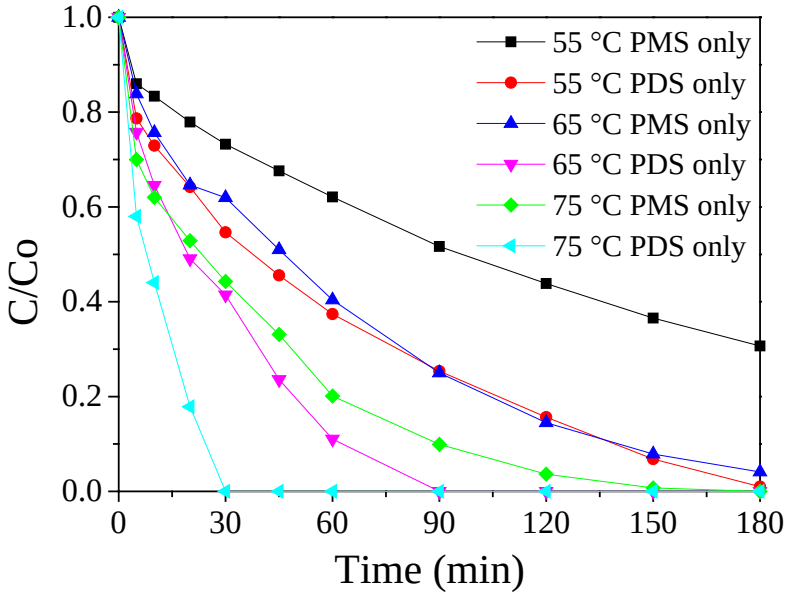

Figure 6.3. Comparison of nitrobenzene degradation using PMS only and PDS only at 55 °C -75 °C reaction temperatures ([pH]= 3).

Kinetic studies were carried out to investigate the effect of reaction temperature on nitrobenzene degradation by PDS with/without the addition of N-SWCNT from 5 to 75 °C. The overall activation energies were estimated to be 53.4 and 9.7 kJ/mol respectively for the catalyst-free and catalytic system using the Arrhenius equation based on the initial reaction rate (**Figure 6.4**). The activation energy decreased with the addition of the carbocatalyst. The existence of N-SWCNT works as a catalyst to lower the activation energy therefore increasing successful molecules collision. It can be seen from **Figure 6.4**, that there is an indication that the degradation of NB took place into two stages for both PDS with/ without N-SWCNT. For PDS only, it appears the first stage is from 5 to 55 °C and the second stage occurs at 55 to 75 °C. For PDS with N-SWCNT, the first stage occurs at 5 to 45 °C, and second stage takes

place at 45 to 75 °C. At the first stage (lower range temperatures), it appears the rate of degradation is not significant due to insufficient thermal activation for the reaction to overcome the barrier of the activation energy. At the second stage (higher range temperatures), it appears the thermal activation is sufficient to overcome the barrier of activation energy for the reaction to occur which results in moderate to significant NB degradation.

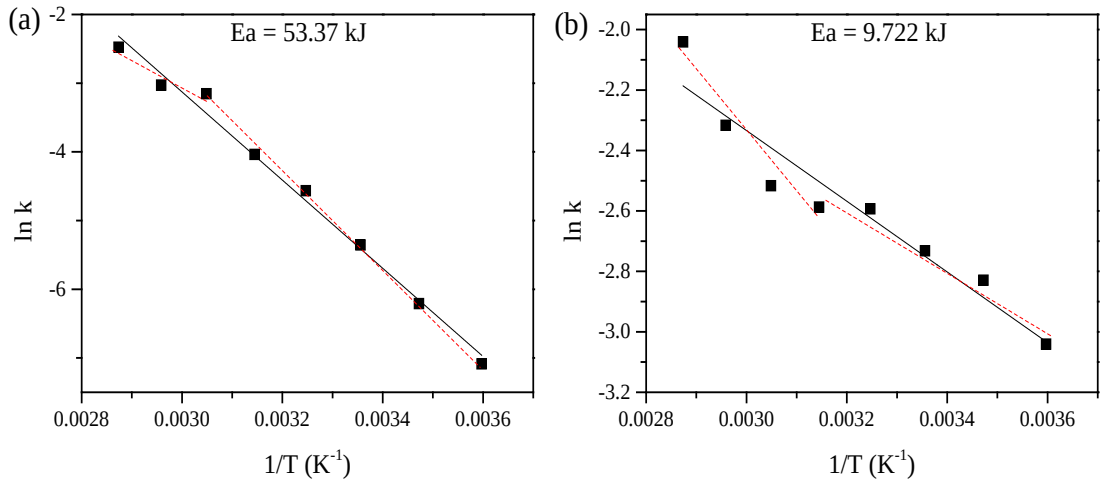

Figure 6.4. Kinetic studies for nitrobenzene degradation using (a) PDS only and (b) PDS and N-SWCNT 700 °C

6.3.3 Mechanism of PDS activation and nitrobenzene degradation

AOPs have demonstrated an excellent performance for complete decomposition of the target organic pollutants into harmless substances. Here catalytic oxidation by $^{\bullet}OH$ and $SO_4^{\bullet-}$ radicals from PDS activation has been applied to degrade typical organic pollutants (SCP, phenol, toluene, NB) [14-15, 21-23]. It is expected that $SO_4^{\bullet-}$ radicals degrade most of the organic pollutants due to the higher oxidative potential 2.5-3.1 V compared to 2.7 V of $^{\bullet}OH$ radicals. In this chapter, faster removal of nitrobenzene is obtained by the combination of PDS and N-SWCNT at higher reaction temperatures. In order to clarify (elucidate) the mechanism of this behaviour, electron paramagnetic resonance (EPR) was employed to study the presence of $^{\bullet}OH$ and $SO_4^{\bullet-}$ radicals during the catalytic oxidation. 5, 5-dimethyl-pyrroline-oxide (DMPO) was used as the spin trapping reagent for $^{\bullet}OH$ and $SO_4^{\bullet-}$ radicals.

Figure 6.5 shows the radical generation of PDS activation with the presence of

nitrobenzene without N-SWCNT as the binary system at different reaction temperatures (5, 25, and 45 °C). At all time, $^{\bullet}OH$ and $SO_4^{\bullet-}$ radicals were detected by EPR spectra. Sulfate radicals are usually considered as the dominant reactive species generated in PDS-based AOPs. Nevertheless, it is known that nitrobenzene will only react with $^{\bullet}OH$ radical due to its high reactivity compared to that of $SO_4^{\bullet-}$ radical [22]. In this study, $^{\bullet}OH$ radicals appeared as the major species at all reaction temperatures. Both the oxidative system and the in situ EPR suggest that the temperature-dependent PDS activation tend to activate PDS to generate hydroxyl radicals for nitrobenzene degradation.

The mechanism is as follow. First PDS is initially hydrolized to peroxymonosulfate and sulfate from **Equation 6.1** [24]. Then, the hydroperoxide generated from the hydrolysis of PDS reduces another PDS forming sulfate radical ($SO_4^{\bullet-}$), sulfate anion and superoxide (O_2) (**Equation 6.2**). At low pH regimes, sulfate radical from **Equation 6.3** reacts with hydroxide to form hydroxyl radical [22].

$$S_2O_8^{2-} + H_2O \xrightarrow{OH^-} SO_5^{2-} + SO_4^{2-} + 2H^+ \quad (6.1)$$

$$S_2O_8^{2-} + HO_2^- \rightarrow SO_4^{\bullet-} + SO_4^{2-} + H^+ + O_2^{\bullet-} \quad (6.2)$$

$$SO_4^{\bullet-} + OH^- \rightarrow SO_4^{2-} + OH^{\bullet} \quad (6.3)$$

$$Nitrobenzene + {}^{\bullet}OH \rightarrow intermediates \quad (6.4)$$

$$Intermediates + {}^{\bullet}OH \rightarrow CO_2 + H_2O + inorganic\ compounds \quad (6.5)$$

Here, NB will react with $^{\bullet}OH$ radical to form intermediates (**Equation 6.4**) [25]. Finally, the intermediates react with another $^{\bullet}OH$ radical to form CO_2, H_2O and inorganic compounds (**Equation 6.5**).

Another NB degradation pathway for higher temperature may also be proposed following the **Equation 6.6** to **6.9** [4, 26].

$$S_2O_8^{2-} \xrightarrow{heat} 2SO_4^{\bullet-} \quad (6.6)$$

$$SO_4^{\bullet-} + H_2O \rightarrow OH^{\bullet} + HSO_4^- \quad (6.7)$$

$$OH^{\bullet} + NB \rightarrow NB^{\bullet} + OH^- \quad (6.8)$$

$$NB^{\bullet} + S_2O_8^{2-} \rightarrow SO_4^{-\bullet} + products \quad (6.9)$$

$SO_4^{\bullet-}$ radicals were generated from heat decomposition of PDS (**Equation 6.6**). The $SO_4^{\bullet-}$ radical generated from **Equation 6.9** reacts with water to form $^{\bullet}OH$ radical (**Equation 6.7**). This $^{\bullet}OH$ radical will further degrade nitrobenzene (**Equation 6.8**).

Equations 6.6 to **6.9** may be able to explain the better performance of NB degradation using PDS only from 55 to 75 °C as compared to PMS only (see **Figure 6.3**). Although the symmetric molecular structure of PDS is more difficult to undergo S-O bond fission compared to the asymmetric structure of PMS.

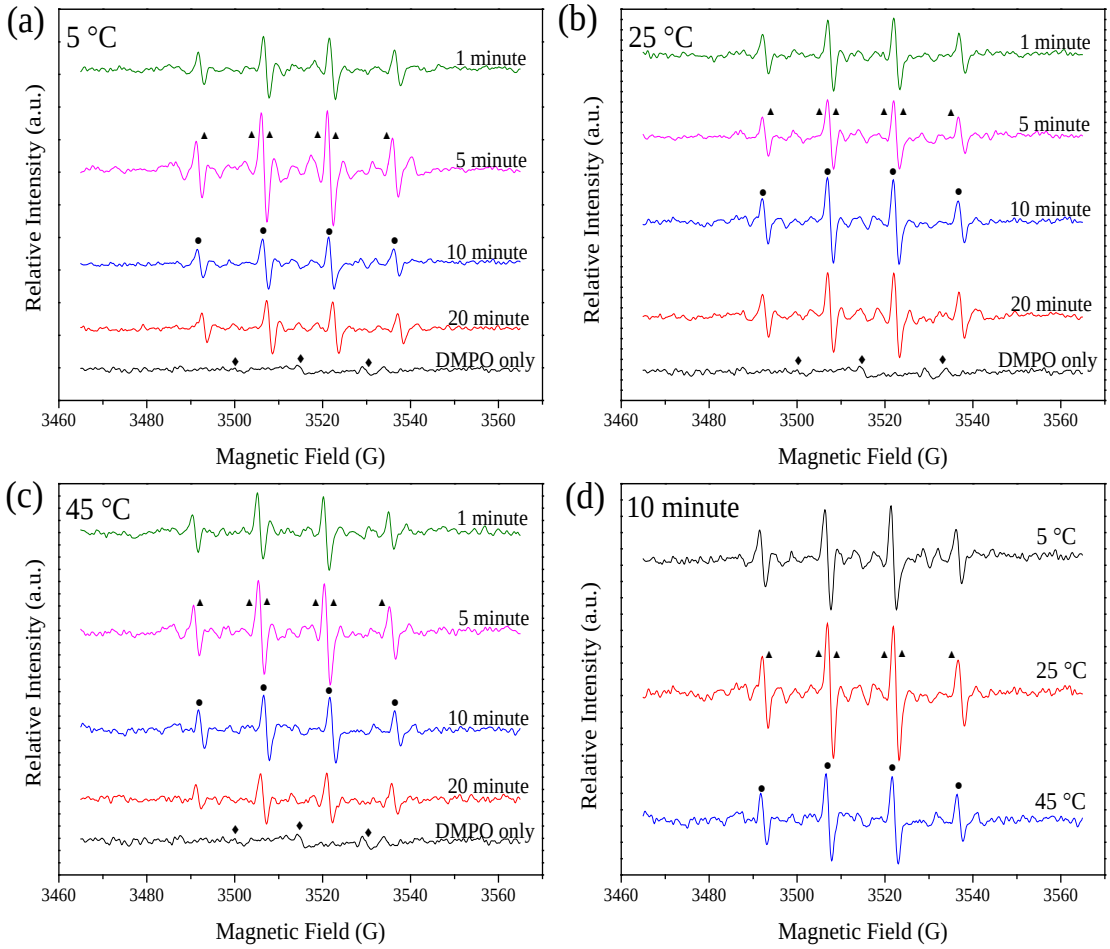

Figure 6.5. EPR spectra of PDS only in nitrobenzene degradation at different reaction temperature (a) 5 °C, (b) 25 °C, (c) 45 °C and (d) Comparison of EPR spectra of PDS activation at 10 minutes without N-SWCNT at 5 °C, 25 °C, and 45 °C (♦) DMPO-X (▲) DMPO- SO_4 (●) DMPO- OH.

Figure 6.6 shows the radical generation of PDS activation with the presence of nitrobenzene and N-SWCNT as the ternary system at different reaction temperatures (5, 25, and 45 °C). It can be seen that $^{\bullet}OH$ radicals also appeared as the major species for all reaction temperatures at all times. The existence of a carbocatalyst not only alters the PDS activation pathways, but also acts as an excellent media for electron transfer. As a result, the enhanced performance in PDS activation to produce hydroxyl radicals was identified in the carbo-catalytic systems.

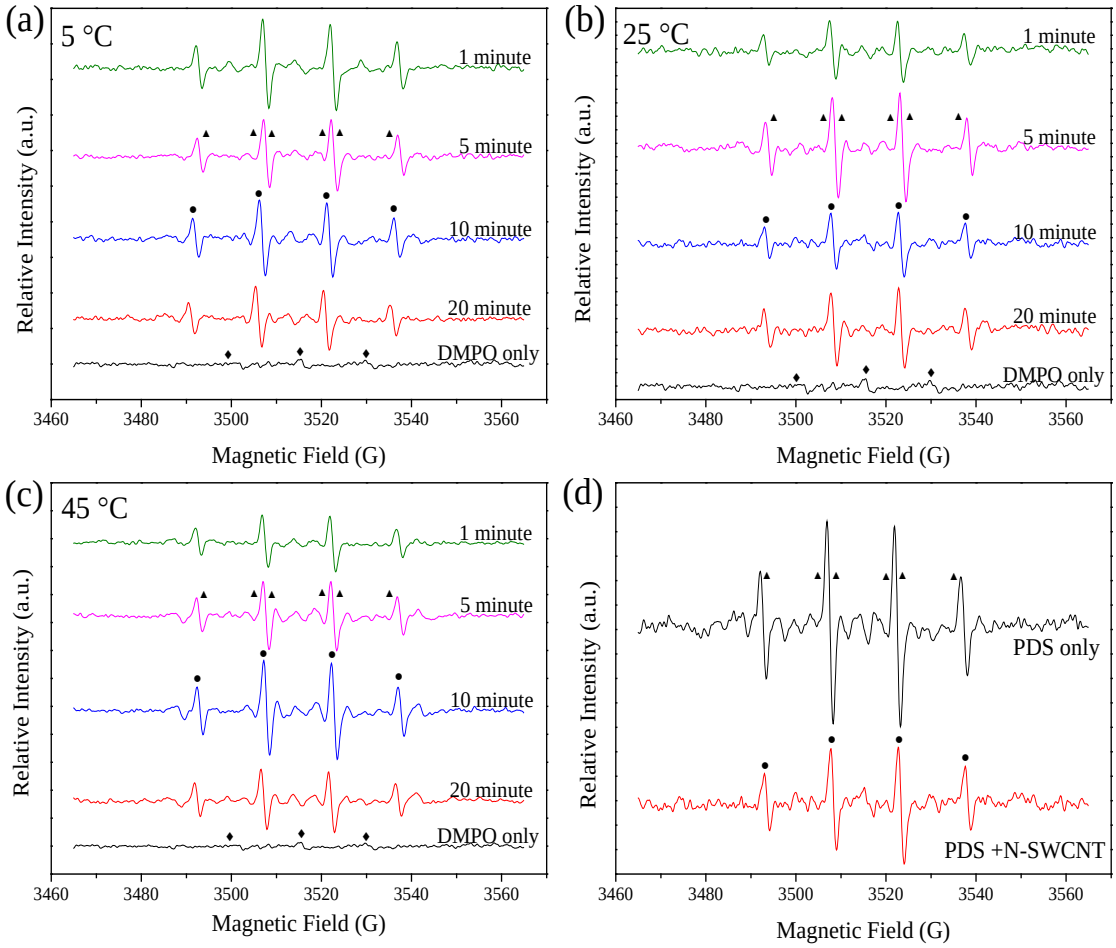

Figure 6.6. EPR spectra of PDS and N-SWCNT 700 °C in nitrobenzene degradation in different reaction temperatures (a) 5 °C, (b) 25 °C, (c) 45 °C and (d) Comparison of EPR spectra of PDS with and without N-SWCNT at 25 °C and 10 min (♦) DMPO-X (▲) DMPO- SO_4 (●) DMPO-OH.

It is well known that $^{\bullet}OH$ and $SO_4^{\bullet-}$ radicals demonstrate different reaction rates toward two radical scavengers, methanol and tert-butyl alcohol (TBA) ($k_{\bullet OH,\ methanol}$ = $9.7 \times 10^8\ M^{-1}s^{-1}$, $k_{SO4^{\bullet-},\ methanol} = 2.5 \times 10^7\ M^{-1}s^{-1}$, $k_{\bullet OH,\ TBA} = 3.8 \times 10^8$ - $7.6 \times 10^8\ M^{-1}s^{-1}$) [27-28]. Methanol can capture both $^{\bullet}OH$ and $SO_4^{\bullet-}$ while TBA prefers to capture $^{\bullet}OH$ radicals rather than $SO_4^{\bullet-}$ radicals. **Figure 6.7** displays nitrobenzene degradation by N-SWCNT activation of PDS with different quenching reagents at 45 °C. It is shown that 60% of NB was degraded within 180 min with the addition of methanol or TBA, which is due to the adsorption. It can be seen that NB degradation performance is hindered by the addition of methanol or TBA. Both PDS and NB are electron acceptors, therefore the performance of NB degradation is hindered by the presence of PDS which appears to be more attracted to N-SWCNT as an electron

donor [29]. This indicates that the hydroxyl radicals are the principal reactive species accounting for nitrobenzene degradation with N-SWCNT as an electron mediator in the ternary system.

PDS reacts with water and therefore generate peroxomonosulfate (SO_5^-, **Equation 6.10**) or peroxymonosulfate (HSO_5^-, **Equation 6.11**) [24, 30]. The nitrobenzene degradation is most likely due to the $^{\bullet}OH$ radicals which were generated from **Equation 6.11** or from $SO_4^{\bullet-}$ radicals (**Equation 6.14**) where N-SWCNT would contribute to the electron and heat transfer processes and facilitate PDS activation processes.

$$S_2O_8^{2-} + H_2O \xrightarrow{OH^-} SO_5^- + SO_4^{2-} + 2H^+ \quad (6.10)$$

$$S_2O_8^{2-} + H_2O \xrightarrow{OH^-} HSO_5^- + SO_4^{2-} + H^+ \quad (6.11)$$

$$HSO_5^- + e^- \rightarrow {}^{\bullet}OH + SO_4^{2-} \quad (6.12)$$

$$HSO_5^- + e^- \rightarrow SO_4^{\bullet-} + OH^- \quad (6.13)$$

$$SO_4^{\bullet-} + OH^- \rightarrow SO_4^{2-} + {}^{\bullet}OH \quad (6.14)$$

$$\text{Nitrobenzene} + {}^{\bullet}OH \rightarrow \text{intermediates} \rightarrow CO_2 + H_2O + \text{inorganic compounds} \quad (6.15)$$

It is noted that the performance of NB degradation using PDS with N-SWCNT is worse than that of PMS with N-SWCNT (**Figure 6.2d** and Chapter 5 **Figure 5.4d**). It may be due to symmetric structure of PDS which made it more difficult to undergo S-O bond fission [15].

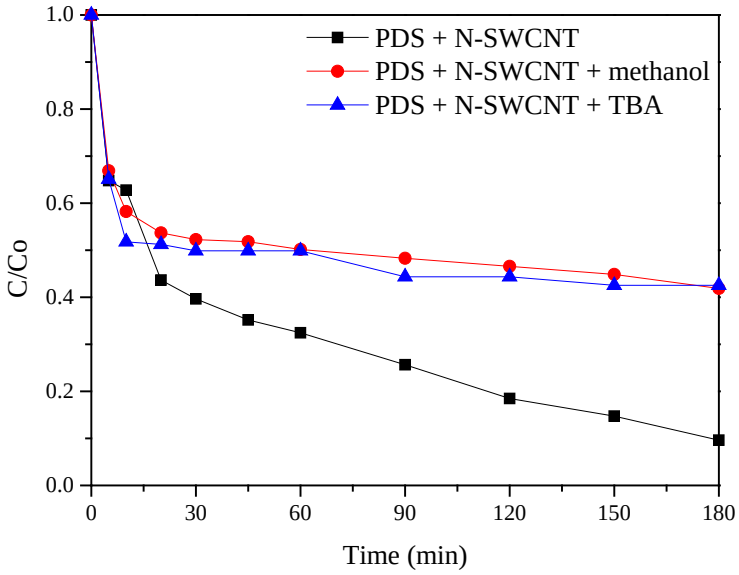

Figure 6.7 (a) Nitrobenzene degradation using N-SWCNT by PDS activation with addition of methanol and TBA at 45 °C ($[methanol]_0$ = 0.22 M , $[TBA]_0$ = 0.2 M, [pH]= 3).

6.3.4. Phenol degradation at higher reaction temperatures

Recent studies of PMS activation on carbocatalysts showed that $SO_4^{\bullet-}$ radicals play a major role in catalytic oxidation of phenol [31-33]. In this chapter, heat activation of PMS have been done in order to elucidate if $SO_4^{\bullet-}$ radicals still play a major role in phenol degradation.

Due to the better performance of NB degradation using PDS only from 55 to 75 °C compared with PMS only (**Figure 6.3**), further experiments have been done by observing the activation of PMS only and PDS only from 55 to 75 °C for phenol degradation (see **Figure 6.8**).

Figure 6.8a shows phenol degradation using PMS only from 55 to 75 °C reaction temperatures. It can be seen that complete phenol removal occurs within 120, 90, and 30 min for reaction temperatures 55, 65, and 75 °C, respectively. Complete phenol removal at 75 °C reaction temperature using PMS with the addition of quenching agent TBA, occurs within 45 min. As discussed in section 6.3.3, TBA prefers to capture $^{\bullet}OH$ radicals rather than $SO_4^{\bullet-}$ radicals. This result shows that $SO_4^{\bullet-}$ radicals are the dominant radical species for phenol degradation.

Figure 6.8b shows phenol degradation using PDS only from 55 to 75 °C reaction temperatures. It can be seen that 70% of phenol was degraded within 180 min for reaction temperature 55 °C. Complete phenol removal occurs within 150, and 30 min for reaction temperatures 65 and 75 °C, respectively. Complete phenol removal occurs within 45 min at 75 °C using PDS with the addition of quenching agent TBA.

Figure 6.8c shows the comparison of phenol degradation from 55 to 75 °C using PMS only and PDS only. It can be seen that the performance of phenol degradation using PMS only is better than using PDS only. This may be due to the asymmetric structure of PMS which makes it easy to undergo fission of the S-O bond, hence a faster degradation, as opposed to the symmetric structure of PDS [15, 23].

Both symmetric PDS and asymmetric PMS can degrade NB and phenol. However, different radicals play a major role in the mechanism degradation. In acidic condition, $SO_4^{\bullet-}$ radicals are more selective for oxidation compared to $^{\bullet}OH$ radicals (see **Figure 6.3** and **Figure 6.8**), even though they have similar reduction potential [34]. Here, it was found that $^{\bullet}OH$ radicals play a dominant role in NB degradation, while $SO_4^{\bullet-}$ radicals play a dominant role in phenol degradation.

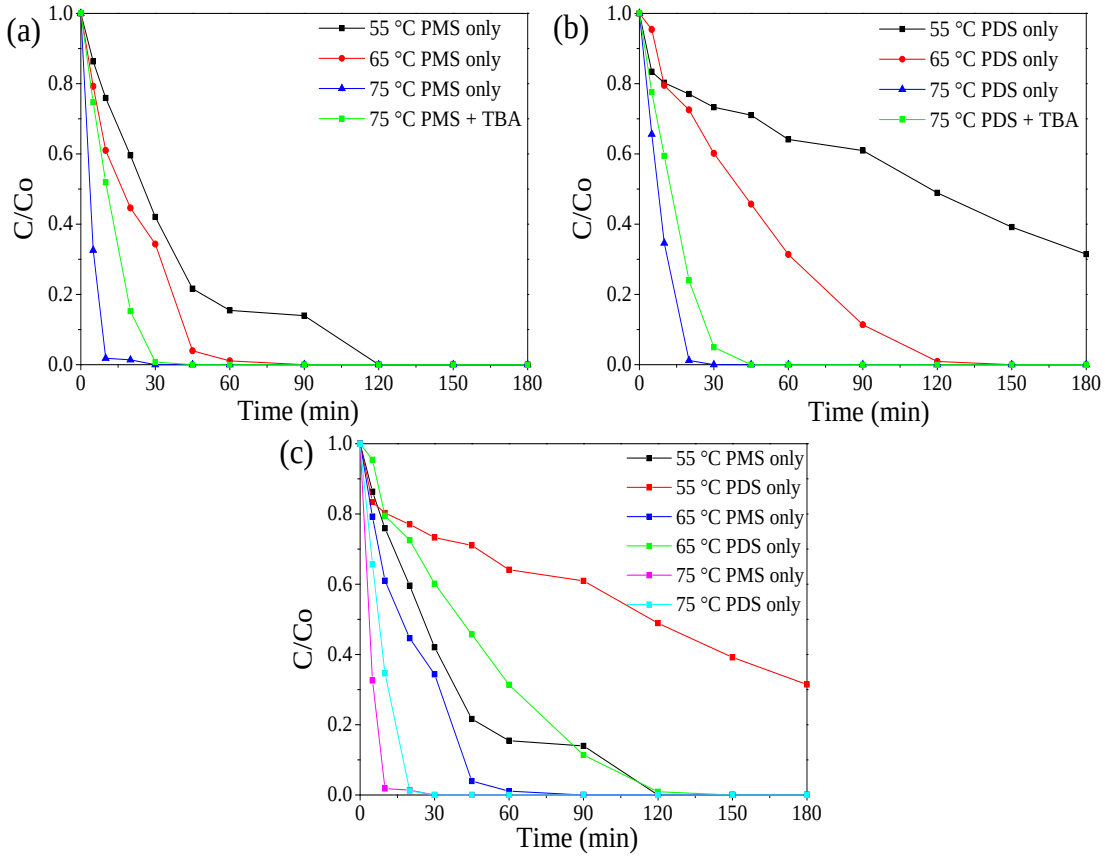

Figure 6.8. Phenol degradation at 55 to 75 °C reaction temperatures using (a) PMS only, (b) PDS only, and (c) Comparison of PMS only and PDS only ([pH]= 3).

6.3.5. Further EPR study of PDS and PMS in water

Figure 6.9a shows the EPR spectra of PMS in water at 25 °C. It shows that $^{\bullet}OH$ and $SO_4^{\bullet-}$ radicals appeared at all time from 3 min to 20 min. It is observed that the intensity of $^{\bullet}OH$ and $SO_4^{\bullet-}$ radicals are apparent at 20 min. The mechanism can be proposed as follows:

PMS in **Equation 6.16** is initially hydrolized to hydroperoxide (HO_2^-) and sulfate[24]. Then, the hydroperoxide generated from the hydrolysis of PMS reduces another PMS forming sulfate radical ($SO_4^{\bullet-}$), sulfate anion and superoxide (O_2) (**Equation 6.17**) [24]. At low pH regimes, sulfate radical reacts with water to form hydroxyl radical (**Equation 6.18**) [22].

$$SO_5^- + H_2O \xrightarrow{OH^-} HO_2^- + SO_4^{2-} + H^+ \qquad (6.16)$$

$$2(SO_5^-) + HO_2^- \rightarrow SO_4^{\bullet-} + SO_4^{2-} + H^+ + 2O_2^{\bullet-} \qquad (6.17)$$

$$SO_4^{\bullet-} + H_2O \rightarrow SO_4^{2-} + OH^{\bullet} + H^+ \qquad (6.18)$$

Figure 6.9b shows the EPR spectra of PMS in water at 45 °C. It shows that $^{\bullet}OH$ and $SO_4^{\bullet-}$ radicals appeared at all time from 1 min to 60 min. It is observed that the intensity of $^{\bullet}OH$ and $SO_4^{\bullet-}$ radicals are apparent at 20 min.

Figure 6.9c shows the EPR spectra of PMS in water at 25 °C with three times higher the PMS concentration (19.5 x 10^{-3} M). It shows that $^{\bullet}OH$ and $SO_4^{\bullet-}$ radicals appeared at all time from 1 min to 60 min, and more apparent at 20 min.

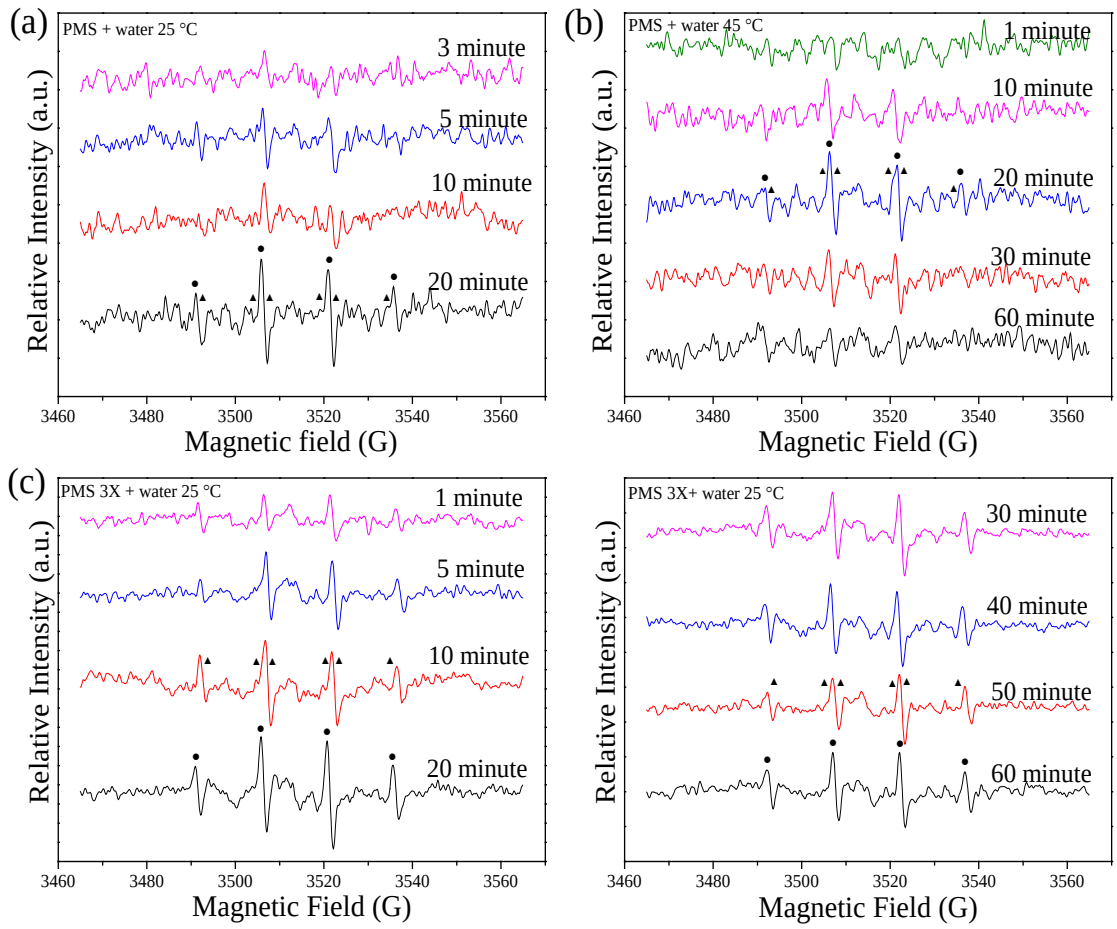

Figure 6.9. EPR spectra of PMS in water (a) [PMS] = 6.5 x 10^{-3} M at 25 °C, (b) [PMS] = 6.5 x 10^{-3} M at 45 °C and (c) [PMS] = 19.5 x 10^{-3} M at 25 °C (▲) DMPO-SO_4 (●) DMPO-OH.

Figure 6.10a shows the EPR spectra of PDS in water at 45 °C. It shows that $^{\bullet}OH$ and $SO_4^{\bullet-}$ radicals appeared at all time from 1 min to 60 min. It is observed that the intensities of $^{\bullet}OH$ and $SO_4^{\bullet-}$ radicals are strong at 20 and 60 min.

Figure 6.10b shows the EPR spectra of PDS in water at 45 °C with three times higher the PDS concentration (19.5 x 10^{-3} M). It shows that $^{\bullet}OH$ and $SO_4^{\bullet-}$ radicals appeared at all time from 1 min to 60 min.

It can be seem from **Figure 6.9b** and **Figure 6.10a** at 20 min and 45 °C, $^{\bullet}OH$ radicals appears to be more dominant in both PMS and PDS activation. This can be explained by **Equation 6.7** (from Section 6.3.3).

In these kinetic studies, the degradation of NB with PMS or PDS occurs in two stages with the transition temperature at about 35 and 45 °C. Here, the temperature was chosen at 45 °C to investigate the behaviour of PMS and PDS in water to generate $^{\bullet}OH$ and $SO_4^{\bullet-}$ radicals. **Figure 6.9** and **Figure 6.10** show that both PMS and PDS have almost similar characteristic to generate $^{\bullet}OH$ and $SO_4^{\bullet-}$ radicals in water at 45 °C for 1 min to 60 min.

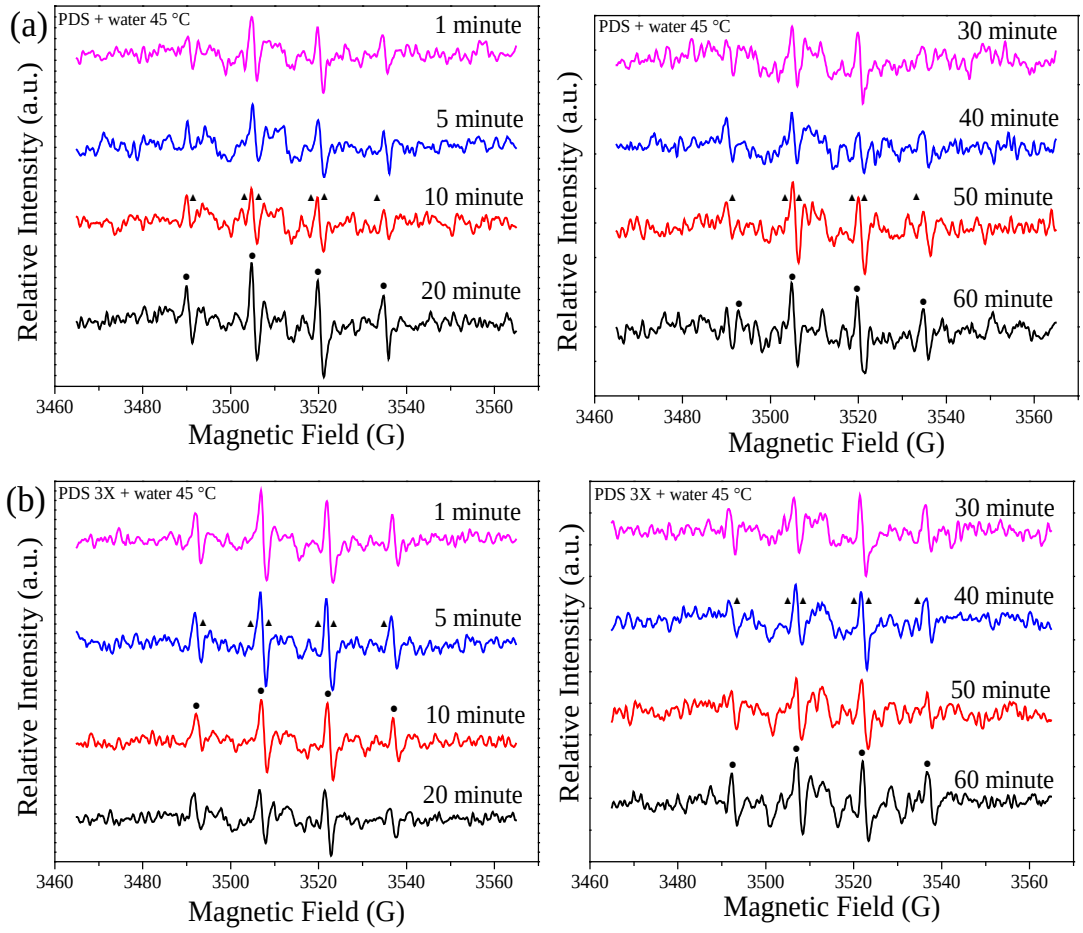

Figure 6.10. EPR spectra of PDS in water 45 °C with (a) [PDS] = 6.5 x 10^{-3} M and (b) [PDS] = 19.5 x 10^{-3} M (▲) DMPO- SO_4 (●) DMPO-OH.

Figure 6.11 shows the comparison of EPR spectra of PMS activation in 20 ppm nitrobenzene solution with/ without the addition of TBA at 20 minutes and room temperature (25 °C). It is seen that the peak intensity of $^{\bullet}OH$ radicals is very strong for PMS activation in NB without the addition of TBA. While the peak intensity of $^{\bullet}OH$ radicals decreased significantly or almost disappeared after the addition of TBA. As explained in section 6.3.3, TBA prefers to capture $^{\bullet}OH$ radicals than $SO_4^{\bullet-}$ radicals. The EPR spectra proved that TBA can indeed capture $^{\bullet}OH$ radicals.

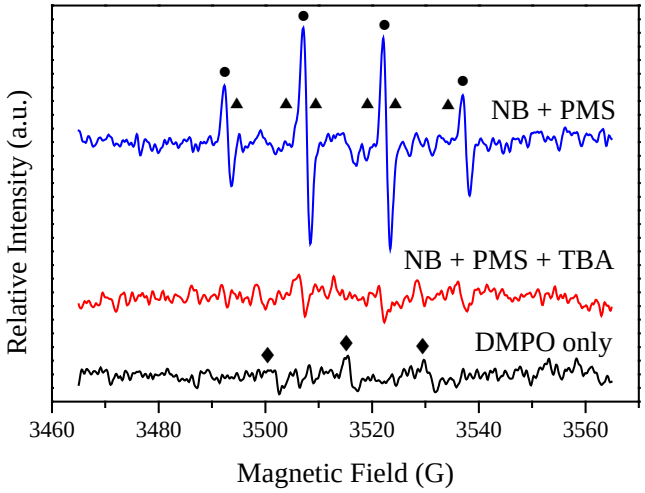

Figure 6.11. Comparison EPR spectra of NB and PMS with the addition of TBA at 20 minutes at 25 °C (♦) DMPO-X (▲) DMPO- SO_4 (●) DMPO-OH.

6.4. Conclusions

N-SWCNT was synthesized by a simple nitrogen doping method, annealing SWCNT with urea at 700 °C. PDS activation for nitrobenzene degradation with/without N-SWCNT was investigated at different reaction temperatures from 5 to 75 °C. PDS and PMS activation for phenol degradation was investigated at temperature 55 to 75 °C. Thermal effect enhanced PDS/PMS activation to generate hydroxyl radicals and further improved the effectiveness of nitrobenzene and phenol degradation. Both symmetric PDS and asymmetric PMS can degrade NB and phenol. However, different radicals play a major role in the mechanism degradation. Hydroxyl radicals contribute as the main radicals to nitrobenzene degradation on PDS with and without N-SWCNT, while sulfate radicals play a dominant role in phenol degradation. In the binary system (NB and PDS), the $^{\bullet}OH$ radicals were generated through the

hydrolysis process and nitrobenzene removal is attributed to the physisorption and chemisorptions via π electron donor-acceptor mechanisms. In the ternary system (NB, PDS and N-SWCNT), the $^{\bullet}OH$ radicals were generated through the electron transfer process.

References

1. Pereira, M. C.; Oliveira, L. C. A.; Murad, E., Iron oxide catalysts: Fenton and Fenton-like reactions - a review. *Clay Min.* **2012,** *47* (3), 285-302.
2. Pera-Titus, M.; Garcia-Molina, V.; Banos, M. A.; Gimenez, J.; Esplugas, S., Degradation of chlorophenols by means of advanced oxidation processes: a general review. *Appl. Catal. B-Environ.* **2004,** *47* (4), 219-256.
3. Rao, D. G.; Senthilkumar, R.; Byrne, J. A.; Feroz, S., *Wastewater Treatment: Advanced Processes and Technologies*. Taylor & Francis: **2012**.
4. Sun, H.; Wang, S., Chapter 6 Catalytic oxidation of organic pollutants in aqueous solution using sulfate radicals. In *Catalysis: Volume 27*, The Royal Society of Chemistry: **2015**, pp 209-247.
5. Zhang, T.; Chen, Y.; Wang, Y.; Le Roux, J.; Yang, Y.; Croué, J.-P., Efficient Peroxydisulfate Activation Process Not Relying on Sulfate Radical Generation for Water Pollutant Degradation. *Environ. Sci. Technol.* **2014,** *48* (10), 5868-5875.
6. Xu, X. R.; Li, X. Z., Degradation of azo dye Orange G in aqueous solutions by persulfate with ferrous ion. *Sep. Purif. Technol.* **2010,** *72* (1), 105-111.
7. Waldemer, R. H.; Tratnyek, P. G.; Johnson, R. L.; Nurmi, J. T., Oxidation of chlorinated ethenes by heat-activated persulfate: Kinetics and products. *Environ. Sci. Technol.* **2007,** *41* (3), 1010-1015.
8. Fang, G. D.; Dionysiou, D. D.; Al-Abed, S. R.; Zhou, D. M., Superoxide radical driving the activation of persulfate by magnetite nanoparticles: Implications for the degradation of PCBs. *Appl. Catal. B-Environ.* **2013,** *129*, 325-332.
9. Oh, S. Y.; Kang, S. G.; Chiu, P. C., Degradation of 2,4-dinitrotoluene by persulfate activated with zero-valent iron. *Science of the Total Environment* **2010,** *408* (16), 3464-3468.
10. Al-Shamsi, M. A.; Thomson, N. R., Treatment of Organic Compounds by Activated Persulfate Using Nanoscale Zerovalent Iron. *Ind. Eng. Chem. Res.* **2013,** *52* (38), 13564-13571.

11. Weng, C.-H.; Tao, H., Highly efficient persulfate oxidation process activated with Fe0 aggregate for decolorization of reactive azo dye Remazol Golden Yellow. *Arabian Journal of Chemistry*.

12. Yan, J. C.; Gao, W. G.; Qian, L. B.; Han, L.; Chen, Y.; Chen, M. F., Remediation of Nitrobenzene Contaminated Soil by Combining Surfactant Enhanced Soil Washing and Effluent Oxidation with Persulfate. *Plos One* **2015,** *10* (8).

13. Lin, Y. T.; Liang, C. J.; Yu, C. W., Trichloroethylene Degradation by Various Forms of Iron Activated Persulfate Oxidation with or without the Assistance of Ascorbic Acid. *Ind. Eng. Chem. Res.* **2016,** *55* (8), 2302-2308.

14. Long, A. H.; Lei, Y.; Zhang, H., Degradation of Toluene by a Selective Ferrous Ion Activated Persulfate Oxidation Process. *Ind. Eng. Chem. Res.* **2014,** *53* (3), 1033-1039.

15. Duan, X. G.; Sun, H. Q.; Kang, J.; Wang, Y. X.; Indrawirawan, S.; Wang, S. B., Insights into Heterogeneous Catalysis of Persulfate Activation on Dimensional-Structured Nanocarbons. *ACS Catal.* **2015,** *5* (8), 4629-4636.

16. Duan, X. G.; Ao, Z. M.; Sun, H. Q.; Zhou, L.; Wang, G. X.; Wang, S. B., Insights into N-doping in single-walled carbon nanotubes for enhanced activation of superoxides: a mechanistic study. *Chem. Commun.* **2015,** *51* (83), 15249-15252.

17. Sun, H.; Kwan, C.; Suvorova, A.; Ang, H. M.; Tadé, M. O.; Wang, S., Catalytic oxidation of organic pollutants on pristine and surface nitrogen-modified carbon nanotubes with sulfate radicals. *Applied Catalysis B: Environmental* **2014,** *154–155*, 134-141.

18. Dresselhaus, M. S.; Jorio, A.; Hofmann, M.; Dresselhaus, G.; Saito, R., Perspectives on Carbon Nanotubes and Graphene Raman Spectroscopy. *Nano Letters* **2010,** *10* (3), 751-758.

19. Anderson, N.; Hartschuh, A.; Cronin, S.; Novotny, L., Nanoscale vibrational analysis of single-walled carbon nanotubes. *Journal of the American Chemical Society* **2005,** *127* (8), 2533-2537.

20. Graupner, R., Raman spectroscopy of covalently functionalized single-wall carbon nanotubes. *Journal of Raman Spectroscopy* **2007,** *38* (6), 673-683.

21. Tian, W. J.; Zhang, H. Y.; Duan, X. G.; Sun, H. Q.; Tade, M. O.; Ang, H. M.; Wang, S. B., Nitrogen- and Sulfur-Codoped Hierarchically Porous Carbon for Adsorptive and Oxidative Removal of Pharmaceutical Contaminants. *Acs Applied Materials & Interfaces* **2016,** *8* (11), 7184-7193.

22. Ahmad, M.; Teel, A. L.; Watts, R. J., Mechanism of Persulfate Activation by Phenols. *Environ. Sci. Technol.* **2013,** *47* (11), 5864-5871.

23. Guan, Y. H.; Ma, J.; Ren, Y. M.; Liu, Y. L.; Xiao, J. Y.; Lin, L. Q.; Zhang, C., Efficient degradation of atrazine by magnetic porous copper ferrite catalyzed peroxymonosulfate oxidation via the formation of hydroxyl and sulfate radicals. *Water Res.* **2013,** *47* (14), 5431-5438.

24. Furman, O. S.; Teel, A. L.; Watts, R. J., Mechanism of Base Activation of Persulfate. *Environ. Sci. Technol.* **2010,** *44* (16), 6423-6428.

25. Celin, S. M.; Pandit, M.; Kapoor, J. C.; Sharma, R. K., Photoperoxidation of nitrobenzene in aqueous phase. *Indian J. Chem. Technol.* **2004,** *11* (2), 266-270.

26. Huang, K.-C.; Couttenye, R. A.; Hoag, G. E., Kinetics of heat-assisted persulfate oxidation of methyl tert-butyl ether (MTBE). *Chemosphere* **2002,** *49* (4), 413-420.

27. Wang, Y. X.; Sun, H. Q.; Ang, H. M.; Tade, M. O.; Wang, S. B., 3D-hierarchically structured MnO2 for catalytic oxidation of phenol solutions by activation of peroxymonosulfate: Structure dependence and mechanism. *Appl. Catal. B-Environ.* **2015,** *164*, 159-167.

28. Buxton, G. V.; Greenstock, C. L.; Helman, W. P.; Ross, A. B., CRITICAL-REVIEW OF RATE CONSTANTS FOR REACTIONS OF HYDRATED ELECTRONS, HYDROGEN-ATOMS AND HYDROXYL RADICALS (.OH/.O-) IN AQUEOUS-SOLUTION. *J. Phys. Chem. Ref. Data* **1988,** *17* (2), 513-886.

29. Lee, H.; Lee, H.-J.; Jeong, J.; Lee, J.; Park, N.-B.; Lee, C., Activation of persulfates by carbon nanotubes: Oxidation of organic compounds by nonradical mechanism. *Chem. Eng. J.* **2015,** *266*, 28-33.

30. Siegrist, R. L.; Crimi, M.; Simpkin, T. J., *In Situ Chemical Oxidation for Groundwater Remediation*. Springer New York: **2011**.

31. Duan, X. G.; Ao, Z. M.; Sun, H. Q.; Indrawirawan, S.; Wang, Y. X.; Kang, J.; Liang, F. L.; Zhu, Z. H.; Wang, S. B., Nitrogen-Doped Graphene for Generation and Evolution of Reactive Radicals by Metal-Free Catalysis. *Acs Applied Materials & Interfaces* **2015,** *7* (7), 4169-4178.

32. Indrawirawan, S.; Sun, H. Q.; Duan, X. G.; Wang, S. B., Low temperature combustion synthesis of nitrogen-doped graphene for metal-free catalytic oxidation. *J. Mater. Chem. A* **2015,** *3* (7), 3432-3440.

33. Indrawirawan, S.; Sun, H. Q.; Duan, X. G.; Wang, S. B., Nanocarbons in different structural dimensions (0-3D) for phenol adsorption and metal-free catalytic oxidation. *Appl. Catal. B-Environ.* **2015,** *179*, 352-362.
34. Anipsitakis, G. P.; Dionysiou, D. D., Radical generation by the interaction of transition metals with common oxidants. *Environ. Sci. Technol.* **2004,** *38* (13), 3705-3712.

CHAPTER 7

Modified nitrogen doped graphene by various metals for catalytic and photocatalytic oxidation of organic contaminants

Abstract

Modified nitrogen doped graphene (N-rGO) by various transition or noble metals such as, Pt-NrGO, Fe-NrGO, Ni-NrGO, Ag-NrGO and Co-NrGO were prepared by a simple method of nitrogen and metal co-doping on graphene oxide (GO) at 350 °C using urea as the N precursor. These various metal doped NrGO samples were investigated by catalytic activation of oxidants such as peroxymonosulfate (PMS), persulfate (PDS) and hydrogen peroxide (H_2O_2) for phenol degradation in water solutions. The results showed that phenol degradation by PMS activation was enhanced by modified N-rGO. Photocatalytic performances in photodegradation of phenol and methylene blue (MB) using ultraviolet and visible (UV-vis) and visible light were also investigated. In general, photodegradation of MB was more efficient using UV-vis light due to the shorter wavelength of UV-vis (< 400 nm). Various characterisation techniques were applied to study the properties of the graphene samples, such as: XRD, FTIR, SEM, EDS, TG-DSC, BET and Raman analysis.

7.1. Introduction

Environmental pollution has become one of major issues in today's life. Not only organic but also inorganic pollutants have contaminated our environment and water sources such as lakes, rivers and oceans. Advanced oxidation processes (AOPs) are an effective water purification technology that has attracted extensive attention [1-2]. This technology depends on highly reactive free radicals, such as hydroxyl radicals ($OH^{\bullet}$) and sulfate radicals ($SO_4^{\bullet-}$). $OH^{\bullet}$ radicals are highly reactive due to their unpaired electrons. An oxidant is able to initiate a chemical reaction to produce unpaired electrons which then generate $OH^{\bullet}$ radicals [3-4]. The contaminants will be degraded after being reacted with the radicals. There are many types of AOPs, such as Fenton reaction, catalytic oxidation, photocatalysis and ozonation processes.

Catalytic oxidation by activation of strong oxidants has also become more promising in the water treatment techniques. Commonly used oxidants are peroxomonosulfate (PMS), peroxydisulfate or persulfate (PDS), and hydrogen peroxide (H_2O_2) [5-7]. Photocatalysis has attracted increasing attention due to its environmental applications such as air clean-up, water purification, water disinfection and hazardous waste remediation [8-10]. In the past years, scientists have been intensively investigating heterogeneous catalytic oxidation and photocatalysis in order to remove organic and inorganic contaminants. Metal catalysts (MnO_2, Co_3O_4, RuO_2, Al_2O_3), metal-free catalysts (graphene, graphene oxide (GO), carbon nanotubes (CNT), mesoporous carbons) and semi conductors (TiO_2, ZnO, ZnS, CdS, Fe_2O_3) that are used for catalytic oxidation and heterogeneous photocatalysis have shown immense potentials for environmental remediation technology due to the advantages over conventional technologies for organic pollutants degradation into harmless final products [9, 11-17].

Over the past decade, graphene has shown to be a promising candidate as a metal-free catalyst due to its superior physical and chemical properties. Previous studies found that graphene doped with organic elements such as boron and nitrogen had enhanced catalytic oxidation performances for phenol degradation [13, 18]. It also has been established that the combination of TiO_2 (P25) and graphene produced potential photocatalysts for air and water purification [19]. P25-graphene displayed superior performances over pure commercial P25 in the photodegradation of methylene blue (MB), a basic dye, under both UV and visible light irradiations. However, the

performance of graphene can still be improved by doping the catalyst with heteroatoms (nitrogen, carbon, halogen and transition metals), by fabricating various composites, and also by manipulating the catalyst morphologies [6, 20-21].

In this chapter, N-rGO was modified by doping with different transition and noble metals to achieve improved performances. Pt-NrGO, Fe-NrGO, Ni-NrGO, Ag-NrGO and Co-NrGO were prepared by a simple nitrogen and metal co-doping process on graphene oxide (GO) at a low temperature using urea as the N precursor. We investigated the catalytic phenol degradation using PMS, PDS, and H_2O_2 as the oxidants. We also further studied the photodegradation activities of MB and phenol under UV-vis and visible light irradiations.

7.2. Experimental Section

7.2.1. Materials and catalysts preparation

All chemicals were obtained from Sigma-Aldrich. A modified Hummers' method was used to synthesis graphene oxide (GO). The graphite powder was mixed with concentrated H_2SO_4 and then $KMnO_4$ was slowly added into the mixture. The mixture was stirred at 35 °C for 5 h. Deionized (DI) water was then slowly added into the mixed solution and the temperature was kept carefully below 98 °C. H_2O_2 is added into the suspension to reduce the residual permanganate. Centrifugation and washing was conducted to obtain GO using hydrochloric acid (HCl) and DI water for three times. The final product was ground after drying in an oven at 60 °C for at least 48 h.

The nitrogen and metal co-doping was conducted simultaneously using urea as the N precursor and respective salts as the metal precursors. Typically, 1.0 g of GO, 1.0 g of urea and 1% of iron nitrate were mixed in 50 mL ethanol at room temperature for 30 min. The temperature was increased to 50 °C and stirred for a few hours until the ethanol was completely evaporated. The dried mixture was thermally annealed at 350 °C for 1 h. The Fe-NrGO was obtained after being washed using ethanol and DI water three times, and dried in the oven at 60 °C. The same process were repeated using different metal compounds, such as nickel (II) nitrate, silver nitrate, cobalt (II) nitrate, and hexachloroplatinic acid hexahydrate.

7.2.2. Characterization of the catalysts

X-ray diffraction (XRD) patterns were acquired on a Bruker D8-Advanced X-ray instrument using Cu-Kα radiation with λ at 1.5418 Å. Nitrogen sorption isotherms were obtained on a Micrometrics Tristar 3000. The Brunauer-Emmet-Teller (BET) and Barrett-Joyner-Halenda (BJH) methods were applied to evaluate the specific surface area (SSA) and pore size distribution. Fourier transform infrared spectra (FTIR) were recorded on a Bruker instrument with an ATR correction mode. Thermogravimetric-differential scanning calorimetry (TG-DSC) was carried out in an air flow at a flowrate of 100 mL/min with a heating rate of 5 °C on a Perkin-Elmer Diamond thermal analyser. Scanning electron microscopy (SEM) and energy dispersive X-ray spectroscope (EDS) were applied to investigate the morphology and the elements of the nanocarbons on Zeiss Neon 40 EsB FIBSEM. Raman analysis was performed on an ISA dispersive Raman spectroscopy using argon ion laser with a wavelength at 514 nm.

7.2.3. Catalytic activity tests

The catalytic oxidation of phenol was carried out in a 500 mL conical flask with phenol solution (20 ppm), catalyst (0.2 g/L) and PMS (2.0 g/L) or PDS (1.76 g/L) or H_2O_2 (3.03 ml/L) in water bath with a constant-temperature controller for the kinetic studies. At each time interval, 1 mL solution was withdrawn by a syringe, filtered by a 0.45 μm Millipore film, and injected into a vial. Then 0.5 mL of methanol as a quenching reagent was also injected into the reaction solution. The mixed solution was analysed by a high performance liquid chromatography (HPLC, Varian) with a C-18 column and a UV detector set at 270 nm.

7.2.4. Photocatalytic activity tests

The photocatalytic degradation of phenol and methylene blue solutions was carried out in a 1 L double-jacket cylindrical reactor with phenol solution (20 ppm) or methylene blue solution (10 ppm) and the catalyst (0.1 g/L) under UV-vis light or visible light in a constant-temperature controlled water bath. For adsorption process the solution was stirred for 30 min, and then by turning on the lamp the photocatalytic degradation was started. At each time interval, about 3 mL solution

was withdrawn by a syringe, injected into a vial, centrifugation and then the solution was analysed by JASCO UV-vis spectrophotometer (664 nm).

7.3. Results and Discussion

7.3.1. Characterization of metal doped N-rGO

Figure 7.1 shows XRD patterns of rGO, N-rGO and various metal doped NrGO. It is seen that two peaks were observed at 2θ = 24° and 43° for rGO, and 2θ = 26° and 43° (corresponding to the interplanar spacing of 0.35 nm) for N-rGO and various metal doped NrGO.

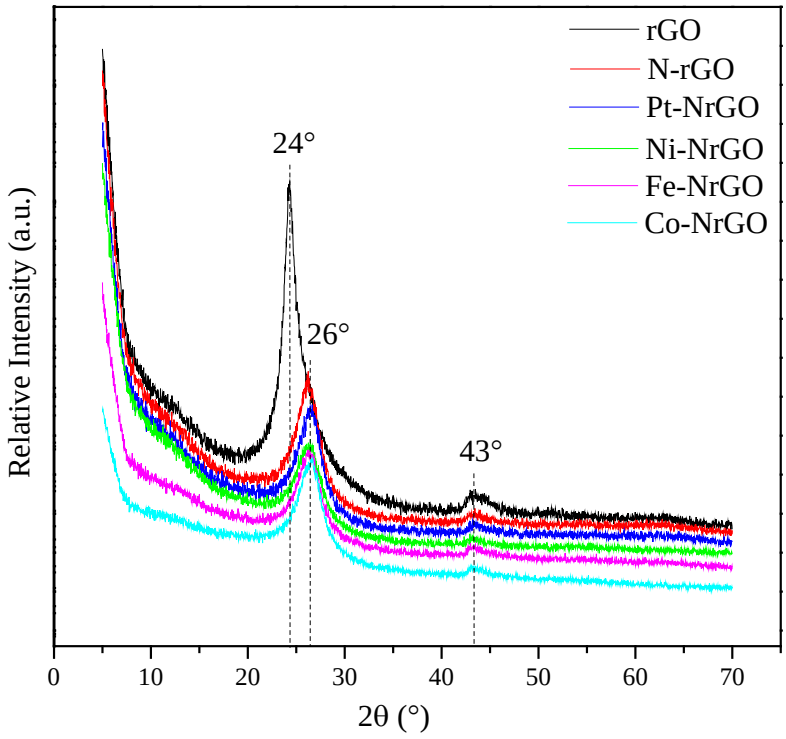

Figure 7.1. XRD patterns of rGO, N-rGO and various metal doped NrGO

The detailed crystal structures of rGO, N-rGO and various metal doped NrGO are shown in **Table 7.1**. Peak broadening at different thermal annealing temperatures can be compared by the half peak width (B). The changes of half peak width values indicated the degree of reduction, removal of oxygen functional groups, and distortion of the lattice periodicity. The origin of the B changes may be due to the increase of the interlayer thickness, L, as shown in **Table 7.1**.

Table 7.1. Crystal- and micro-structures of various metal doped N-rGO samples.

Sample	Half peak width (B, ^{o})	Interlayer material thickness (L, nm)	D band (cm^{-1})	G band (cm^{-1})	I_D/I_G ratio	SSA (m^2/g)
rGO	1.7	4.78	-	-	-	129
N-rGO	2.7	3.02	-	-	-	10.1
Pt-NrGO	3.02	2.7	1333	1588	1.41	11.6
Ni-NrGO	3.23	2.53	1332	1583	1.37	10.3
Fe-NrGO	2.77	2.95	1330	1588	1.42	10.5
Co-NrGO	2.7	3.02	1330	1583	1.42	8.2
Ag-NrGO	-	-	1330	1580	1.37	7.2

Figure 7.2 shows Raman spectra of various metal doped N-rGO. Strong D bands (related to the edges, defects, and structurally disordered carbon) occur at about 1330 cm^{-1} and the G bands (originated from in-plane vibrations of sp^2 carbon) at about 1580 cm^{-1}. The I_D/I_G ratios (intensity ratio of D band to G band) of various metal-doped N-rGO are tabulated in **Table 7.1**. The I_D/I_G ratio shows the degree of defects in the rGO-based materials.

The I_D/I_G ratios of the various metal-doped N-rGO varied between 1.37 and 1.42. Pt-NrGO, Fe-NrGO and Co-NrGO have higher I_D/I_G ratios indicating enhanced defective edges, and declined sp^2 carbon of rGO structures. These results are consistent with higher catalytic oxidation performances shown by Pt-NrGO, Fe-NrGO and Co-NrGO in **Figure 7.7**. However, among the various metal-doped N-rGO samples, no element-dependent I_D/I_G ratio was observed, indicating the complicated processes of simultaneous metal and nitrogen doping, as nitrogen doping might be able to adjust the defective structure as well.

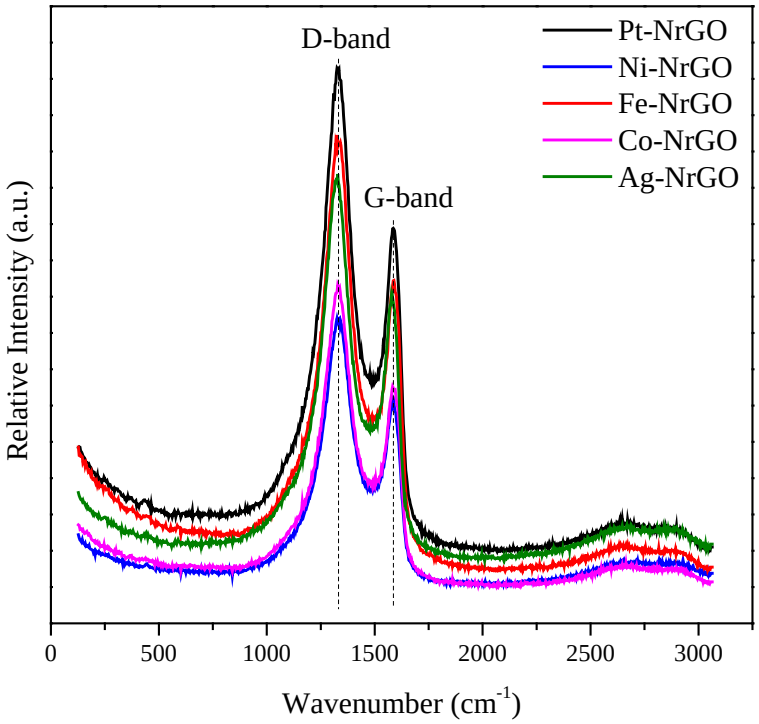

Figure 7.2. Raman spectra of various metal doped N-rGO samples

Figure 7.3 shows nitrogen sorption isotherms of rGO, N-rGO and various metal-doped N-rGO. Pt-NrGO and Fe-NrGO demonstrated higher nitrogen adsorption volumes and larger specific surface area (SSA) values. The SSA values are tabulated in **Table 7.1**. SSA values of N-rGO were slightly increased after metal doping from 10.1 to 10.3, 10.5, and 11.6 m^2/g for Ni-NrGO, Fe-NrGO and Pt-NrGO, respectively. The SSA was decreased to 8.2 and 7.2 m^2/g for Co-NrGO and Ag-NrGO, respectively.

The morphologies of N-rGO and various metal-doped N-rGO were observed by SEM imaging in **Figure 7.4**. N-rGO had a wrinkled structure due to the exfoliation and restacking processes. **Figure 7.4b-f** show the SEM images of various metals-doped N-rGO with irregularly enfolding and wrinkled layered structures.

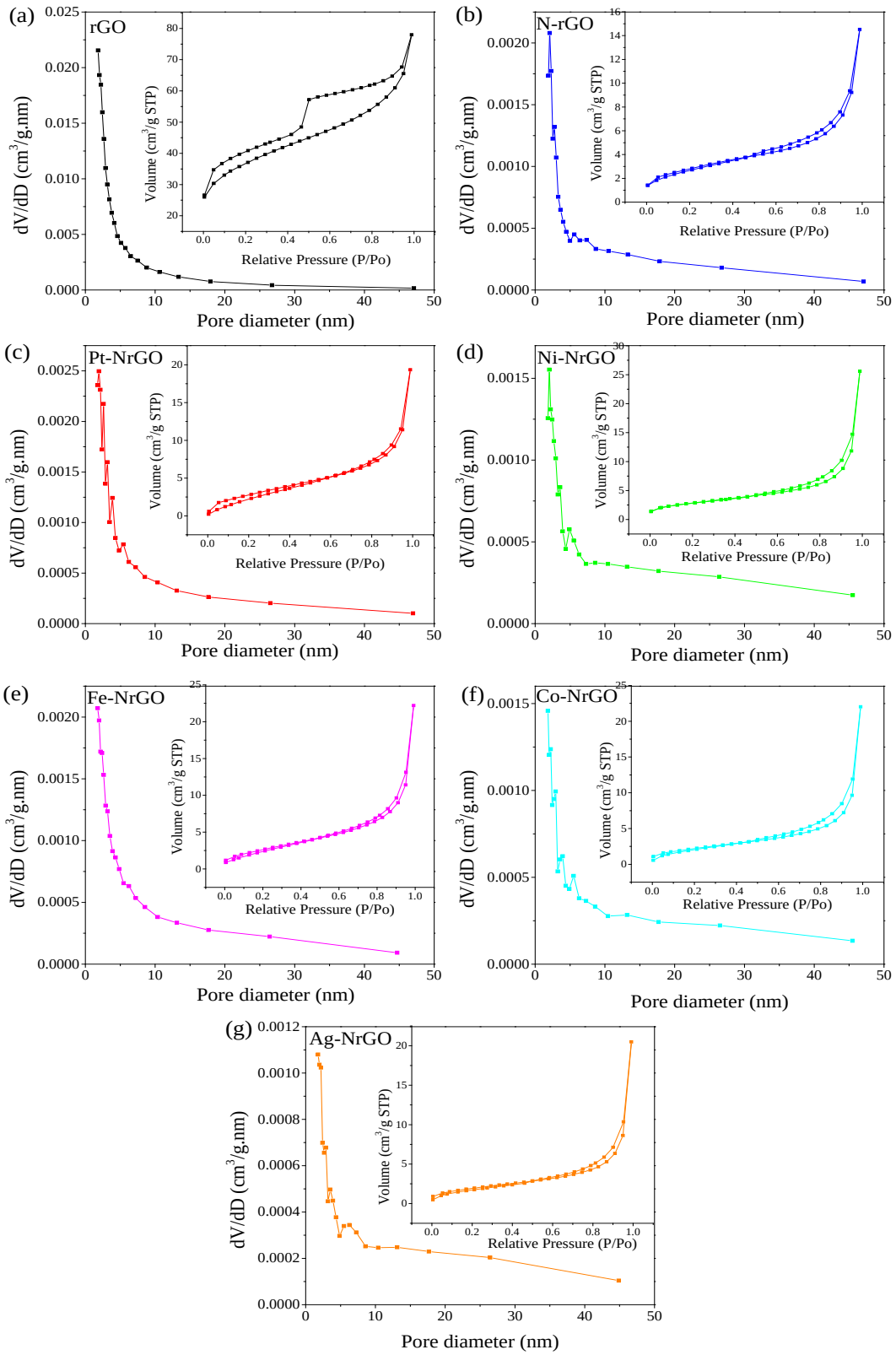

Figure 7.3. Nitrogen sorption isotherm of (a) rGO, (b) N-rGO, (c) Pt-NrGO, (d) Ni-NrGO, (e) Fe-NrGO, (f) Co-NrGO, and (g) Ag-NrGO.

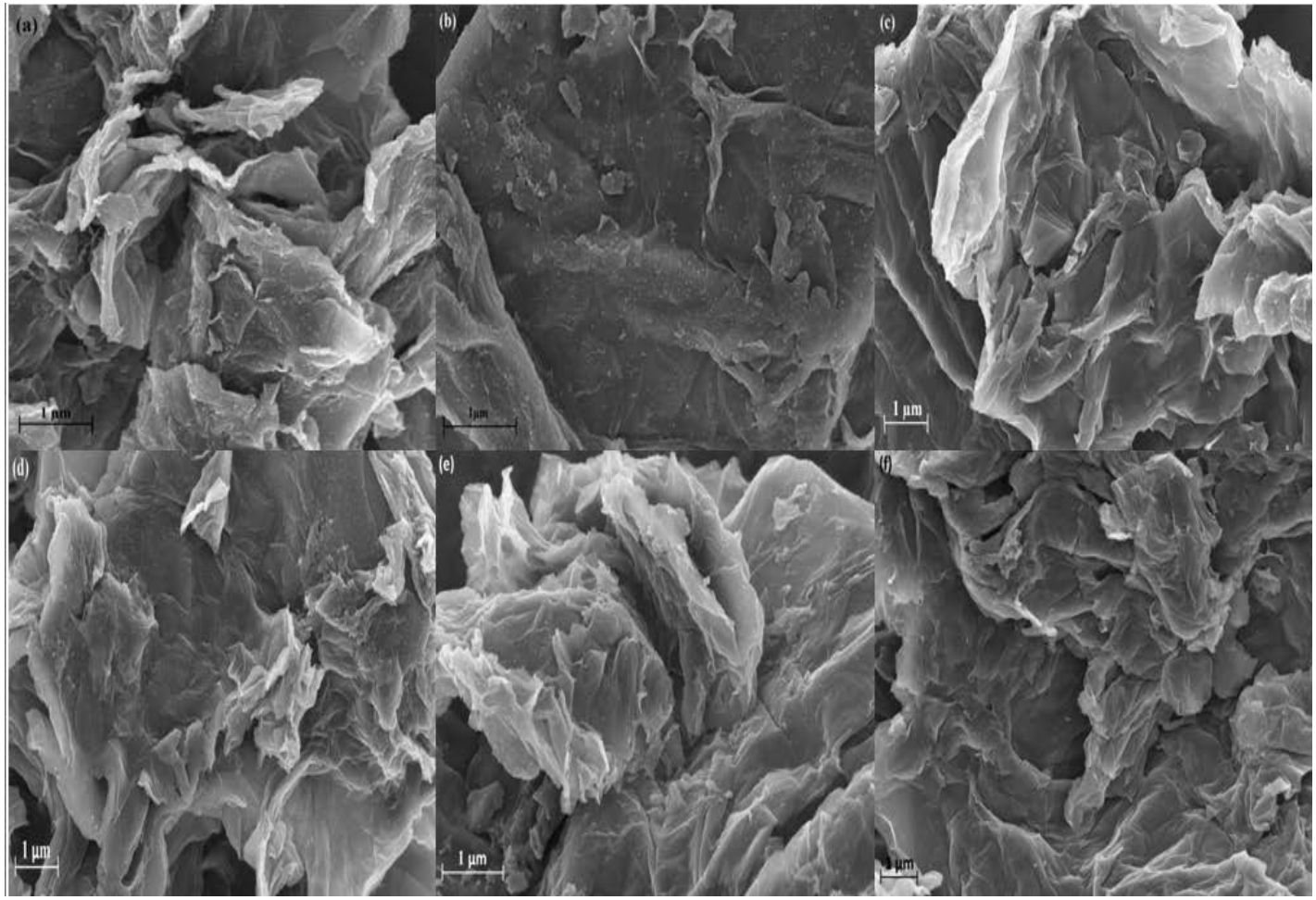

Figure 7.4. SEM images of (a) N-rGO, (b) Pt-NrGO, (c) Ni-NrGO, (d) Fe-NrGO, (e) Co-NrGO, and (f) Ag-NrGO.

Figure 7.5 shows the EDS spectra of N-rGO and various metal-doped N-rGO. Aluminium (Al), platinum (Pt) and magnesium (Mg) were detected in all samples due to the sample stubs and the platinum coating. Carbon (C), oxygen (O), and nitrogen (N) detected in all the samples are attributed to the carbon in graphene and nitrogen doping. A low content of metal shown by the EDS spectra for all different metal-doped N-rGO was ascribed to the low level of metal doping, which is about 1% weight ratio.

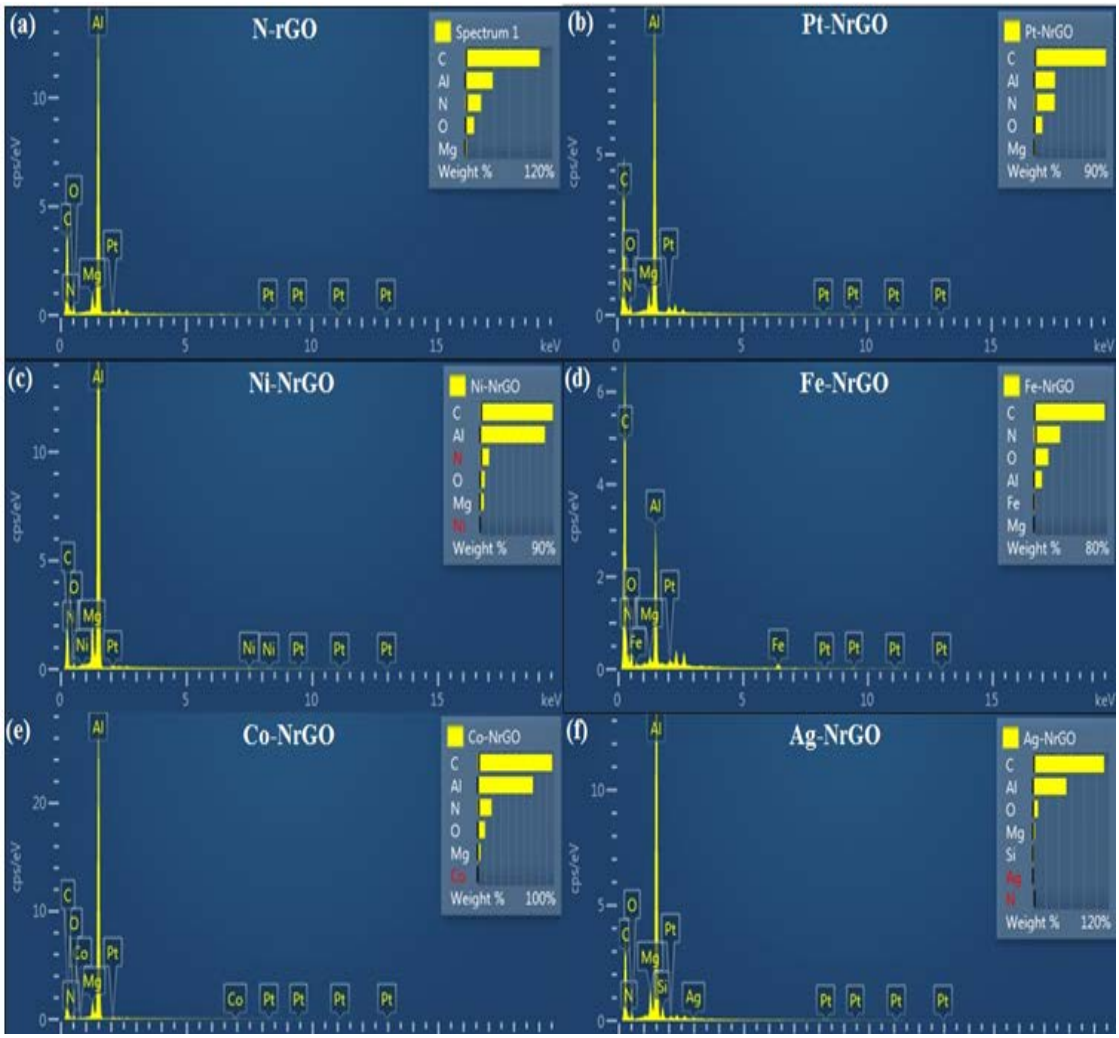

Figure 7.5. EDS spectra of (a) N-rGO, (b) Pt-NrGO, (c) Ni-NrGO, (d) Fe-NrGO, (e) Co-NrGO, and (f) Ag-NrGO.

The thermal behaviour of rGO, N-rGO and different metal-doped N-rGO were investigated by TGA-DSC, as presented by **Figure 7.6**. The analysis was performed in air at a heating rate of 10°C/ min.

Figure 7.6a shows that the weight loss of rGO occurs from 320 up to 580 °C, which may be due to the loss of oxygen functional groups [22]. It was found that from 320 up to 580 °C, the DSC curve shows a characteristic peak at 565 °C for rGO corresponding to thermal decomposition of carbon structure [13]. There was no further weight loss on rGO after reaching the temperature of 580 °C.

Figure 7.6b shows that a weight loss of N-rGO occurs from 370 up to 675 °C. The DSC curve for N-rGO shows a strong exothermal peak at 665 °C. There is no further weight loss after 675 °C for N-rGO.

Figure 7.6c shows that a major weight loss of Pt-NrGO occurs from 370 up to 660 °C due to the combustion and decomposition of carbon skeleton and oxygen functional group. The DSC curve of Pt-NrGO shows a strong exothermal peak at about 645 °C. There is no further weight loss for Pt-NrGO after 660 °C.

Figure 7.6d shows that a major weight loss of Ni-NrGO occurs from 370 up to 630 °C. The DSC curve of Ni-NrGO shows only one exothermal peak at about 570 °C. There is no further weight loss for Ni-NrGO after 630 °C.

Figure 7.6e shows that a major weight loss of Fe-NrGO occurs from 360 up to 570 °C. The DSC curve for Fe-NrGO shows an exothermal peak at 500 °C. There is no further weight loss for Fe-NrGO after 570°C.

Figure 7.6f shows that a major weight loss of Co-NrGO occurs from 370 up to 610 °C. The DSC curve for Co-NrGO shows an exothermal peak at 575 °C. There is no further weight loss for Co-NrGO after 610°C.

Overall, it can be seen in **Figure 7.6a-f** that all material are stable in air before 300 °C and there is no weight loss from the room temperature up to about 100°C. Further observation can be made from Pt-NrGO, Ni-NrGO, Fe-NrGO, and Co-NrGO TGA curves which are showing the remaining weight of 3.8%, 4.5%, 4.4% and 4%, respectively. This residual weight is higher than the metal contents, which might be

caused by incomplete combustion and decomposition of metal-doping N-rGO (metal impurities).

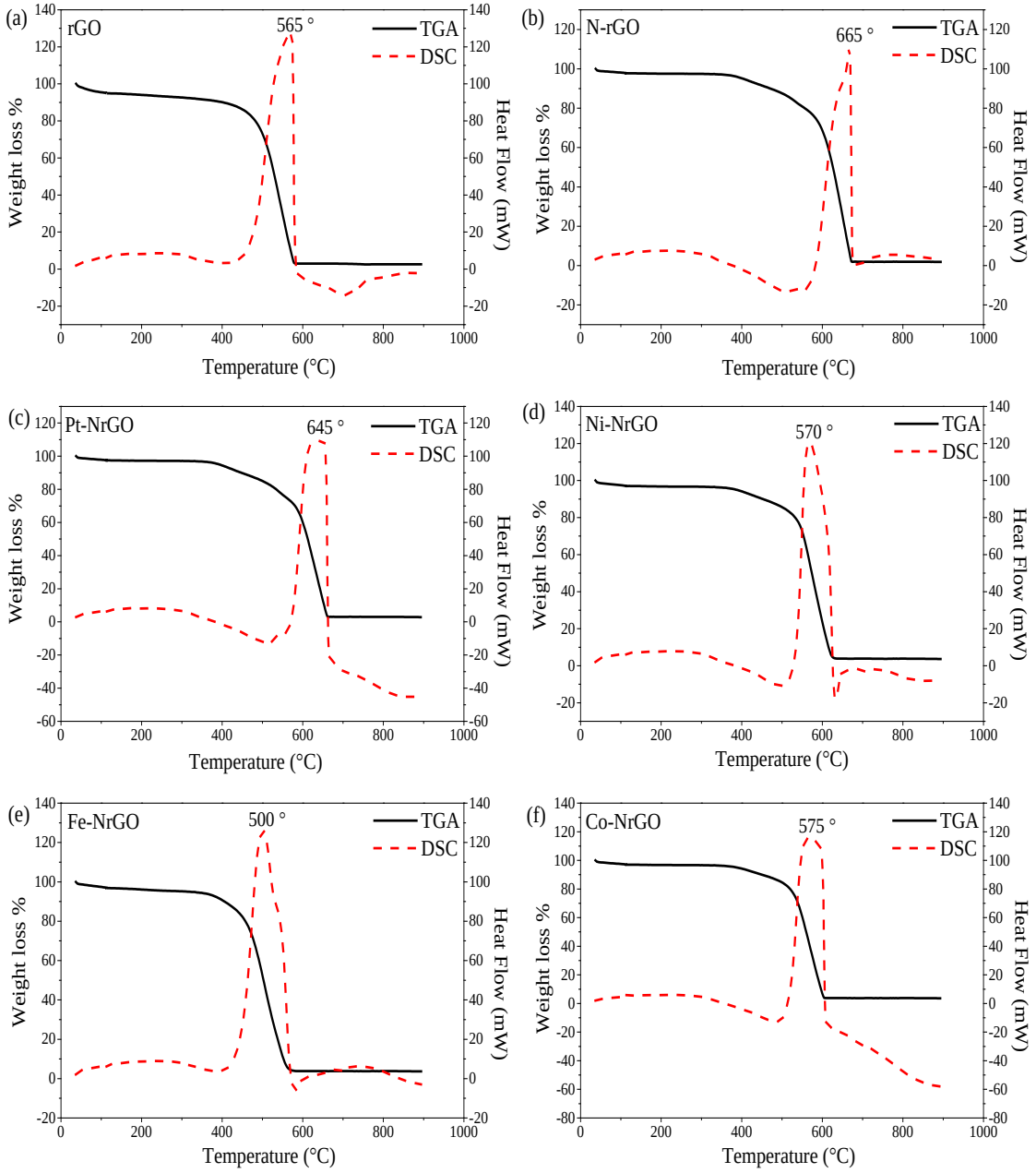

Figure 7.6. TGA/DSC curves of (a) rGO, (b) N-rGO, (c) Pt-NrGO, (d) Ni-NrGO, (e) Fe-NrGO, and (f) Co-NrGO.

Figure 7.7 shows FTIR spectra of N-rGO and different metal-doped N-rGO samples. The spectra of N-rGO and various different metal-doped N-rGO display two characteristic peaks at 2150 and 800 cm^{-1} which are attributed to C≡C and C=C / C=N groups, respectively [23-24]. It is seen that the functional groups are not affected by doping metal into the N-rGO.

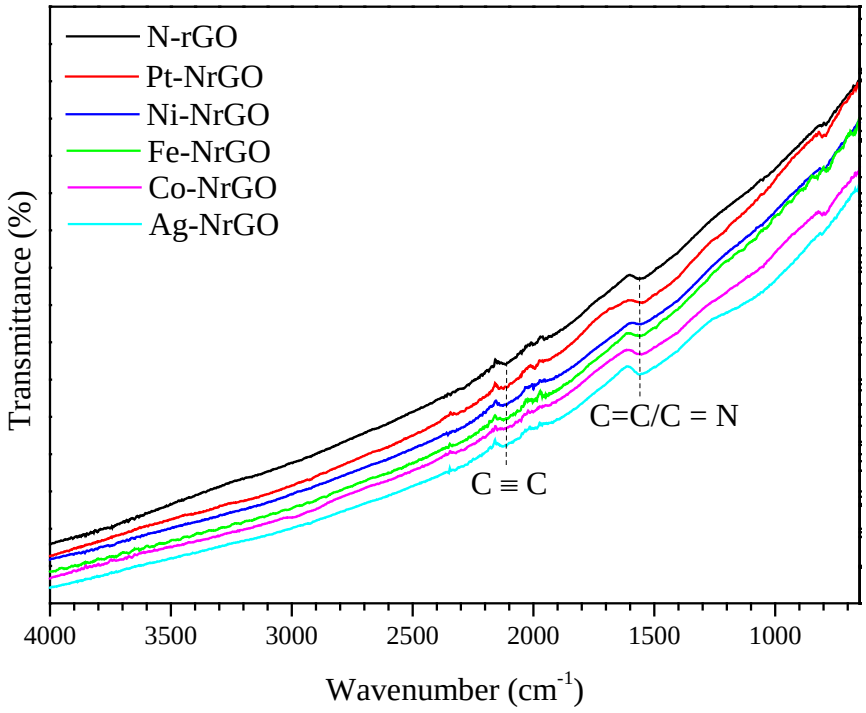

Figure 7.7. FTIR spectra of N-rGO and various metal-doped N-rGO

7.3.2. Catalytic oxidation of phenol

Figure 7.8a shows phenol degradation by PMS activation using rGO, N-rGO and various metal-doped N-rGO catalysts. It is seen that the addition of nitrogen to rGO (N- rGO) improved the catalytic performance of rGO from 18% to 63% phenol removal within 180 min. Further improvement was obtained for the combination of metal and nitrogen for rGO. Phenol removals at 79%, 85%, 95%, and 95% were achieved with Ni- NrGO, Pt- NrGO, Fe- NrGO, and Co- NrGO within 180 min, respectively. A recent study showed that only about 3% of phenol is degraded by N-rGO due to adsorption for 150 min [25]. As seen in **Figure 7.8a**, the degradation of rGO and N-rGO is not because of adsorption but due to catalytic oxidation with the

assistance of PMS. The improvement of phenol degradation using N-rGO and various metal-doped N-rGO may be due to the nitrogen and metal co-doping of rGO which contribute to the electron transfer [13]. This can be described as follow:

$$HSO_5^- + e^- \rightarrow {}^{\bullet}OH + SO_4^{2-} \quad (7.1)$$

$$HSO_5^- + e^- \rightarrow SO_4^{\bullet -} + OH^- \quad (7.2)$$

$$HSO_5^- - e^- \rightarrow SO_5^{\bullet -} + H^+ \quad (7.3)$$

$${}^{\bullet}OH + SO_4^{2-} \rightarrow SO_4^{\bullet -} + OH^- \quad (7.4)$$

$$SO_4^{\bullet -} + OH^- \rightarrow SO_4^{2-} + {}^{\bullet}OH \quad (7.5)$$

$$\text{Phenol} + SO_4^{\bullet -} ({}^{\bullet}OH) \rightarrow \text{several steps} \rightarrow CO_2 + H_2O + SO_4^{2-} \quad (7.6)$$

The moderate improvement of phenol degradation between various metal doped N-rGO may be due to the low SSA values and asymmetric structure of PMS.

Figure 7.8b shows phenol degradation by PDS activation using rGO, N-rGO and various metal doped N-rGO. It is seen that the addition of nitrogen to rGO (N- rGO) improves phenol degradation from 33% to 67% within 180 min. This is as expected from nitrogen doping which induces more electron transfer hence improves phenol degradation. However, the addition of nitrogen and metal to rGO do not have a significant effect on the degradation of phenol by PDS activation, which may be due to the strong bond of symmetric structure of PDS which makes it more difficult to undergone fission of S-O bond [5, 26]. As seen in **Figure 7.8b**, the degradation of rGO and N-rGO is not because of adsorption but due to catalytic oxidation with the help of PDS.

Figure 7.8c shows phenol degradation by H_2O_2 using rGO, N-rGO and various metal-doped N-rGO. It can be seen there is very little improvement on phenol degradation with the addition of nitrogen and metal to rGO. It appears that the presence of H_2O_2 with the addition of various metal-doped N-rGO catalysts lowered the phenol degradation efficiency, which is in agreement to the previous study [26]. This might be due to its inability to generate any free radicals such as hydroxyl ($^{\bullet}OH$) and sulfate ($SO_4^{\bullet -}$) radicals.

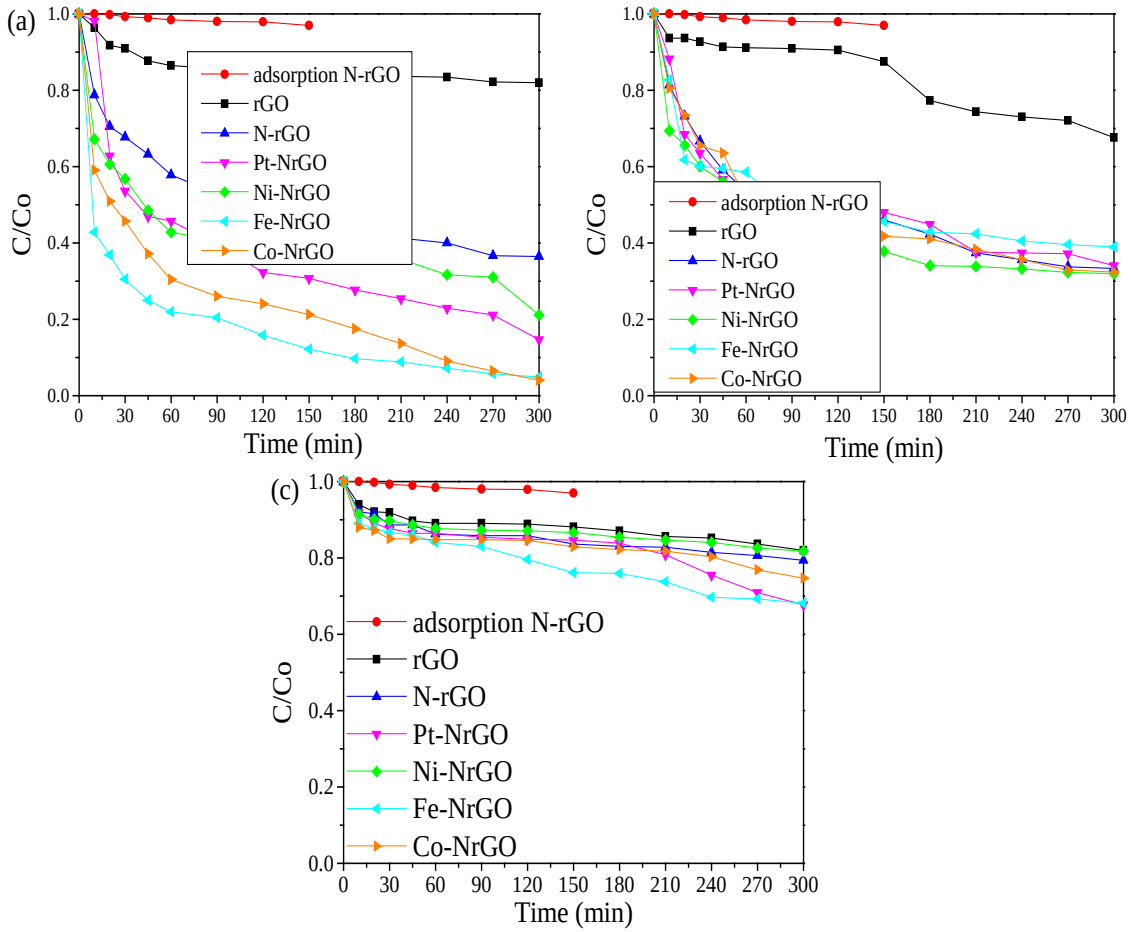

Figure 7.8. Phenol degradation using various catalysts with (a) PMS, (b) PDS, and (c) H_2O_2

7.3.3. Photocatalytic activity

7.3.3.1. Photocatalytic degradation of phenol

Figure 7.9a shows the photodegradation of phenol under UV-vis light using GO, rGO, N-rGO, and Ag-NrGO. It can be seen there is very little effect on phenol degradation with the addition of various catalysts. The degradation of phenol using GO was achieve 20% within 330 min. Slightly improvement in phenol degradation can be seen from 3% adsorption of N-rGO to 15% phenol removal using rGO, N-rGO, and Ag-NrGO with the addition of UV-vis light within 330 min. UV-vis light has wavelength of less than 400 nm, therefore it has higher photon energy which can generate $^{\bullet}OH$ radicals easily. However, $SO_4^{\bullet-}$ radicals are the dominant radicals in phenol degradation, therefore the addition of UV-vis light is insignificant [11].

Figure 7.9b shows the photodegradation of phenol with visible light using GO, rGO, N-rGO, and Ag-NrGO. It can be seen that there is very little effect on phenol degradation with the addition of various catalysts. GO can degrade 35% of phenol within 330 min, while 13.5%, 8 % and 7.3% phenol removals were achieved on rGO, Ag-NrGO, and N-rGO within 330 min, respectively. As seen in **Figure 7.9b**, the performance of N-rGO is purely adsorption even with the addition of visible light. This might be due to longer wavelength of visible light (> 380 nm), therefore it has smaller energy which is not strong enough to generate $^{\bullet}OH$ radicals.

The better GO performances in photodegradation of phenol using visible light only may be due to the many oxygen functional groups that are attached to the GO such as O-H, C-O, C=C and C=O groups [13].

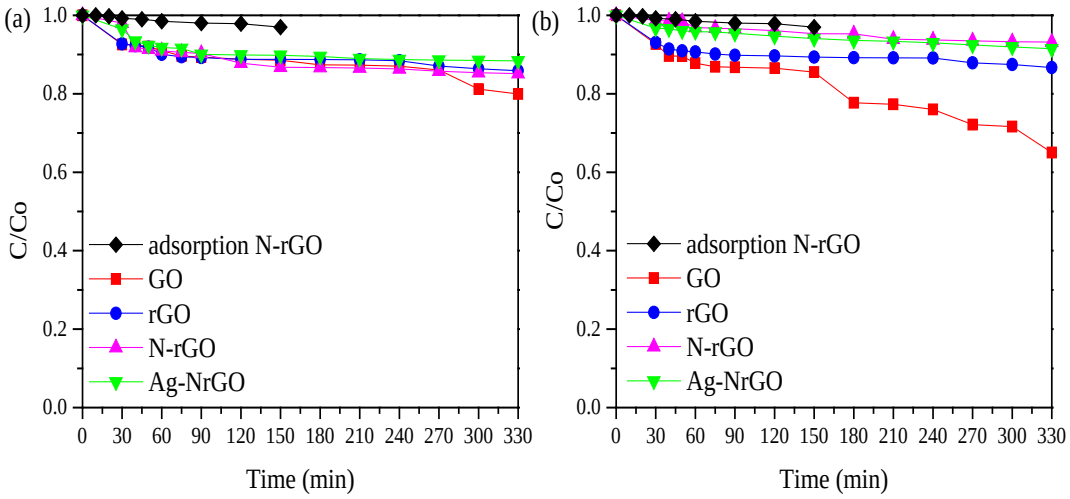

Figure 7.9. Photodegradation of phenol using various catalysts under (a) UV-vis light and (b) visible light.

Figure 7.10a shows the comparisons of phenol degradation using GO under UV-vis light and visible light. It is seen that under UV-vis light, phenol can be degraded up to 20% within 330 min, while under visible light, phenol degradation was achieved at about 35% within 330 min.

Figure 7.10b shows the comparisons of phenol degradation using rGO under UV-vis light and visible light. It is seen that under UV-vis light, phenol can be degraded up to 14% within 330 min, while under visible light, phenol degradation was achieved at about 13% within 330 min.

Figure 7.10c shows the comparisons of phenol degradation using N-rGO under UV-vis light and visible light. It is seen that under UV-vis light, phenol can be degraded up to 15% within 330 min; while under visible light, phenol degradation was achieved at about 7% within 330 min.

Figure 7.10d shows the comparisons of phenol degradation using Ag-NrGO under UV-vis light and visible light. It is seen that under UV-vis light, phenol can be degraded up to 15% within 330 min; while under visible light, phenol degradation was achieved at about 8% within 330 min.

Overall, **Figure 7.10** shows that the photodegradation of phenol was more efficient using UV-vis light for N-rGO and Ag-NrGO, which may be due to the shorter wavelength of UV-vis (< 380 nm), compared to visible only (380 - 700 nm). Shorter wavelength of the UV-vis light reflects higher energy photons which make it easier to break up stronger bonds hence improving the degradation performance [27].

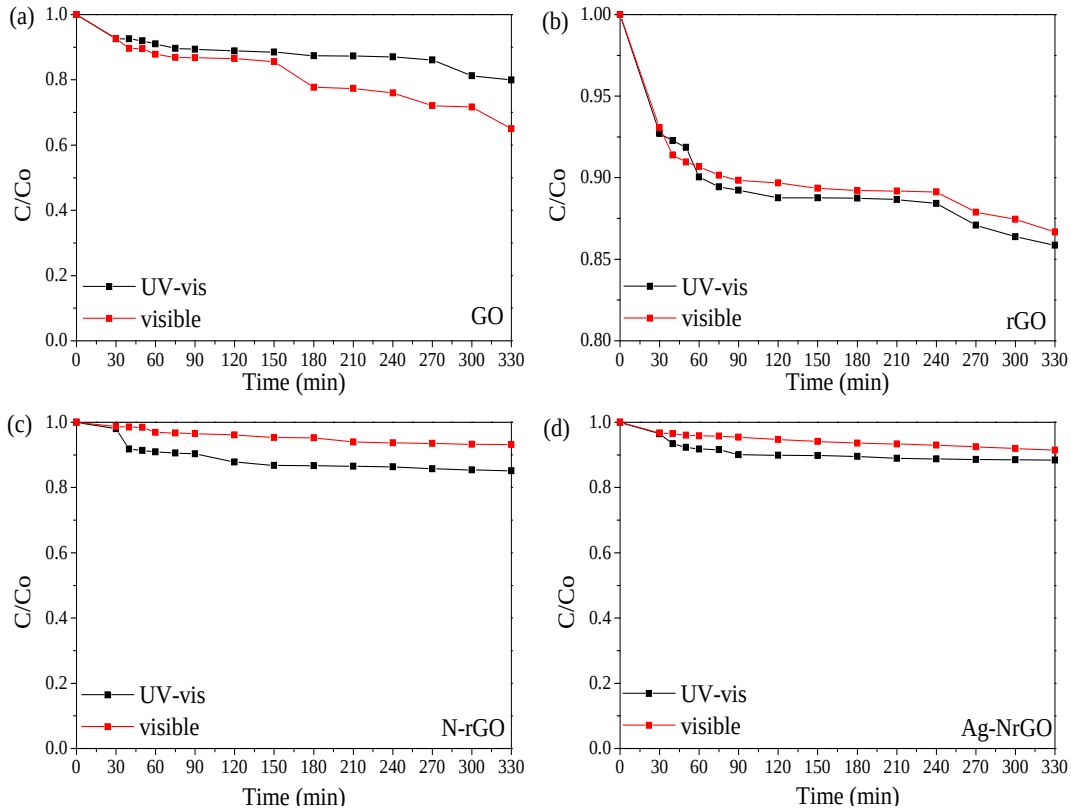

Figure 7.10. Comparison of phenol degradation under UV-vis light and visible light with (a) GO, (b) rGO, (c) N-rGO, and (d) Ag-NrGO.

7.3.3.2 Photocatalytic degradation of methylene blue

Figure 7.11a shows the photodegradation of methylene blue (MB) under UV-vis light using GO, rGO, and N-rGO. It is seen that 85% of MB was degraded within 330 min using GO, while rGO and N-rGO can degrade about 60% MB within 330 min.

Figure 7.11b shows the photodegradation of MB under visible light using GO, rGO, and N-rGO. It is seen that GO can degrade 86% of MB within 330 min, while rGO and N-rGO can degrade about 16% and 5% MB within 330 min, respectively.

Figure 7.11c shows the adsorption of MB using GO, rGO, and N-rGO. It is seen that GO can degrade 88% of MB within 330 min, while rGO and N-rGO can degrade about 17% and 4% MB within 300 min, respectively.

The better GO performances in photodegradation of phenol using UV-vis or visible light may be due to the many oxygen functional groups that are attached to the GO [13, 28].

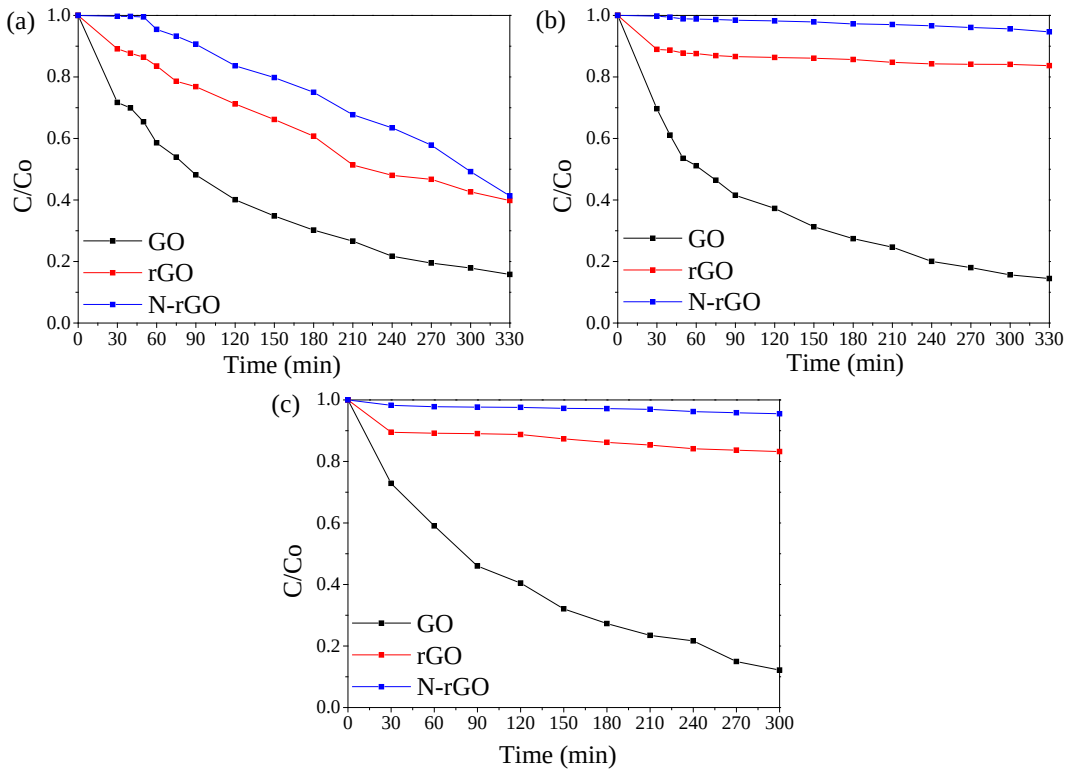

Figure 7.11. Photodegradation of methylene blue using various catalysts under (a) UV-vis light, (b) visible light, and (c) Adsorption of methylene blue using various catalysts.

Figure 7.12a shows the comparisons of MB degradation using GO under UV-vis light, visible light and adsorption (no light). It is seen that under UV-vis light, visible light and adsorption, MB was degraded at about 85 - 88% within 330 min. This result shows that degradation of MB using GO under UV-vis and visible light are mostly just adsorption. Previous studies have shown that GO and rGO have excellent adsorption ability for MB due to the surface chemistry which has several oxygen functional groups such as carbonyl, carboxyl, hydroxyl and epoxide [28-29].

Figure 7.12b shows the comparisons of MB degradation using rGO under UV-vis light, visible light and adsorption (no light). It is seen that under UV-vis light, MB can be degraded up to 60% within 330 min, while under visible light and adsorption, MB degradation was achieved at about 16% within 330 min.

Figure 7.12c shows the comparisons of MB degradation using N-rGO under UV-vis light, visible light and adsorption (no light). It is seen that under UV-vis light, MB can be degraded up to 60% within 330 min, while under visible light and adsorption, MB degradation was achieved at about 5% within 330 min.

Overall, **Figure 7.12** shows that photodegradation of MB was more efficient using UV-vis light on rGO and N-rGO, which may be due to the shorter wavelength of UV-vis (< 400 nm) that provides higher energy photons which make it easier to break stronger bonds. Degradation of MB using rGO and N-rGO under visible light is mostly adsorption, showing that visible light does not have enough energy to degrade MB. There are two types of adsorption: physisorption which depends on porosity or surface geometrical heterogeneity of the catalyst and chemisorptions which depends on the availability of the basal planes in the catalyst (surface chemical heterogeneity). In this chapter, degradation of MB and phenol are not significant due to low SSA values for physisorption and the presence of surface oxygen sites on GO, rGO, and N-rGO for chemisorptions.

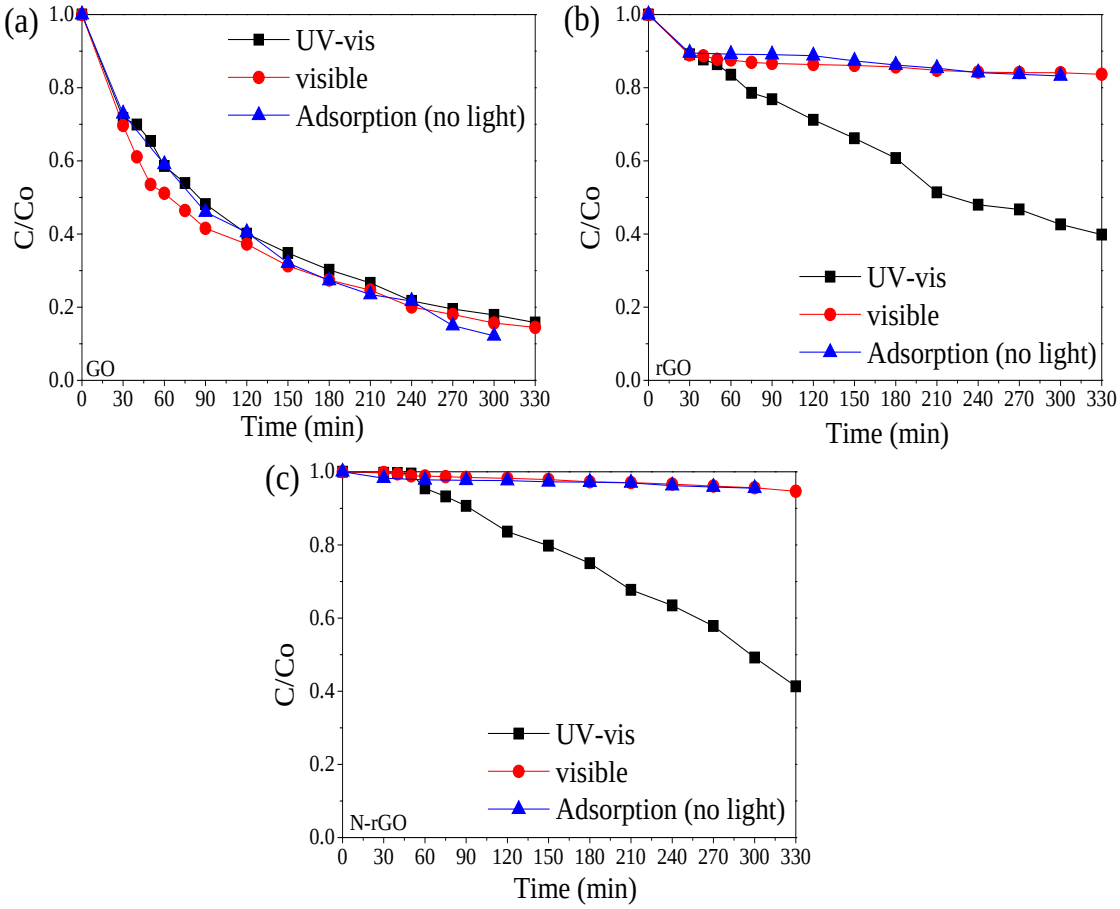

Figure 7.12. Comparison of MB degradation under adsorption condition (no light), UV-vis and visible light with (a) GO, (b) rGO and (c) N-rGO.

7.4. Conclusions

In this study, a simple method was used to prepare metal and nitrogen co-doped graphene (metal-N-rGO) by a simultaneous nitrogen and metal doping of GO at a temperature of 350 °C. Various characterisation techniques showed that crystal, structural and compositional modifications can be achieved by heteroatoms doping or co-doping. The results showed that modified N-rGO enhanced the catalytic oxidation of phenol in aqueous solution by PMS activation. The moderate improvement of phenol degradation may be due to the nitrogen and metal co-doping of rGO which contributes to the electron transfer. There is no significant effect observed in phenol degradation by PDS and H_2O_2 activation using various metals-doped N-rGO, which may be due to the strong bond of symmetrical structure of PDS and its inability to generate hydroxyl radicals (to degrade phenol), respectively. Nevertheless, GO showed better photodegradation of both phenol and methylene blue. This may be due to the oxygen functional groups that are attached to the GO.

References

1. Saputra, E.; Muhammad, S.; Sun, H.; Patel, A.; Shukla, P.; Zhu, Z. H.; Wang, S., α-MnO2 activation of peroxymonosulfate for catalytic phenol degradation in aqueous solutions. *Catalysis Communications* **2012,** *26*, 144-148.

2. P. Shukla, S. W., H. Q. Sun, H. M. Ang and M. O. Tade, Activated carbon suported cobalt catalysts for advanced oxidation of organic contaminants in aqueous solution. *Appl. Catal. B: Environ.* **2010,** *100*, 529-534.

3. Parsons, S., *Advanced Oxidation Processes for Water and Wastewater Treatment*. IWA Publishing: **2004**.

4. Howe, K. J.; Hand, D. W.; Crittenden, J. C.; Trussell, R. R.; Tchobanoglous, G., *Principles of Water Treatment*. Wiley: **2012**.

5. Duan, X. G.; Sun, H. Q.; Kang, J.; Wang, Y. X.; Indrawirawan, S.; Wang, S. B., Insights into Heterogeneous Catalysis of Persulfate Activation on Dimensional-Structured Nanocarbons. *ACS Catal.* **2015,** *5* (8), 4629-4636.

6. H. Sun, Y. W., S. Liu, L. Gei, L. Wang, Z. Zhu, and S. Wang, Facile synthesis of nitrogen doped reduced graphene oxide as a superior metal-free catalyst for oxidation. *RSC. Chem. Comm.* **2013,** *10*.

7. Saputra, E.; Muhammad, S.; Sun, H. Q.; Ang, H. M.; Tade, M. O.; Wang, S. B., Different Crystallographic One-dimensional MnO2 Nanomaterials and Their Superior Performance in Catalytic Phenol Degradation. *Environ. Sci. Technol.* **2013,** *47* (11), 5882-5887.

8. Liu, S.; Li, D.; Sun, H.; Ang, H. M.; Tadé, M. O.; Wang, S., Oxygen functional groups in graphitic carbon nitride for enhanced photocatalysis. *Journal of colloid and interface science* **2016,** *468*, 176-182.

9. Wang, S. B.; Ang, H. M.; Tade, M. O., Volatile organic compounds in indoor environment and photocatalytic oxidation: State of the art. *Environ. Int.* **2007,** *33* (5), 694-705.

10. Sun, H.; Bai, Y.; Liu, H.; Jin, W.; Xu, N., Photocatalytic decomposition of 4-chlorophenol over an efficient N-doped TiO 2 under sunlight irradiation. *Journal of Photochemistry and Photobiology A: Chemistry* **2009,** *201* (1), 15-22.

11. Sun, H.; Feng, X.; Wang, S.; Ang, H. M.; Tadé, M. O., Combination of adsorption, photochemical and photocatalytic degradation of phenol solution over

supported zinc oxide: Effects of support and sulphate oxidant. *Chem. Eng. J.* **2011,** *170* (1), 270-277.

12. H. Sun, H. L., G.Zhou, and S. Wang, Supported cobalt catalysts by one pot aqueous combustion synthesis for catalytic phenol degradation. *J. Colloid Interface Sci.* **2013,** *394*, 394-400.

13. Indrawirawan, S.; Sun, H. Q.; Duan, X. G.; Wang, S. B., Low temperature combustion synthesis of nitrogen-doped graphene for metal-free catalytic oxidation. *J. Mater. Chem. A* **2015,** *3* (7), 3432-3440.

14. Indrawirawan, S.; Sun, H. Q.; Duan, X. G.; Wang, S. B., Nanocarbons in different structural dimensions (0-3D) for phenol adsorption and metal-free catalytic oxidation. *Appl. Catal. B-Environ.* **2015,** *179*, 352-362.

15. Busca, G., *Heterogeneous Catalytic Materials: Solid State Chemistry, Surface Chemistry and Catalytic Behaviour*. Elsevier: **2014**.

16. Wang, Y. X.; Sun, H. Q.; Ang, H. M.; Tade, M. O.; Wang, S. B., 3D-hierarchically structured MnO2 for catalytic oxidation of phenol solutions by activation of peroxymonosulfate: Structure dependence and mechanism. *Appl. Catal. B-Environ.* **2015,** *164*, 159-167.

17. Esteves, A.; Oliveira, L. C.; Ramalho, T. C.; Goncalves, M.; Anastacio, A. S.; Carvalho, H. W., New materials based on modified synthetic Nb 2 O 5 as photocatalyst for oxidation of organic contaminants. *Catalysis Communications* **2008,** *10* (3), 330-332.

18. Duan, X.; Indrawirawan, S.; Sun, H.; Wang, S., Effects of nitrogen-, boron-, and phosphorus-doping or codoping on metal-free graphene catalysis. *Catalysis Today* **2015,** *249*, 184-191.

19. Zhang, H.; Lv, X.; Li, Y.; Wang, Y.; Li, J., P25-graphene composite as a high performance photocatalyst. *ACS nano* **2009,** *4* (1), 380-386.

20. S. Liu, H. S., S. Liu and S. Wang, Graphene facilitated visible light photodegradation of methylene blue over titanium dioxide photocatalysts. *Chem. Eng. J* **2013,** *214*, 298-303.

21. Wen, Q.; Wang, S.; Yan, J.; Cong, L.; Pan, Z.; Ren, Y.; Fan, Z., MnO 2–graphene hybrid as an alternative cathodic catalyst to platinum in microbial fuel cells. *J. Power Sources* **2012,** *216*, 187-191.

22. Loryuenyong, V.; Totepvimarn, K.; Eimburanapravat, P.; Boonchompoo, W.; Buasri, A., Preparation and characterization of reduced graphene oxide sheets via

water-based exfoliation and reduction methods. *Advances in Materials Science and Engineering* **2013,** *2013*.

23. S. Boncel, S. W. P., V. Geiser, M.S.P. Shaffer, and K.K.K. Koziol, En route to controlled catalytic CVD synthesis of densely packed and vertically aligned nitrogen-doped carbon nanotube arrays. *Beilstein J. Nanotechnol.* **2014,** *5*, 219-233.

24. Meyers, R. A., *Encyclopedia of Analytical Chemistry*. Wiley: **2012**.

25. Sun, H. Q.; Wang, Y. X.; Liu, S. Z.; Ge, L.; Wang, L.; Zhu, Z. H.; Wang, S. B., Facile synthesis of nitrogen doped reduced graphene oxide as a superior metal-free catalyst for oxidation. *Chem. Commun.* **2013,** *49* (85), 9914-9916.

26. Duan, X. G.; Ao, Z. M.; Sun, H. Q.; Zhou, L.; Wang, G. X.; Wang, S. B., Insights into N-doping in single-walled carbon nanotubes for enhanced activation of superoxides: a mechanistic study. *Chem. Commun.* **2015,** *51* (83), 15249-15252.

27. Andrady, A. L., Ultraviolet radiation and polymers. In *Physical properties of polymers handbook*, Springer: **2007**, pp 857-866.

28. Bradder, P.; Ling, S. K.; Wang, S.; Liu, S., Dye Adsorption on Layered Graphite Oxide. *Journal of Chemical & Engineering Data* **2011,** *56* (1), 138-141.

29. Ramesha, G. K.; Vijaya Kumara, A.; Muralidhara, H. B.; Sampath, S., Graphene and graphene oxide as effective adsorbents toward anionic and cationic dyes. *Journal of Colloid and Interface Science* **2011,** *361* (1), 270-277.

CHAPTER 8. CONCLUSIONS AND FUTURE WORK

8.1. Concluding comments

The main objectives of this research are to develop highly efficient and robust non-metal and metal doped graphene for catalytic oxidation of aqueous organic contaminants, such as phenol, nitrobenzene and methylene blue. With the addition of oxidants such as peroxymonosulfate (PMS), persulfate (PDS) or hydrogen peroxide (H_2O_2), the effects of the carbon catalysts to activate those oxidants on degradation of contaminants were investigated. These objectives have been achieved satisfactorily. Various nano-carbons have been synthesized and developed such as graphene, nitrogen doped graphene (N-rGO), various metal doped N-rGO, graphene nanoplate (GNP), fullerene (C60), single-walled carbon nanotube (SWCNT), nitrogen doped SWCNT (N-SWCNT) and mesoporous carbons. Various characterization techniques were done to study the physical properties of carbon catalysts and also to study free radicals generated during the catalytic activation. Major results of this research study are further described in this section.

8.1.1. Catalytic oxidation of nitrogen doped graphene

A simple method was used to successfully prepare nitrogen-doped reduced graphene oxide (N-rGO) by a simultaneous reduction and nitrogen doping of GO at low temperatures ranging from 300 to 400 °C. Comprehensive studies by a variety of characterization techniques suggested that significant crystal, structural and compositional modifications could be achieved by simply varying the calcination temperature for synthesis of highly efficient metal-free catalysts. These N-rGO materials as green catalysts were demonstrated to be efficient in catalytic activation of PMS for phenol degradation in water. For N-rGO via thermal annealing temperatures between 300 to 325 °C, the improvement of phenol degradation may be primarily due to the nitrogen dopant. Whereas for N-rGO from thermal annealing temperatures between 350 to 400 °C, the improvement of phenol degradation may be due to both nitrogen dopants and relatively high SSA. Combination of EPR studies

and quenching tests indicated that N-rGO can activate PMS to produce both hydroxyl and sulfate radicals, which induce phenol degradation.

8.1.2. Catalytic oxidation of 0D-3D nano-carbons

Properties of carbon nanomaterials in different structural dimensions (0-3D) before and after thermal annealing employing nitrogen gas at 350 °C were investigated and used for phenol adsorption and metal-free catalytic oxidation. The materials are C_{60}, SWCNTs (single wall carbon nanotubes), GNP (graphene nanoplate), CMK-3 and CMK-8 (ordered mesoporous carbon). Pristine nanocarbons showed varied phenol adsorption and the adsorptive performances followed the order of GNP ~ CMK-3 > CMK-8 > SWCNTs > C_{60}, while the catalysis followed another order of CMK-3 > SWCNTs > CMK-8 > GNP > C_{60}. Thermal treatment at a lower temperature would not significantly change the SSA and crystal structure but could dramatically modify the surface functional groups. As a result, enhanced adsorption was found on SWCNTs by 2-fold and superior catalysis was achieved on CMK-8 by 7.5-fold after thermal treatment. Structural dimension can influence nanocarbon performance in adsorption and catalysis and surface oxygen functionality can also affect the adsorption and catalysis. 0D C_{60} exhibited the lowest adsorption capacity and catalytic activity while 3D CMK-3 generally presented higher adsorption capacity and catalytic activity than 1D SWCNT and 2D GNP. The adsorption and catalysis were controlled by the integrated effects of structure, surface and chemical composition of the different nanocarbons.

8.1.3. Catalytic oxidation of N-SWCNT with PMS activation

N-SWCNT was synthesized by simple nitrogen doping of SWCNT at 700 °C. The excellent adsorption and PMS activation for nitrobenzene degradation with/without N-SWCNT were investigated at different reaction temperatures from 5 °C to 75 °C. Nitrobenzene was selected as the target organic and electron acceptor for catalytic evaluation in both binary and ternary systems. Nitrobenzene degradation, quenching test, and radical trapping method indicated that the PMS activation with/without N-SWCNT is a temperature-dependent process. The thermal activation tends to improve PMS activation to generate hydroxyl radicals and further improve the effectiveness of nitrobenzene degradation. Hydroxyl radicals contribute as the main

radicals to nitrobenzene degradation on PMS with and without N-SWCNT. In the binary system (NB and PMS), the ˙OH radicals were generated through the hydrolysis process; whereas in the ternary system (NB, PMS and N-SWCNT), the ˙OH radicals were generated through the electron transfer process. These ˙OH radicals can react with nitrobenzene non-selectively and convert it into non-toxic inorganic compounds. In the binary system (NB and N-SWCNT), the nitrobenzene removal is attributed to the physisorption and chemisorptions via π electron donor-acceptor mechanisms. Moreover, PMS as an electron acceptor and metal-free N-SWCNT catalyst as an electron donor show a promising result for removal of nitrobenzene in aqueous solution with controlled reaction temperatures. Although both PMS and NB are electron acceptors, it appears that PMS is more attracted to N-SWNCT.

8.1.4. Catalytic oxidation of N-SWCNT with PDS activation

PDS activation for nitrobenzene degradation with/without N-SWCNT was also investigated at different reaction temperatures from 5 to 75 °C. PDS and PMS activations for phenol degradation were investigated at temperature 55 to 75 °C. Thermal effect enhanced PDS/PMS activation to generate hydroxyl radicals and further improved the effectiveness of nitrobenzene and phenol degradation. Both symmetric PDS and asymmetric PMS can degrade NB and phenol. However, different radicals play a major role in the mechanism degradation. Hydroxyl radicals contribute as the main radicals to nitrobenzene degradation on PDS with and without N-SWCNT, while sulfate radicals play a dominant role in phenol degradation. In the binary system (NB and PDS), the ˙OH radicals were generated through the hydrolysis process and nitrobenzene removal is attributed to the physisorption and chemisorption via π electron donor-acceptor mechanisms. In the ternary system (NB, PDS and N-SWCNT), the ˙OH radicals were generated through the electron transfer process.

8.1.5. Catalytic and photocatalytic oxidation by metal-doped N-rGO

A simple method was used to prepare metal and nitrogen co-doped graphene (metal-N-rGO) by a simultaneous nitrogen and metal doping of GO at a low temperature of 350 °C. Various characterisation techniques showed that crystal, structural and

compositional modifications can be achieved by heteroatoms doping or co-doping. The results showed that modified N-rGO enhanced the catalytic oxidation of phenol in aqueous solution by PMS activation. The moderate improvement of phenol degradation may be due to the nitrogen and metal co-doping of rGO which contributes to the electron transfer. There is no significant effect observed in phenol degradation by PDS and H_2O_2 activation using various metals-doped N-rGO, which may be due to the strong bond of symmetrical structure of PDS and its inability to generate hydroxyl radicals (to degrade phenol), respectively. Nevertheless, GO showed better photodegradation of both phenol and methylene blue. This may be due to the oxygen functional groups that are attached to the GO.

8.1.6. Adsorption of phenol and nitrobenzene in N-SWCNT.

Adsorptions of phenol and nitrobenzene in N-SWCNT were carried out to investigate the different characteristics of those pollutants in the adsorption mechanism. The adsorption of phenol in N-SWCNT is negligible compared to that of nitrobenzene in N-SWCNT. This result may be explained by the electron donor-acceptor mechanism. Here, both phenol and SWCNT have very little interaction because both of them are electron donors. In contrary, nitrobenzene as an electron acceptor has a higher interaction with N-SWCNT.

8.2. Recommendation for future work

This research focused on phenol and nitrobenzene degradation with the addition of PMS and PDS in both binary and ternary catalytic oxidation systems. However, further studies need to be done for future work, such as:

1. For binary systems
    - Pollutant and catalyst

      Discovering more different carbon catalysts for adsorption process for degradation of different organic pollutants (besides phenol and nitrobenzene). To find out which organic pollutant is an electron acceptor or donor and which catalyst is an electron donor.
    - Pollutant and oxidant

      More investigation on catalytic oxidation of different oxidants' activation for different organic pollutants degradation should be done.

Improving catalytic oxidation by binary systems might be a major breakthrough to reduce the usage of either catalyst or oxidant.

2. For ternary systems
    - Pollutant, oxidant and catalyst

      Catalytic oxidation by strong oxidants such as PMS, PDS or H_2O_2 activation should be done using different variety of organic pollutants (besides phenol and nitrobenzene) in order to understand the mechanism and free radicals that are involved in the degradation processes.
    - Further studies on catalysts durability and the target pollutants efficiencies in the complex water matrix should be done to eliminate inefficient catalysts and study their compatibilities with the target contaminants.
    - Determination of free radicals using different organic pollutants with the addition of quenching agents, methanol and TBA, to find out whether hydroxyl or sulfate radicals that plays dominant roles in the degradation process. Comprehensive understanding on EPR to elucidate this mechanism.
    - This research was analysed without considering the intermediate products generated in the degradation process of phenol and nitrobenzene. Therefore, further study needs to be done to investigate these intermediates to get more accurate results and understanding.
    - The leach of metal concentration in the water after treatment using metal modified graphene as the catalyst should be monitored.